Dissertation

submitted to the

Combined Faculty of Natural Sciences and Mathematics

of the Ruperto Carola University Heidelberg, Germany

for the degree of

Doctor of Natural Sciences

presented by

Dipl.- Pharm. Juliane Buhl née Hohloch

born in: Tuebingen, Germany

Oral examination: 17.06.2019

The senescence-associated secretory phenotype regulates the growth behavior of pediatric pilocytic astrocytoma

Referees: Prof. Dr. Peter Angel

Prof. Dr. Olaf Witt

Declaration

I hereby declare that I have written the submitted dissertation “The senescence-associated secretory phenotype regulates the growth behavior of pediatric pilocytic astrocytoma” myself, using only the cited literature and sources.

I hereby declare that I have not applied to be examined at any other institution, nor have I used the dissertation in this or any other form at any other institution as an examination paper, nor submitted it to any other faculty as a dissertation.

Parts of the text contain passages from Buhl *et al.* 2018, Clinical Cancer Research, and have been originally written by myself.

Juliane Buhl

ABSTRACT

Brain tumors are the second most common malignancy diagnosed in children, with low-grade gliomas (LGG) being the most common childhood brain tumor, and pilocytic astrocytoma (PA) the most common LGG. LGGs are typically driven by aberrant MAPK pathway activation commonly induced by *BRAF* fusions or mutations. These genetic alterations activate the tumor-suppressive mechanism oncogene-induced senescence (OIS), resulting in growth arrest of transformed cells. OIS has been shown to be regulated by a complex network of inflammatory molecules, referred to as the senescence-associated secretory phenotype (SASP). Single markers of OIS have been detected in primary PAs, but its functional role in PA remains unknown to date.

A patient-derived PA cell line with a *BRAF* fusion was generated via lentiviral transduction with a doxycycline-inducible construct coding for the SV40 Large T antigen (SV40-TAg). This novel PA model, DKFZ-BT66, enabled the analysis of the growth-arrested OIS state of PA cells as well as the proliferating state during SV40-TAg expression. Both conditions were characterized and analyzed by means of gene expression profiling (GEP), western blot, ELISA and cell viability testing via automated trypan blue exclusion staining. Primary PA material was analyzed by GEP as well as a multiplex assay.

The SASP was upregulated in the OIS state of the human PA cell line DKFZ-BT66 as well as in primary human and murine PAs. Conditioned medium of senescent cells was shown to arrest growth and induce the senescence-characteristic enlarged cellular phenotype in proliferating PA cells. The SASP factors IL1B and IL6 were both upregulated and secreted by senescent PA cells and their respective pathways were shown to be regulated during OIS. Treatment of proliferating DKFZ-BT66 cells with recombinant IL1B (rIL1B), but not rIL6, reduced cell growth of proliferating PA cells. Both SASP expression as well as changes in cell morphology, reminiscent of the enlarged senescent phenotype, were induced by rIL1B treatment. However, neither pharmacological nor shRNA-mediated inhibition of the IL1 or IL6 pathway led to a bypass of the OIS state in the DKFZ-BT66 cell line. Treatment with the anti-inflammatory drug dexamethasone induced regrowth of senescent DKFZ-BT66 cells and suppressed SASP gene expression. The clinical relevance of the SASP in PA was confirmed by the identification of two patient cohorts with differing clinical outcome related to SASP expression. Elevated expression of the SASP as well as of IL1B alone was predictive for favorable progression-free survival (PFS) in PA patients independent of tumor resection status. To exploit OIS therapeutically, DKFZ-BT66 cells were treated with senolytic BCL2 family member inhibitors, specifically targeting senescent cells. Senescent PA cells were more sensitive to senolytics in comparison to proliferating DKFZ-BT66 cells or normal human astrocytes.

In summary, the SASP was shown to regulate OIS in pediatric PA, with IL1B as an important mediator. Elevated SASP expression was prognostic for a favorable PFS in the analyzed cohort and will have to be validated as a prognostic marker in prospective clinical trials. The combination of senolytic agents, targeting senescent PA cells, together with chemotherapy, targeting cycling PA cells, may be a novel therapeutic approach and will have to be evaluated in further preclinical studies.

ZUSAMMENFASSUNG

Niedriggradige Gliome (low-grade gliomas, LGG) sind die häufigsten Hirntumore im Kindesalter, und pilozytische Astrozytome (PA) die häufigsten LGGs. Die Tumorentität zeichnet sich durch anhaltend gesteigerte Aktivität des MAPK Signalwegs aus. Induziert durch genetische Veränderungen einzelner Faktoren des Signalwegs, wird ein Schutzmechanismus namens Onkogen-induzierter Seneszenz (OIS) aktiviert, der das Wachstum der genetisch veränderten Zellen stoppt. In früheren Studien wurde bereits gezeigt, dass die OIS durch ein Netzwerk von Entzündungsmediatoren, dem sogenannten Seneszenz-assoziierten sekretorischen Phänotyp (SASP), reguliert werden kann. Welche Rolle die OIS in Bezug auf das Wachstumsverhalten von PAs spielt ist bis heute ungeklärt.

Mit Hilfe des ersten, aus Patientenmaterial gewonnen Zellmodells eines PAs mit einer *BRAF*-Fusion, DKFZ-BT66, konnte die Expression von SASP Faktoren in PA-Zellen nachgewiesen werden und der Einfluss des SASP auf das Wachstum von PA-Tumorzellen untersucht werden. Durch eine reversible Doxycyclin-induzierbare Aktivierung des Zellwachstum mittels SV40 Large T Antigen Expression ermöglicht das DKFZ-BT66 Modell die Untersuchung von PA-Zellen im Wachstum sowie im Wachstums-Stopp unter dem Einfluss der OIS. Beide Stadien wurden anhand von Genexpressionsprofilen (GEPs), Westernblots, ELISAs und Zellviabilitätstests verglichen. Primäre PA Tumoren wurden zudem mit GEPs und einem Multiplex Assay untersucht.

Die untersuchten SASP Faktoren wurden sowohl in primären humanen und murinen PA Tumoren, als auch im seneszenten Zustand der DKFZ-BT66 Zelllinie, erhöht exprimiert. Konditioniertes Medium von seneszenten DKFZ-BT66 Zellen löste einen Wachstumsarrest in proliferierenden PA-Zellen aus. Die zwei SASP Faktoren IL1B und IL6 wurden von seneszenten PA-Zellen sekretiert und beide Signalwege waren im seneszenten Zustand der DKFZ-BT66 Zelllinie reguliert. Die Stimulation von proliferierenden Zellen mit dem rekombinanten (r) Zytokin rIL1B, nicht aber mit rIL6, führte zu reduziertem Wachstum der PA-Zellen und induzierte die Expression der SASP Faktoren. Die Behandlung von seneszenten Zellen mit entzündungshemmenden Medikamenten wie Dexamethason führte zur Wiederaufnahme des Wachstums von seneszenten PA-Zellen und hemmte die Expression von SASP Faktoren. Eine hohe IL1B sowie SASP Expression in primären PA Tumoren konnte mit einem guten Progressions-freien Überleben der PA Patienten assoziiert werden. Behandlungen mit senolytischen Medikamenten zeigte ein Ansprechen bei niedrigen Konzentrationen in seneszenten im Vergleich zu proliferierenden DKFZ-BT66 Zellen.

Die hier präsentierten Daten liefern damit erste Beweise für eine Regulation der OIS und dem damit verbundenen Tumorzellwachstum durch die SASP Faktoren, mit IL1B als einem wichtigen Mediator, im kindlichen PA. Die Messung der SASP Genexpression könnte zukünftig eine Vorhersage des Progressions-freien Überlebens von PA Patienten ermöglichen. Ein therapeutischer Ansatzpunkt könnte die Behandlung mit senolytischen Medikamenten bieten, welche durch eine Kombination mit Chemotherapie sowohl die teilenden als auch die ruhenden, seneszenten Tumorzellen angreifen könnte.

Abbreviations

AST	Aspartate aminotransferase
BCL2	B-cell lymphoma-2
BRAF	v-raf murine sarcoma viral oncogene homolog B
CDKN1A	Cyclin dependent kinase inhibitor 1A
CDKN1B	Cyclin dependent kinase inhibitor 1B
CDKN2A	Cyclin dependent kinase inhibitor 2A
CDKN2B	Cyclin dependent kinase inhibitor 2B
CEBPB	CAAT/enhancer-binding protein beta
CNS	Central nervous system
CPK	Creatine phosphokinase
DAPI	4',6-Diamidino-2-Phenylindole
DDR	DNA-damage response
DMSO	Dimethylsulfoxide
EFS	Event-free survival
FGFR1	Fibroblast growth factor receptor 1
FU	Follow-up
GEP	Gene-expression profile
GFP	Green fluorescent protein
GTR	Gross-total resection
HGG	High-grade glioma
HRAS	Harvey rat sarcoma viral oncogene homolog

hTERT	Human telomerase reverse transcriptase
HUVEC	Human umbilical vein endothelial cells
IF	Immunofluorescence
IL1B	Interleukin 1B
IL6	Interleukin 6
IL1R1	Interleukin 1 receptor 1
IL1Ra	IL1 receptor antagonist
IL1RAcP	IL1 receptor accessory protein
IL6Ra	Interleukin 6 receptor alpha
IL6ST	Interleukin 6 signal transducer
IPA	Ingenuity pathway analysis
IRAK1	Interleukin 1 receptor-associated kinase 1
IVIS	*In vivo* imaging system
JAK	Janus kinase
KRAS	Kirsten rat sarcoma viral oncogene homolog
LCA	Leukocyte common antigen
LGG	Low-grade glioma
MAPK	Mitogen-activated protein kinase
NF1	Neurofibromatosis type 1
NFκB	Nuclear factor kappa B
NSC	Neuronal stem cells
NSCLC	Non-small cell lung cancer

OIS	Oncogene-induced senescence
OS	Overall survival
PA	Pilocytic astrocytoma
PDX	Patient-derived xenograft
PIN	Prostatic intraepithelial neoplasia
PFS	Progression-free survival
PI3K	Phosphatidyl-inositol-3-kinase
RB	Retinoblastoma
RELA	REL-associated protein
RFP	Red fluorescent protein
RT	Room temperature
SAHF	Senescence-associated heterochromatin foci
SASP	Senescence-associated secretory phenotype
SOCS1	Suppressor of cytokine signaling 1
SH2	Src Homology 2
SSA	Sessile serrated adenoma
STAT3	Signal transducer and activator of transcription 3
STR	Sub-total resection
TNFRSF1B	Tumor necrosis factor receptor superfamily member 1B
t-SNE	t-distributed stochastic neighbor embedding
WB	Western blot
WHO	World health organization

TABLE OF CONTENTS

FIGURES

1. INTRODUCTION

1.1 Pediatric oncology

There are 10.9 million children under the age of fifteen living in Germany. In 2016, n=1714 of these children were diagnosed with cancer. This means that 1 out of 409 new born children will be diagnosed with cancer before its 15th birthday (1). Approximately n=420 of the children diagnosed with cancer die within 15 years after diagnosis per year, and 8.4% will present with a secondary neoplasm within 30 years after their first cancer diagnosis (children < 15 years). Among all cancer types, the most prevalent malignancies in childhood are hematological diseases (30.3%), followed by CNS tumors (23.8%) (Fig. 1) (1).

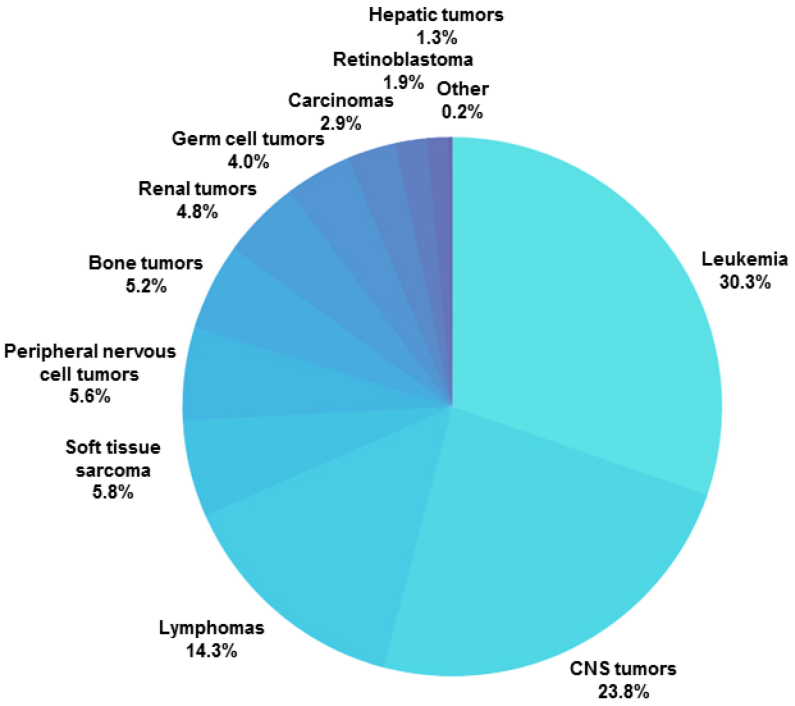

Figure 1: Relative frequency of childhood cancer diagnoses in Germany. Adapted from the German Childhood Cancer Registry 2017 (1).

Fortunately, a clear trend emerged during the last decades showing a drastic improvement in prognosis for children with cancer (Fig. 2) (2). Taking all pediatric tumor entities into account, 82% of the children (< 15 years) diagnosed with cancer survive for at least 15 years (1). However, cancer is still one of the main causes of death in childhood, and children who survive the disease often suffer from therapy-

related long-term impairments. Furthermore, entities associated with poor survival rates still represent clinical challenges. And finally, a plateau in survival rates has formed over the last 1-2 decades, implying that the classic therapy modalities (surgery, radiotherapy, chemotherapy) will not further improve survival (Fig. 2). Thus, there is a need for a better understanding of the tumor biology, ultimately leading to improved therapeutic options.

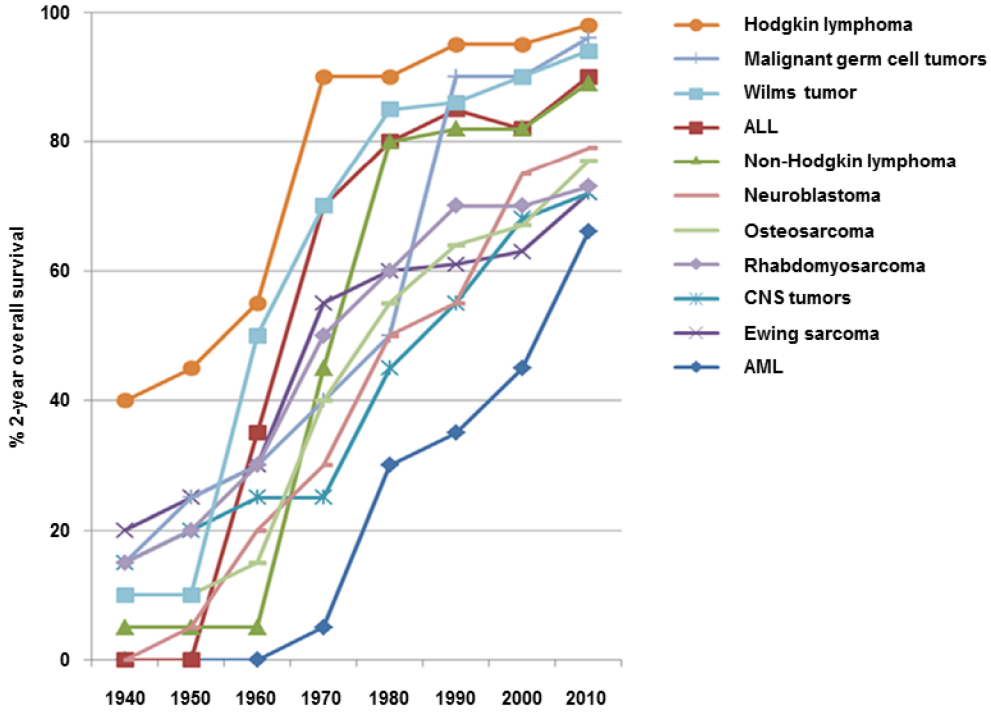

Figure 2: Survival rate of childhood cancer patients in Germany and Austria. Adapted from Rossig *et al.* (2).

1.1.1 Pediatric neuro-oncology

The second most common malignancies in children are brain tumors. On average, 1 out of 1600 children (< 15 years) is diagnosed with a central nervous system (CNS) tumor. The median age at diagnosis is between six to seven years. The incidence rate in Germany is 41.2/million/year with a 20% increased risk for boys compared to girls (1). The 15-year survival probability for patients with CNS tumors is 71% on average.

CNS tumors represent a very heterogeneous class including benign as well as highly malignant entities. They are graded I-IV in accordance with the World Health Organization (WHO) Classification of Central Nervous System Tumors (3). The recent addition of novel molecular methods in routine (neuro-) pathology diagnostics (3) has improved the detail and accuracy of CNS tumor diagnoses. These novel

molecular methods comprise, but are not limited to, genome-wide DNA methylation analysis (4,5) and next-generation sequencing (6). By screening thousands of tumors for their genetic and epigenetic profile, the understanding of the tumor biology has dramatically improved (7). The integration of the identified molecular parameters, such as DNA methylation patterns, with the histological diagnosis, has improved the diagnosis of brain tumors (Fig. 3) (3,4). In addition, genome-wide DNA methylation analysis has led to the identification of previously unknown as well as re-classification of misdiagnosed tumor entities. Ultimately, the correct and reliable identification of a given molecular entity will enable more specific clinical trial designs and therapeutic regimens (8).

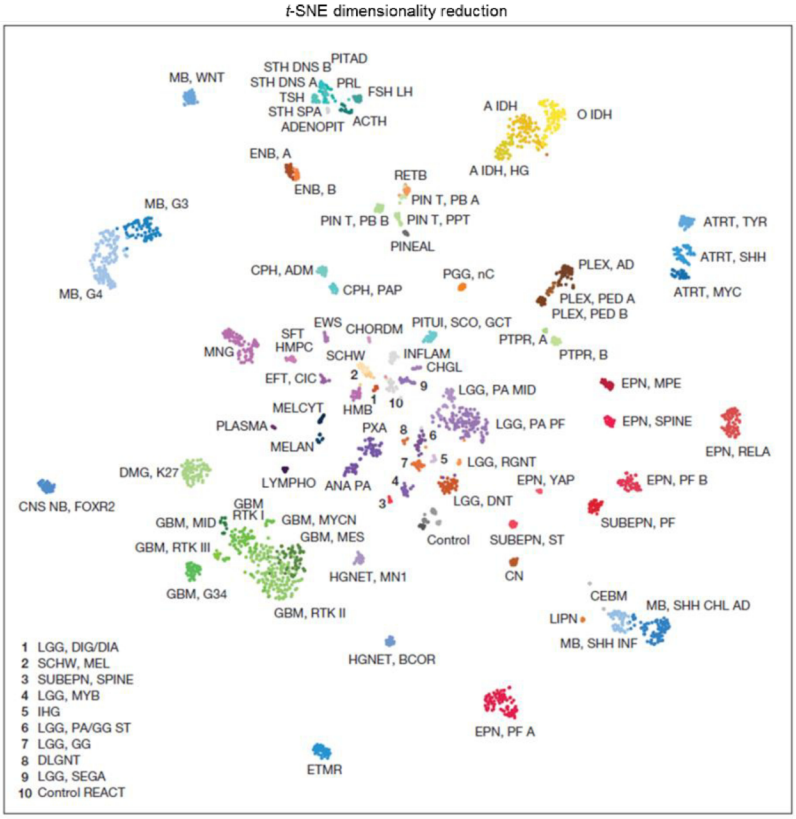

Figure 3: DNA methylation-based clustering of CNS tumor subgroups. Adapted from Capper *et al*. (4). Unsupervised clustering of n=2801 brain tumor samples using t-SNE dimensionality reduction. Every dot represents one sample and the color code is representative of one subgroup (n=91).

In general, pediatric tumors carry fewer somatic mutations, i.e. have a lower mutational burden, in comparison to adult tumor entities. This reflects the different origin of pediatric vs. adult tumors: while pediatric tumors are thought to be mostly developmental disorders, adult tumors frequently develop from exogenously induced mutations due to exposure to environmental factors (9,10). One of the

tumors with the lowest mutational burden is the most common type of low-grade gliomas, the pilocytic astrocytoma (11).

1.1.2 Low-grade gliomas

The most benign class of CNS tumors are low-grade gliomas (LGG). LGGs are a very heterogeneous group, but all entities within this group are classified as WHO grade I or II. Overall, LGGs are the most common solid tumors occurring in children and comprise one-third of all CNS tumors (Fig. 4) (12).

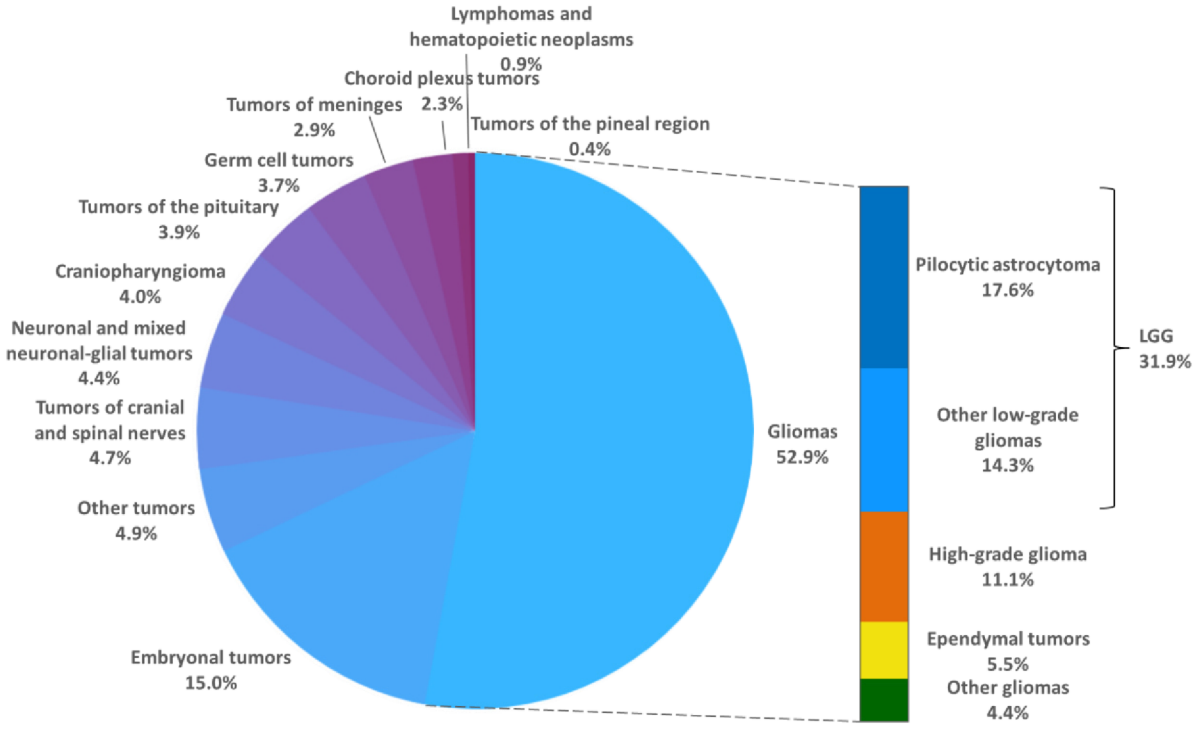

Figure 4: Distribution of brain tumor entities by histology (age: 0-14 years, CBTRUS 2007-11). Adapted from Ostrom *et al*. (12).

While patients with a LGG have an excellent overall survival (OS), the progression-/ event-free survival of patients varies greatly (Fig. 5). Hence, though not deadly, LGG is a chronic disease with a high psychosocial and medical burden for the rest of the patients´ life. Therefore, in comparison to malignant CNS tumors, the challenge with LGGs lies in finding a balance between appropriate treatment and avoidance of long-term side effects, as the majority of LGG patients survive and grow up to live with the consequences of their disease (13).

During the last decade, more information on the molecular drivers of these tumors became available and is already being implemented into early-stage clinical studies. Most of the LGGs display aberrations in

the Ras/mitogen-activated protein kinase (MAPK) pathway, which can be targeted specifically (14-16). This is also true for the most common type of LGGs, the pilocytic astrocytoma.

1.1.3. Pilocytic astrocytoma

1.1.3.1 Clinical information

The pilocytic astrocytoma (PA) is the most common brain tumor in children, accounting for nearly 20% of pediatric CNS tumors (Fig. 4, see above). The incidence rate is 0.91/100 000/year in children and adolescents (age 0-19 years) with an annual average of 750 new cases in the United States (17). The estimated 5- and 10-year overall relative survival rates are 94.1% and 92.2%, respectively (17). The tumor is classified as a WHO grade I glioma. PA growth behavior is typically slow and benign, as pediatric PAs are not invasive, do not metastasize nor develop into high-grade malignancies (18). As the growth speed of PAs is very slow, allowing the surrounding tissue to adapt to a certain extent, PAs can grow to a substantial size before giving rise to symptoms (18). After an initial growth phase, most tumors arrest in a dormant phase (19). Although the overall survival rates look very promising, the 10-year progression-free survival is 50% on average (Fig. 5) (20,21). The tumors have a tendency to recur and progress, sometimes even years after diagnosis. This can also occur in cases of complete tumor resection (18). The 10-year event-free survival (EFS) is highly correlated with the extent of resection: EFS is 85% for patients with complete resection, 52% for sub-total resection and 18% for partial resection. It is evident that especially unresectable tumors pose a clinical challenge due to the high risk of progression (20).

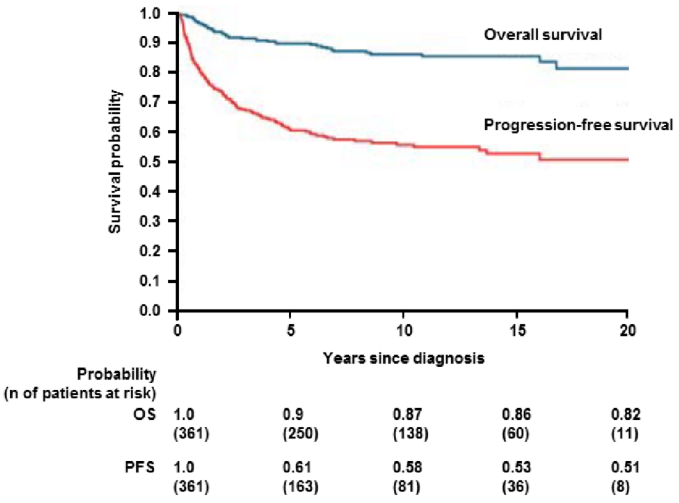

Figure 5: Overall (OS) and progression-free survival (PFS) after diagnosis for low-grade glioma patients (n=361). Adapted from Armstrong *et al*. (21).

Children with a PA require long-term care and clinical supervision, as the disease is not deadly and has to be monitored for years to decades. PAs can arise throughout the brain with most PAs being located in the cerebellum or the supratentorial midline. Other sites are the caudal brainstem, the cerebral hemisphere or the spinal cord (20). PA patients can experience morbidities significantly impacting their quality of life, either from the tumor itself or the therapy. Depending on the tumor location, patients can experience loss of vision, endocrinological dysfunction, focal paralysis, coordination dysfunction or general psychomotor retardation. Long-term side effects due to treatment can include hearing loss, impaired endocrine function, neuropathy, nephropathy, and cognitive impairment, with approximately one third of the survivors having an intelligence quotient below average (< 85) (21). Thus, despite the benign tumor growth, the long-term effects of both the tumor itself as well as the treatment significantly reduce the quality of life of the patients. It is therefore imperative to improve medical care of PA patients by increasing the understanding of the tumor biology, ultimately leading to the development of new treatment strategies.

1.1.3.2 Tumor biology

During the last decade, major progress has been achieved in identifying the key drivers of PA. As mentioned above, a characteristic feature is the low amount of somatic mutations (11). Aberrant activation of the MAPK pathway is the main alteration observed in PAs. Activating *KIAA-BRAF* fusions are the most common aberration, with fewer tumors harboring e.g. point mutations in v-raf murine sarcoma viral oncogene homolog B (*BRAF*), fibroblast growth factor receptor 1 (*FGFR1*) or Kirsten rat sarcoma viral oncogene homolog (*KRAS*) as well as germline mutations in neurofibromatosis type 1 (*NF1*) (Fig. 6) (14). Typically, PAs are considered a single-pathway disease as all genetic aberrations target only one pathway, the MAPK pathway (Fig. 6).

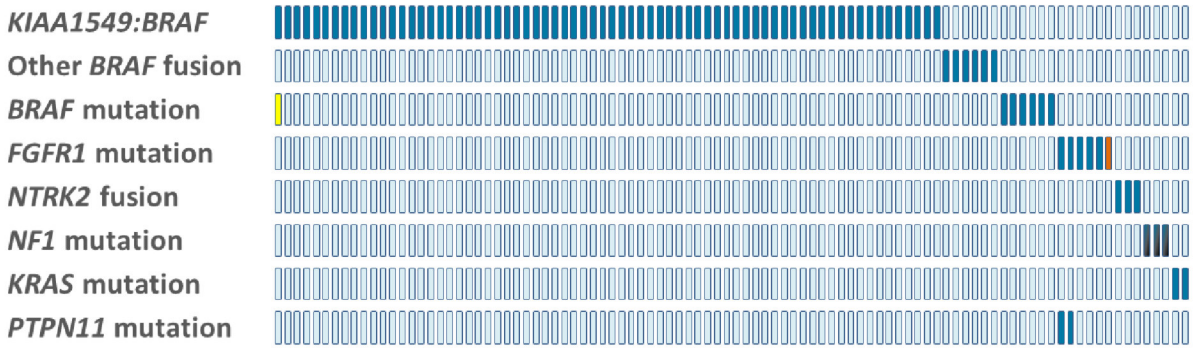

Figure 6: MAPK pathway alterations in pilocytic astrocytoma. Adapted from Jones *et al.* (14). Alterations detected in n=96 PA samples with each box representing one tumor sample. Dark blue boxes indicate presence of a mutation/fusion in the tumor

sample. Aberrations are mutually exclusive besides for *FGFR1* and *PTPN11*. Orange box = FGFR1-ITD, yellow box = BRAF p.Glu451Asp alteration, blue/black box = one germline and one somatic *NF1* alteration.

In approximately 70% of all PA cases, a *KIAA1549:BRAF* fusion caused by tandem duplication is the driving MAPK alteration (14). This gene fusion is a defining feature of PAs, occurring only very rarely in other pediatric brain tumors such as e.g. gangliogliomas (13). The fused BRAF does not contain the N-terminal regulatory domain which results in constitutive activity of the kinase. The tandem duplication is detectable by a gain in copy number at 7q34. There are three mRNA breakpoints observed. The most common version is a fusion between *KIAA1549* exon 16 and *BRAF* exon 9 ($K^{Ex16}B^{Ex9}$), followed by $K^{Ex15}B^{Ex9}$and $K^{Ex16}B^{Ex11}$, respectively. NIH3T3 cells transduced with a truncated version of the fusion gene showed accelerated growth in soft agarose, demonstrating the transforming potential of the fusion (22). Further proof of the oncogenic potential of the fusion was provided by Kaul *et al*. (23), who could show increased proliferation as well as colony formation in a soft agarose assay of neural stem cells expressing the *KIAA1549:BRAF* fusion. In mice, activation of a truncated version of $BRAF^{V600E}$ alone was sufficient to induce PA-like tumors (24). This proves that the single-pathway activation is sufficient for tumor formation.

The oncogenic stimulus from e.g. the *BRAF* fusion results in a downstream activation of the MAPK pathway (Fig. 7). The increased phosphorylation of MEK1/2 and ERK1/2 initially leads to elevated tumor growth by activating cell proliferation. Over the long term however, this aberrant signal is thought to activate a tumor-suppressive mechanism called oncogene-induced senescence (OIS), resulting in growth cessation (18).

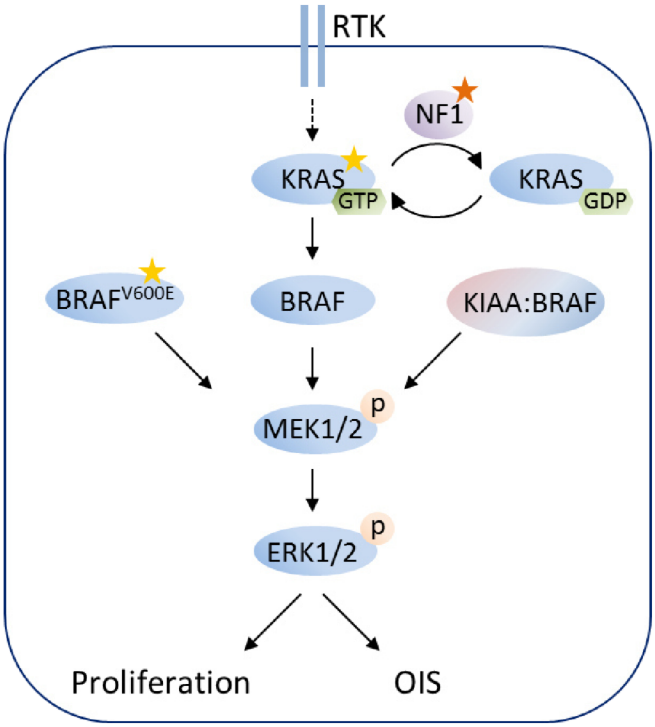

Figure 7: MAPK pathway signaling cascade. Adapted from Jones *et al.* (18). The MAPK pathway can either be activated by activating mutations (represented by the yellow stars), inactivating mutations (represented by the orange star) or fusions (represented by the two colors).

1.1.3.3 Therapy

In contrast to malignant brain tumors, not every PA patient has to be treated. The decision to treat is guided by a multitude of factors such as clinical symptoms, growth dynamics, imminent danger of irreversible damage, threat to highly vulnerable structures and many other aspects. In case of progressive or symptomatic disease complete resection is the first choice, unless the location does not allow for surgery. In this case or in case of incomplete resection, the alternative treatment options are radiotherapy or chemotherapy. For non-symptomatic small tumors or small residual tumors after resection a 'watch & wait' approach is warranted. Radiotherapy is effective, but should be postponed as long as possible and especially avoided in young children and NF1 patients. The standard of care chemotherapeutic regimen is the combination of vincristine and carboplatin. Patients with NF1 usually show a better response to chemotherapy and superior outcome compared to patients without NF1 (25). In a randomized study conducted to compare the addition of etoposide (E) to the classic combination of vincristine and carboplatin (VC) in non-NF1 LGG patients, no difference could be observed. VC treatment led to a tumor volume reduction of 46% vs. 41% for VCE, a 5-year PFS of 46% vs. 45% for VCE and 5-year OS of 89% for both VC and VCE. (25). Another chemotherapeutic regimen with a similar outcome to VC is

vinblastine monotherapy. In a phase II study treatment of pediatric LGG patients, including NF1 patients (24% of all treated patients), with vinblastine resulted in a 5-year PFS of 53% and a 5-year OS of 94% (26), comparable to the outcome of patients treated with VC.

In the era of targeted therapy and in light of the increasing knowledge regarding the genetic drivers of PAs, the standard of care has to be reassessed. Early clinical trials with MEK inhibitors are ongoing and only few results are available to date (27). A recent phase II study reported partial response in 32% of n=25 patients treated with selumetinib, a MEK inhibitor, in recurrent or refractory LGG patients (28). The 2-year PFS was 66% +/- 11% in non-NF1 patients, while the outcome was better for NF1 patients with a 2-year PFS of 96% +/- 4%. Currently, Novartis is recruiting patients with $BRAF^{V600E}$ mutations in either LGGs or relapsed high-grade gliomas (HGGs) for a phase II study to investigate the efficacy of trametinib, a MEK inhibitor, in combination with dabrafenib, an inhibitor of mutated *BRAF*, versus standard of care chemotherapy (NCT02684058). In 2019, the European LOGGIC trial will start recruitment, and compare trametinib versus standard of care VC versus vinblastine monotherapy in pediatric patients with *BRAF*-fusion positive PAs.

In this benign tumor entity, future therapies cannot only be judged by the short-term outcome, but their effects on the developing brain have to be considered. Hopefully, side effects can be reduced with the application of targeted therapy. The most common toxicities under treatment with selumetinib were reported to be CTCAE (common terminology criteria for adverse events) grade I and II creatine phosphokinase (CPK), skin and gastrointestinal side effects as well as hypoalbuminemia and elevated aspartate aminotransferase (AST). Of course, the long-term effects of these new treatments will have to be monitored closely. One important question that remains to be answered is the duration of treatment. In the initial trials with selumetinib, patients with responding or stable disease could choose to stop treatment after 1 to 2 years and resume treatment in case of tumor progression (13). The upcoming LOGGIC trial will treat patients for 18 months with the MEK inhibitor trametinib.

Unraveling the mechanism of growth regulation will facilitate informed treatment decisions of either adjuvant treatment versus a ‘watch & wait’ approach. Therefore models of the disease are urgently needed.

1.1.3.4 Models of PAs

The variety of LGG models is very limited. Primary cells quickly go into oncogene-induced (OIS) or replicative senescence after only a few passages. This has greatly impeded the study of the biology of this tumor entity. Due to the lack of faithful models, a clinical study using the multikinase inhibitor sorafenib was conducted in children without preclinical testing (29). This resulted in unexpected tumor growth under treatment (29,30). Retrospectively, it could indeed be shown *in vitro* that sorafenib leads to paradoxical MAPK activation (30,31).

The first *in vitro* PA model was established in 2011 by Raabe and colleagues (32). Transduction of the $BRAF^{V600E}$ mutation into human neurospheres promoted colony formation in soft agarose. After an initial phase of slow proliferation, cell growth stopped completely and markers of OIS were detectable, which have been detected in primary PA samples as well (see chapter 1.2.3 OIS in PA). The transduced cells stained positive for the senescence-associated ß-galactosidase (SA-ß-Gal) and expressed elevated protein levels of CDKN2A. At the same time, Jacob *et al*. overexpressed $BRAF^{V600E}$ in human immortalized astrocytes and fetal astrocytes. This resulted in elevated oncogene-induced morphologic changes typical for OIS such as enlarged, flat cellular bodies and SA-ß-Gal expression (19). CDKN2A protein levels increased under expression of the oncogene and the cell cycle was arrested (19), just as Raabe and colleagues had observed (32). A murine *in vitro* LGG model was established by Sun and colleagues. The group transduced either $BRAF^{V600E}$ or the *KIAA1549:BRAF* fusion in *TP53* null murine neural progenitor cells (33). Usually, *TP53* is intact in LGG tumors, but the authors argued that its ablation was necessary to ensure proliferation of the cultures (33,34). Additionally, they developed an organotypic assay culturing fresh brain tumor material from surgery on brain slices from neonatal (E14) mice to test drug response in presence of microenvironment (33,35). Finally, our group has generated the first patient-derived PA *in vitro* model, DKFZ-BT66, with the advantage of endogenous expression of the *KIAA1549:BRAF* fusion (31). The cell line was established by transducing primary tumor material with the Simian Vacuolating Virus 40 large T antigen (SV40-TAg). The expression of SV40-TAg is doxycycline-inducible with its activation leading to inhibition of two OIS-relevant pathways, the TP53/CDKN1A and CDKN2A/RB1 pathway (36,37), thereby interfering with induction and maintenance of OIS.

The number of *in vivo* models of PAs is even more limited than the cell culture models. Generation of patient-derived xenografts has been proven impossible due to growth arrest resulting from OIS as well as replicative senescence. The first model of a NF1-optic pathway glioma was developed by Gutman *et al*. via an inducible knock-out deleting the residual copy of *NF1* in astrocytes of *NF1*+/- mice (38). A PA-like

mouse model was generated by Gronych *et al*. via injection of virus-producing cells, containing a $BRAF^{V600E}$-coding plasmid, into the hemispheres or the brainstem of neonatal mice (24). The construct codes for the activated kinase domain of $BRAF^{V600E}$ and only infects nestin-expressing neural progenitor cells in Ntv-a mice. $BRAF^{V600E}$ expression led to the development of PAs, as determined by histopathologic evaluation. The model also recapitulated the benign behavior of PAs, as mice did not succumb to their tumors and rather died of old age (18). Kaul and colleagues had observed elevated proliferation and soft agar colony formation of fusion-transduced neuronal stem cells (NSCs) *in vitro* as well as development of glioma-like lesions after injection of these cells into the cerebellum of 3-week old mice (23). In a following study using Cre driver lines, the scientists generated another *in vivo* model by specifically expressing the *KIAA:BRAF* fusion in either NSCs, astrocytes or NG2 progenitor cells in mice. Increased glial cell proliferation was detected only in the cerebellum originating from NSCs, indicating brain region- and cell type-specific effects of *BRAF*-fusion activity (23,39). No changes in survival were observed for mice injected with *BRAF*-fusion expressing NSCs compared to control mice injected with an empty vector (23). Again, this reflects the benign, slow growth behavior observed in PA patients which is thought to result from activation of oncogene-induced senescence.

1.2. Oncogene-induced senescence

Senescence was first discovered in normal human fibroblasts that stopped dividing after reaching their proliferative capacity by Hayflick and Moorhead, now referred to as the 'Hayflick limit' (40). In contrast, cells derived from malignant tumors proliferate and divide indefinitely. Senescence was therefore defined as a protective mechanism leading to growth arrest of premalignant, damaged cells without inducing cell death. Senescence can be activated by several stimuli, including DNA damage through chemotherapeutic agents or radiation, telomere erosion resulting from old age, known as replicative senescence, and cellular stress induced by aberrant signaling of oncogenes, termed oncogene-induced senescence (OIS). All stimuli lead to cell cycle arrest and thereby prevent proliferation and spread of damaged, potentially transformed cells (41,42). However, it has been shown that cancer cells can evade this tumor suppression via different mechanisms (43-47).

OIS was first described in 1997 by Serrano and colleagues. The scientists observed that transformation of human or murine primary cells with the activated Harvey rat sarcoma viral oncogene homolog ($HRAS^{V12}$) resulted in G1 cell cycle arrest (48). Markers of OIS have been detected in a variety of pre-malignant human lesions. The best-known examples for OIS in healthy humans are benign nevi carrying a $BRAF^{V600E}$

mutation. After an initial growth phase, the *BRAF*-mutated melanocytes are arrested in growth via activation of OIS, stopping them from developing into malignant melanoma (49). Other examples of pre-cancerous lesions displaying markers of OIS are serrated sessile adenomas (SSA) of the colon driven by *BRAF* mutations (46,50), dermal neurofibromas in NF1 patients (51) and prostate intraepithelial neoplasia (PIN) mostly associated with loss of one allele or mutation of *PTEN* (52). In all of these pre-neoplastic lesions OIS provides a barrier to cancer progression.

As senescent cells are resistant to apoptosis they are cleared by immune cells, another tumor-suppressive mechanism initiated by OIS. Immune cells are attracted by the secretome of senescent cells comprising several cytokines, chemokines and many other inflammatory factors (53-56). Senescence was further shown to be involved in wound healing (54,57) and embryonal development (58-60).

However, OIS does not only have beneficial effect, but is also associated with age-related pathologies as well as tumor progression. Many age-related diseases may results from insufficient clearing of senescent cells by the immune system resulting in chronic inflammation at the site of accumulated senescent cells (61,62). Dependent on the biological context, senescence can paradoxically enhance tumor proliferation and invasiveness. The secretion of factors associated with inflammation were shown to stimulate angiogenesis in neighboring cells (63) and thereby induce tumor growth and invasion (64-66). Co-injection of senescent normal human cells enhances tumor development of cancer cells *in vivo* (67,68). For this reason, OIS is often described as a double-edged sword. The biological progress is beneficial in young organisms, e.g. embryonal development, in wound healing and tumor suppression, but with increasing age, it can be detrimental in age-related pathologies, or cancer progression for instance (69).

1.2.1 Markers of OIS

The lack of specific markers for OIS has hampered research on this multifaceted mechanism (70). The first marker used to identify senescent cells was elevated activity of the SA-ß-Gal (71). However, this marker is not specific for OIS and should only be used to identify OIS together with other markers (72). Finding a single marker for senescence remains a challenge until today as hallmarks of senescence can differ depending on the tissue type or inducing stimulus. Therefore the research community has agreed on verifying senescence by combining several markers (72).

Senescent cells are characterized by enlarged, flat cellular bodies, increased metabolism, formation of senescence-associated heterochromatin foci (SAHF), absence of proliferative markers, as well as secretion of the senescence-associated secretory phenotype (SASP) (42). Even though it is known that

pathways inducing senescence vary in different cell types, the main signaling cascades which are activated in senescence are the TP53 and the retinoblastoma (RB) pathway (48,53,73-75). Both TP53 and RB are regulated by cyclin-dependent kinase inhibitors (CDKi) such as CDKN1A, CDKN1B, CDKN2A, and CDKN2B, with their activation resulting in growth arrest (61).

Markers of OIS	**Examples**	**Detection**	**References**
Enlarged cell morphology	Flat cell shape	Microscopy	(40,48)
Absence of proliferative markers	Cell cycle arrest	Cell counts, immunohistochemistry (IHC) for Ki67, detection of reduced bromodeoxyuridine incorporation	(76)
Upregulation of cyclin-dependent kinase inhibitors	p16, p21, p14, p15, p53	qPCR, Western blot, IHC	(48,77-79)
SASP	IL1, IL6, IL8	qPCR, enzyme-linked immunosorbent assay (ELISA), cytokine arrays	(46,47,80)
Chromatin restructuring	SAHF	4’,6-diamidino-2-phenylindole (DAPI) staining followed by microscopy	(81)
Increased lysosome content	Detection of SA-ß-Gal at suboptimal pH	Staining followed by microscopy	(71,82)

Potentially, the variety of markers could also result from the fact that senescence develops over time and the different markers are present at different stages during induction of senescence (Fig. 8) (83).

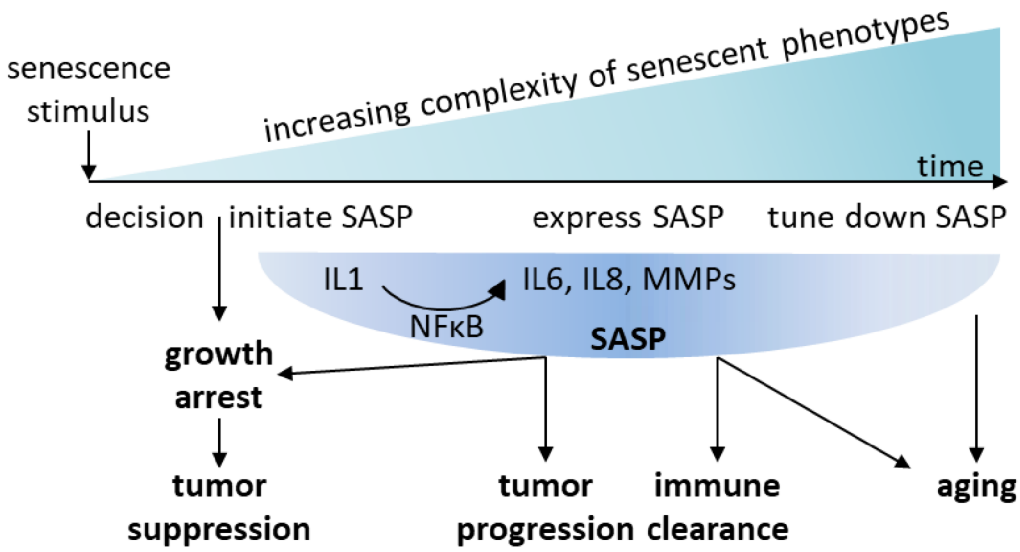

Figure 8: Senescence phenotype over time. Adapted from Rodier and Campisi (69). Abbreviations: MMPs = Matrix metalloproteinases, SASP= senescence-associated secretory phenotype.

As observed by Michaloglou, there is an initial proliferation phase before senescence develops, which could be seen as a decision phase (49). The SASP was observed to develop slowly over the course of several days, with IL1 being one of the first factors to initiate SASP expression via NFκB activation (50,66,80). The transcribed SASP factors then either reinforce senescence and lead to clearance of cells, or controversially can also promote tumor growth in a paracrine manner (46,47,53,63). Over time, the SASP is tuned down potentially via miRNAs (84). Senescent cells can then accumulate with age either due to insufficient clearance or increased generation, and the chronic inflammation caused by remaining levels of SASP expression may be the cause of age-related pathologies (69).

1.2.2 Regulation of OIS

i. TP53 and RB pathway

As mentioned above, the most common activated pathways in senescence are the TP53 and the RB pathway (48,53,73-75). Matching this observation is the fact that the most common mutations in tumors are detected in regulators of this pathway (85). Mutations or loss of *TP53*, *RB1* or *CDKN2A* enable bypass of senescence (34,36,41,48,52). One example for this phenomenon was described in different stages of development of colon adenoma and carcinoma. While sections of preneoplastic colon adenoma were positive for senescence markers, malignant colon carcinoma samples were associated with reduced signs

of senescence which coincided with *TP53* mutations (41). As a tool for the study presented here, OIS was circumvented by inhibition of RB and TP53 by transducing cells with the SV40-TAg (36,37).

ii. The SASP

As described above, one of the hallmarks of OIS is the SASP (66,86-88). When first fully characterized in 2008, Coppé and colleagues observed the phenomenon of increased secretion of factors associated with inflammation by fibroblasts transduced with oncogenic *RAS* (66). The observed elevated secretion occurred gradually over the course of several days after senescence was induced. The secreted components included cytokines, chemokines, growth factors, proteases and several other inflammation-related molecules. However, each cell line displayed a unique composition of the secreted factors. After verifying their findings by RT-qPCR, the researchers observed that most factors were upregulated on mRNA level, concluding that they were regulated on transcription level (66). The SASP was later found to be mediated by the transcription factors nuclear factor kappa B (NFκB) and CCAAT/enhancer-binding protein beta (CEBPB) (46,47,89).

The SASP was described to reinforce the growth arrest under OIS in an autocrine as well as paracrine signaling mode (46,47,50). The relevance of the SASP in inducing growth arrest of neighboring cells was elegantly demonstrated by Acosta and colleagues (50). Co-cultures of senescent with cycling fibroblasts led to stable growth arrest and expression of OIS markers of the previously proliferating cell fraction. This effect was also observed in transwell systems as well as conditioned medium experiments, indicating that the effect was mediated by secreted factors (90). The role of the secreted factors on the microenvironment was shown to vary depending on cell type, location, stimuli and many other factors. However, certain factors are highly conserved and play an important role in maintaining senescence (46,47).

The SASP is responsible for the tumor-protective as well as pro-tumorigenic effects of senescent cells. The beneficial effects of the SASP include stabilization of the growth arrest of senescent cells as well as the activation of an immune response that leads to clearance of the damaged cells. But the SASP can also fuel growth and invasiveness of neighboring cells in a paracrine manner (46,50,63,64,66).

In a screen aimed at the suppression of the SASP in senescent fibroblasts, Laberge and colleagues identified two glucocorticoids, corticosterone and cortisol, as potential candidates (91). The group could show that treatment with glucocorticoids was sufficient to reduce the secretion of several SASP factors, including IL1A and IL6 both mediated by NFκB signaling. In their experiments glucocorticoid treatment of

senescent cells did not lead to bypass of senescence. However, through the reduced secretion of inflammatory molecules under treatment, the capacity to drive invasiveness of neighboring cells was reduced (91). In 2018, Ge and colleagues observed that the glucocorticoid dexamethasone reduced the sensitivity of non-small cell lung cancer (NSCLC) cells to chemotherapy (92). The combination treatment led to increased growth of NSCLC cells *in vitro* and *in vivo* in comparison to chemotherapy treatment alone. The DNA-damage resulting from chemotherapy induced senescence in NSCLC cells, as observed by elevated SA-ß-Gal activity, upregulated SASP secretion and altered cell morphology. Co-treatment with dexamethasone reduced secretion of SASP factors, including IL1B and IL6, and induced tumor sphere formation. Ge and colleagues concluded that dexamethasone inhibited the SASP and thereby weakened the senescence-induced growth arrest of chemotherapy (92). The fact that glucocorticoids inhibit IL1 production as well as other cytokines was already described two centuries ago (93) and the effect was shown to be mediated by NFκB (94,95). The IL1 pathway, which activates NFκB, is known to be an important regulator of the SASP (50).

iii. IL1 signaling pathway

IL1 is one of the major cytokines regulating the SASP. There are two forms of the cytokine IL1, the alpha and the beta version (96), both involved in inflammation and regulation of immune response (97). IL1A as well as IL1B signal through the IL1R1, a receptor belonging to the immunoglobulin supergene family (98). Both forms are synthesized as precursors (31kDa). While pro-IL1A is immediately active, pro-IL1B has to be activated by Caspase 1 cleavage into its mature form (17kDa) (99,100). The active version of IL1B is secreted into the extracellular space upon pathway activation, while IL1A mainly stays and acts intracellular. IL1 is involved in gene expression, cell growth, senescence and differentiation (80,97,101). After binding of IL1 to the IL1R1, a second chain, the IL1 receptor accessory protein (IL1RAcP), is recruited (102) and the complex leads to activation of the downstream target IL1 receptor-associated kinase 1 (IRAK1) (97,103). IRAK1 is phosphorylated after activation and quickly degraded (104). This ultimately leads to the activation of NFκB (105) and the transcription of many inflammatory signaling molecules, including *IL1* itself (106) (Fig. 9). Through an autocrine mechanism IL1 initiates its own transcription through a positive feedback via activation of NFκB (107). The signaling pathway is tightly regulated by several mechanisms. The IL1 receptor antagonist (IL1Ra) is a physiological inhibitor of the IL1 pathway and binds the IL1R1 without activating the downstream pathway (97). In addition to the IL1RI (80 kDa), there are soluble IL1 receptors as well as the IL1RII (68 kDa), which binds the cytokines and can thereby limit responsiveness (108) (Fig. 9).

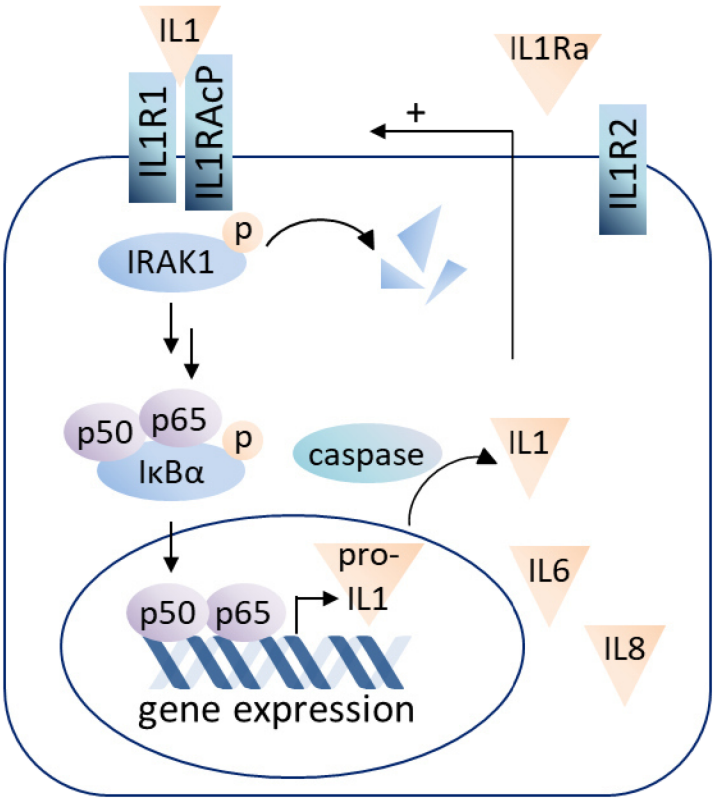

Figure 9: IL1 signaling pathway. Adapted from Martin and Wesche (109).

Upregulation of *IL1A* and *IL1B* on transcription level was detected in 2004 by Mason *et al*. in gene expression profiles of human fibroblasts in OIS induced by *HRAS* (86). Elevated protein levels of IL1B were later observed in the antibody array of the secretome of senescent fibroblasts transduced with oncogenic *RAS* by Coppé (66). IL1 seems to be one of the conserved SASP factors present in OIS, as well as replicative senescence and drug-induced senescence (90,101). In 2009, Orjalo demonstrated that IL1A is an upstream regulator of IL6 and IL8, two major SASP factors shown to play a role in OIS induction and maintenance (46,47,80). Overexpression of IL1A induced the SASP as well as other OIS markers such as growth arrest of cells, elevated SA-ß-Gal activity and CDKN1A expression (50,80,89). Pharmacological as well as shRNA-mediated interference with the IL1 pathway led to reduced secretion of IL6 and IL8 via reduced DNA binding activity of NFκB and CEBPB (80). The role of IL1 as a key regulator of senescence and activator of the SASP was further studied by Acosta (50) showing that expression of the SASP was mediated by IL1 signaling. Treatment of senescent fibroblasts with an IL1R antagonist resulted in reduced mRNA expression of the SASP factors. Knock-down of the IL1R partially led to bypass of OIS and induced cell growth. Treatment with an IL1R antagonist of a $NRAS^{G12V}$-mediated OIS model in murine hepatocytes *in vivo* led to reduced CDKN1A and CDKN2A levels and to elevated numbers of cells

expressing NRAS. The IL1R antagonist seemed to prevent clearance of the senescent cells by the immune system, inhibit senescence and led to proliferation of previously senescent cells (50). All these results suggest that IL1 signaling does play a major role in regulating the SASP.

iv. IL6 signaling pathway

IL6 was one of the first discovered SASP factors, just like IL1 (46,86). Kuilman specifically detected and analyzed the role of the cytokine when comparing the gene expression profile of fibroblasts in OIS to cells that bypassed OIS. IL6 is involved in immune response, inflammation, proliferation, and tumorigenesis (110,111). The IL6 pathway is activated by binding of the cytokine to a receptor composed of two subunits. The IL6Ra (80 kDa) contains the cytokine binding domain, while the second subunit IL6 signal transducer (IL6ST, 130 kDa) transfers the signal further downstream (112). Additionally, there is a soluble IL6 receptor that can also bind to IL6ST and activate signaling (112). IL6ST associates with Janus kinase (JAK) tyrosine kinase family members, mainly JAK1, which phosphorylate themselves as well as IL6ST (113,114). This leads to downstream activation of signal transducer and activator of transcription 3 (STAT3) as well as STAT1 by phosphorylation (115,116). The activated STATs then dimerize, transfer to the nucleus and initiate transcription. In addition, through JAK activation and phosphorylation of IL6ST, a docking site for Src homology 2 (SH2) is created, which can stimulate the MAPK and phosphatidyl-inositol-3-kinase (PI3K) cascade (117-119). Long-term activation of the IL6 pathway activates a negative feedback mechanism, which induced internalization and degradation of IL6Ra (120), as well as downregulation of p-STAT3 via the suppressors of cytokine signaling 3 (SOCS3) (Fig. 10) (121).

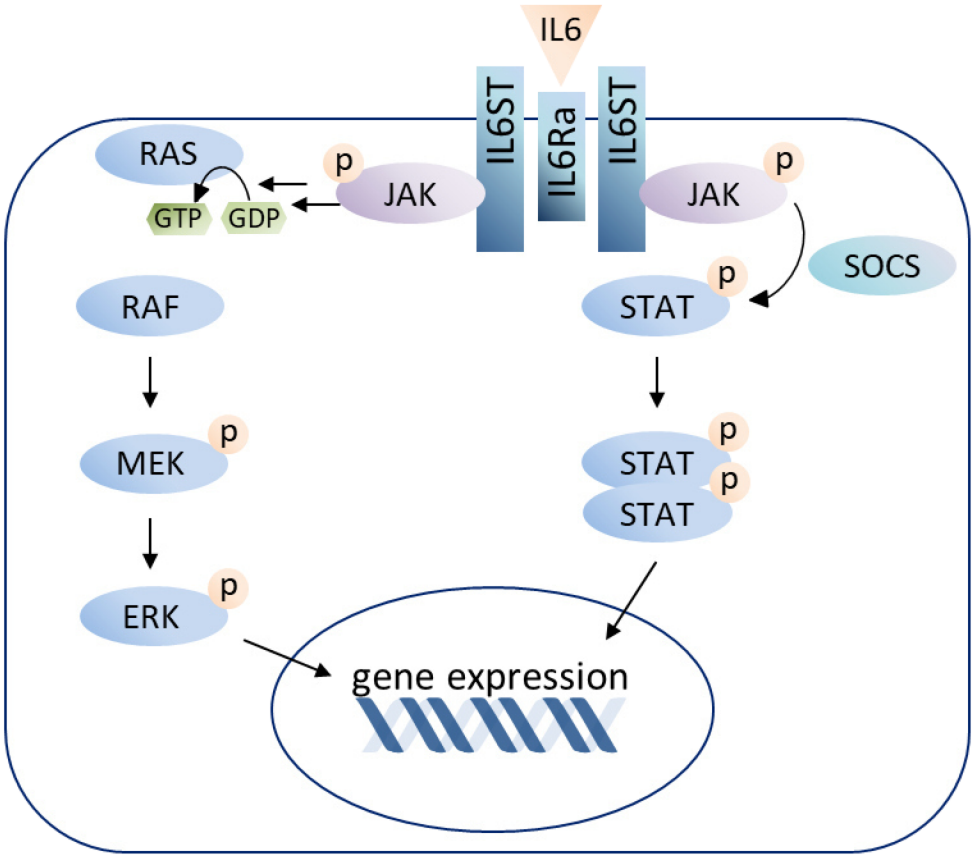

Figure 10: IL6 signaling pathway. Adapted from Heinrich *et al*. (122).

IL6 is upregulated during OIS in fibroblast and melanocyte models on mRNA and protein level (46,66,86). Treatment with the recombinant cytokine and its receptor in the presence of an oncogene (melanocytes expressing $BRAF^{E600}$) could induce growth arrest. Depletion of the cytokine as well as its receptor led to bypass of OIS-related growth arrest. This phenomenon was not observed under pharmacological inhibition of the cytokine. Knock-down of IL6 coincided with a reduction of other OIS markers, such as SAHF, CDKN2B as well as expression of genes correlated with inflammation (46). IL6 was found to be secreted by senescent HER2-positive breast cancer cells *in vitro* and *in vivo* models. Inhibition with blocking antibodies of IL6 impaired growth of HER2-positive PDX models (123).

1.2.3 OIS in PA

The downstream consequence of the constitutively activated MAPK pathway in PA is the activation of OIS. Jacob as well as Raabe and colleagues detected markers of OIS in primary PA material. Both observed elevated expression of CDKN2A in tissue samples and could show activity of SA-ß-Gal in primary PA cultures (19,32). Further evidence was provided by Raabe *et al*., showing that the

transduction of neuronal precursor cells with $BRAF^{V600E}$ led to grow arrest of cells, which were positive for SA-ß-Gal and CDKN2A (32). Additionally, Jacob and colleagues detected a low mitotic index in n=52 analyzed PA tumor samples as well as an overexpression of senescence-associated genes on mRNA level such as *CDKN1A*, *CDKN2A*, *CEBPB* and *IGFBP7*. The upregulation of senescence- and inflammation-associated genes in PA was later confirmed by Jones and colleagues (124). Looking at miRNA and gene expression in n=14 PA samples, the authors detected elevated expression of miRNAs regulating the NFκB pathway and upregulation of factors of the SASP such as *IGFBP7*, *TIMP1*, *IL6*, *IL8* and *IL1B,* as well as *CDKN1A*, *CDKN2A*. The mechanism of OIS is thought to induce growth arrest in PA cells, which could be the main reason for the slow and benign growth behavior typically observed in PA patients.

1.3 Aim

The aim of this thesis was the development of LGG models to improve the understanding of the molecular mechanisms governing tumor growth behavior of LGGs and to identify novel treatment options.

The first aim of this thesis was to support the establishment of a primary *in vitro* and *in vivo* model of a LGG. As described above, the lack of *in vitro* and *in vivo* models hampers research in LGGs. Models are urgently needed to better study and understand the biology of this tumor entity and subsequently develop new therapies.

The second aim of the thesis was to utilize the established LGG models to prove presence and characterize OIS as well as the concurrent inflammatory signaling. The benign growth behavior of LGG is considered to result from OIS (19), which in turn has been reported to be regulated by the inflammatory network for the SASP (87), but the role of the SASP in PA is unknown.

The third and fourth aim was the identification of specific markers for OIS in PA and the investigation of their regulation during OIS. LGG tumor growth is unpredictable to date, making it vital to understand the regulation of tumor recurrence or induction of growth arrest. Stimulation or inhibition of the identified OIS-regulating signaling networks could modulate tumor growth and represent putative targets.

The final aim of the project was to implement the findings into a clinical context, by identifying novel targets or biomarkers, which would enable prediction of clinical outcome. As prediction of recurrence or progression remains poor to date, prognostic markers identifying patient populations at low or high risk of relapse or recurrence could improve clinical decision-making.

2. MATERIALS AND METHODS

2.1 Materials

2.1.1 Cell lines and cell culture

Cell lines

Cell line	Origin	Cat. no.	Supplier
BT-40	Human pediatric low-grade glioma (125)	-	A kind gift from Dr. P. Houghton, University of Texas Health Science Center at San Antonio, TX, USA
DKFZ-BT66	Human pediatric pilocytic astrocytoma	-	Generated in the CCU Pediatric Oncology, Heidelberg, Germany (31).
HEK293T	Human embryonic kidney	HCL4517	GE Healthcare Dharmacon, Lafayette, CO, USA
MED8A	Human medulloblastoma, group 3 (126)	-	A kind gift from Dr. R. Gilbertson, St. Jude, Memphis, TN, USA
NHA	Normal human astrocytes	CC-2565	LONZA, Basel, Switzerland
Platinum GP cells	Based on HEK293T human embryonic kidney cells	RV-103	Cell Biolabs, San Diego, CA, USA

Cell culture reagents

Article	Cat. no.	Supplier
ABM basal medium	CC-3187	LONZA, Basel, Switzerland
Acetylcystein (100 µg/mL)	BG0012	BIOTREND Chemikalien, Cologne, Germany
AGM SingleQuot Kit Supplements & Growth Factors	CC-4123	LONZA, Basel, Switzerland
B-27 Supplement (50x)	17504044	Thermo Fisher Scientific, Waltham, MA, USA
Basic-FGF (20 µg/mL)	AF-100-18B	Peprotech Rocky Hill, NJ, USA
Blasticidin S HCl (10 mg/mL)	A1113903	Thermo Fisher Scientific, Waltham, MA, USA
DMEM	BE12-604F/U1	LONZA, Basel, Switzerland
DMSO (Dimethyl sulfoxide), cell culture grade	M6323.0100	Genaxxon bioscience, Ulm, Germany
Doxycycline	sc-337691	Santa Cruz, Dallas, TX, USA
EGF (20 µg/mL)	AF-100-15	Peprotech Rocky Hill, NJ, USA
FBS (fetal bovine serum)	F7524	Sigma-Aldrich, St. Louis, MO, USA
Glucose solution (200 g/L)	A2494001	Thermo Fisher Scientific, Waltham, MA, USA
GlutaMAX-I supplement (100x)	35050038	Thermo Fisher Scientific, Waltham, MA, USA
heat-inactivated horse serum	10368902	Thermo Fisher Scientific, Waltham, MA, USA
HEPES buffer solution (1M)	15630049	Thermo Fisher Scientific, Waltham, MA, USA
Hygromycin-B (50 mg/mL in PBS)	sc-29067	Santa Cruz, Dallas, TX, USA
Insulin human	I3536	Sigma-Aldrich, St. Louis, MO, USA

Leukemia Inhibitory Factor human (LIF) (10 µg/mL)	L5283	Sigma-Aldrich, St. Louis, MO, USA
MEM	11095080	Thermo Fisher Scientific, Waltham, MA, USA
N2	17502048	Thermo Fisher Scientific, Waltham, MA, USA
Neurobasal A NeuroCult™ NS-A Basal Medium (human)	05750	Stemcell Technologies, Vancouver, Canada
Neural Survival Factor-1 (NSF-1)	CC-4323	LONZA, Basel, Switzerland
Phosphate Buffered Saline (PBS)	D8537	Sigma-Aldrich, St. Louis, MO, USA
Puromycin	13884	Cayman Chemicals, Ann Arbor, MI, US
RPMI 1640	21875034	Thermo Fisher Scientific, Waltham, MA, USA
0.05% Trypsin-EDTA	25300054	Thermo Fisher Scientific, Waltham, MA, USA
X-VIVO medium	04-418Q	LONZA, Basel, Switzerland

2.1.2 Treatment reagents and drugs

Article	**Cat. no.**	**Supplier**
ABT-737	ab141336	Abcam, Cambridge, UK
Anakinra (Kineret 150 mg/mL)	2426499	Sobi, Stockholm, Sweden
Anti-human IL1B neutralizing antibody	MAB201-100	R&D Systems, Minneapolis, MN, USA
Bepanthen	01578847	Bayer, Leverkusen, Germany
Betaisadona solution	04923204	Mundipharma, Limburg, Germany
Bupivacaine (0.25%)	07703489	Jenapharm, Jena, Germany

Caprofen Rimadyl	-	Pfizer, New York, NY, USA
Carboplatin	S1215	Selleckchem, Houston, TX, USA
Dasatinib	S1021	Selleckchem, Houston, TX, USA
Dexamethasone (water soluble)	D2915	Sigma-Aldrich, St. Louis, MO, USA
IsoFlo® (100% w/w)	-	Zoetis, Kalamazoo, MI, USA
Navitoclax (ABT-263)	11500	Cayman chemical, Ann Arbor, MI, USA
Quercetin	S2391	Selleckchem, Houston, TX, USA
rIL1B	201-LB-005	R&D Systems, Minneapolis, MN, USA
rIL6	206-IL-010	R&D Systems, Minneapolis, MN, USA
Tocilizumab (RoActemra 20 mg/mL)	7286809	Hoffmann-LaRoche, Basel, Switzerland
Trametinib	A3018	ApexBio, Houston, TX, USA
Vincristine sulfat	S1241	Selleckchem, Houston, TX, USA

2.1.3 Bacteria

Article	**Cat. no.**	**Supplier**
One Shot™ TOP10 chemically competent *E.coli*	C4040-03	Invitrogen, Carlsbad, CA, USA

Antibiotics for bacterial selection

Article	**Cat. no.**	**Dilution**	**Supplier**
Ampicillin sodium salt dissolved in sterile water (100 mg/mL)	sc-202951	1:1000	Santa Cruz, Dallas, TX, USA

Kanamycin sulfate min. 750 I.U./mg dissolved in sterile water (10 mg/mL)	T832.1	1:100	Carl Roth, Karlsruhe, Germany

2.1.4 Antibodies

Primary antibodies for western blot (WB)/immunofluorescence (IF)

Article	**Cat. no.**	**Dilution (1:x)**	**Supplier**
monoclonal mouse anti-β-actin	A5441	1000	Sigma-Aldrich, St. Louis, MO, USA
monoclonal rabbit anti-CDKN2A	108349	1000	Abcam, Cambridge, UK
monoclonal mouse anti-CDKN1A	sc-6246	200	Santa Cruz, Dallas, TX, USA
monoclonal rabbit anti-ERK (1/2)	4695	1000	Cell Signaling, Danvers, MA, USA
monoclonal rabbit anti-pERK (1/2) (Thr202/ Tyr204)	4377	1000	Cell Signaling, Danvers, MA, USA
monoclonal rabbit anti-human IL1B	ab9722	1000	Abcam, Cambridge, UK
polyclonal rabbit anti-human IL1R1	sc-688	100	Santa Cruz, Dallas, TX, USA
polyclonal rabbit anti-human IL6Ra	sc-661	200	Santa Cruz, Dallas, TX, USA
monoclonal mouse anti-human IRAK1	sc-5288	200	Santa Cruz, Dallas, TX, USA
monoclonal rabbit anti-MEK (1/2)	9122	1000	Cell Signaling, Danvers, MA, USA
monoclonal rabbit anti-pMEK (1/2) (Ser217/ Ser221)	9154	1000	Cell Signaling, Danvers, MA, USA
monoclonal rabbit anti-NFκB p65/RELA Clone C22B4	4764S	1000	Cell Signaling, Danvers, MA, USA

monoclonal rabbit anti-Phospho-NFκB p65/RELA (Ser536) Clone 93H1	3033S	1000	Cell Signaling, Danvers, MA, USA
monoclonal mouse anti-human phosho-STAT3 (Tyr705)	9138	1000	Cell Signaling, Danvers, MA, USA
monoclonal mouse anti-human STAT3	9139	1000	Cell Signaling, Danvers, MA, USA
monoclonal mouse anti-SV40 large T antigen	ab80564	1000 (WB) 250 (IF)	Abcam, Cambridge, UK
monoclonal mouse anti-TP53	sc-126	200	Santa Cruz, Dallas, TX, USA

Primary antibodies for immunohistochemistry

Article	**Cat. no.**	**Dilution**	**Pretreatment**	**Supplier**
monoclonal mouse anti-CDKN2A clone GI75-405	551153	1:200	64 min with CC1+OptiVew	BD Pharmingen, San Jose, CA, USA
polyclonal rabbit clone anti-pERK (1/2)	9101S	1:100	4 min with protease	Cell Signaling, Danvers, MA, USA
polyclonal rabbit anti-GFAP	Z0334	1:1000	None	Dako, Stanta Clara, CA, USA
polyclonal rabbit clone C-20 anti-IL6Ra	sc-661	1:100	64 min with CC2	Santa Cruz, Dallas, TX, USA
monoclonal rabbit clone 30-9 anti-Ki67	REF790-4286	3:4	64 min with CC1	Ventana, Tucson, AZ, USA
monoclonal mouse anti-LCA clone 2B11+PD7/26	M0701	1:200	52 min with CC1	Dako, Stanta Clara, CA, USA

Secondary antibodies

Article	**Cat. no.**	**Dilution (1:x)**	**Supplier**
polyclonal donkey-anti-rabbit IgG HRP	V795A	10000	Promega, Madison, WI, USA

polyclonal goat-anti-mouse IgG HRP	115-035-003	10000	Dianova, Hamburg, Germany
goat anti-mouse- Alexa Fluor® 488	A28175	500	Cell Signaling, Danvers, MA, USA

2.1.5 Primers

Gene name	Cat. no./sequence	Supplier
ACTB forward	ctggaacggtgaaggtgaca	Invitrogen, Carlsbad, CA, USA
ACTB reverse	aagggacttcctgtaacaatgca	Invitrogen, Carlsbad, CA, USA
CDKN1A	QT00062090	Qiagen, Hilden, Germany
CDKN2A	QT00089964	Qiagen, Hilden, Germany
hTERT	QT00073409	Qiagen, Hilden, Germany
IL1B	QT00021385	Qiagen, Hilden, Germany
IL6	QT00083720	Qiagen, Hilden, Germany
IL1R1	QT00081263	Qiagen, Hilden, Germany
IL6R	QT00023660	Qiagen, Hilden, Germany
KIAA1549:BRAF forward	gtccttctacagcccagccca	Invitrogen, Carlsbad, CA, USA
KAA1549:BRAF reverse	tggagatttctgtaaggctttcacgt	Invitrogen, Carlsbad, CA, USA
SV40 large T antigen forward	gatgatgatgatgaagacagccagg	Invitrogen, Carlsbad, CA, USA
SV40 large T antigen reverse	tgatcatgaacagactgtgaggact	Invitrogen, Carlsbad, CA, USA
TBP forward	agaacaacagcctgccac	Invitrogen, Carlsbad, CA, USA
TBP reverse	gttgctcttccaaaatagacagac	Invitrogen, Carlsbad, CA, USA
TNFRSF1B	QT00029232	Qiagen, Hilden, Germany

2.1.6 Plasmids

Article	Cat. no.	Supplier
GIPZ IL1B shRNA	RHS4531-EG3553 glycerol set: #1: RHS4430-200270175 - V3LHS_321412 #2: RHS4430-200270935 - V3LHS_321414 #3: RHS4430-200266465 - V3LHS_321415	GE Healthcare Dharmacon, Lafayette, CO, USA
GIPZ IL6 shRNA	RHS4531-EG3569 glycerol set: #1: RHS4430-200211138 - V2LHS_111640 #2: RHS4430-200240808 - V3LHS_390095 #3: RHS4430-200236401 - V3LHS_390097	GE Healthcare Dharmacon, Lafayette, CO, USA
GIPZ IL1R1 shRNA	RHS4531-EG3554 glycerol set: #1: RHS4430-200179369 - V2LHS_131081 #2: RHS4430-200207931 - V2LHS_131083 #3: RHS4430-200282217 - V3LHS_403370 #4: RHS4430-200280062 - V3LHS_403365 #5: RHS4430-200281507 - V3LHS_403366 #6: RHS4430-200283912 -	GE Healthcare Dharmacon, Lafayette, CO, USA

	V3LHS_403367	
GIPZ IL6R shRNA	RHS4531-EG3570 glycerol set: #1: RHS4430-200179323 - V2LHS_93695 #2: RHS4430-200252062 - V3LHS_387501 #3: RHS4430-200251326 - V3LHS_387502	GE Healthcare Dharmacon, Lafayette, CO, USA
pBABE-hygro-hTERT plasmid	1773 (Addgene)	A kind gift from Dr. B. Weinberg, MIT, Cambridge, MA, USA
pCMV-VSV-G	VPK-302	Cell Biolabs, San Diego, CA, USA
pFRIPZ SV40-TAg	-	Generated from the pTRIPZ plasmid (Open Biosystems), by Dr. F. Selt, CCU Pediatric oncology, Heidelberg, Germany (31)
pGreenFire reporter vector	TR011PA/VA-1	System Biosciences, Palo Alto, CA, USA
Thermo Scientific™ GIPZ™ Non-silencing Control	RHS4346	GE Healthcare Dharmacon, Lafayette, CO, USA

2.1.7 Biochemicals and Reagents

Article	**Cat. no.**	**Supplier**
Acrylamide/Bis Solution, 37.5:1 (40 % w/v)	10681.01	SERVA, Heidelberg, Germany
Agar	S210.3	Carl Roth, Karlsruhe, Germany
Agarose, low gelling temperature	A9414	Sigma-Aldrich, St. Louis, MO, USA
Albumin Standard (2 mg/mL)	23209	Thermo Fisher Scientific, Waltham, MA, USA
Ammonium persulfate	A3678	Sigma-Aldrich, St. Louis, MO, USA

(APS)		
ß-mercaptoethanol	39563	SERVA, Heidelberg, Germany
Brilliant Blue G	27815	Sigma-Aldrich, St. Louis, MO, USA
Bromophenol blue	A2331,0005	AppliChem, Darmstadt, Germany
BSA	A4612	Sigma-Aldrich, St. Louis, MO, USA
CellTiter-Glo One Solution	G8461	Promega, Madison, WI, USA
CellTracker™ CM-DiI Dye	C7001	Thermo Fisher Scientific, Waltham, MA, USA
DAPI (4',6-Diamidino-2-phenylindol) (0.25 µg/mL dissolved in PBS)	A1001	AppliChem, Darmstadt, Germany
Dimethylformamide (DMF)	20270	SERVA, Heidelberg, Germany
Dithiothreitol (DTT)	A1101	AppliChem, Darmstadt, Germany
ECL Prime Amersham	RPN2232	GE Healthcare Dharmacon, Lafayette, CO, USA
Ethylene diamine tetraacetate (EDTA)	1034	GERBU Biotechnik GmbH, Heidelberg, Germany
Ethanol, absolute	20821.321	VWR chemials, Radnor, PA, USA
Glycerol	15523	Honeywell Riedel-de-Haën, Seelze, Germany
Glycine 100%	33226	Sigma-Aldrich, St. Louis, MO, USA
HEPES	9105.2	Carl Roth, Karlsruhe, Germany
Hydrochlorid acid (HCl) (12.1 M)	13-1683	Sigma-Aldrich, St. Louis, MO, USA
Incidin™ Foam	110566	Ecolab, Monheim am Rhein, Germany
Lemon fresh AF	-	L.C. PLIWA, Malsfeld-Ostheim, Germany
Methanol	M/4000/PC17	Thermo Fisher Scientific, Waltham, MA, USA

Milk powder	T145.2	Carl Roth, Karlsruhe, Germany
Normal goat serum	5-000-121	Dianova, Hamburg, Germany
Paraformaldehyde (PFA) 16% MeOH free	43368	Alfa Aesar, Karlsruhe, Germany
Peptone	8986	Carl Roth, Karlsruhe, Germany
PhosSTOP	4906845001	Sigma-Aldrich, St. Louis, MO, USA
Polybrene	sc-134220	Santa Cruz, Dallas, TX, USA
Poly-L-Lysine	102691	MP Biomedicals, Santa Ana, CA, USA
Ponceau S solution	A2935,0500	AppliChem, Darmstadt, Germany
Potassium chloride (KCl)	6781.1	Carl Roth, Karlsruhe, Germany
Precision Plus Protein™ Kaleidoscope™	1610375	Bio-Rad, Hercules, CA, USA
2- Propanol	20842.330	VWR chemials, Radnor, PA, USA
Soldium Chloride (NaCl)	BP358-1	Thermo Fisher Scientific, Waltham, MA, USA
Sodium dodecyl sulfate (SDS) pellets	2326.1	Carl Roth, Karlsruhe, Germany
Sodium hydroxide (NaOH) pellets	30620	Sigma-Aldrich, St. Louis, MO, USA
StayBrite D-Luciferin	7903	BioVision, Milpitas, CA, USA
Sterile water for injection purposes Ampuwa®	06605508	Fresenius Kabi, Bad Homburg, Germany
SYBR™ Green Platinum™ qPCR SuperMix-UDG	11733046	Thermo Fisher Scientific, Waltham, MA, USA
N, N, N, N-Tetramethyl-Ethylenediamine (TEMED)	2367.3	Th.Geyer, Renningen, Germany
Tris (Trisma Base)	T1503	Sigma-Aldrich, St. Louis, MO, USA

Triton-X 100	A4975,0500	AppliChem, Darmstadt, Germany
Tween 20 (polyoxyethylene sorbitan monolaureate)	500-018-3	MP Biomedicals, Santa Ana, CA, USA
Vi-Cell XR Cell Viability Analyzer™ solutions		Beckmann Coulter, Brea, CA, USA
Yeast extract	70161	Sigma-Aldrich, St. Louis, MO, USA

2.1.8 Buffers and solutions

Article	**Ingredients**
Agar in LB medium	15 g agar mixed with 1 L LB medium: 10 g sodium chloride, 10 g peptone, 5 g yeast extract dissolved in 1 L of de-ionized water, autoclaved and supplemented with appropriate antibiotic.
10% APS	5 g APS dissolved in 50 mL autoclaved de-ionized water, aliquoted to 1 mL and stored at -20°C.
Block milk 100% (WB)	Dissolve 200 g milk powder and 30 g BSA in 500 mL PBS. Dissolve goat serum powder in 10 mL sterile water. Add 10 mL of the dissolved goat serum, 2 mL of Tween 20 and 200 mL of FBS (not inactivated) to milk powder and BSA and fill-up with PBS to 1 L volume in total. Aliquot in 50 mL Falcons and store at -20°C.
Blocking solution (IF)	3% BSA plus 0.05% TritonX 100 in PBS, store at 4°C
2.5M $CaCl_2$	27.7 g $CaCl_2$ in 100 mL de-ionized water, sterile filter, aliquot to 2 mL and store at -20°C.
Coomassie Brilliant Blue staining solution	0.05% Brilliant Blue G, 25% isopropanol, 10% acetic acid in de-ionized water. Filtered and stored at RT protected from light.
DAPI/TritonX 100 solution	0.1% TritonX 100 and 1 µg/mL DAPI both dissolved in PBS.
10x Doxycycline for cell culture	100 mg doxycycline (4°C) are dissolved in 10 mL sterile water,

	aliquoted to 1 mL and stored at -20°C.
1x Doxycycline (1 mg/mL) for cell culture	Under sterile conditions dilute 2 mL doxycycline (10 mg/mL) in 18 mL autoclaved de-ionized water, aliquot to 1 mL and store at -20°C.
Doxycycline for mice	2.5 cubes of sugar and 0.7 g doxycycline are dissolved in 50 mL sterile water.
DTT 1 M	1.54 g DTT are dissolved in 10 mL autoclaved de-ionized water, aliquoted to 1 mL and stored at -20°C.
FBS for cell culture	FBS is thawed, heat-inactivated in a water bath at 56°C for 30 minutes and aliquoted to 50 mL. Storage at -20°C.
2x HBS pH 7.12	Dissolve 8.2 g sodium chloride, 11.9 g HEPES and 0.1 g NA_2HPO_4 in 500 mL de-ionized water, adjust pH and sterile filter. Aliquot to 10 mL and store at -20°C.
LB Medium	10 g sodium chloride, 10 g peptone, 5 g yeast extract are dissolved in 1 L of de-ionized water, autoclaved and stored at 4°C.
3% Low-melting agarose	Mix 0.9 g low-melting agarose in 31 mL of PBS and dissolve under heat using the microwave.
Mastermix SYBR Green	Per sample: 10 µL 2x SYBR Green, 2 µL primer mix (forward + reverse), 3µL de-ionized water
2% Milk in TBS-T	Dissolve 4 g milk powder in 200 mL of TBS-T, store at 4°C.
Permeabilization solution (IF)	0.2% TritonX 100 in PBS
PhosSTOP	Dissolve one tablet of PhosSTOP in 1 mL SDS lysis buffer, vortex, aliquot to 100 µL, store at -20°C.
Poly-L-Lysine solution (100 µg/mL)	Dissolve 1 mg PLL in 10 mL sterile water and store at -20°C.
Ponceau S solution	5 mL Ponceau S are diluted in 45 mL de-ionized water and stored at RT.

Resolving gel buffer pH 8.8 (1.5 M)	36.34 g Tris are dissolved in 150 mL de-ionized water, the pH is adjusted to 8.8 and filled-up with water to 200 mL. Store at RT.
20% SDS	20 g of SDS pellets are dissolved in 100 mL of de-ionized water and stored at RT.
10x SDS running buffer	30.3 g Tris, 144.1 g glycine and 10 g SDS pellets are dissolved in 700 mL of de-ionized water, pH is adjusted to 8.3 and filled-up to result in 1 L final volume with de-ionized water. Store at RT.
1x SDS running buffer	100 mL of 10x SDS running buffer are diluted in 900 mL of de-ionized water.
SDS lysis buffer	12.4 mL of stacking gel buffer, 10 mL of 20% SDS, 10 mL of 100% glycerol are filled-up to 100 mL with de-ionized water. To 1 mL aliquots (stored at -20°C), 1 µL DTT (1M) and 100 µL dissolved PhosSTOP are added fresh.
Stacking gel buffer pH 6.8 (0.5 M)	12.12 g Tris are dissolved in 150 mL of de-ionized water, the pH is adjusted to 6.8 and filled-up with water to 200 mL. Store at RT.
10x TBS	Dissolve 60 g Tris and 440 g sodium chloride in 4 L of de-ionized water, adjust pH to 7.6 and fill-up with de-ionized water to 5 L total. Store at RT.
1x TBS-T	100 mL of 10x TBS are diluted in 900 mL of de-ionized water and 2 mL of Tween 20 are added. Store at RT.
1x TE puffer pH 8.0	Dissolve 0.121 g Tris (10 mM), 0.0292g EDTA (1 mM) in 100 mL water, adjust pH and sterile filter, store at 4°C.
0.1x TE puffer pH 8.0	Dilute 1x TE puffer 1:10 in de-ionized water and sterile filter.
0.1x TE with dH2O (1:2)	Dilute 5 mL of 0.1xTE with 10 mL of sterile water.
10x Transfer buffer	58 g Tris and 29.3 g glycine are dissolved in 1 L of de-ionized water. Store at RT.

1x Transfer buffer	Mix 100 mL of 10x transfer buffer, 200 mL of 100% methanol and 700 mL de-ionized water. Store at RT.

2.1.9 Consumables

Article	Supplier
Anti-A2B5 MicroBeads, human, mouse, rat (130-093-392)	Miltenyi Biotec, Bergisch Gladbach Germany
Chromatography Paper "Whatman CHR 3mm"	GE Healthcare Dharmacon, Lafayette, CO, USA
Conical tubes, 15 mL and 50 mL	Thermo Fisher Scientific, Waltham, MA, USA
Cryovial	Carl Roth, Karlsruhe, Germany
Falcon® 5 mL Round Bottom Polystyrene Test Tube	Thermo Fisher Scientific, Waltham, MA, USA
Glassware	SCHOTT AG, Mainz, Germany
Ibidi 8-well µ-slides	Ibidi GmbH, Martinsried, Germany
Microplates, 96 well, clear	Greiner Bio-One, Frickenhausen, Germany
Microplates, 96 well, white	Greiner Bio-One, Frickenhausen, Germany
Millicell® CM 0.4 µm (co-culture inserts)	Merck Millipore, Burlington, MA, USA
Needle 27G 0.4 x 20 mm	Terumo, Leuven, Belgium
Nitrocellulose (NC) membrane Whatman® Protran®	Sigma-Aldrich, St. Louis, MO, USA
Parafilm® M	Benis, Braine-l'Alleud, Belgium
PCR tube strips and domed caps	Thermo Fisher Scientific, Waltham, MA, USA
Pipette filter tips, 10 µL, 20 µL, 100 µL, 200 µL and 1000 µL	Nerbe plus, Winsen/Luhe, Germany
Polystyrene Round-Bottom Tube with Cell-Strainer Cap	Corning, Kaiserslautern, Germany

Polyvinylidene difluoride (PVDF) membrane	Bio-Rad, Hercules, CA, USA
PROLENE® Polypropylene Suture, C1, 13 mm	Ethicon, Somerville, NJ, USA
Reaction tubes "Safe-Lock Tubes", 0.5 mL, 1.5 mL and 2.0 mL	Eppendorf, Hamburg, Germany
Serological pipettes, 5 mL, 10 mL and 20 mL	Sigma-Aldrich, St. Louis, MO, USA
Sterile filter 0.22 µm	Merck Millipore, Burlington, MA, USA
Syringe 1 mL Megro™ Luer Luck tuberkulin softject	Thermo Fisher Scientific, Waltham, MA, USA
Syringe 10 mL	Terumo, Tokyo, Japan
Tissue culture dishes, 100 x 20 mm	Thermo Fisher Scientific, Waltham, MA, USA
Tissue culture flasks "Cellstar" 25 cm^2, 75 cm^2, 175 cm^2	Greiner Bio-One, Frickenhausen, Germany
Tissue culture plates, 6 well and 96 well	Corning, Kaiserslautern, Germany
Tissue culture plates 96 well round bottom (U-base) TPP®	Sigma-Aldrich, St. Louis, MO, USA
Tissue culture 96-well flat bottom black opaque wall plates	Corning, Kaiserslautern, Germany
ViCell 4 mL tube	Beckmann Coulter, Brea, CA, USA

2.1.10 Kits

Article	Cat. no.	Supplier
Amersham ECL Prime Western Blotting Detection Reagent	RPN2232	GE Healthcare Dharmacon, Lafayette, CO, USA
Bio-Plex® Cell Lysis Kit	171304011	Bio-Rad, Hercules, CA, USA
Bio-Plex Pro™ Human Cytokine 27-plex Assay	m500kcaf0y	Bio-Rad, Hercules, CA, USA

Brain Tumor Dissociation Kit	130-095-942	Miltenyi Biotec, Bergisch Gladbach Germany
ELISA Kit for IL1B	DLB50	R&D Systems, Minneapolis, MN, USA
ELISA Kit for IL6	D6050	R&D Systems, Minneapolis, MN, USA
Pierce™ BCA Protein Assay Kit	23227	Thermo Fisher Scientific, Waltham, MA, USA
PlasmoTest™ Mycoplasma Detection Kit	Rep_ptrk	InvivoGen, Toulouse, France
QIAGEN Plasmid Maxi Kit	12145	Quiagen, Hilden, Germany
RevertAid First Strand cDNA Synthesis Kit	K1622	Thermo Fisher Scientific, Waltham, MA, USA
RNeasy Mini Kit	74104	Quiagen, Hilden, Germany
qPCR Mastermix for SYBR® Green I	4309155	Thermo Fisher Scientific, Waltham, MA, USA
Senescence ß-galactosidase staining kit	9860	Cell Signaling, Danvers, MA, USA
Thermo Scientific™ Trans-Lentiviral™ Packaging System	TLP5912	GE Healthcare Dharmacon, Lafayette, CO, USA
Venor® GenM Classic Mycoplasma Detection Kit	11-1250	Minerva Biolabs, Berlin, Germany

2.1.11 Software

Software	Company
ABI 7500 Software v2.3	Applied Biosystems, Thermo Fisher Scientific, Waltham, MA, USA
CellB 2.3 Soft imaging software	Olympus Biosystem GmbH, Shinjuku, Tokyo, Japan
Chemi-Capt 5000	Vilber Lourmat, Eberhardzell, Germany

EndNote X8	Clarivate Analytics, Philadelphia, PA, USA
FlowJo v10	FlowJo, LLC, Ashland, OR, USA
GraphPad Prism v5.01	GraphPad Software Inc., San Diego, CA, USA
Microsoft office 2007/2010	Microsoft, Redmond, WA, USA
OPTIMA Microplate Reader Software v2.20R2	BMC Labtech, Ortenberg, Germany
R 3.4	The R Foundation, Vienna, Austria
R2	R2 Academic Medical Center (AMC), Amsterdam, Netherlands
Vi-CELL™ XR 2.03 software	Beckmann Coulter, Brea, CA, USA

2.1.12 Instruments and machines

Machine	Company
ABI 7500 Real Time PCR cycler	Applied Biosystems, Foster City, CA, USA
Analytical Balance "BP 121S"	Sartorius, Göttingen, Germany
Barnstead™ GenPure™ xCAD Plus Ultrapure Water Purification System	Thermo Fisher Scientific, Waltham, MA, USA
BD FACS Canto II flow cytometer	Becton, Dickinson and Company, Heidelberg, Germany
Benchtop centrifuge Allegra X-12R	Beckmann Coulter, Brea, CA, USA
Biometra T3000 Thermocycler	LabRepCo, Horsham, PA, USA
Blotting chamber "TransBlot® SD Semi-Dry Transfer Cell"	Bio-Rad, Hercules, CA, USA
CellMate® II Serological Pipette	Matrix Technologies Corporation, Thermo Fisher Scientific, Waltham, MA, USA
Cell culture incubator "C200"	Labotect, Rosdorf, Germany

Cell culture sterile bench "Safe 2020"	Thermo Fisher Scientific, Waltham, MA, USA
Chemi-Smart 5000 Technology, Chemiluminescence imaging system	Vilber Lourmat, Eberhardzell, Germany
Cryo Freezing container Nalgene® Cryo 1°C “Mr. Frosty”	Thermo Fisher Scientific, Waltham, MA, USA
Electrophoresis chamber "Mini-Protean® Tetra System"	Bio-Rad, Hercules, CA, USA
Epson perfection V700 Photo scanner	EPSON, Nagano, Japan
FLUOstar OPTIMA automated plate reader	BMC Labtech, Ortenberg, Germany
Hamilton Microliter™ #701	Hamilton, Reno, NV, USA
Heating block "Thermomixer® comfort"	Eppendorf, Hamburg, Germany
Heat sealer "Folio"	Severin Elektro, Sundern, Germany
Incubator Heraeus B6420	Heraeus, Leverkusen, Germany
Innova 4230 refrigerated benchtop incubator	New Brunswick Scientific, Nürtingen, Germany
Instruments for surgery	FST fine science, Foster City, CA, USA
Isoflurane Vapor 19.3	Dräger, Lübeck, Germany
Light microscope "CKX31"	Olympus, Hamburg, Germany
Light microscope "CKX41" with reflected fluorescence system	Olympus, Hamburg, Germany
Light microscope Leica M205 FA	Leica, Wetzlar, Germany
Light microscope "Zeiss LSM710" confocal microscope for fluorescence imaging	Carl Zeiss, Oberkochen, Germany
LS Column	Miltenyi Biotec, Bergisch Gladbach Germany
Magnetic stirrer with heating "MR-3001"	Heidolph Instruments, Schwabach, Germany
Micro 4™ Micro Syringe Pump Controller	World precision instruments, Sarasota, FL, USA

Microcentrifuge "5417 R"; rotor: "F 45-24-11"	Eppendorf, Hamburg, Germany
Micropipette “PIPETMAN Neo® P2N”, P10N”, P20N”, P200N”, P1000N”	Gilson, Limburg-Offheim, Germany
Micropipette "Eppendorf Research® 10-100 µL", 0.5-10 µL"	Eppendorf, Hamburg, Germany
Microplate fluorescence reader "FLUOstar OPTIMA"	BMG Labtech, Ortenberg, Germany
Microwave Severin MW 7869	Severin Elektro, Sundern, Germany
MidiMACS™ Separator	Miltenyi Biotec, Bergisch Gladbach Germany
Multi-axle rotating mixer "TRM 56"	IDL GmbH, Nidderau, Germany
Multichannel pipette "Finnipipette® Digital 40-200 µL"	Thermo Fisher Scientific, Waltham, MA, USA
Nano-Drop ND-1000 Spectrophotometer	PEQLab, Erlangen, Germany
pH meter "SevenEasy"	Mettler-Toledo, Gießen, Germany
Pipette controller "accu-jet® pro"	BRAND, Wertheim, Germany
Power supply "EV231"	PEQLab, Erlangen, Germany
Power supply "PowerPac™ Basic Power Supply"	Bio-Rad, Hercules, CA, USA
Precision balance "440-47N"	KERN & SOHN, Balingen, Germany
Refrigerator with freezer	Liebherr, Biberach an der Riß, Germany
Rocking platform "WT 16"	Biometra, Göttingen, Germany
Test tube shaker "Reax top"	Heidolph Instruments, Schwabach, Germany
Ultra-low temperature freezer	Thermo Fisher Scientific, Waltham, MA, USA
UMP3 UltraMicroPump	World precision instruments, Sarasota, FL, USA
Universal 320R tabletop centrifuge (for plates)	Hettich Lab Technology, Tuttlingen, Germany
Vi-CELL XR automated cell counter	Beckmann Coulter, Brea, CA, USA

Vortexer "IKA VF2"	IKA Janke & Kunkel, Staufen im Breisgau, Germany
Water bath	Memmert, Schwabach, Germany

2.2 Methods

2.2.1 Cell culture and methods used to generate an *in vitro* LGG model

All cells were cultured at 37°C in humidified atmosphere containing 5% CO_2. Cell stocks were tested for contamination with the Multiplex cell Contamination Test (McCT) (127) as well as for identity via single nucleotide polymorphism profiling in the Multiplex Cell Line Authentication test (MCA) (127) prior to use for experiments. Only tested stocks were used for all experiments. The analyzed cell lines were free of virus and *Mycoplasma* contamination, no contamination with other species and no cross-contamination with other cell lines was detected. Cells in culture were tested for *Mycoplasma* contamination every week with the PlasmoTest™ Mycoplasma Detection Kit (InvivoGen) and every month via PCR with the Venor®GeM kit (Minerva Biolabs) and for fungal or bacterial contamination by visual control by microscopy every two days. No *Mycoplasma* contamination was detected throughout the experiments.

Cell culture was performed under the laminar flow cell culture hood under sterile conditions. Cell culture medium and supplements were kept sterile, stored in the fridge or freezer and allowed to reach room temperature (RT) before being added to the cells.

2.2.1.1 Thawing of cells

Cryostocks were preserved in liquid nitrogen for long-term storage or in the -80°C freezer for short-term storage. Before thawing, a 15 mL Falcon tube was prepared with 10 mL of the appropriate cell culture medium and adjusted to RT. As the cryopreservation medium contains 10% of dimethylsulfoxide (DMSO), rapid defrosting, to remove the cytotoxic agent, reduces stress on the cells. Frozen cells were thawed in a pre-warmed 37°C water bath for two minutes, transferred to the prepared 15 mL Falcon tube and centrifuged at 230 x g for 5 minutes at RT. The supernatant was removed and the cell pellet resuspended in 3-5 mL of fresh medium. Cells were seeded in T25 culture flasks or in one well of a six-well plate.

To facilitate attachment of cells after long-term storage, six-well plates were coated with poly-L-lysine (PLL, see 2.1.7) before seeding. PLL is a naturally occurring polyamino acid, which is positively charged and facilitates attachment of negatively charged proteins on the cell surface (128). For this purpose, PLL (1 mg/mL, stored at -20°C) was diluted 1:10 in sterile PBS and 200 µL of the dilution were spread per well. The coated plate was incubated at 37°C for 1 hour followed by two washing steps with PBS before cells were seeded.

2.2.1.2 Culture of different cell lines

The patient-derived cell line **DKFZ-BT66** was established from a pilocytic astrocytoma with a *KIAA:BRAF* fusion (31). DKFZ-BT66 cells (passages 8-17) and DKFZ-BT66 hTERT cells (passages 16-36) were cultured as monolayer in ABM basal medium supplemented with the AGM Kit from LONZA (see table 2.1.1). Doxycycline (1 µg/mL) from Santa Cruz (see table 2.1.1) was added together with fresh cell culture medium to activate transcription of the doxycycline-inducible SV40-TAg for expansion purposes (for details on the generation of the cell culture model see 3.1.1). Medium was changed on Monday, Wednesday and Friday to achieve consistent levels of doxycycline in proliferating DKFZ-BT66 cells. The senescent state of the cell line was obtained by seeding the cells in culture medium without the addition of doxycycline and subsequent culture for five days. After five days, the cell state was considered to be senescent (see Fig. 19) and experiments in the senescent condition were initiated. Cell medium (without doxycycline) was changed in the same intervals as for DKFZ-BT66 cells in proliferation (with doxycycline) to ensure that differences in both conditions did not result from addition of fresh medium supplemented with growth factors in different time intervals. In contrast to other cell lines, proliferating DKFZ-BT66 cells were cultivated to a confluency of up to 90% before passaging, as the fastest growth rate was observed during dense seeding conditions. On average, cells were passaged after seven to fourteen days using 0.05% trypsin-EDTA from Thermofisher (see 2.1.1) (3-5 min incubation at 37°C). Incubation times with trypsin were longer (up to 10 min) for senescent DKFZ-BT66 cells, to account for the increased attachment of the cells to the cell culture flasks, most likely due to the enlarged cellular phenotpye.

The patient-derived **BT-40** cell line is representative for a WHO grade II/III glioma with a $BRAF^{V600E}$ mutation and a homozygous *CDKN2A* loss (125). BT-40 (passage 3-22) cells were cultured as monolayer in RPMI1640 medium supplemented with 10% FBS and 2 mM L-glutamine (see table 2.1.1). Cells were cultivated until 60% confluent, when they start to form honeycomb shaped clusters, and passaged at least every seven days using 0.05% trypsin-EDTA. Cell culture medium was changed twice a week.

Normal human astrocytes (**NHA**) cells (passage 2-3) were cultured as monolayer in ABM basal medium supplemented with the AGM Kit from LONZA (see table 2.1.1). Cells were cultivated until 70% confluent and passaged after seven to fourteen days using 0.05% trypsin-EDTA from Thermofisher (see table 2.1.1). Cell culture medium was changed twice a week.

Human embryonic kidney (**HEK)293T** from GE Healthcare (passage 2-15), **Platinum GP** cells from Cell Biolabs (passage 2-15) and the medulloblastoma cell line **MED8A** a kind gift from Dr. R. Gilbertson, St. Jude, Memphis, TN, US. (passage 22-25) were cultured as monolayer in DMEM supplemented with 10%

FBS and 2 mM L-glutamine (see table 2.1.1). For Platinum GP cells blasticidin (c= 1 µL/mL) was added to the cell culture medium. Cells were cultivated until 70% confluent and passaged at least once or twice a week using 0.05% trypsin-EDTA. Cell culture medium was changed twice a week.

2.2.1.3. Harvesting of cells

All cell lines grew adherent to cell culture plastic. Before harvesting, medium was removed and cells were washed with sterile PBS to remove dead cells or residual protein of e.g. FBS. To detach cells 0.05% trypsin-EDTA (0.5 mL/well for six-well plates, 1 mL for T25 flasks, 2 mL for T75 flasks or 10 cm dishes, 4 mL for T175 flasks) was added, evenly spread on the attached cells and incubated at 37°C for 3-5 minutes. The enzymatic cleavage was arrested by addition of fresh medium (3-4 x the volume of trypsin). The cell culture flask was rinsed with fresh medium repeatedly and a single cell suspension was generated by pipetting up and down. The suspension was either used to determine cell numbers (2.2.1.4) for seeding or cells were split for continued culture. For this purpose a fraction of the suspension (1:10 or 1:20) was reseeded in a new culture flask and fresh medium was added (final volume: 3 mL/well for six-well plates, 5 mL for T25 flasks, 8 mL for T75 flasks or 10 cm dishes, 15 mL for T175 flasks).

2.2.1.4 Determination of viability and cell numbers

To assess cell viability as well as cell numbers, 1 mL of the generated single cell suspension (2.2.1.3) was stained with trypan blue in an automated fashion. Trypan blue can penetrate dead cells due to their reduced membrane integrity. The Vi-CELL XR automated cell counter was used for the automated trypan blue exclusion staining. Cell numbers were determined per milliliter of cell suspension. For seeding of specific cell numbers for an experiment, the appropriate volume of cell suspension was centrifuged in a 15 mL Falcon tube at 230 x g for 5 minutes, the supernatant was removed, the cell pellet was resuspended with the appropriate amount of cell medium and seeded in a new culture flask.

In case cell counts were used as readout, after e.g. drug treatments, the generated single cell suspension after trypsinization was combined with the original cell culture medium to include floating dead cells for the determination of cell viability.

2.2.1.5 Cryopreservation

For long-term storage of cell lines, n= 1-2 x 10^6 viable cells of a single cell suspension (2.2.1.3) were resuspended in 1 mL of cryopreservation medium. Cryopreservation medium contained 10% DMSO,

which prevents the formation of ice crystals during the freezing process. DMSO was added to the appropriate cell culture medium for each cell line. To ensure a gradual freezing process (-1°C/min), which reduces damage of cell membranes due to formation of crystals, the vial was then transferred to a container surrounded by isopropanol (Mr. Frosty™ Freezing container) and stored at -80°C. After the cell line was proven to be free of *Mycoplasma* contamination, the cells were transferred to the liquid nitrogen tank for long-term storage.

2.2.1.6 Microscopy

Bright field pictures were captured using the Olympus CXK41 microscope and images of fluorescent cells or cell staining were captured using the same microscope in combination with the Olympus U-RFL-T reflected fluorescence system. Images were captured with the CellB 2.3 software with 25 ms of exposure time for bright field images and 500 ms for fluorescence images.

2.2.1.7 Conditioned medium (CM)

In order to generate medium enriched with secreted factors and proteins from senescent or proliferating DKFZ-BT66 cells, cells were seeded in six-well plates at different densities with (n= 1 x 10^6 cells/well) or without (n= 7 x 10^6 cells/well) doxycycline, in order to end up at n= 2 x 10^6 cells after five days in culture. The different cell numbers account for the doubling time of 44 hours of proliferating DKFZ-BT66 cells as well as for the drop in cell numbers observed upon withdrawal of doxycycline (see Fig. 12). The final cell number (n= 2 x 10^6) was shown to result in an estimated secretion of 100 pg/mL IL1B at day five, as determined by ELISA (see Fig. 24). After seeding, medium change (3 mL) was conducted at day three, and medium was collected at day five, resulting in two days of conditioning. The freshly collected medium was centrifuged (230 x g, RT, 5 Min), filtered (0.2 µm filter) and added to n= 1.5 x 10^5 proliferating DKFZ-BT66 cells/well (seeded one day prior to CM treatment) together with doxycycline in six-well plates. CM was added to the proliferating DKFZ-BT66 cells every second day. Therefore, both cultures (cells for conditioning and treated cells) have to be conducted simultaneously, to ensure continuous supply with fresh CM.

2.2.1.8 Drug and cytokine treatments

Recombinant IL1B and IL6 were dissolved in sterile PBS containing 0.1% BSA, aliquoted and stored at -80°C. Anakinra and tocilizumab, both pre-dissolved in sterile water, were stored in aliquots at 4°C. Human IL1B antibody was dissolved in sterile PBS, aliquoted and stored at -20°C. Dexamethasone was dissolved in sterile water, aliquoted and stored at -20°C. Navitoclax, ABT-737, dabrafenib, quercetin,

vincristine and trametinib were dissolved in DMSO, aliquoted and stored at -80°C. Carboplatin was dissolved in sterile water, aliquoted and stored at -80°C. Drugs and cytokines were added together with fresh cell culture medium every second day for the durations and concentrations indicated for each experiment. See table 2.1.2 for information on suppliers.

2.2.1.9 Lenti- and retroviral production for transduction of primary tumor cell cultures

Retro- and lentiviral transduction of mammalian cells enables stable expression of a gene of interest, as the gene is integrated into the genomic DNA of the host cell. The lentiviral transduction has the advantage that non-dividing cells can be infected, which is especially relevant in the primary cultures of mostly senescent LGG tumor cells.

To achieve stable expression of a gene of interest, such as the SV40-TAg, in primary LGG cultures, the encoding plasmid was packaged in a lentivirus. In addition, lentiviral transduction was used to transduce the generated DKFZ-BT66 cell line with a construct coding for luciferase as well as the shRNA constructs coding for IL1B, IL6, IL1R1 and IL6Ra (see 2.1.6, see appendix B for plasmid maps).

Lentivirus production and transduction was conducted in a biosafety level 2 (S2) laboratory. In brief, HEK293T cells (n= 5 x 10^6) were seeded in 10 cm dishes, cultured for 24 hours (see 2.2.1.2) and co-transfected with the plasmid of interest using the Trans-Lentiviral Packaging system from Invitrogen by means of calcium phosphate transfection. The Trans-Lentiviral Packaging system includes five plasmids encoding for: 1. *gag-pro*, the viral capsid and protease (pTLA1-PAK), 2. *vpr-RT-IN* (pol), the viral protein r, the viral reverse transcriptase and integrase (pTLA1-ENZ). The vpr-RT-IN fusion protein is controlled by HIV-2-LRT and transactivated by the Tat protein. 3. *tat-IRES-rev*, gene regulatory proteins controlling 5'LTR transactivation, nuclear export and protein expression (pTLA1-TAT/REV), 4. *env* (VSV-G), the viral envelope (pTLA1-ENV) and 5. *Tet-Off*, the tetracycline-controlled transactivator (pTLA1-TOFF), controlling the expression of *gag-pro* and *tat-rev* (see appendix B). For optimal virus production, a young passage (< passage 15) of HEK293T cells should be used and cells should be actively proliferating (40-60% confluent) before seeding. The prepared DNA plasmid mix, including the plasmid of interest (4 µg) and the 5 plasmids of the lentiviral packaging system (2 µg per packaging plasmid), was mixed with 0.1xTE/dH2O (1:2) (see table 2.1.8) to result in a final volume of 450 µL and incubated for 2 hours at RT. In the meantime, medium was changed on HEK293T cells 2 hours before transfection. 50 µL of 2.5 M $CaCl_2$ (see table 2.1.8) were added to the DNA mix and incubated for 5 minutes at RT. To form precipitates, 500 µL 2xHBS (see table 2.1.8) were added dropwise to the DNA/calcium mix, while vortexing under the laminar flow hood. The precipitates were added dropwise to the prepared HEK293T cells. The transfected

HEK293T cells were incubated with the mix overnight in the incubator at 37°C. HEK293T cell culture medium was changed 16-20 hours after transfection. 24 hours after medium change, the virus-enriched medium was collected with a 10 mL syringe, filtered (0.45 µm), aliquoted in 3 mL/Falcon tube and stored at -80°C until use. Before transduction, the viral supernatant was supplemented with polybrene to a final concentration of 8 µg/mL. Cells to be transduced (n= 5 x 10^5) were seeded in 10 cm dishes, allowed to attach for 24 hours and infected with 3 mL of virus supernatant plus polybrene. Medium was filled-up to 10 mL total volume after six hours and completely changed one day later. For transduction with the doxycycline-inducible SV40-TAg construct, doxycycline (c= 1 µg/mL) was added to the cell culture medium together with the top-up. Successful transduction was determined by red or green fluorescent protein (RFP or GFP) expression, co-expressed from the transduced plasmid. Fluorescence was visible 3-7 days after transduction using luminescence microscopy. Transduced cells were selected either with antibiotic treatment such as puromycin (c= 1 µg/mL) for 10 days (for SV40-TAg), pac from *Streptomyces alboniger* co-expressed from the transduced plasmid, or by FACS sorting according to RFP/GFP expression (for shRNA constructs). In case transduction was not successful the process was repeated once every week for up to four weeks.

The construct coding for hTERT was transduced into DKFZ-BT66 cells via retroviral transduction. Packaging was performed using the pantropic Platinum-GP Retrovirus Expression System from Cell Biolabs. Platinum-GP cells (n= 5 x 10^6) were seeded in 10cm dishes and cultured for 24 hours before transfection. A transfection mix was prepared with 5 µg of the pBABE-hygro-hTERT plasmid and 2.5 µg of the packaging pCMV-VSV-G plasmid using the described method of calcium phosphate transfection. Successfully transduced cells were selected by treatment with hygromycin-B (c=250 µg/mL) for 10 days.

2.2.1.10 Dissociation and viral transduction of primary tumor material to generate an *in vitro* LGG model

For the generation of *in vitro* LGG models, fresh primary tumor material was received from the Departments of Neurosurgery from Tübingen, Freiburg, Berlin, and Heidelberg. The investigation was approved by the institutional review board of the University of Heidelberg (S-304/2014). The establishment of *in vitro* LGG models was conducted in collaboration with Florian Selt and Daniela Kuhn from the CCU Pediatric Oncology, DKFZ, Heidelberg in Germany.

In a first step, tumor material was processed to result in a single cell suspension. The material was transferred to a 10 cm dish and kept covered with a few drops of PBS. Using scalpels, blood vessels and necrotic tissue was removed. A small piece of tumor was transferred to a 15 mL Falcon tube, frozen in

liquid nitrogen and stored at -80°C for further molecular analysis.

Three different cell culture methods were used to culture primary LGG material: first generation of a single cell suspension, second explant cultures and finally co-cultures on murine brain slices.

For culture of a single cell suspension: The fresh tumor tissue was kept in a few drops of PBS and minced with two scalpels for several minutes. After thorough mincing, the material was transferred to a 15 mL Falcon tube with 5 mL of PBS and further disintegrated using different size pipet tips. The single cell suspension was centrifuged (5 min, 230 x g) and resuspended in cell culture medium. Cells were cultured as monolayer in ABM basal medium supplemented with the AGM Kit in six-well plates.

For tumor explant culture: To generated tumor explants, small pieces (1-2 mm) of the fresh tumor material were cut using scalpels. The explants were transferred to six-well plates, allowed to attach for 15 minutes at 37°C and carefully covered with cell culture medium. Explants were cultured in X-VIVO medium supplemented with LIF (final c= 10 ng/mL), EGF (final c= 20 ng/mL), bFGF (final c= 20 ng/mL), acetylcysteine (final c= 60 ng/µL) and neuronal survival factor 1 (NSF-1) (final conc. 2% of the solution purchased from LONZA, 200 µL/10 mL medium) as well as Neurobasal A medium supplemented with EGF (final c= 20 ng/mL) and bFGF (final c= 20 ng/mL).

Organotypic brain slice co-culture: Another method tested to culture primary LGG cells was a co-culture system on healthy murine brain tissue according to the protocol published by Chadwick *et al.* (35). For this purpose, brain slices were generated from healthy P6 C57BL/6 mice (internal DKFZ proposal for organ collection: DKFZ348). All instruments were sterilized with 70% ethanol. Pups were decapitated using sharp scissors. Skin and skull were removed with scissors and forceps by cutting from the posterior towards the front of the brain on both sides of the head as well as one cut along the midline of the skull. While cutting the skull, the scissors should remain as close to the skull as possible to avoid damage of the brain. Forceps were used to peel off the skin and the two halves of the skull. Once the brain was revealed, it was isolated by carefully inserting a flat-faced spatula between the base of the skull and the bottom of the brain. The isolated brain was transferred to ice-cold PBS in a 10 cm dish. The brain was transferred into liquid 3% low-melting agarose in 35 mm^2 dishes and allowed to set for 5-10 minutes. Embedding the soft brain tissue in agarose keeps the brain structure intact during the cutting process in the vibratome. The agarose was trimmed with a razor blade to result in a straight agarose cube surrounding the brain. Superglue was used to fix the agarose cube to the plate inserted into the vibratome and allowed to set for 10 minutes. Before cutting, six-well plates with cell culture inserts were prepared and covered with 3 mL cell culture medium. Sagittal brain slices of 200-300 µm thickness were

generated in PBS in the cutting reservoir of the vibratome, which was kept on ice. Using a brush and a slotted spoon, brain slices were transferred to the cell culture medium on top of the prepared cell culture inserts. Different cell culture media were tested (Fig. 15). 1 mL of medium was withdrawn from the top of the insert and added to the bottom of the well. Excess media was removed until the agarose surrounding the brain was visible. Excess agarose was carefully removed with forceps. Slices were kept at 37°C in humid atmosphere in 5% CO_2. To test the co-culture system DKFZ-BT66 cells were used. After 24 hours DKFZ-BT66 cells (n = 2 x 10^4 as single cell suspension in 2 µL, n = 5 x 10^3 as sphere) were seeded on top of the slices. For the control cell line MED8A, cells were stained with red-fluorescent CellTracker™ CM-DiI Dye before seeding. For this purpose n= 1 x 10^6 cells in 1 mL medium were incubated with 5 µL of CM-DiI at 37°C for 30 minutes, centrifuged (230 x g, RT, 5 min), washed with medium twice and the cell pellet was resuspended in 2 µL of medium. Medium on the bottom of the six-well plate was changes every second day and drops of medium, containing doxycycline for culture of DKFZ-BT66 cells, were added on top of the seeded cells. Bright field and fluorescent images were captured using the Leica M205 FA light microscope.

Finally, the cultured tumor cells were transduced with a lentiviral construct coding for the SV40-TAg (see 2.2.1.9) in either condition. The SV40-TAg construct co-expresses turboRFP as well as puromycin for selection purposes. The expression of the SV40-TAg as well as RFP, separated by an IRES site, are both doxycycline inducible. Doxycycline was added to the cell culture medium after transduction (c= 1 µg/mL). Once RFP expression was detectable by fluorescence microscopy, puromycin selection (c= 1 µg/mL) was initiated for 10 days. Cells were then expanded and analyzed for expression of the *KIAA:BRAF* fusion by RT-qPCR (2.2.2.4) or the $BRAF^{V600E}$ mutation by western blot (2.2.3.3).

2.2.2 Nucleic acids

2.2.2.1 Plasmid DNA amplification and isolation

Bacterial cells can integrate plasmid DNA into their own genome, in a process called transformation, which can be used for amplification of a plasmid of interest. In order for exogenous DNA to be successfully replicated in bacteria, it needs to contain a sequence recognized by the bacterial polymerase, called origin of replication (ori C). In addition, the plasmid needs to include a sequence coding for an antibiotic resistance, which is later used for selection of successfully transfected cells. The transformation efficiency can be enhanced by chemical pre-treatment of bacterial cells, followed by induction of a heat-shock (chemical transformation) or by electric impulses (electroporation) to facilitate plasmid DNA uptake through increased permeability of the cell membrane.

Here, chemical transformation was used to amplify plasmid DNA (see appendix B for plasmid maps). The procedure was performed under aseptic conditions (below the flame of a Bunsen burner) to avoid contamination. First, 25 µL of One Shot™ TOP10 chemically competent *E.coli* were thawed on ice, 1-10 ng of the plasmid of interest were added to the bacterial cells and carefully mixed by flicking the tube. The bacterial cells were incubated on ice for 20 minutes. Heat-shock was induced in a preheated water bath set to 42°C for 90 seconds followed by transfer of the bacteria cells on ice for 2 minutes. 250 µL of S.O.C. medium were added and bacteria growth was induced for 1 hour at 37°C, while kept on a shaking-block set to 220 rpm. Agar plates (see table 2.1.8) were prepared in advance, supplemented with the antibiotic matching to the resistance encoded on the plasmid of interest. 30 µL of the bacteria mix were plated onto the prepared pre-warmed agar plates and incubated at 37°C overnight, kept upside-down to avoid condensation. Single bacteria colonies were picked the next day with a sterile pipet tip and grown in 3 mL LB medium (see table 2.1.8) supplemented with the appropriate antibiotic (see table 2.1.3). The suspension was cultured overnight at 37°C in an incubator on a shaking-block set to 220 rpm. 500 µL of the bacteria mix were transferred to 400 mL of LB medium containing the appropriate antibiotic and incubated at 37°C overnight while shaking at 220 rpm in an orbital shaker. Before the plasmid was isolated, a glycerol stock was prepared by mixing 500 µL of bacteria culture with 500 µL of 50% glycerol. The mix was stored in cryopreservation vials at -80°C.

The plasmid DNA was isolated from bacteria using the QIAGEN Plasmid Maxi Kit according to manufacturer's instructions. Using this protocol, DNA is extracted from bacteria cells after an alkaline lysis step followed by binding of DNA is to a QIAGEN resin column, followed by washing steps and elution of DNA in a high-salt buffer. In brief, the bacteria cell suspension was centrifuged at 4°C for 15 minutes at

6000 x g. The pellet was resuspended in P1 buffer containing RNase. P2 buffer was added, containing the lysis reagent sodium hydroxide - sodium dodecyl sulfate (NaOH-SDS), mixed thoroughly and incubated for 5 minutes at RT. SDS induces lysis of bacteria cells by solubilizing components of the cell membrane, while NaOH leads to denaturation of proteins and genomic DNA. The addition of pre-chilled, acidic potassium acetate P3 buffer (4°C) neutralizes the alkaline lysis process and induces formation of potassium dodecyl sulfate precipitates. The precipitates contain the denaturated genomic DNA, proteins and cell debris in a salt-detergent complex. The P3 buffer was added, mixed and incubated on ice for 20 minutes. In comparison to the genomic DNA, the small plasmid DNA renaturates quickly and remains in solution. After two centrifugation steps of the supernatant (1. 30 min, 4°C, 20 000 x g; 2. 15 min, 4°C, 20 000 x g), the clear solution was transferred to an equilibrated QIAGEN DNA-binding column and allowed to enter the resin by gravity flow. The following two washing steps with QC buffer remove remaining contaminations. Finally, DNA was eluted from the column with QF buffer, followed by DNA precipitation induced by addition of isopropanol and centrifugation for 30 minutes at 4° and 15 000 x g. The DNA pellet was washed with 70% ethanol, centrifuged at 15 000 x g for 10 minutes and the remaining DNA pellet was air-dried for 5 to 10 minutes. The dried pellet was dissolved in TE buffer at pH 8.0.

Plasmid DNA concentration was determined by measuring absorbance of nucleic acid at 260 nm using the Nanodrop™ UV spectrophotometer. DNA was considered as pure, when the ratio of absorbance at 260 nm versus 280 nm was at around 1.8 to 2.0. The purified plasmid DNA was stored at -20°C.

2.2.2.2 RNA extraction

RNA was isolated from mammalian cells after guanidine-isothiocyanate lysis followed by a silica-membrane purification step using the QUIAGEN RNeasy® Mini Kit. At least n= 2-4 x 10^6 DKFZ-BT66 cells were used to isolate sufficient amounts of RNA. After centrifugation of the trypsinized cells (230 x g, 5 min, RT), cell pellets were lysed in 350 µL RLT buffer (or 700 µL for large pellets), containing guanidine-thiocyanate as well as 1% ß-mercaptoethanol, which inactivates RNases. RNA was isolated using the QUIAGEN RNeasy® Mini Kit according to manufacturer's instructions. In brief, the same volume of 70% ethanol was added to the lysed sample and mixed thoroughly to improve column-binding conditions. The lysate was transferred to an RNeasy Mini spin column, containing an RNA-binding silica-membrane, by vacuum suction. The column was washed with RW1 buffer first and twice with RPE buffer under vacuum followed by a 1 min centrifugation step to remove all remaining contaminations. RNA was eluted into a fresh tube by adding 50 µL RNase-free water, followed by centrifugation (8 000 x g, 1 min, RT). RNA concentration was determined using the NanoDrop™ UV spectrophotometer measuring absorbance at

260 nm. RNA was considered as pure, when the ratio of absorbance at 260 nm versus 280 nm was at around 1.8 to 2.0. The purified RNA was stored at -80°C.

2.2.2.3 Complementary DNA (cDNA) synthesis

From the isolated RNA (2.2.2.2), a cDNA strand can be synthesized by reverse transcription. Reverse transcriptases can generate a DNA strand using RNA as a template.

Synthesis of cDNA was performed from 1 µg RNA using the RevertAid First Strand cDNA Synthesis Kit from ThermoFisher according to manufacturer's instructions. First strand cDNA was generated from total RNA using reverse transcriptase M-MuLV. Components of the kit were thawed on ice. Template RNA was mixed with oligo (dT) primer (1 µL) and filled-up to 10 µL total volume with nuclease-free water in a PCR tube. After an incubation for 5 minutes at 70°C and cooling on ice, 7µL of a mix of: 4 µL 5 x reaction buffer, 1 µL of RiboLock RNase Inhibitor (20 U/µL) and 2 µL of 10 mM dNTP mix were added. The mix was incubated at 25°C for 10 minutes. Finally, 2 µL of M-MuLV reverse transcriptase (200 U/µL) were added and mixed gently. After brief centrifugation, the mix was incubated for 10 minutes at 25°C and for 60 minutes at 37°C. The reaction was terminated by heating to 70°C for 10 minutes. The resulting cDNA was stored at -80°C for long-term or used for RT-qPCR amplification immediately.

2.2.2.4 Quantitative reverse transcription real-time polymerase chain reaction (RT-qPCR)

RT-qPCR allows for amplification of a gene of interest from a cDNA template by DNA polymerase in a PCR reaction in a first step. In a second step, the product is quantified by detection of the DNA-intercalating agent SYBR Green, a fluorescent dye emitting fluorescence upon DNA binding. The proportional increase in fluorescence signal correlates to the amount of PCR product of the gene of interest. Several PCR cycles result in an increase in fluorescence signal until it reaches a pre-defined threshold (Cycle of Threshold (CT) value). The fluorescence signal of the gene of interest at this cycle can be compared to the level of constitutively expressed house-keeping genes in the same sample, enabling the calculation of the relative amount of template present in the original sample.

RT-qPCR was conducted in a 96-well PCR plate using the mastermix for Platium SYBR Green including forward/reverse primer together with the respective cDNA. In brief, the cDNA (2.2.2.3) was diluted in water (1:10), 5 µL of the dilution were mixed with 15 µL of a mastermix containing: 1 µL of the respective forward and 1 µL of the respective reverse primer (10x) for the gene of interest or house-keeping gene, 10 µL of 2X SYBR Green qPCR SuperMix-UDG containing Taq DNA polymerase and 3 µL of distilled water. The 96-well was covered with an adhesive film and centrifuged at 230 x g at RT for 5 minutes.

The PCR was run using the ABI 7500 Real-Time PCR cycler from Applied Biosystems by life technologies in standard mode in the advanced setup with the ABI 7500 Software v2.3. The PCR reaction was initiated at 50°C (2 min), followed by at 95°C (10 min), and 40 cycles of each 95°C (15 s) for denaturation of the double-strand DNA structure and 60°C (1 min) for annealing of the primers to the DNA and elongation by the DNA polymerase, followed by a dissociation state including 1 cycle at 95°C (15 s), 60°C (1 min), 95°C (30 s) and 60°C (15 s). Data was analyzed with the ΔΔCt method to assess relative quantities by comparing the expression of the gene of interest to housekeeping genes (in this study *TBP* and *ACTB*) as control genes first, followed by calculation of the fold change to a control samples e.g. untreated cells (129).

2.2.2.5 mRNA gene expression profiles (GEPs)

GEPs measure the transcription of thousands of genes, which can be used to e.g. predict the activation status of cellular functions. Comparing the GEP of different cell types or different treatment conditions can give insights into differences on gene expression level and differing underlying signaling mechanisms.

GEP of patient samples as well as the DKFZ-BT66 cell line were performed using the Affymetrix U133 Plus 2.0 expression array according to manufacturer's instructions at the Genomics and Proteomics Core Facility of the German Cancer Research Center, Heidelberg, Germany. The GEP of the murine PA model was conducted using the Affymetrix Mouse Genome 430 2.0 array. Values for patient samples were MAS5 normalized, while murine and cell line expression values were RMA normalized and log2-transformed. The probe-set with the highest expression value was chosen in case there were multiple probe-sets per gene. Calculations were performed in collaboration with Thomas Hielscher from the Division of Biostatistics at the DKFZ Heidelberg in Germany. All GEP datasets generated in the study presented here are publicly available on the R2 platform.

The publicly available datasets used to generate a list of OIS-controlling genes (see 2.2.6.1) were E-NCMF-12 (human fibroblasts/BRAFV600E, n=20) (46), E-NCMF-13 (human fibroblasts/BRAFV600E, n=16) (46), GSE54402 (human fibroblasts/HRASG12V, n=10) (130), GSE46801 (primary human melanocytes/BRAFV600E, n=9) (131), GSE41318 (human fibroblasts/RAS, n=6) (Acosta *et al.*, unpublished), and GSE60652 (human fibroblasts/RAS, n=4) (132).

2.2.3 Protein

2.2.3.1 Protein isolation

To isolate proteins from mammalian cells their membranes are disrupted with ionic detergents. This was achieved by using a lysis buffer with sodium dodecyl sulfate (SDS) and dithiothreitol (DTT). SDS binds to proteins of the cell membrane and together with the reducing agent DTT, leads to the destruction of tertiary protein structures by disrupting non-covalent bonds and disulfide bridges. To avoid secondary protein modifications, phosSTOP™ was added to the lysis buffer, which prevents dephosphorylation of proteins by phosphatases.

Proliferating DKFZ-BT66 cells (n= 1 x 10^6) were seeded one day in advance of treatment and lysate were generated after treatments at the indicated times. To generate lysates from senescent DKFZ-BT66 cells, n= 3-5 x 10^6 cells were seeded in T75 flasks. Cells were cultured without doxycycline for five days. Drug treatments were added at day five for the indicated times. For long-term treatments, drugs were added every second day. Cells were harvested by trypsination (see 2.2.1.3., exception: centrifugation for 5 minutes at 4°C, 8600 x g) and the resulting cell pellet was resuspended in 150 µL to 300 µL SDS lysis buffer plus DTT plus phosSTOP™, depending on cell pellet size, followed by 95°C heat denaturation for 10 minutes. After centrifugation (5 min, 15°C, 11 000 x g), the supernatant of the lysates was transferred to a new, pre-cooled tube and kept at -80°C for long-term storage or was used for western blotting (2.2.3.3) immediately.

2.2.3.2 Protein quantification

Protein concentrations were determined with the Pierce™ BCA Protein Assay Kit according to manufacturer's instructions together with a BSA standard in defined concentrations, using the FLUOstar OPTIMA plate reader for readout (absorbance at 570 nm). The BCA assay is based on a colorimetric reaction correlated to the amount of protein. In a first step, the protein reduces Cu^{2+} to Cu^{+} in an alkaline environment, resulting from addition of sodium potassium tartrate to the reaction. In a second step, Cu^{+} forms a purple-colored chelate complex with two bicinchoninic acid (BCA) molecules, a chromogenic reagent. The colored complex exhibits linear absorbance at 562 nm correlating directly to protein concentrations.

For detection of protein concentrations, the cell lysates (2.2.3.1) were diluted 1:5 with SDS lysis buffer. Per sample 5 µL of the dilution were added to two wells of a 96-well plate, to conduct the measurement in duplicates. To enable quantification of the protein concentration in the lysates, a standard was

generated by diluting bovine serum albumin (BSA) in known concentration steps. 200 µL of the BCA Protein Assay reagent mix were added to each well and the plate was incubated at 37°C for 30 minutes before absorbance was determined in the FLUOstar OPTIMA plate reader. A standard curve (range: 0 – 2000 µg/mL) was calculated from the known BSA concentration steps. The mean of the measured absorbance values of each sample was calculated. The protein concentration of each sample was calculated in relation to the standard curve.

2.2.3.3 Western Blot

The western blot technique enables the identification and semi-quantification of a protein of interest. The principle relies on three steps: First, all proteins of a cell lysate (2.2.3.1) are separated by molecular weight through electrophoresis in an acrylamide gel with varying pore sizes. The proteins move towards the anode, as they are negatively charged from the treatment with the anionic SDS detergent. Small proteins are able to migrate through the pores of the acrylamide gel much faster in comparison to large proteins. In a second step, the proteins are transferred to a membrane by electrotransfer. Finally, a specific protein of interest can be detected by staining the membrane with a matching primary antibody and visualized with a secondary antibody, which binds the primary antibody and is linked to a reporter enzyme. One example for such a reporter is the horseradish peroxidase (HRP), which can cleave a chemiluminescent substrate leading to emission of light. The chemiluminescent signal can be correlated to the amount of HRP-conjugated antibody, which correlates to the amount of protein. The amount of protein in the sample can be calculated semi-quantitatively by comparing the expression of the protein of interest to the expression of a stably expressed house-keeping protein such as ß-actin.

The first step for the preparation of a western blot was the casting of the acrylamide gel. The acrylamide gel was prepared with two different buffers. The top layer of the gel, called stacking gel (see table 1), is slightly more acidic, has a lower acrylamide concentration and therefore bigger pores. It enables collection of all proteins in sharp bands on the same height. The lower layer of the acrylamide gel, called resolving gel (see table 2), separates the proteins by size. The gel has a higher pH and can be prepared with different acrylamide concentrations (10-15%) depending on the size of the protein of interest. Small proteins are best separated in gels with a smaller pore size resulting from a higher acrylamide concentration. The acrylamide gels were prepared as described in **Fehler! Verweisquelle konnte nicht efunden werden.** and Table using the buffers for the resolving and stacking gel described in 2.1.8. First the resolving gel was prepared, poured into the gel casting form and covered with isopropanol to receive a smooth boarder, get rid of air bubbles and avoid drying-out.

Table 1: Reagents for preparation of 12% resolving gel (4 gels)

Reagent	Amount
De-ionized water	10.2 mL
1.5 M Tris-HCl, pH 8.8	7.5 mL
20% SDS	0.15 mL
Acrylamide/Bis-acrylamide (30%/0.8% w/v)	12 mL
10% (w/v) ammonium persulfate (APS)	0.15 mL
TEMED	0.02 mL

After the resolving gel solidified (30 min), isopropanol was removed and the stacking gel was poured on top. A comb was inserted into the liquid gel to form wells that later enable loading of the samples.

Table 2: Reagents for preparation of stacking gel (2 gels)

Reagent	Amount
De-ionized water	3.075 mL
0.5 M Tris-HCl, pH 6.8	1.25 mL
20% SDS	0.025 mL
Acrylamide/Bis-acrylamide (30%/0.8% w/v)	0.67 mL
10% (w/v) ammonium persulfate (APS)	0.025 mL
Tetramethylethylenediamine (TEMED)	0.005 mL

For each western blot all samples were prepared with the same protein concentration, determined by BCA assay (2.2.3.2). Usually 30 µg of total protein were loaded per lane, but if the total amount of protein from the cell lysates was low, 10 µg of protein were used. The total volume per sample was 20 µL for 15-well combs or 25 µL for 10-well combs. The appropriate amount of protein lysate was diluted in SDS lysis buffer and mixed with 1 µL of diluted bromophenol blue (1:10). Bromophenol blue enables the visualization of the separation process. The samples were heated after dilution to 95°C for five minutes to denaturate tertiary protein structures.

The electrophoresis chamber was filled with 1x running buffer (see table 2.1.8), the acrylamide gel was placed into the chamber and the prepared protein lysates were added to the wells. A protein standard (5 µL) was added to the first well, to later estimate protein size according to the known sizes of the standard marker bands. The voltage of the electrophoresis chamber was set to 80 V until the proteins, visualized by bromophenol blue, were assembled at the boarder of the stacking to the resolving gel. Then the voltage was set to 120 V until sufficient separation was achieved, visible by the pre-stained protein standard (usually after 1-2 hours). Transfer of proteins from the resolving gel to the methanol-activated (5 min) PVDF membrane was conducted in presence of 1x transfer buffer (see table 2.1.8) in a 'sandwich' between soaked Whatman chromatography paper in the blotting chamber for 2 hours and 15 minutes at 35 mA/gel. After blotting the gel was stained with Coomassie solution (see table 2.1.8) for 30 minutes and the methanol-activated PVDF membrane was stained with Ponceau S solution (see table 2.1.8) for 5 minutes to control for uniform protein loading and transfer. Both, the Coomassie and the Ponceau S dyes are negatively charged and reversibly bind to the positively charged amino groups of the protein. An image of the stained membrane and gel was captured with the Epson perfection V700 Photo scanner. Afterwards the membrane was washed with distilled water and blocked for unspecific antibody binding with blocking milk (see table 2.1.8) for 1 hour at RT. The primary antibody was diluted (see 2.1.4 for dilutions) in 5 mL 2% milk in TBS-T (see table 2.1.8) and the membrane was incubated with primary antibody in 2% milk in TBS-T in a 50 mL Falcon tube overnight at 4°C while rolling on a roller mixer. All antibodies were used with PVDF membranes, besides anti-IL1R1 which was used with a nitrocellulose membrane.

After washing the membrane with 10 mL of TBS-T three times for 10 minutes each, secondary antibody diluted in 5 mL 2% milk in TBS-T was added for 1 hour at RT while rolling on a roller mixer. After washing the membrane three times for 10 minutes with 10 mL TBS-T, detection of chemiluminescence was performed with ECL Prime Western Blotting Detection System according to manufacturer's instructions using the Chemi-Smart 5000 imaging system. The Amersham™ ECL Prime is a chemiluminescent detection reagent with stable signal emission. 2 mL of the ECL Prime solution were pipetted onto one membrane, allowed to incubate for 2 minutes and placed into the Chemi-Smart imaging system. Pictures of the membrane were captured at different exposure times and contrast was enhanced using the Chemi-Capt 5000 software. Afterwards the membrane was shrink-wrapped in autoclave bags and stored at -20°C.

2.2.3.4 Enzyme linked immuno-sorbent assay (ELISA)

Quantitative detection of cytokines in cell culture supernatant was investigated using an ELISA. In principle, the protein of interest is captured in a two-sided antibody sandwich. A 96-well microplate is pre-coated with a capture antibody specific to the protein of interest. The microplate is incubated with the experimental samples, controls and a standard made from different known dilutions of the recombinant protein of interest. After aspirating the samples, the microplate is washed repeatedly. Next, a HRP-conjugated detection antibody is added to each well and binds the protein of interest at a different epitope, making the sandwich complete. A HRP substrate is added to the wells and absorbance is detected in the FLUOstar OPTIMA plate reader at 450 nm. A standard curve can be generated from the known concentrations of the protein standard and the protein concentration of the experimental samples is calculated in correlation.

DKFZ-BT66 cells (n= 1 x 10^6 cells/well) were seeded on day -1 in six-well plates with doxycycline. To detect the cytokine release upon withdrawal of doxycycline, the medium was replaced after 24 hours (day 0) without the addition of doxycycline and collected at the indicated time points (see Fig. 24). Upon collection, the supernatant was centrifuged and stored at -80°C and cells in the respective well were counted. Protein cytokine concentrations were determined in duplicates per experimental sample using the ELISA Kits for IL1B and IL6 according to manufacturer's instructions (see table 2.1.10). For detection of IL6 the collected medium had to be diluted 1:100 in medium to achieve concentrations in the detectable range of the rIL6 standard curve. Absorbance was detected using the FLUOstar OPTIMA plate reader at 450 nm. After calculation of the cytokine concentrations (pg/mL) in correlation to the standard curve, the values were normalized to cell counts for each well (cell number/mL) to result with cytokine concentrations secreted per cell (pg/cell).

2.2.3.5 Cytokine measurement in primary tumors by multiplex assay ("Luminex")

For simultaneous detection of several cytokines in lysates from fresh frozen primary tumor samples a multiplex assay, called Luminex was utilized. The Bio-Plex Pro™ Human Cytokine 27-plex assay enables the detection of protein concentrations of 27 cytokines via an antibody-coated magnetic bead system. The principle is very similar to an ELISA (2.2.3.4) relying on a two-side antibody sandwich for detection, with the exception that the capture antibody is linked to a magnetic bead. For the Luminex assay, the detection antibody is labeled with a fluorescent reporter dye. In order to differentiate the 27 cytokines within one sample, the beads for each analyte have distinct colors created by mixing two fluorescent dyes in a specific ratio. With a dual detection flow cytometer the color of the bead (635 nm laser) as well

as the concentration of the analyte correlating to the intensity of the fluorescence signal emitted by the reporter dye (525 nm laser) can be detected in two channels. The concentration of the experimental samples is correlated to values of a standard curve generated from known concentrations of the recombinant cytokines.

The measurement of the multiplex assay was conducted in collaboration with the Immune Monitoring Unit (Dennis Riehl), at the DKFZ/NCT in Heidelberg, Germany. Lysates of 1-3 mm^3 sized fresh frozen PA tumor samples (n=22) and normal fetal brain (n=1) were prepared using the Bio-Plex® Cell lysis Kit according to manufacturer's instructions (see table 2.1.10). The Pierce™ BCA assay was used to determine total protein concentrations and samples were normalized to 1 mg/mL. The Bio-Plex Pro™ Human Cytokine 27-plex assay was used according to manufacturer's protocol to determined 27 cytokines and chemokines of which 14 are SASP factors. The clinical annotations of all samples are in appendix C.

2.2.3.6 Immunohistochemistry (IHC)

Immunohistochemistry enables the detection of a protein of interest in tissue sections. The method is based on binding of a reporter-conjugated antibody to the protein of interest. Common reporters are enzymes catalyzing color-inducing reactions such as HRP. A chromogenic substrate for HRP such as 3,3'-diaminobenzidine (DAB) is added and the colored precipitates are visible in bright field microscopy.

To preserve the cellular protein as well as the architecture of the tissue, the tissue sample has to be fixed in formaldehyde, which crosslinks proteins in a semi-reversible manner. After fixation, the tissue is embedded in paraffin wax to maintain the natural structure of the tissue and enable sectioning into 4-5 µm thin slices in the microtome. The sections of tissue are mounted onto glass slides. To retrieve the epitope and enable antibody binding, the paraffin has to be removed by treatment of the slides with xylene, an organic solvent and formaldehyde is removed through heat-induced epitope retrieval by boiling the sections in buffers with different pH values. Finally, non-specific binding sites are blocked with e.g. bovine serum albumin.

IHC analysis was performed on paraffin sections of n=14 primary human pilocytic astrocytoma samples. Clinical parameters are summarized in the appendix D. Staining was performed in collaboration with Felix Sahm at the Department of Neuropathology of the Heidelberg University Hospital, Germany, using the Ventana machine and antibodies for Ki67, IL-6Ra, LCA and CDKN2A (see table 2.1.4). All antibody staining were previously established in the laboratory, but the dilution of the IL-6Ra antibody was first

tested on control tissue expressing the receptor from normal human spleen, thyroid carcinoma or breast cancer provided by the National Center for Tumor Diseases (NCT) in Heidelberg, in accordance with the regulations of the tissue bank and the approval of the ethics committee of Heidelberg University. Paraffin sections of the tumor isolated from the DKFZ-BT66 hTERT mouse model (n=1) were stained with antibodies for p-ERK, GFAP, as well as Ki67. Incubation time was 32 minutes for all antibodies, except for the MIB1 antibody (for Ki67) which had an incubation time of 60 minutes. Dilutions and pretreatments are listed in the material section (see 2.1.4). Images were captured with the Olympus CXK41 microscope using the CellB 2.3 software.

2.2.3.7 Immunofluorescence (IF) staining

A protein of interest can be visualized in fixed cells or tissue by means of IF. The method relies on antigen-binding of either a fluorophore-conjugated primary antibody or a primary antibody which is later bound by a fluorophore-conjugated secondary antibody. After excitation of the fluorophore, the protein of interest can be detected by fluorescence microscopy. Information on location, activation status and relative expression of the target protein in the cells or tissue can be obtained.

For the detection of SV40-TAg in DKFZ-BT66 cells, the cells were seeded in ibidi 8-well µ-slides in cell culture medium supplemented with doxycycline (n= 3 x 10^4 cells/well) or without doxycycline (n= 1.5 x 10^5 cells/well). After five days in culture, cells were washed with PBS (200 µL/well) twice, fixed with 160 µL/well 4% PFA for 20 minutes at RT (protected from light) and washed with PBS afterwards. Fixed cells were permeabilized with TritonX 100 0.2% in PBS (150 µL/well) (see table 2.1.8) for 30 minutes at RT, followed by incubation with blocking buffer (3% BSA plus 0.05% TritonX 100 in PBS see table 2.1.8) for 1 hour at RT. The primary SV40-TAg antibody diluted 1:250 in blocking puffer (200 µL/well), was added to the cells and incubated overnight at 4°C covered in Parafilm®. The next day, cells were washed with PBS twice and incubated with secondary antibody (1:500 anti-mouse Alexa Fluor 488, 200 µL/well) at RT for 2 hours protected from light. Cells were washed with PBS twice, followed by counterstaining with DAPI (0.25 µg/mL in PBS) for 10 minutes at RT. The slide was washed with PBS and imaged using the Zeiss LSM710 confocal microscope in collaboration with Johannes Ridinger from the CCU Pediatric Oncology, DKFZ, Heidelberg in Germany. To control for autofluorescence and unspecific binding, one well of each condition, senescent or proliferating DKFZ-BT66 cells, was incubated with the secondary antibody only.

2.2.4 Functional assays

2.2.4.1 Metabolic activity assay

The metabolic assay as measured by the CellTiter-Glo kit is a fast assay, suitable to determine drug response by ATP production of healthy cells. The number of healthy cells correlates to levels of ATP, which in turn correlates to a luminescence signal produced by an enzymatic reaction using luciferase. In the presence of ATP and molecular oxygen, beetle luciferin is oxygenated by luciferase to oxyluciferin and the resulting excited state intermediate emits light. The number of viable cells directly correlates to the luminescence output determined in the FLUOstar OPTIMA plate reader.

Drug treatments with senolytic agents were conducted in collaboration with Juan Pedro Martinez-Barbera from the Developmental Biology and Cancer Programme, Birth Defects Research Centre, Great Ormond Street Institute of Child Health, University College London in England. Five days prior to treatment of DKFZ-BT66 cells, technical triplicates of n= 5 x 10^2 cells/well were seeded with doxycycline and n= 8 x 10^3 cells/well were seeded for cells treated without doxycycline in a 96-well plate, accounting for proliferating and senescent cells. For normal human astrocytes, technical triplicates of n= 4 x 10^3 cells/well were seeded in a 96-well plate one day prior to treatment. 100 µL of the different drug dilutions in cell culture medium were added per well. Three wells containing no cells, but medium only, served as control for luminescence background signal. After 72 hours of incubation with the drugs at 37°C, metabolic activity was determined with the CellTiter-Glo assay following manufacturer's instructions (2.1.7). The prepared 96-well plate was equilibrated to room temperature for 30 minutes. 100 µL of CellTiter-Glo Reagent were added to each well. The CellTiter-Glo Reagent is a master mix which induces cell lysis and contains all reagents to generate the luminescent signal. The solution was mixed with the cell culture medium for two minutes on an orbital shaker and incubated at RT for 10 minutes. Luminescence was detected using the FLUOstar OPTIMA plate reader. The mean of the control sample (medium only) was subtracted from all values. Dose-response curves and IC50 concentrations were calculated relative to solvent-treated cells and depicted using GraphPad Prism v5.01.

2.2.4.2 Senescence-associated ß-galactosidase (SA-ß-Gal) staining

A commonly used biomarker for senescence is increased activity of the senescence-associated ß-galactosidase. Normal cycling cells produce ß-galactosidase, which is located in the lysosome and can be detected at pH 4.0. In senescent cells lysosomal ß-galactosidase activity is increased and the enzyme accumulates, which is why its activity can be determined at a suboptimal pH of 6.0. The enzymatic

activity is determined by staining with the chromogenic substrate 5-bromo-4-chloro-3-indolyl ß D-galactopyranoside (X-gal). Cleavage of X-gal by ß-galactosidase results in a blue precipitate, which can be observed in bright field microscopy.

DKFZ-BT66 cells (n= 2 x 10^4 cells/well) were cultured in six-well plates for five days with or without addition of doxycycline. SA-ß-Gal staining was performed following manufacturer's instructions (Cell Signaling see table 2.1.10) and pictures were captured using the Olympus CXK41 microscope. In brief, 20 mg X-gal were dissolved in 1 mL dimethylformamide (DMF). The ß-galactosidase staining solution was prepared fresh by mixing the supplied reagents from the manufacturer: 930 µL 1x staining solution, 10 µL 100x solution A, 10 µL solution B and 50 µL X-gal solution per well and the pH was adjusted to 6.0. Before staining, the medium was removed, the plate was washed with PBS and 1 mL 1x fixative solution (supplied by manufacturer) was added to each well. After fixation for 15 minutes at RT, the plate was washed with PBS once more. 1 mL of the prepared ß-galactosidase staining solution was added to each well, the plate was sealed with Parafilm® and incubated overnight at 37°C in a dry incubator. The next day bright field images of the stained cells were captured using the Olympus CXK41 microscope.

2.2.4.3 Flow cytometry

Flow cytometry is a laser-based technology that enables the quantitative detection of light emitted from fluorescence-labeled antibodies binding proteins in single cells, which run through a stream of fluid. In addition, the technique can be used to sort single cells according to a fluorescent signal.

Here, flow cytometry was used for the analysis of the cell cycle. During proliferation cells pass through different stages of the cell cycle. The DNA content within a cell is reflective of its cell cycle phase. During the G0/G1 phase, cells have one copy of DNA. During the S phase, DNA is synthesized and finally results in two copies of DNA in the following G2/M phase. To determine the DNA content, cells are stained with a DNA intercalating agent, such as 4',6-Diamidino-2-Phenylindole (DAPI). DAPI is a blue-fluorescent stain that can pass through intact cell membranes and can be detected after excitation at 405 nm and quantified by flow cytometry. The intensity of fluorescence directly correlates to the amount of DNA per cell. Depicting cell counts in a histogram relative to DAPI fluorescence intensity, shows the three phases of the cell cycle: the first peak equals the G0/G1 phase with one set of DNA, the following valley, represents the S-phase and the second peak are the cells in G2/M phase, with two copies of DNA (see Fig. 11).

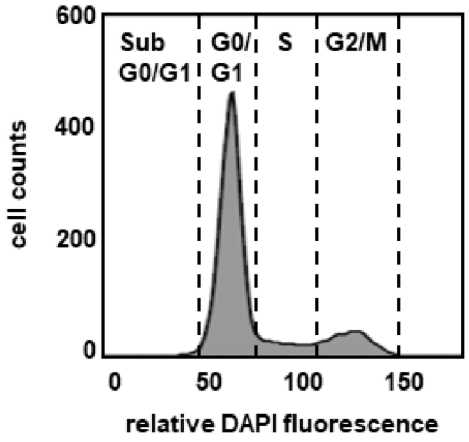

Figure 11: Exemplary histogram of a cell cycle analysis.

Cell cycle analysis was performed for DKFZ-BT66 cells at different stages of OIS induction, by withdrawal of doxycycline from cell culture medium for the indicated times. DKFZ-BT66 cells n= 2 x 10^6 were seeded in six-well plates and cultured in presence of doxycycline for 24 hours. After 24 hours, the day 0 sample was collected and new medium without doxycycline was added for all other wells. At the indicated time points, cells were trypsinized (see 2.2.1.3, exception: centrifugation conducted at 4°C), transferred to a 15 mL falcon on ice, washed with cold PBS and fixed by dropwise addition of 1 mL ice-cold 70% ethanol, while the samples were vortexed. After incubation for 30 minutes on ice, cells were washed with cold PBS once more, followed by staining for 30 minutes with 200 µL 0.1% TritonX 100 plus 1 µg/mL 4',6-Diamidino-2-Phenylindole (DAPI) (see table 2.1.8) at RT protected from light. Cells were analyzed using the BD FACS Canto II flow cytometer with a 405 nm excitation laser and a 450 nm/50 bandpass Pacific-Blue emission filter in collaboration with Johannes Ridinger from the CCU Pediatric Oncology, DKFZ, Heidelberg in Germany. In a SSC-W/SSC-H plot doublets were discriminated and the cell cycle stages were plotted in a cell count/Pacific-Blue histogram. The percentage of cells for each cell cycle phase was determined per time point of OIS induction. The FlowJo-V10 software was used for data analysis.

In addition, flow cytometry-based sorting was used to separate successfully transduced DKFZ-BT66 cells with shRNA constructs expressing GFP (2.2.1.9/10, see appendix B for plasmid maps) from non-transduced cells. As the DKFZ-BT66 cells are resistant to puromycin, due to stable transduction with the SV40-TAg construct co-expressing puromycin resistance, antibiotic selection was not feasible. For sorting, a single cell suspension of all transduced DKFZ-BT66 cells was prepared and run under sterile

conditions at the Imaging and Cytometry Core Facility of the German Cancer Research Center, Heidelberg, Germany.

2.2.5 *In vivo* techniques and methods involving primary human and murine tumors

2.2.5.1 *In vivo* imaging system (IVIS)

IVIS is a tool to visualize tumor formation and growth in small animals by detection of bioluminescence emitted after injection of luciferin in animals transplanted with luciferase-transduced cells. The firefly luciferase catalyzes luciferin oxidization in presence of oxygen and ATP, which leads to the emission of light. The enzyme is encoded on a lentiviral construct and stably transduced into the injected tumor cells (2.2.1.9). As D-luciferin is not a substrate for any other mammalian enzyme, the detected signal is very specific and highly sensitive, as it has a very low background signal.

To image the tumor growth of mice injected with luciferase-expressing tumor cells, the animals were narcotized with isoflurane (1.5-2.5 Vol.%). After assessing the level of anesthesia by pedal reflex, their eyes were protected with Bepanthen® lotion, the mice were weighted and D-luciferin was injected intraperitoneally (0.01 mL/g, c=15 mg/mL in sterile PBS). After five minutes, mice were transferred to the IVIS Lumina III machine with their nose facing the nose cones, which were attached to the anesthetic system. IVIS measurement (exposure times: 5 minutes and 30 seconds) was conducted. After the measurement, the mice were transferred back to their cage and observed until the anesthesia had worn off.

2.2.5.2 Transplantation of DKFZ-BT66 cells *in vivo*

To generate an *in vivo* model of the established DKFZ-BT66 cell line, the patient-derived cells were orthotopically injected into the cerebellum of immunodeficient mice in collaboration with Florian Selt and Daniela Kuhn from the CCU Pediatric Oncology, DKFZ, Heidelberg in Germany. Before injection, DKFZ-BT66 cells were stably transduced with a construct coding for luciferase (see 2.2.1.9/10, see appendix B for plasmid maps) to enable visualization via IVIS.

A single cell suspension of n= 1 x 10^6 DKFZ-BT66 LUC +/- hTERT cells in 4 µL sterile medium were intracranially injected in 6-week old NOD.Cg-Prkdcscid Il2rgtm1Wjl/SzJ mice (NOD-SCID gamma-mice [NSG]). Before surgery, the mice were injected with Caprofen (5 mg/kg) subcutaneously. After 20 minutes, the mice were narcotized with isoflurane (1.5-2.5 Vol.%), kept on a heating pad, the head was fixed in a stereotaxtic instrument and eyes protected with Bepanthen® lotion. The mice were kept under

isoflurane-induced anesthesia through a hose attached to the nose. Bupivacaine (0.25%) was applied to the site of injection before surgery. After assessing the level of anesthesia by pedal reflex, a scalpel was used to cut a 2-3 mm long incision on top of the skull. The site of cell injection was located 7 mm behind the bregma, 1.5 mm to the left and 2 mm deep. A hole was drilled into the scull with a sterile cannula at the described site. Tumor cells were injected with a Hamilton syringe, adjusted at the correct height for injection (2 mm deep). The injection rate was regulated by a microinjection pump with a rate of 400 nL per minute (4 µL injected in 10 minutes). To avoid leakage after injection, the syringe was removed 5 minutes after the end of the injection. The site was disinfected with betaisadona solution, closed with 2-3 stiches and the mouse was observed after the surgery to ensure well-being. Caprofen (5 mg/kg) was given for the following two days in 12 hour intervals.

After injection of DKFZ-BT66 cells, mice received doxycycline (1,4 mg/mL) in their drinking water to induce SV40-TAg expression. Tumor growth was monitored via bioluminescence (IVIS see 2.2.5.1) every month. If mice showed signs of disease or discomfort (e.g. signs of pain, hunching, slow movement, hyperactivity, problems with balance) they were anesthetized with CO_2 and decapitated.

In case of tumor development, as discovered by symptoms of disease such as hunched posture, head dome or tilting and abnormal gaits, the brain was isolated by opening the scull with sharp scissors and forceps (for more detail see 2.2.1.10). The brain was carefully transferred to PBS in a 10 cm dish and a sagittal cut was performed to detect the tumor location. Tumors from DKFZ-BT66 cells were visible by eye via strong RFP expression, which is co-expressed on the SV40-TAg construct. The tumor was isolated from normal brain and cut into two pieces using scalpels. One piece was preserved in 4% formaldehyde for IHC analysis. The second piece was mechanically dissociated into a single cell suspension with different size pipet tips. The tumor cell suspension was counted and n= 2-5 x 10^6 cells were frozen in liquid nitrogen for DNA or RNA isolation and n= 2 x 10^6 cells/cryovial were frozen in 10% DMSO-containing cell culture medium for retransplantation. The animal procedure was approved by the German authorities (Regierungspräsidium Karlsruhe; G64/14).

2.2.5.3 $BRAF^{V600E}$-expressing PA mouse model

The murine PA *in vivo* model was generated by Alexander Sommerkamp and Britta Ismer from the Pediatric Glioma Research, DKFZ, Heidelberg in Germany. In brief, the tumors were generated by injecting RCAS $BRAF^{V600E}$-expressing DF-1 cells into the cerebral hemisphere of neonatal Nestin Tv-a (Ntv-a) mice as described by Gronych and colleagues (24). Five to six weeks after injection, mice were sacrificed and PA tumors were isolated. Non-injected Ntv-a mice of the same age were used as controls.

Protocols of all animal procedures were approved by the German authorities (Regierungspräsidium Karlsruhe; G-69/13, DKFZ342).

2.2.5.4 DNA-methylation array of murine and human PA tumor samples

As methylation patterns are preserved and therefore specific for each tumor entity, analysis of methylation profiles can be used as a tool to classify tumors. Epigenetic changes regulate the accessibility of chromatin and can thereby alter gene transcription without inducing changes to the DNA sequence. One common mechanism of epigenetic regulation is the methylation of cytosine at the 5´-carbon in a CpG dinucleotide. Hypermethylation leads to reduced accessibility of the DNA strand and therefore results in reduced transcription. In tumors, hypermethylation of promoter regions is a common mechanism to inactivate e.g. tumor suppressor genes. As these alterations are preserved from the cell of origin throughout tumor development, analysis of the methylation status of CpG dinucleotides in a tumor sample on a genome-wide level can be used for classification purposes by differential comparison of the identified pattern to the signatures of other tumor entities.

The Illumina Infinium HumanMethylation450 Beadchip (450K) array was used for all human tumor samples as well as the DKFZ-BT66 cell line and the Illumina Infinium HumanMethylationEPIC (850K) Beadchip was used for the DKFZ-BT66 hTERT mouse model both performed according to manufacturer's instructions at the Genomics and Proteomics Core Facility of the German Cancer Research Center, Heidelberg, Germany. Methylation-DNA array data was used for molecular subgrouping and copy number profiling as described before by Hovestadt *et al.* (5) and Capper *et al.* (4). t-Distributed Stochastic Neighbor Embedding (t-SNE) analysis was performed as described before by Sturm *et al.* (8) and Capper *et al*. (4). The analysis was performed in cooperation with David Jones from the Pediatric Glioma Research, DKFZ, Heidelberg in Germany.

2.2.6 Statistical analysis

2.2.6.1 Identification of OIS-controlling candidate genes specific for PA

Step 1: OIS-controlling candidate genes were identified in a first approach by comparing publicly available gene expression datasets from several human OIS models, generated in fibroblasts or melanocytes. The goal was to identify genes that were upregulated in multiple OIS models in comparison to their matching proliferating counterparts and to generate an OIS candidate gene list. Six publicly available gene expression datasets were compared to each other (GEO: GSE54402, GSE46801, GSE60652, GSE41318, ArrayExpress: E- NCMF12, E-NCMF13, also see 2.2.2.5). First, upregulated genes during the

OIS condition were ranked for every dataset separately according to their moderated t-statistic based on the empirical Bayes approach (133) as implemented in the Bioconductor package limma (134). If a gene was represented by multiple probes, the probe with the strongest effect was chosen. Genes which were consistently upregulated in all datasets (n=332) were identified with the rank-product approach (135). The rank-product is the geometrical mean of ranks. The analysis was based on the overlap of genes determined in each data set. Significance of rank-product was tested according to Eisinga *et al.* (136) and p-values were adjusted to control the false discovery rate using Benjamini-Hochberg correction. The statistical analysis was conducted in collaboration with Thomas Hielscher from the Division of Biostatistics at the DKFZ Heidelberg in Germany.

To account for pathways that are altered during OIS, ingenuity pathway analysis (IPA) was conducted for the n=332 identified OIS-related genes. A list was generated from all genes that appeared in the top-upregulated pathways predicted by IPA (n=36 genes in total).

Finally, the most common SASP factors have been summarized by Coppé *et al.* (87) and a list with the SASP factors was included in the analysis.

Step 2: The expression level of the OIS-related genes selected from public GEPs, the IPA pathway genes and the SASP genes were analyzed in pediatric and adult PA patient samples (n=182) (appendix E, GEO: GSE16011 (137), GSE5675(138)) and compared to the corresponding expression level in unmatched normal fetal cerebellum samples (n=5) from non-patients (GEO: GSE44971 (139)) using the R2 web-based genomics analysis and visualization platform (http://r2.amc.nl). Genes which were significantly upregulated in PA were considered for further analysis.

Step 3: Finally, only genes were considered, which overlapped in all three candidate gene lists and could be targeted by a small molecule inhibitor or antibody.

2.2.6.2 Gene set enrichment analysis (GSEA)

GSEA is a computational method that enables testing for differential expression of a defined gene set between two biological states (140).

To test for differential gene expression of the SASP factors (87) in different biological samples or experimental settings, the limma approach (134) was used. GSEA was performed using the camera test (141). The most specific probe set per gene was selected using the jetset algorithm (142). All analyses

were performed with statistical software R 3.4 in collaboration with Thomas Hielscher from the Division of Biostatistics at the DKFZ Heidelberg in Germany.

2.2.6.3 Correlation of progression-free survival (PFS) and SASP factor expression

The patient data utilized to look for correlations between gene expression and clinical outcome were part of the ICGC PedBrain cohort (14). PFS was defined as time from diagnosis to recurrence or death, whichever occurred first. The distribution of PFS was depicted using the method of Kaplan and Meier and compared between groups using the log-rank test. Univariate and multivariate Cox Regression models were used to estimate the hazard ratio and corresponding 95% confidence interval of prognostic factors (appendix G-L). IL1B log2-expression and SASP sum score were standardized to give the hazard ratio per one standard deviation increase. Groups were based on median cut-off for IL1B or tertiles for the SASP score. The calculations were conducted in collaboration with Thomas Hielscher from the Division of Biostatistics at the DKFZ Heidelberg in Germany.

2.2.6.4 Experimental settings

In vitro experiments were performed in a minimum of three biological replicates, as indicated, besides the senolytic drug screen which was conducted in three technical replicates. All data is presented as mean ± SD. Testing for statistical significance of differences between two groups was done by unpaired Student´s t-Test with Welch´s correction. P-values below 0.05 were considered as significant. Graphs were generated using GraphPad Prism version 5.01, R 3.4 and Microsoft Powerpoint 2010 for Windows.

3. RESULTS

3.1 Establishment of an *in vitro* and *in vivo* model of LGG

3.1.1 The DKFZ-BT66 PA model

An *in vitro* LGG model, DKFZ-BT66, was successfully generated from a patient tumor sample of a two year old, male patient with a PA (31). The diagnosis was confirmed by the local neuropathology in Tübingen and by the central German reference pathology board in Bonn. The tumor was located in the cerebellum and presented with a *KIAA:BRAF* ($K^{EX16}B^{EX9}$) fusion.

Due to fast onset of growth arrest, most likely resulting from OIS, primary LGG tumor cells cannot be cultured over the long-term (19,32). To overcome OIS-induced growth arrest, the primary material was stably transduced with inducible SV40-TAg, which interferes with the OIS-relevant TP53/CDKN1A and CDKN2A/RB1 pathways. The tumor was processed by mechanical dissociation into a single cell suspension and transduced at with a lentiviral construct coding for SV40-TAg as well as RFP at passage 2, both regulated by a doxycycline-inducible promoter (see 2.2.1.10). Successful transduction as well as active transcription of the SV40-TAg coding plasmid could be determined by assessment of RFP expression via fluorescence microscopy (Fig. 12A). After antibiotic selection the transduced cells uniformly expressed RFP, as detected by flow cytometry (Fig. 12B). To induce SV40-TAg expression and proliferation of the LGG cells, the medium was supplemented with doxycycline. Upon withdrawal of doxycycline from the cell culture medium, SV40-TAg mRNA expression decreased substantially within two days (Fig. 12C). Protein expression of SV40-TAg was reduced after two days and could no longer be detected at day five after doxycycline withdrawal (Fig. 12D). Withdrawal of doxycycline from the cell culture resulted in growth arrest of DKFZ-BT66 cells. In a cell count, comparing doxycycline-treated, proliferating DKFZ-BT66 cells (+DOX) to cells under doxycycline withdrawal (-DOX), a significant difference in growth could be determined at day five (Fig. 12E). Withdrawing doxycycline from the medium was accompanied by an initial drop in cell number, likely resulting from sudden activation of p53. The doubling time of doxycycline-treated, proliferating DKFZ-BT66 cells was calculated to be 44 hours (passage 11-13). In summary, addition of doxycycline induced SV40-TAg expression and subsequent steady proliferation, while withdrawal of doxycycline resulted in reduction of SV40-TAg levels within five days and subsequent growth arrest of DKFZ-BT66 cells.

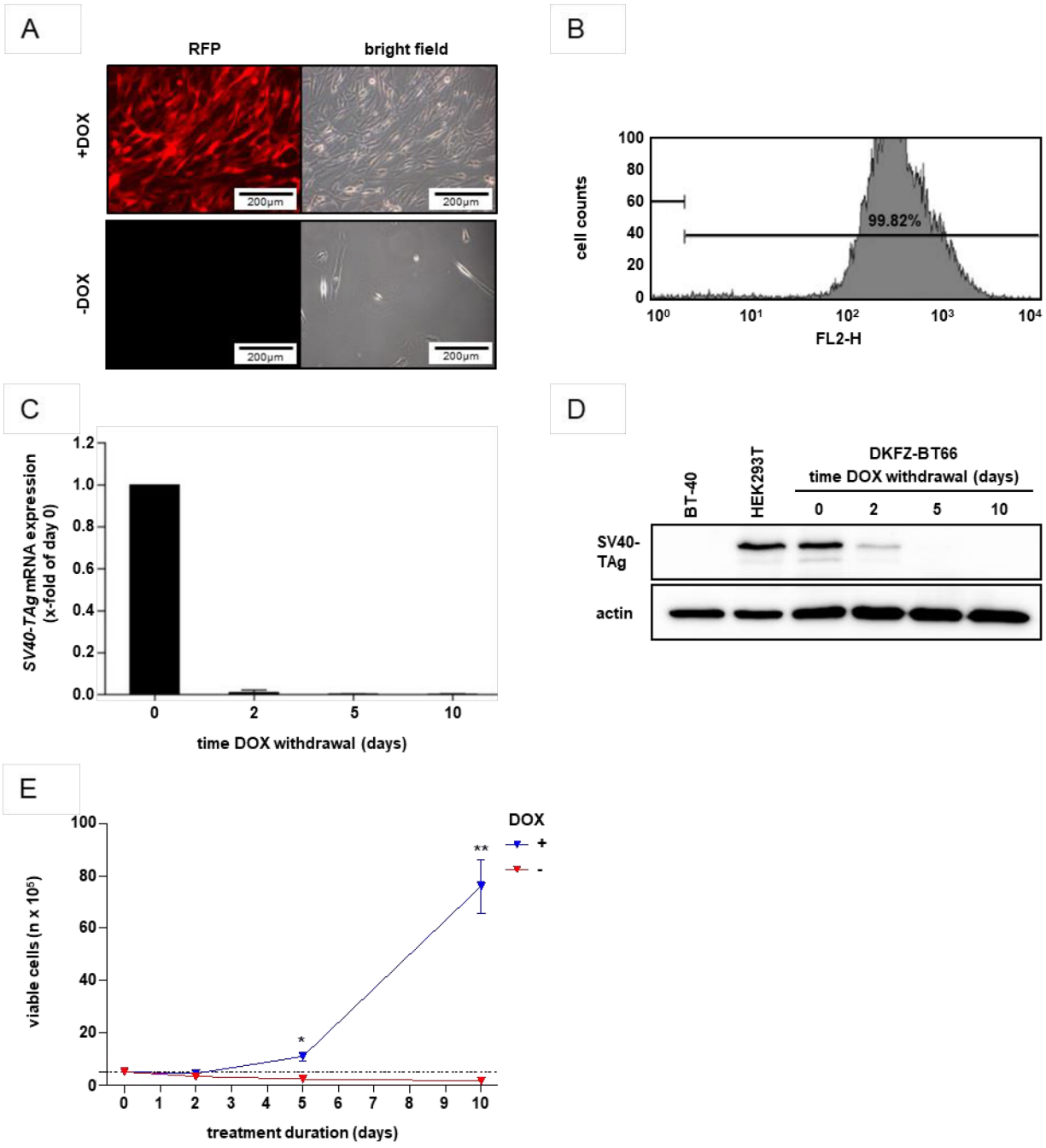

Figure 12: Characterization of the doxycycline-inducible expression of SV40-TAg in the DKFZ-BT66 cell line. Adapted from Selt *et al.* (31). A) Light and fluorescence microscopic comparison of DKFZ-BT66 cells grown under treatment with 1 µg/mL doxycycline (+ DOX) or without (- DOX) at day 10. B) Flow cytometric detection of red fluorescence indicating RFP (FL2-H) positivity in DKFZ-BT66 cells cultured in the presence of doxycycline (representative plot). C) Fold change of *SV40-TAg* transcript levels measured by RT-qPCR during induction of OIS in DKFZ-BT66 cells in comparison to expression levels of DKFZ-BT66 cells in proliferation (= day 0). Depicted are mean +/- SD of three independent experiments. D) Protein levels of SV40-TAg were determined by western blot in DKFZ-BT66 cells during induction of OIS at the indicated times with HEK293T (constitutively expressing SV40-TAg) and BT-40 (not expressing SV40-TAg) as control cells. Actin serves as loading control. E) Cell count of DKFZ-BT66 cells under treatment with doxycycline (+ DOX) or without (- DOX) for 10 days. Depicted are mean +/- SD of three independent experiments. Significant differences are indicated as * $p<0.05$; ** $p<0.01$ (Student´s t-Test). The dashed line represents the number of cells seeded at day 0.

To verify the origin of the DKFZ-BT66 cell line from the PA patient sample, a genome-wide methylation analysis, RT-qPCR for the *KIAA:BRAF* fusion and a western blot for MAPK pathway activity was conducted. Patterns derived from DNA methylation analysis are highly conserved for each tumor entity and allow for identification and classification of tumor samples via unsupervised clustering (4,5). The t-SNE plot generated from methylation array data showed a clustering of the original PA patient sample close to the established DKFZ-BT66 cell line. In addition, the original tumor sample clustered in the same methylation group as other infratentorial PAs compared to other pediatric high- and low-grade tumors (Fig. 13A). Furthermore, the *KIAA-BRAF* fusion, expressed in the original PA tumor, resulting in a duplication on chromosome 7q34, could be detected in the copy number plot derived from the methylation array of the DKFZ-BT66 cell line (Fig. 13B). Presence of the fusion in the cell line was additionally confirmed by RT-qPCR using primers designed around the different break points of the *KIAA:BRAF* fusion. The original tumor presented with a $K^{EX16}B^{EX9}$ fusion, which could be detected in the DKFZ-BT66 cell line as well (Fig. 13C). Aberrant MAPK pathway activity was evident from elevated phosphorylation of MEK and ERK in comparison to BRAF wild-type expressing HEK293T cells, as determined by western blot. ERK activation in the *BRAF* fusion expressing DKFZ-BT66 cell line was comparable to the $BRAF^{V600E}$ expressing BT-40 cell line (Fig. 13D).

In summary, the patient-derived DKFZ-BT66 cell line shows a preserved methylation profile compared to primary infratentorial PAs, expresses the original *KIAA-BRAF* fusion and exhibits elevated MAPK activity. Therefore, it is a representative *in vitro* model of a LGG.

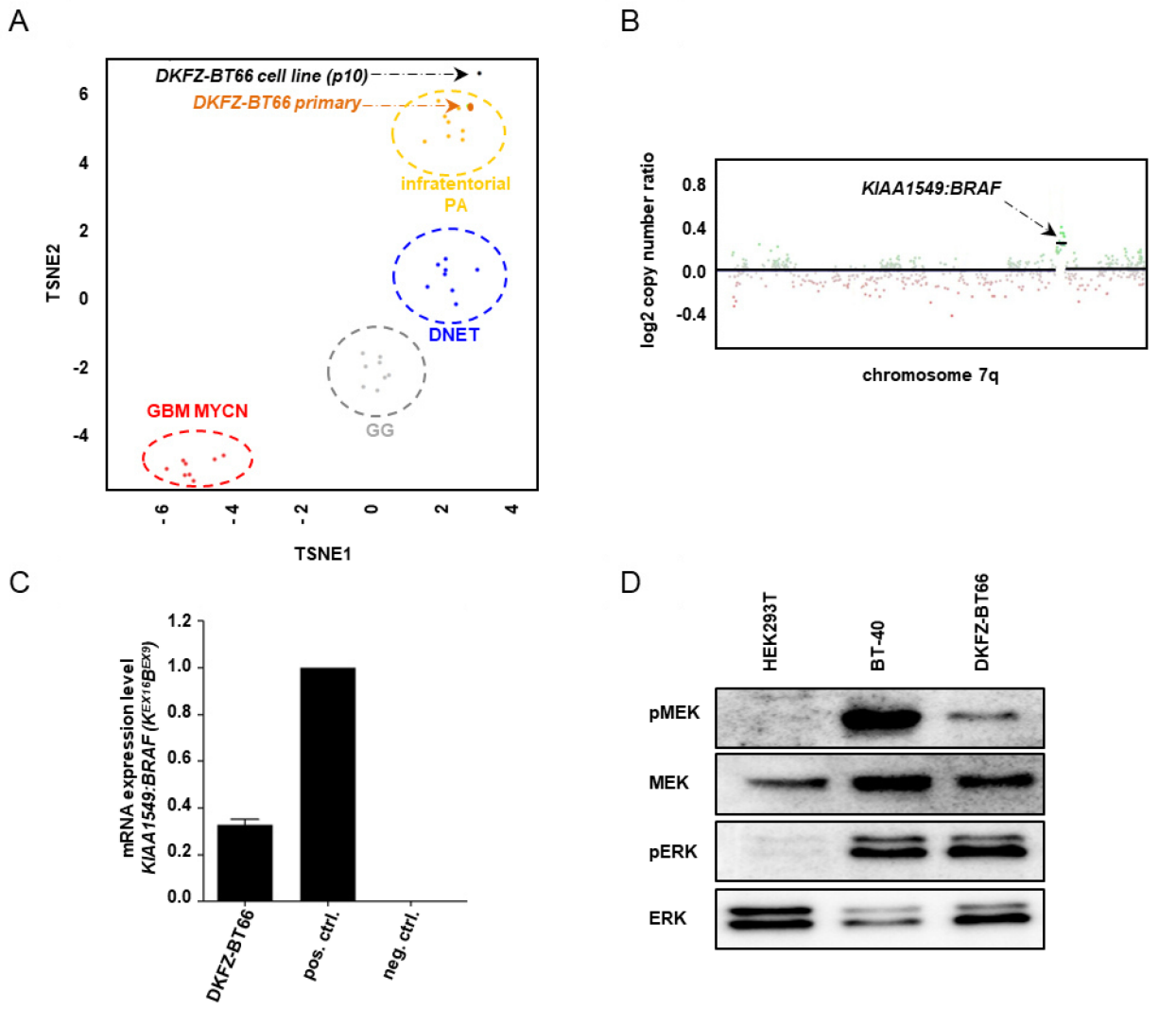

Figure 13: Characterization of the DKFZ-BT66 cell line. Adapted from Selt *et al.* (31). A) TSNE analysis (t-Distributed Stochastic Neighbor Embedding) of whole genome DNA-methylation data. Shown are the DKFZ-BT66 cell line (passage 10, black dot), the primary tumor the cell line was derived from (orange dot) and the group of infratentorial pilocytic astrocytomas (PA), as well as other pediatric low- and high-grade tumors: DNET: Dysembryoplastic neuroepithelial tumor, WHO grade I; GG: Ganglioglioma, WHO grade I; GBM MYCN: MYCN-amplified glioblastoma, WHO grade IV. B) Copy number plot of chromosome 7q calculated from DNA-methylation array data showing presence of a chromosomal gain typical for the tandem duplication that leads to a *KIAA1549:BRAF* fusion. C) Detection of *KIAA1549:BRAF* ($K^{EX16}B^{EX9}$) fusion gene mRNA by RT-qPCR using fusion break point specific primers. An astrocyte cell line (TÜ-DKFZ-002) transduced with a retroviral construct coding for the full length form of *KIAA1549:BRAF* ($K^{EX16}B^{EX9}$) fusion served as positive control (pos. ctrl.) and reference for expression level. Neuroblastoma cell line BE-(2)C served as a fusion negative control (neg. ctrl.) D) Protein levels of pMEK (Ser217/Ser221) and pERK (Thr202/Tyr204) were determined by western blot in DKFZ-BT66 cells cultured in presence of doxycycline with HEK293 (neg. ctrl.) and BT-40 ($BRAF^{V600E}$ positive patient-derived low-grade glioma cell line, pos. ctrl.) as control cells. Total ERK and MEK serve as loading control.

3.1.2 Optimization of conditions for the future establishment of further *in vitro* models

To generate further LGG *in vitro* models different tumor dissociation and cell culture conditions were explored in a total of n=117 LGG samples.

Several parameters of cell isolation, dissociation, culture conditions, medium and viral production and transduction were varied for optimization.

Handling of primary material and dissociation technique: The tumor tissue was initially dissociated using the Brain Tumor Dissociation Kit from Miltenyi Biotec, which included an enzymatic digestion step as well as filtering steps, but the resulting yield in cell number was very low. When comparing the approach to simple mechanical dissociation (2.2.1.10), a single cell suspension could be established with both methods, while the number of vital cells was much higher after mechanical dissociation. Therefore mechanical dissociation was chosen to generate single cell suspensions from primary LGG material (Fig. 14A,B I).

In addition to cultures of single cells, explant cultures were tested (2.2.1.10). Small pieces of the tumor, not containing blood vessels or necrotic tissue, were directly transferred to six-well plates. They were allowed to attach, before medium was carefully added. The explant cultures did successfully attach showing outgrowth of cells, especially in serum-free medium (Fig. 14A,B II). However, these neuron-like cells could never be successfully transduced with the SV40-TAg lentivirus. In addition, the cells could not be detached from their original culture flask without irreversibly damaging the cells (Fig. 14B, right image after detachment).

Cell culture plastic coating: To increase attachment of freshly dissociated LGG cells, six-well plates were pre-coated with poly-L-lysine (PLL) for 1 hour prior to seeding (2.2.1.1). However, this coating step did not lead to significant increase in cell numbers and was therefore discontinued.

Positive selection of primary tumor cells: In another attempt to increase the attachment of tumor cells and reduce the contamination with stroma cells, the tumor cell suspension was positively selected with anti-A2B5 beads using the MACS technology from Miltenyi Biotec. A2B5 is a surface marker of glial progenitor cells (143), which are putative cells of origin of PAs (138). Selection of the established DKFZ-BT66 cell line as positive control however, resulted in a very small yield of isolated cells. In addition, after five attempts of filtering primary LGG material for A2B5, the success rate in transduction of tumor material could not be increased, and this step was therefore also discontinued.

Culture medium: In addition to the astrocyte medium ABM (Fig. 14A,B I), the serum free medium X-VIVO plus supplements including growth factors and the Neurobasal-A medium with supplements (Fig. 14A,B II) was tested. Phenotypically different cells did attach in the serum-free media in comparison to full ABM medium. As no marker for positive selection for PA cells is available, all cell culture media conditions were utilized for further processing of primary material, since both of the observed cell phenotypes could be tumor cells.

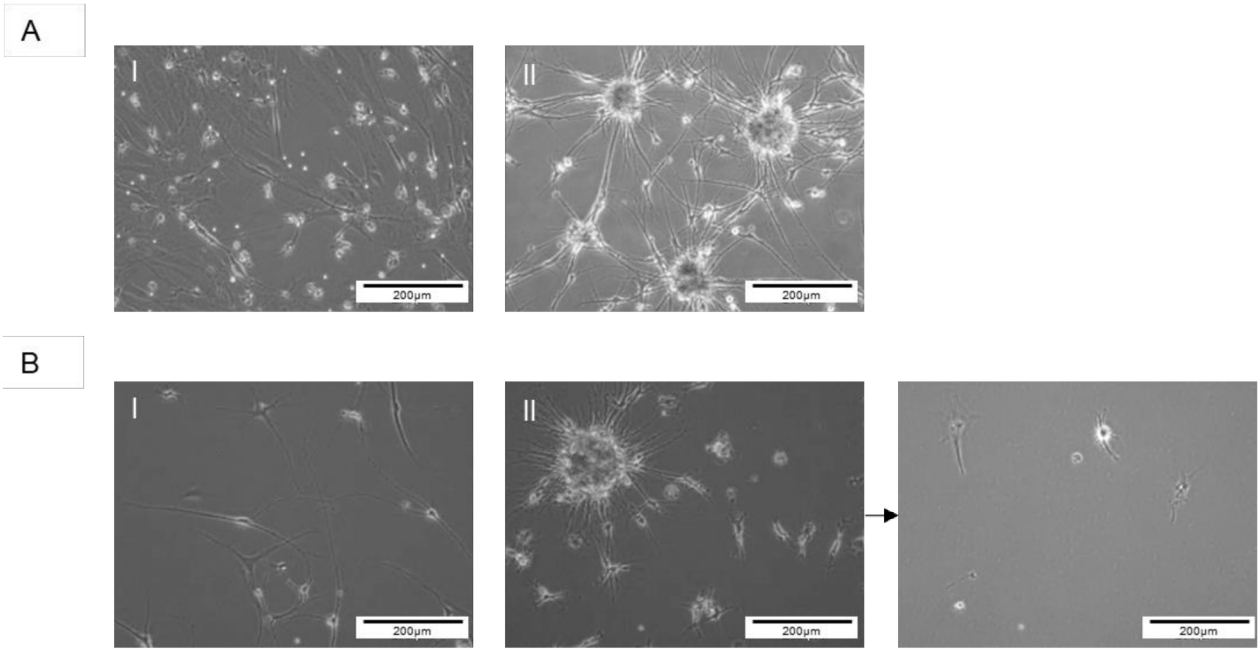

Figure 14: Exemplary images of culture attempts of primary material of LGGs. A) Patient-derived cells from a cerebellar PA TÜ-DKFZ-043 were cultured in either ABM supplemented with the AGM Kit (I) or cultured in Neurobasal-A medium supplemented with growth factors (II). B) Patient-derived cells from a tumor sample suspected to be a PA at first diagnosis FR-DKFZ-LGG007 cultured in full ABM medium (I) or full Neurobasal-A medium (II). Attempt of passaging FR-DKFZ-LGG007 cells from their first culture flask in full Neurobasal-A medium to a new flask (right).

Culture conditions: Another method tested to expand primary LGG cells was a co-culture system on murine brain slices. The group of Charles Stiles reported successful culture of primary LGG cells with their organotypic brain slice co-culture protocol (33,35). The microenvironment from brain of young mice (e.g. at P6) could facilitate growth of primary LGG cells, as it may simulate the microenvironment present in pediatric LGGs to a certain extent. For this purpose, brain slices were generated from P6 C57BL/6 mice and co-cultured with tumor cells for one week (2.2.1.10). First, different cell culture media were tested in the co-culture system with DKFZ-BT66 cells (Fig. 15A I-III). Full ABM medium (Fig. 15A I) was used as the medium best suited for the (regular) culture of DKFZ-BT66 cells. The medium contains FBS, possibly damaging the brain slices as seen by deterioration of the slices. The brain slices were best preserved in

full Neurobasal-A medium (Fig. 15A III), used by Chadwick and colleagues (35), however the DKFZ-BT66 cells did not grow under these conditions. As none of the tested media led to proliferation of the DKFZ-BT66 cells in single cell suspension, seeding of DKFZ-BT66 cells as spheres was tested. For this purpose, DKFZ-BT66 cells were seeded in coated u-bottom plates to cluster in spheres and injected into the slices after 48 hours using a Hamilton syringe. However, embedding of the DKFZ-BT66 spheres in the brain slices did not result in proliferation either (Fig. 15B I-II). A highly aggressive medulloblastoma cell line, MED8A, was used as a proliferation control (Fig. 15C). No cell growth could be observed over the course of one week, even for cells of this high-grade tumor entity. A possible explanation for the failure to establish culture conditions suitable for LGG cells could therefore be an insufficient permissive environment, since even highly proliferative cells did not grow. The protocol will have to be optimized further, e.g. first by slowly adapting cells to a serum-free cell culture medium and testing the method with fresh patient-derived cells, which are not (yet) dependent on serum. In addition, in the original protocol the Stiles group used P6 mice (35), but in their publication on LGG cells, brain slices from E14 mice were used (33). The differences in microenvironment resulting from a younger age of the mice could be even more suitable for the culture of pediatric LGG samples. Using E14 mice therefore could be an additional option for further optimization.

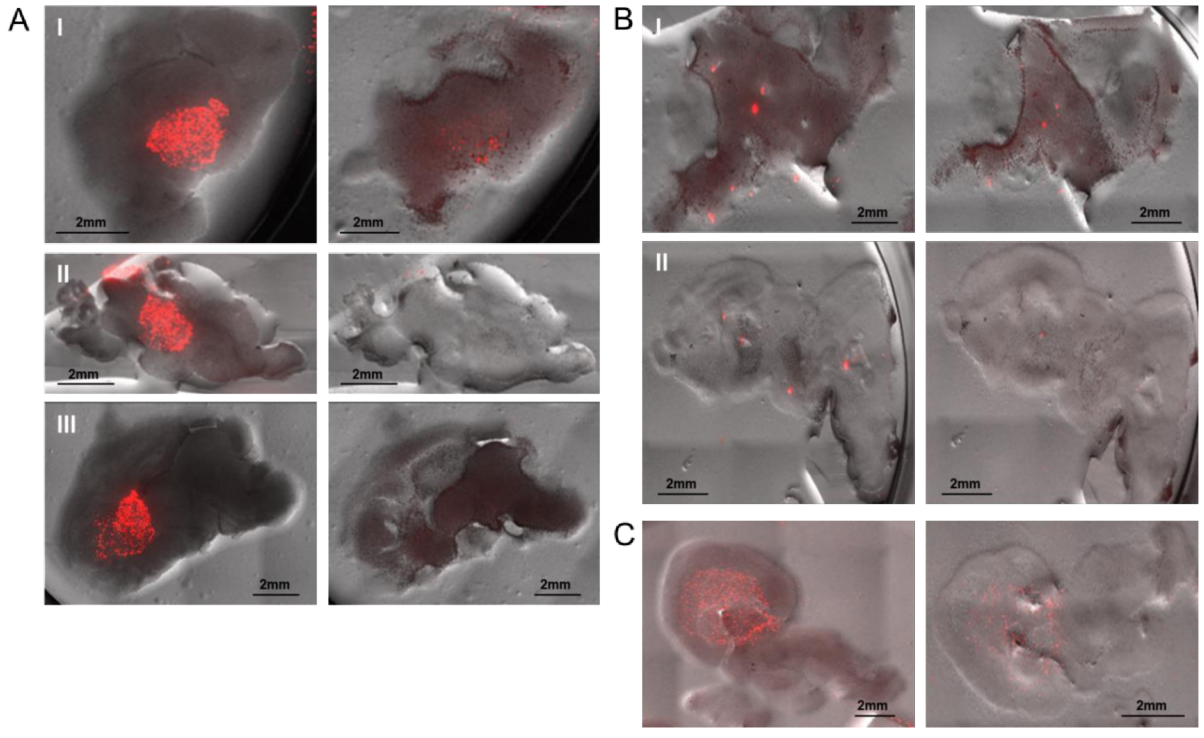

Figure 15: Organotypic brain slice co-cultures with DKFZ-BT66 and MED8A cells. A) DKFZ-BT66 (n= 2 x 10^4) cells were seeded in 2 µL medium on top of 200 µm thick brain slices (cut in 3% low-melting agarose) of P6 C57BL/6 mice. Three different cell culture media conditions were tested: I full ABM, used to culture DKFZ-BT66 cells, II MEM (+ 25% heat-inactivated horse serum, 25 mM

HEPES, 1mM L-glutamine, 5 mg/mL glucose), III Neurobasal-A medium (+ 2% B-27, 1% N2, 1% Glutamax, 1,5 mg/mL glucose from Chadwick *et al*. protocol). The first picture was taken on day 0 and the second picture on day 8. Doxycycline was added every second day together with fresh medium to induce SV40-TAg expression. B) DKFZ-BT66 cells (n= 5 x 10^3) were allowed to form spheres in u-bottom plates and were injected into the brain slices. Cells were cultured in I full ABM medium or II MEM plus supplements. The first picture was taken on day 0 and the second picture on day 4. Doxycycline was added every second day together with fresh cell culture medium. C) MED8A cells (n= 6 x 10^3) were seeded in MEM medium plus supplements using the same experimental setup as in A.

Viral production and transduction: Even though, in some cases primary material was successfully transduced as evident from RFP expression, the analysis of the isolated cells after antibiotic selection was negative for the two markers of LGG tumors, the $BRAF^{V600E}$ mutation and the *KIAA:BRAF* fusion. To further increase the yield of transduced cells, the lentivirus production procedure was optimized. First, different transduction methods were compared such as polyethylenimine (PEI), Lipofectamine and calcium phosphate. The calcium phosphate transduction showed the best efficiency and was therefore used for all further experiments. Here the protocol was optimized as well by e.g. testing different pH values of 2x HBS. The best transduction efficiency was detected at pH 7.12, which was used for all following experiments. An attempt to increase viral transduction efficiency was to increase viral titers by ultracentrifugation of the virus supernatant. However, this did not result in higher transduction efficiency and was therefore not utilized in further experiments.

In summary, establishing an *in vitro* model from LGG tumor samples remains difficult due to their benign growth behavior. Further systematic efforts will be necessary to improve the very low success rate.

3.1.3 Characterization of orthotopically injected DKFZ-BT66 cells

To exploit the full potential of the established DKFZ-BT66 cell line, the cells were utilized for the generation of an *in vivo* model. First, the DKFZ-BT66 cell line was stably transduced with a construct coding for luciferase as well as green fluorescent protein (GFP) (2.2.1.9), to enable detection of tumor engraftment and growth in mice (2.2.5.1). Successfully transduced cells were selected for high GFP expression and isolated by fluorescence activated cell sorting (2.2.4.3). The luciferase expressing DKFZ-BT66 cells were injected into the cerebellum of n=12 6-week old NOD.Cg-Prkdcscid Il2rgtm1Wjl/SzJ mice (NOD-SCID gamma-mice [NSG]). All mice continuously received doxycycline (1,4 mg/mL) in their drinking water to induce SV40-TAg expression and subsequent tumor cell proliferation. Tumor growth was monitored via bioluminescence using IVIS (2.2.5.1). In the time frame of nine months no tumor formation was observed and the experiment was terminated (Fig. 16).

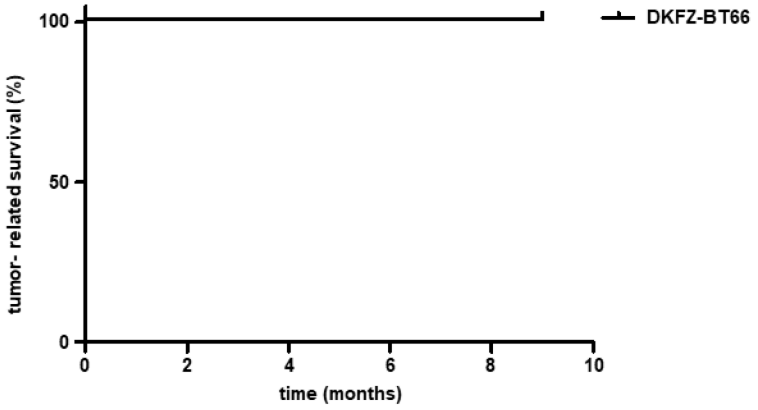

Figure 16: *In vivo* modelling with DKFZ-BT66 cells. A) Tumor-related survival of NSG mice intracranially injected with the DKFZ-BT66 LUC cell line (n=12).

It is conceivable that the lack of tumor growth resulted from the benign nature of the tumor cells in addition to the fact that the cells are derived from primary material and go into replicative senescence over time. Onset of replicative senescence was observed in *in vitro* cultures after passage 17 (Fig. 17A,B). At passage 20, DKFZ-BT66 cells presented with an enlarged, flat cellular morphology, typical for senescence (Fig. 17B) (40,48). To overcome replicative senescence DKFZ-BT66 cells were stably transduced with a construct coding for human telomerase reverse transcriptase (hTERT). Expression of hTERT allowed for extended growth of the LGG cells (Fig. 17C). Transcription of the telomerase was not detectable in DKFZ-BT66 cells and could only be observed in the transduced cell line on mRNA level (Fig. 17D).

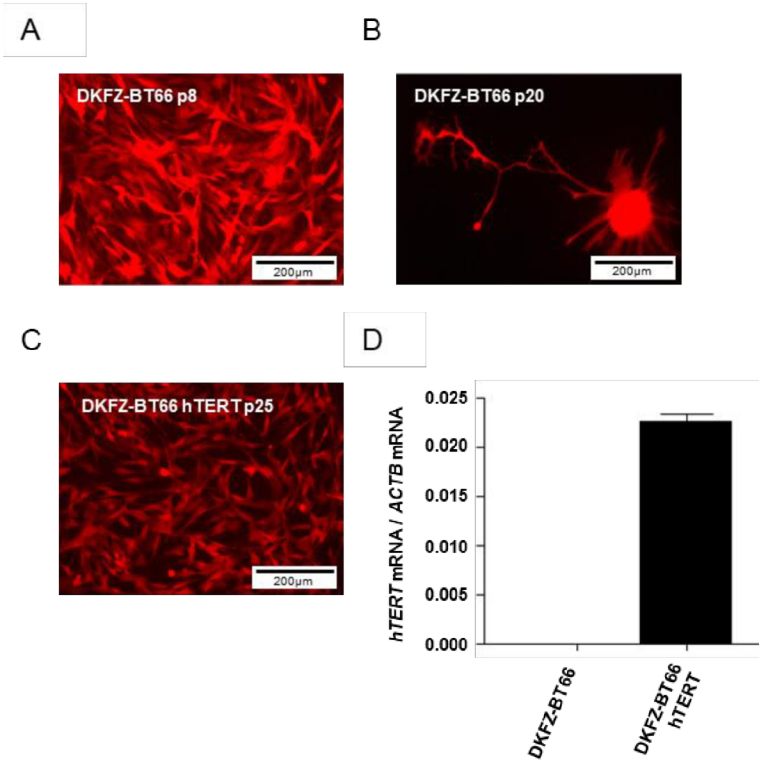

Figure 17: DKFZ-BT66 hTERT cell characterization. Adapted from Selt *et al.* (31). A) Fluorescence microscopic image of DKFZ-BT66 cells, expressing RPF, grown under doxycycline at an early passage 8. B) Fluorescence microscopic image of DKFZ-BT66 cells grown under doxycycline at a late passage 20. C) Fluorescence microscopic image of DKFZ-BT66 hTERT cells grown under doxycycline at passage 25. D) Fold change of *hTERT* transcript levels measured by RT-qPCR in comparison to expression levels of *ACTB* in DKFZ-BT66 cells in proliferation. Depicted are mean +/- SD of three independent experiments.

Transduction of the DKFZ-BT66 LUC cell line with hTERT enabled bypass of replicative senescence (Fig. 17) (31) and thereby may permit tumor growth *in vivo*. NSG mice were intracranially injected with the DKFZ-BT66 LUC hTERT cell line and tumor growth was monitored via IVIS. For this second attempt, mice were observed for a longer time frame, with the end of observation determined either as death due to old age or signs of disease. Indeed, a luminescence signal was first detected 11 months after injection and two tumor-bearing mice had to be sacrificed at months 16 and 18 due to increasing tumor size (Fig. 18A, orange line). Histopathological analysis could be conducted for one of the resected tumors, but did not show any resemblance with a PA. H&E staining showed a pleomorphic tumor with high mitotic activity. The tumor was analyzed by immunohistochemistry staining for Ki67, GFAP and pERK (Fig. 18B). A proliferative index of approximately 30% was determined by Ki67 staining and indicated high proliferative activity, as opposed to PAs which typically have a much lower proliferative index of 1-2% (144). GFAP, a marker of PA, could not be detected by IHC (Fig. 18B). Phosphorylation of ERK, as a marker of active MAPK pathway signaling, was detected by IHC in several cells (Fig. 18B). To further

characterize the murine model, a copy number plot derived from DNA methylation array data was generated from one of the DKFZ-BT66 hTERT tumors. The tumor still showed presence of the typical tandem duplication leading to the *KIAA:BRAF* fusion (chromosome 7q), but the copy number plot revealed numerous atypical chromosomal aberrations for a PA (Fig. 18C). In addition, the methylation profile did not cluster with the established methylation reference class of PAs (4). When one of the DKFZ-BT66 hTERT tumors was re-transplanted into NSG mice, tumors grew so fast that all mice had to be sacrificed within one month (Fig. 18A, green line). In conclusion, the DKFZ-BT66 cell line alone can not induce PA tumors, most likely due to early onset of replicative senescence, and the DKFZ-BT66 hTERT cell line induces tumors which do not resemble a PA, but higher-grade, more malignant tumors.

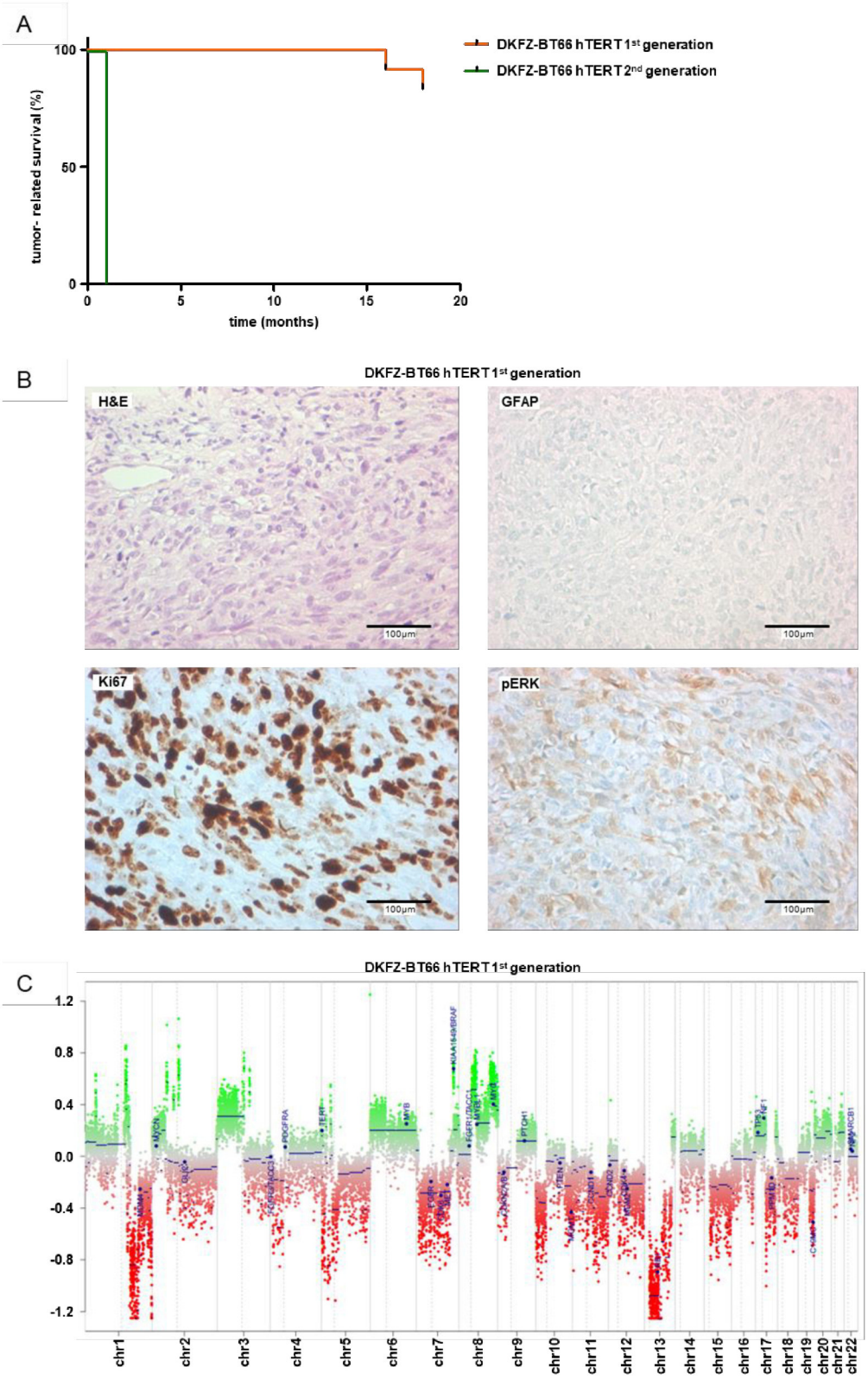

Figure 18: *In vivo* modelling with DKFZ-BT66 hTERT cells. A) Tumor-related survival of NSG mice intracranially injected with the DKFZ-BT66 LUC hTERT cell line (n=12) (orange) and mice retransplanted with a primary tumor of a DKFZ-BT66 LUC hTERT mouse

(n=6) (green). B) Immunohistochemistry of a first generation DKFZ-BT66 hTERT mouse tumor stained for H&E, GFAP, Ki67 and pERK. C) Copy number plot from DNA-methylation array data of a first generation murine DKFZ-BT66 hTERT tumor.

3.2 Proof and characterization of OIS in PA

Due to the inducible nature of SV40-TAg expression and the resulting switch from growth arrest to proliferation, the DKFZ-BT66 cell line is a suitable model to study OIS. To prove that the growth arrested condition of the DKFZ-BT66 cell line is indeed representative of OIS, DKFZ-BT66 cells cultured in the absence of doxycycline were characterized by RT-qPCR, western blot, immunofluorescence and flow cytometry. Common markers of OIS such as expression of CDKN1A, CDKN2A and senescence-associated ß-galactosidase (SA-ß-Gal), cell cycle arrest and senescence-associated heterochromatin foci (SAHFs) were analyzed. For all experiments in the OIS state, DKFZ-BT66 cells were cultured in proliferation in the presence of doxycycline until seeded. After seeding cells for the respective experiment, cells were cultured without doxycycline.

3.2.1 Detection of common OIS markers in DKFZ-BT66 cells

The first observation after withdrawal of doxycycline was a change in cell morphology to the senescence-characteristic enlarged, flat phenotype (Fig. 19A) (48). The OIS marker CDKN2A was expressed on mRNA and protein level, but not differentially regulated during withdrawal of doxycycline (Fig. 19B,D). As the SV40-TAg interferes with the CDKN2A/RB1 pathway further downstream of CDKN2A, its levels are not altered by withdrawal of doxycycline und subsequent activation status of SV40-TAg. Upon withdrawal of doxycycline the mRNA expression of the OIS marker CDKN1A was significantly upregulated (Fig. 19C). However, CDKN1A expression is regulated by p53 (145), which is inhibited during expression of SV40-TAg (Fig. 19D). SV40-TAg inhibits p53 signaling, including the autoregulatory feedback loop leading to its degradation by MDM2 (146), therefore p53 protein levels accumulate (147) (Fig. 19D). Again, this is reflected in the protein level of CDKN1A, which is absent while SV40-TAg is expressed and only transcribed once doxycycline is withdrawn and p53 signaling is activated. Cell cycle analysis of DKFZ-BT66 cells during doxycycline withdrawal revealed a GO/G1 cell cycle arrest, as indicated by a significant reduction of the S-phase after two days of doxycycline withdrawal and an increase in G0/G1-phase (Fig. 19E). Representative images of the analyzed histograms at day ten after doxycycline withdrawal show the reduction of the S phase and increase of the G0/G1 phase (Fig. 19F).

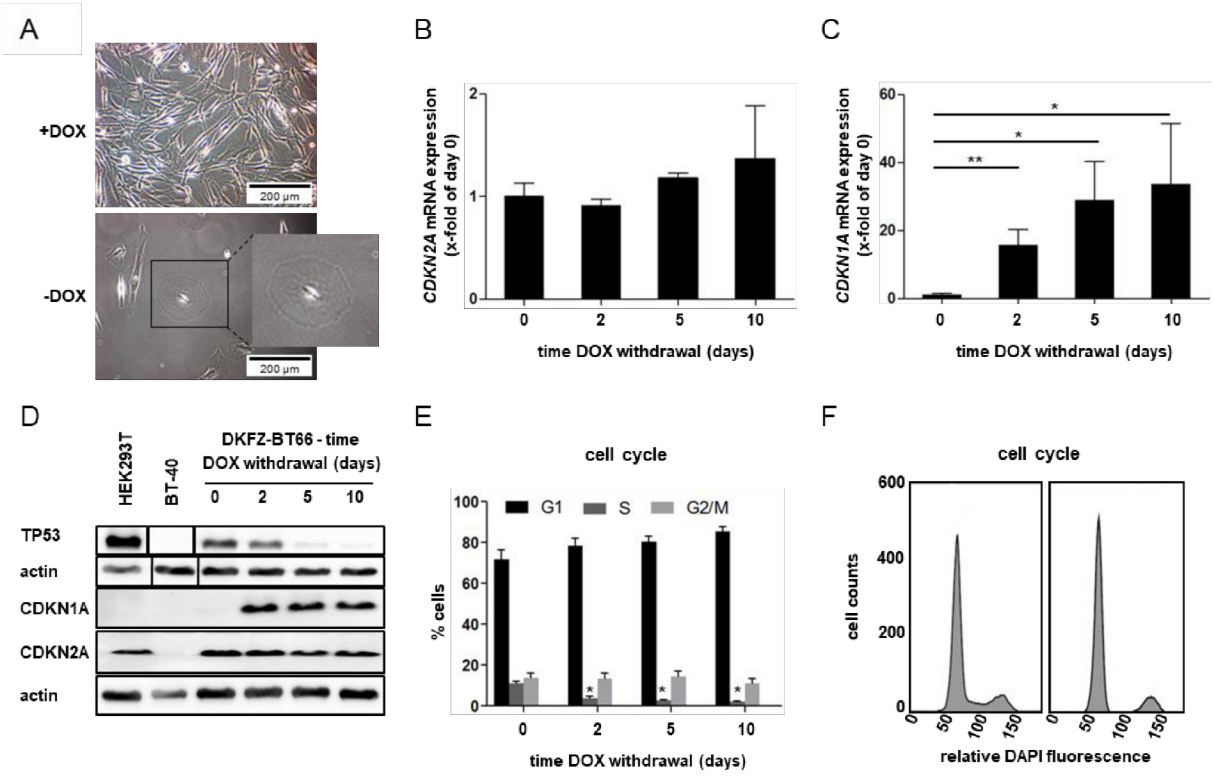

Figure 19: Markers of OIS can be detected in DKFZ-BT66 cells. Adapted from Selt *et al.* (31). A) Light microscopic comparison of DKFZ-BT66 cells grown under treatment with 1 µg/mL doxycycline (+DOX) versus untreated (-DOX) at day 21. B, C) Fold change of *CDKN2A* (B) and *CDKN1A* (C) transcript levels measured by RT-qPCR during induction of OIS in DKFZ-BT66 cells in comparison to expression levels of DKFZ-BT66 cells in proliferation (= day 0). Depicted are mean +/- SD of three independent experiments. Significant differences are indicated as * $p<0.05$; ** $p<0.01$ (Student´s t-Test). D) Protein levels of TP53, CDKN1A and CDKN2A were determined by western blot in DKFZ-BT66 cells during induction of OIS at the indicated times with HEK293T and BT-40 as control cells. Actin serves as loading control. The membrane stained for TP53 was cut, as the control cell lysates were loaded the other way around. E) Changes in cell cycle distribution after the induction of OIS in DKFZ-BT66 cells compared to DKFZ-BT66 cells in proliferation (= day 0). Depicted are mean +/- SD of three independent experiments. Significant differences are indicated as * $p<0.05$ (Student´s t-Test). F) Representative cell cycle histograms of DKFZ-BT66 cells cultured with doxycycline (+DOX) versus untreated (-DOX) at day 10.

Two additional OIS markers, SA-ß-Gal activity (2.2.4.2) as well as SAHF (2.2.3.7), were detectable in both states, growth arrest and proliferation. SA-ß-Gal was detected in the proliferating as well as in the growth arrested condition (Fig. 20A). As the DKFZ-BT66 cell line was derived from senescent tumor cells, the elevated levels of SA-ß-Gal remain accumulated in lysosomes. The increased activity of SA-ß-Gal is irreversible in senescent cells, which has been described previously (148). The same phenomenon was observed for staining for SAHF. Both conditions, proliferation and OIS, were positive for SAHF (Fig. 20B). It was previously shown that activation of TP53 in senescent cells has no influence on heterochromatic markers: SAHF, induced by oncogenic stimuli, were retained in a *RAS*-induced OIS fibroblast model independent on TP53-induced proliferating or senescent state of the cells (149).

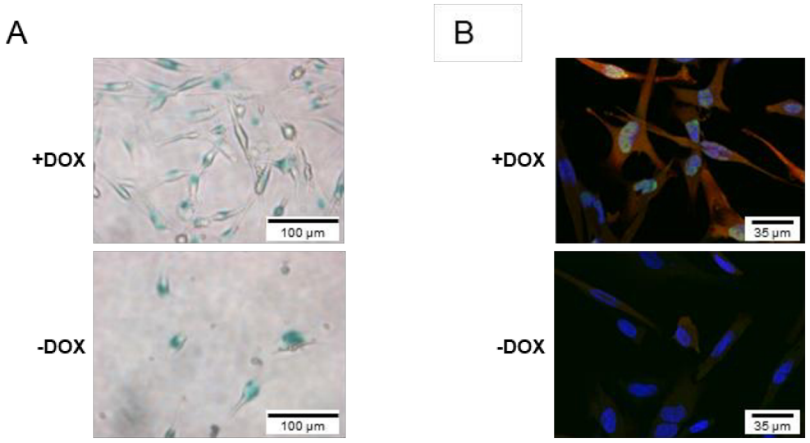

Figure 20: Further markers for OIS in DKFZ-BT66 cells. Adapted from Selt *et al.* (31). A) Staining for SA-ß-Gal in DKFZ-BT66 cells cultured with doxycycline (+DOX) versus untreated (-DOX) at day 5. B) Staining for senescence-associated heterochromatin foci (SAHF) by DAPI (blue) and staining for SV40-TAg (green) in DKFZ-BT66 cells cultured with (+DOX) or without (-DOX) doxycycline at day 5.

In summary, once doxycycline is withdrawn from the medium DKFZ-BT66 cells enter senescence, as indicated by growth arrest with a G0/G1 cell cycle arrest and the typical enlarged morphology. Other markers of OIS cannot be determined either due to restrictions resulting from the model, such as p53 manipulation resulting in expression changes of CDKN1A, or are not reversible by SV40-TAg expression, such as CDKN2A, SAHF or SA-ß-Gal. The time point of five days after doxycycline withdrawal was determined as the OIS state, as it coincides with significant differences in cell count, degradation of SV40-TAg protein, restored CDKN1A transcription (as measure of loss of SV40-Tag mediated p53 suppression) and cell cycle arrest.

3.2.2 Expression of the SASP in DKFZ-BT66 cells and primary PA

To further characterize the OIS state, the expression of the SASP, another senescence marker, was determined in DKFZ-BT66 cells. A SASP gene set was previously defined by Coppé, but may vary depending on cell type, oncogene and a variety of other factors (87). When comparing the mRNA expression of the SASP factors in the proliferating to the senescent condition of DKFZ-BT66 cells by gene expression microarrays, a significant upregulation of the SASP was observed in the OIS state overall (Fig. 21A), and n=38/62 (61%) of the analyzed SASP factors were significantly elevated (Fig. 21B). Presence of the SASP in PA could further be confirmed by examining the mRNA expression of the same gene set in human PA tumor samples (n=182) in comparison to normal fetal brain samples (n=5). In human PA patient samples the SASP genes were significantly upregulated in comparison to normal brain (Fig. 21C). An *in vivo* PA mouse model, induced by expression of the $BRAF^{V600E}$ mutation in neural progenitor cells

(2.2.5.3) (24), was investigated for SASP expression as well. The SASP was also significantly upregulated in the murine PA model (n=8) in comparison to normal brain of mice of the same age (n=8) (Fig. 21D).

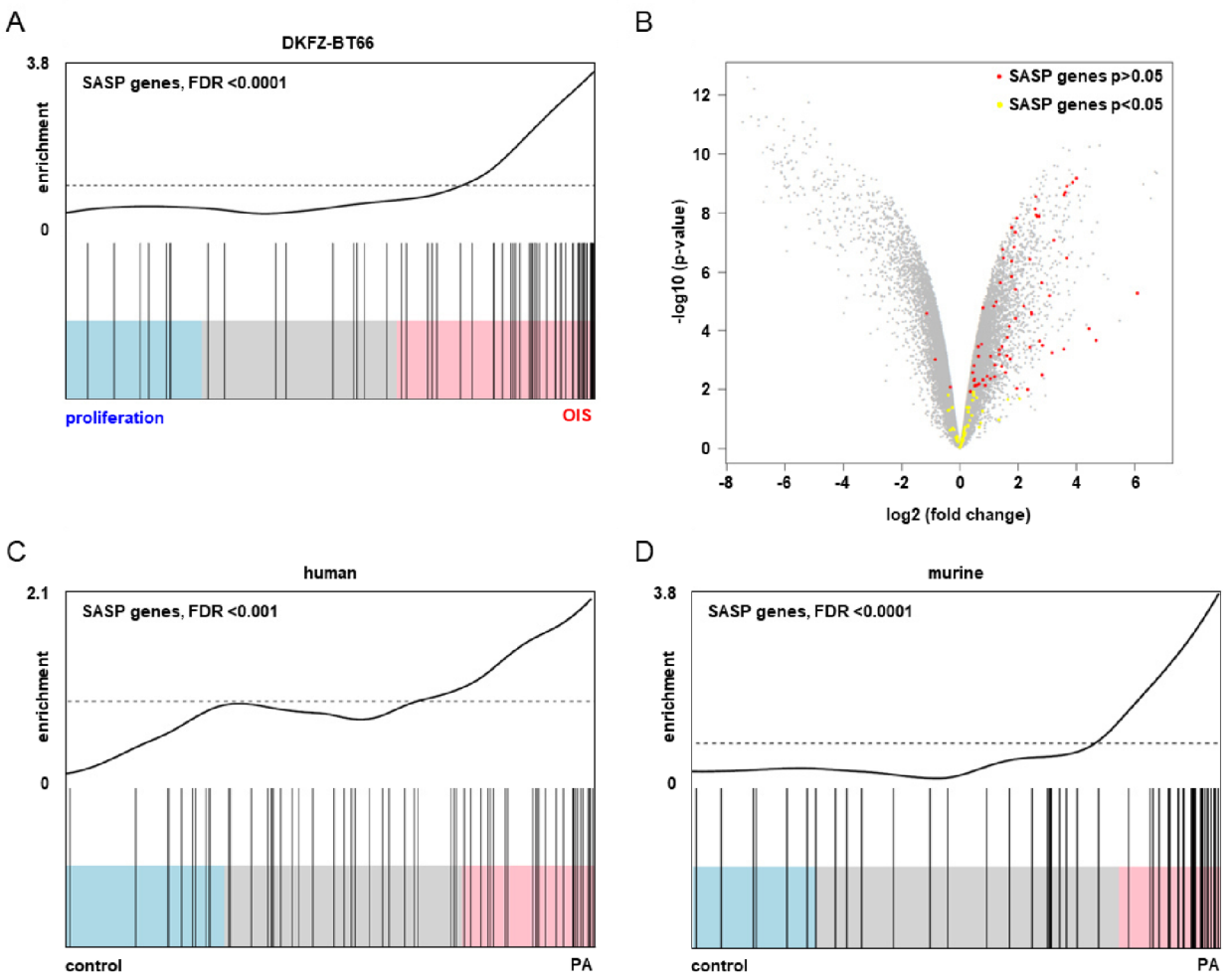

Figure 21: SASP factors are upregulated in pilocytic astrocytoma cells. From Buhl *et al.* (150). A) Barcode plot of gene set enrichment analysis (GSEA) depicting significant upregulation of the SASP genes in DKFZ-BT66 cells in OIS versus proliferation. B) Volcano plot depicting all probe sets regulated in DKFZ-BT66 during OIS, as compared to proliferation. C) Barcode plot of GSEA depicting significant upregulation of the SASP genes in PA patient samples (n=182) versus fetal normal brain (n=5). D) Barcode plot of GSEA depicting significant upregulation of the SASP genes in the murine PA model (n=8) versus normal brain of healthy mice of the same age (n=8).

The secretion and activity of the SASP as an inductor of senescence was investigated by conditioned medium (CM) experiments (2.2.1.7). CM of either senescent or proliferating DKFZ-BT66 cells was supplemented with doxycycline and added to proliferating DKFZ-BT66 cells. Treatment with CM of senescent cells for 20 days resulted in significant growth arrest of proliferating DKFZ-BT66 cells. In comparison, cells treated with CM of proliferating cells continued to grow (Fig. 22A). The cell morphology of DKFZ-BT66 cells treated with CM of senescent cells was altered to the senescent-

characteristic enlarged, flat cell shape (Fig. 22B). These data indicate that the SASP is secreted by senescent DKFZ-BT66 cells and active in the CM.

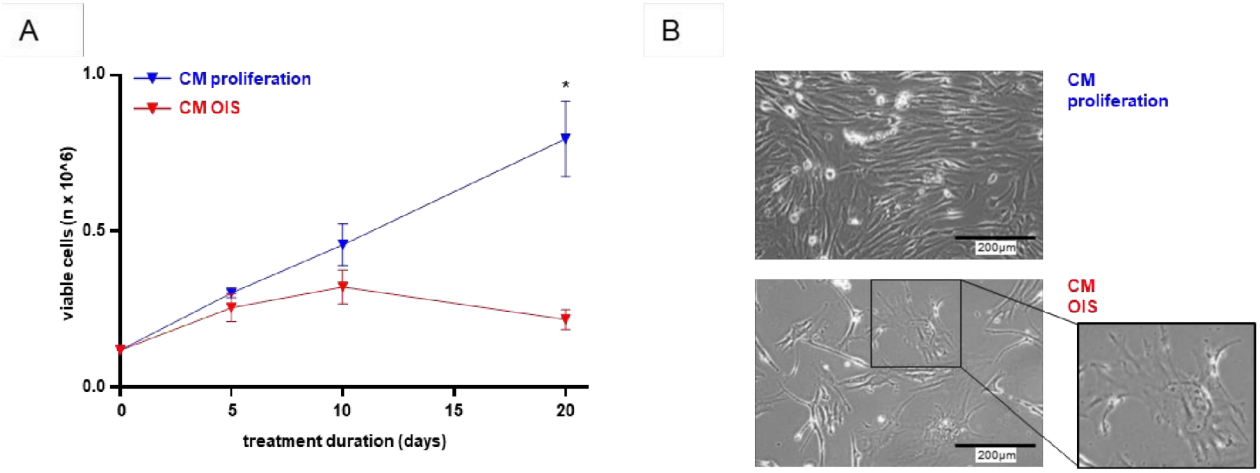

Figure 22: Secreted factors of senescent DKFZ-BT66 cells induce growth arrest. From Buhl *et al.* (150). A) Cell count of proliferating DKFZ-BT66 cells treated with conditioned medium (CM) every second day from DKFZ-BT66 cells in proliferation (blue) or OIS (red), supplemented with doxycycline (1 µg/mL) for 20 days. Depicted are mean +/- SD of three independent experiments. Significant differences are indicated as * $p<0.05$ (Student´s t-Test). B) Light microscopic comparison of DKFZ-BT66 cells grown under CM from proliferating or senescent (OIS) DKFZ-BT66 cells (as in A) at day 20.

Overall, elevated mRNA expression of the SASP was detected in human and murine PA tumors. Factors secreted from senescent PA cells in CM induced a senescent phenotype, as indicated by growth arrest and the senescence-characteristic cell morphology.

3.3 Identification of SASP candidate genes controlling OIS in PA

SASP factor composition differs depending on cell type and mechanism of OIS induction (66). Therefore, SASP candidate genes specific for pediatric PA were investigated.

3.3.1 Identifying OIS-controlling putative SASP candidate genes in PA

OIS-controlling SASP genes in PA were identified by generating three OIS-specific datasets (Step 1), screening for upregulated expression of those factors in human PAs versus normal brain (Step 2), with the resulting consensus genes filtered for druggability (Step 3) (Fig. 23A).

The first OIS-specific dataset (“SASP genes”) utilized for step1 (Fig. 23A) was the published SASP gene set (n=62) defined by Coppé (87). The second OIS-specific dataset (“Published OIS genes”, Fig. 23A) was

generated from publicly available gene expression datasets (n=6) by comparing gene expression from experiments conducted in human OIS models to their cycling counterparts. The analyzed OIS models were generated by overexpression of either mutated *BRAF* or *RAS* in fibroblasts or melanocytes. Therefore, the gene list represents OIS-specific genes detected in independent OIS models. By comparing the six analyzed datasets via rank product analysis, a list of n=332 genes specifically upregulated during OIS was generated. The third OIS-specific dataset ("Top IPA pathway genes", Fig. 23A) was generated by analyzing the dataset "Published OIS genes" using the software "Ingenuity Pathway Analysis" (IPA) for the top upregulated pathways. The upregulated pathways in the "Published OIS genes" were all related to inflammation. In total, the overlap of all genes relevant to the single pathways, resulted in a list of n=36 genes (Fig. 23A). This list additionally adds all genes related to pathways upregulated in OIS, which may not have been included in the single gene analysis. To identify which OIS genes are specifically relevant in PA, the three OIS-specific datasets ("SASP genes", "Published OIS genes", "Top IPA pathway genes") were screened for elevated expression in primary PA samples (n=182) versus normal fetal brain samples (n=5) in step 2 (Fig. 23A). In the final step 3, the consensus genes of all three lists were filtered for targetability with a small molecule inhibitor or antibody (Fig. 23A). This enabled to filter for therapeutically relevant targets.

The three final OIS-controlling candidate genes identified with this approach were *IL1B, IL6* and *TNFRSF1B* (Fig. 23A,B). The expression of the three candidate genes was also significantly upregulated in the murine PA model (24) in comparison to healthy brain of mice of the same age (Fig. 23C). In addition, the gene expression of all candidates was significantly upregulated during the senescent condition of the DKFZ-BT66 cell line compared to its proliferating state (Fig. 23D).

In summary, three SASP candidate genes were identified which are upregulated on mRNA level in murine as well as human PA cells.

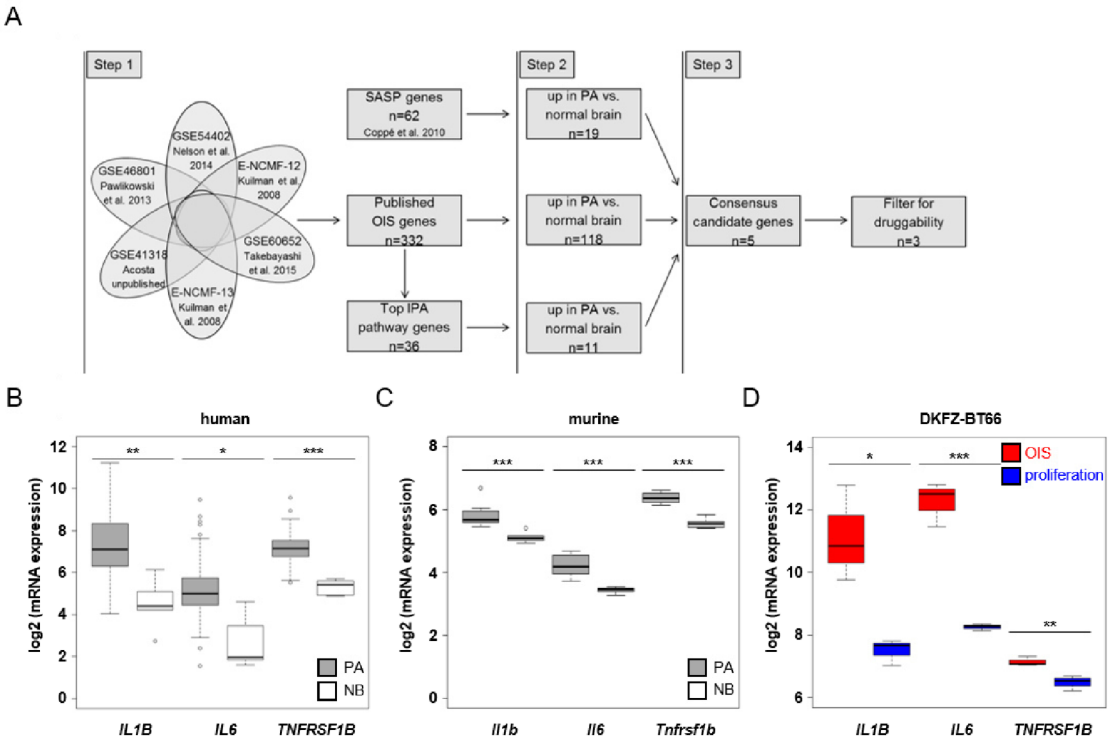

Figure 23: Identification of OIS-controlling putative SASP candidate genes in pediatric pilocytic astrocytoma. From Buhl *et al.* (150). A) Graphical workflow: in step 1, OIS-controlling candidate genes were identified from published SASP factors (n=62), from publicly available OIS datasets (n=332), and related upregulated IPA pathway genes (n=36). In Step 2, the candidate gene lists were screened for genes upregulated in primary PA, as compared to normal brain. In step 3, a final OIS-controlling candidate gene list was generated by filtering for consensus in all three datasets and for druggability (n=3). B) Boxplot of log2 mRNA expression of the final OIS-controlling candidate genes in primary PAs (n=182, grey) versus normal brain (NB) (n=5, white). Depicted are median (black bar), quartiles (box), median +/- 1.5 IQR (interquartile range) (whiskers), and outliers (circles). C) Boxplot of log2 mRNA expression of OIS-controlling candidate genes in the murine PA model (n=8, grey) versus normal brain (NB) of healthy control mice (n=8, white). Depicted are median (black bar), quartiles (box), median +/- 1.5 IQR (interquartile range) (whiskers), and outliers (circles). D) Boxplot of log2 mRNA expression of OIS-controlling candidate genes in DKFZ-BT66 cells in OIS (n=3, red) versus proliferation (n=3, blue), as measured by gene expression profiling. Depicted are median (black bar), quartile (box) and median +/- IQR (whiskers). Significant differences are indicated as * p<0.05; ** p<0.01; *** p<0.001 (Student´s t-Test).

3.3.2 Verifying SASP candidate genes in DKFZ-BT66 cells

This result was validated by RT-qPCR in DKFZ-BT66 cells upon withdrawal of doxycycline for ten days to induce OIS. Upregulation of both *IL1B* and *IL6,* but not of *TNFRSF1B,* was validated on mRNA level during OIS induction (Fig. 24A). Therefore *IL1B* and *IL6* were chosen as SASP candidate genes in PA for all further analyses. The increased secretion of IL1B and IL6 protein during induction of OIS could be validated using an IL1B and IL6 specific ELISA. Elevated protein levels of both cytokines were detected in cell culture medium of DKFZ-BT66 cells driven into OIS (Fig. 24B).

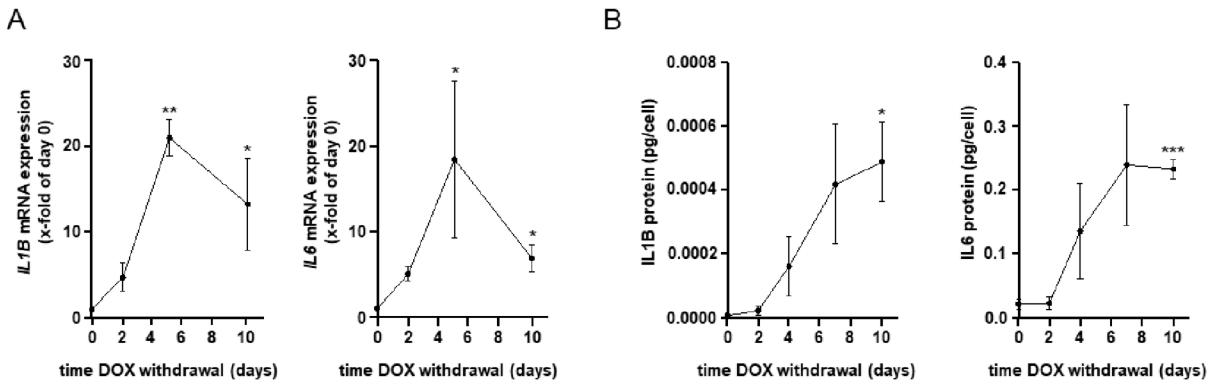

Figure 24: Identification of IL1B and IL6 as OIS-controlling SASP candidate genes in pediatric pilocytic astrocytoma. From Buhl *et al.* (150). A) Fold change of *IL1B* and *IL6* transcript levels measured by RT-qPCR during induction of OIS in DKFZ-BT66 cells in comparison to expression levels of DKFZ-BT66 cells in proliferation (=day 0). Depicted are mean +/- SD of three independent experiments. B) IL1B and IL6 protein secretion measured in the supernatant of DKFZ-BT66 cells upon OIS induction by ELISA. Concentration was normalized to cell number on the day of collection (pg/cell). Depicted are mean +/- SD of three independent experiments. Significant differences are indicated as * p<0.05; ** p<0.01; *** p<0.001 (Student´s t-Test).

In summary, IL1B and IL6 are significantly upregulated in human and murine PA samples in comparison to normal brain and are upregulated and secreted during the senescent state of PA cells, suggesting they are indeed SASP candidates in PA. Both cytokines have already been described to be relevant for induction as well as maintenance of OIS in several OIS models, suggesting that they are both important regulators of OIS (46,50,66,80,151,152). Analysis of the role of OIS in PA was therefore pursued with the two SASP candidate genes IL1B and IL6.

3.3.3 Protein expression of SASP candidate genes in primary PA

To further prove presence of the identified cytokines IL1B and IL6 in primary pediatric PA, their protein expression was determined together with n=12 other SASP factors in a multiplex assay (Fig. 25A). All analyzed SASP factors, including IL1B and IL6, were detectable in n=22 fresh frozen PA samples. As control only one fresh frozen normal fetal brain sample could be acquired, accordingly no statistical comparison could be conducted. In addition, an attempt was made to determine the presence of the cytokine receptors IL1R1 and IL6R on protein level in primary PA sections by immunohistochemistry. Only the IHC for IL6R could be established, but presence of the receptor was only detected in 1 out of n=14 PA samples (Fig. 25B). The IHC for IL1R1 was not successful. Even though three antibodies for IL1R1 were systematically tested under several conditions, a specific staining for the IL1R1 could not be established. CDKN2A expression could be observed in the analyzed PA samples, as described by Jacob *et al.* previously (19). In addition, positivity for Ki67 staining was low as expected (Fig. 25B) (144). Leukocyte

common antigen (LCA, also known as CD45) staining was conducted to identify immune cells, which may have elevated cytokine receptor expression (Fig. 25B). In summary, both cytokines IL1B and IL6 could be detected on protein level in primary PA samples, indicating the presence of the SASP in primary PA. A pattern of CDKN2A positivity and low proliferation index was observed, typical for PA in OIS.

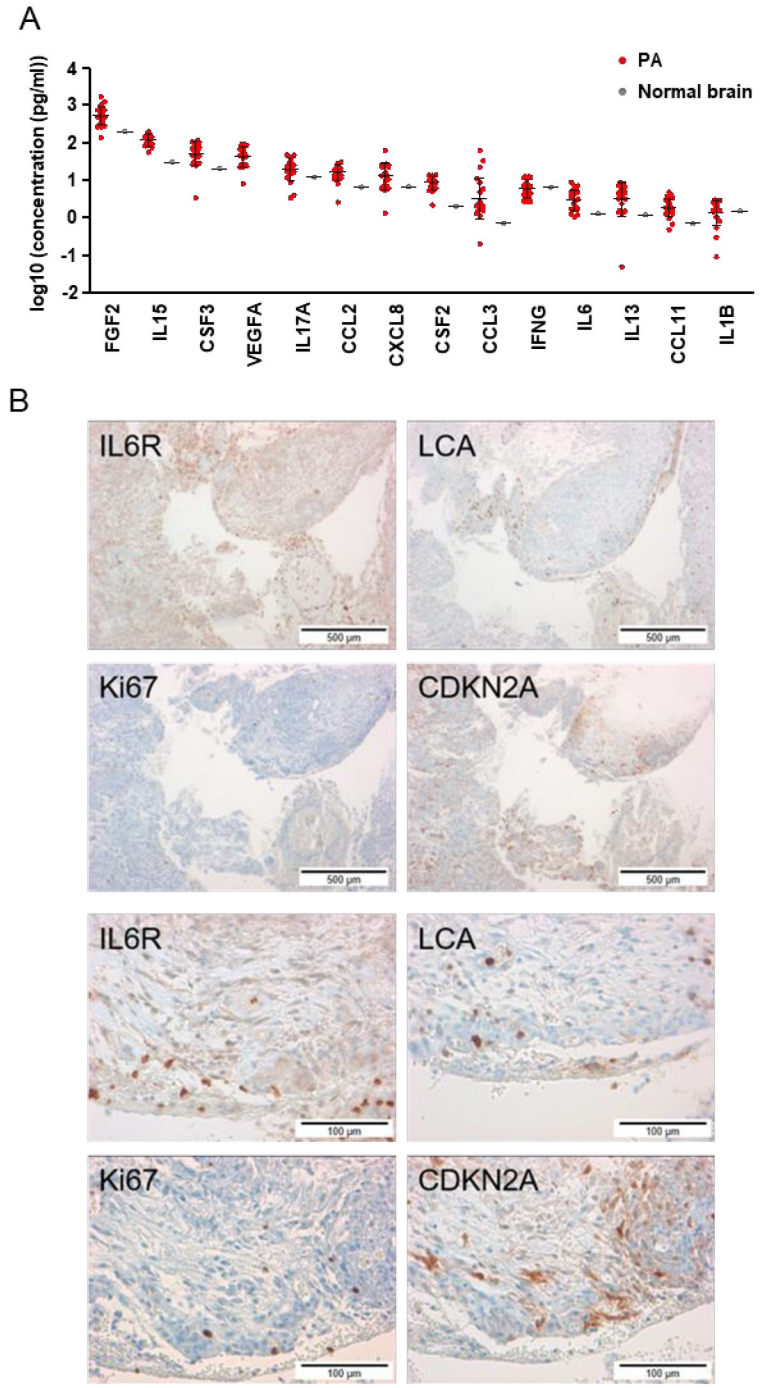

Figure 25: SASP factors are detectable on protein level in primary pediatric PA. A) Multiplex assay including 14 SASP factors, conducted in n=22 fresh frozen primary PA samples (red) and n=1 normal fetal brain sample (grey) showing presence of all 14

SASP factors on protein level in every PA sample. VEGFA is not expressed to a detectable level in the fetal brain sample. Depicted is mean +/- SD. Dots indicate values of individual samples. B) Protein expression of IL6R, Ki67, LCA and CDKN2A determined by immunohistochemistry (brown staining) in a PA sample of a 4-year old, male patient. The tumor was located in the cerebellum and positive for the *KIAA:BRAF* fusion. Scale bar size 500 µm upper panel, 100 µm lower panel.

3.3.4 Validation of SASP candidate pathway activity

Presence of the cytokine receptors as well as activity the IL1B and IL6 signaling pathways was further investigated in the DKFZ-BT66 cell line. The IL1R1 was detectable on mRNA as well as protein level in DKFZ-BT66 cells, but was not regulated during induction of OIS (Fig. 26A,B). As described in 1.2.2.iii the IL1 signaling pathway is regulated by several mechanisms, but the IL1R1 receptor is rarely regulated in disease models (104,153). Downstream signaling of IL1B was investigated by detection of IRAK1 protein and phosphorylation of RELA. IRAK1 is degraded upon activation of the IL1 pathway (104). IRAK1 levels were gradually decreasing upon induction of OIS in DKFZ-BT66 cells (Fig. 26B). Phosphorylation of RELA, which is a known downstream target of IL1 and an important regulator of the SASP (89,107,154), increased during induction of OIS in DKFZ-BT66 cells (Fig. 26B). Overall, the IL1 pathway was found to be activated during the OIS state of the PA model DKFZ-BT66.

For the IL6 signaling pathway expression of the IL6Ra was determined by RT-qPCR as well as western blot. While the IL6Ra was expressed, but not regulated on mRNA level, its protein levels decreased once DKFZ-BT66 cells were driven into OIS (Fig. 26C,D). As described in 1.2.2 iv, the IL6Ra is internalized and degraded upon continuous activation of the IL6 pathway as a negative feedback regulation (120). A further indication for activation of the negative feedback mechanism was the decreasing level of phosphorylated STAT3 (Fig. 26D). While the downstream target STAT3 is phosphorylated within minutes after IL6 signal activation (115), long-term activation of the pathway results in downregulation of pSTAT3 (121). As observed in the ELISA (Fig. 24B), IL6 was secreted over a course of several days. In summary, downregulation of the IL6 pathway was observed during OIS induction of DKFZ-BT66 cells, in line with a negative feedback loop during long-term stimulation with IL6.

Taken together, the data indicates that both pathways, IL1B and IL6, are regulated during OIS in DKFZ-BT66 cells. The IL1 pathway, which induces its own activation via a positive feedback loop (107), stays active during IL1B secretion in senescent DKFZ-BT66 cells, while the IL6 pathway is regulated by a negative feedback mechanism.

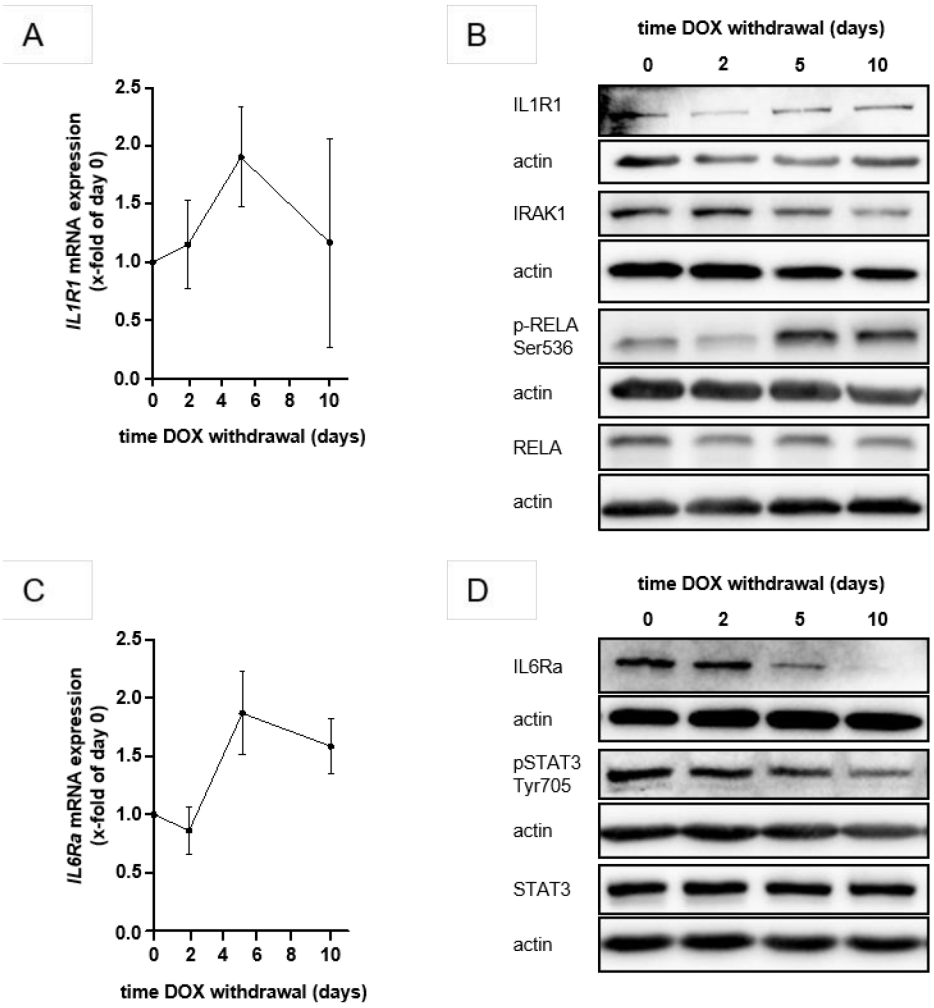

Figure 26: Functional validation of the IL1 and IL6 signaling pathway during OIS. From Buhl *et al.* (150). A) Fold change of *IL1R1* transcript levels were measured by RT-qPCR in DKFZ-BT66 upon OIS induction relative to levels during proliferation (=day 0). Depicted are mean +/- SD of three independent experiments. B) IL1 pathway activity was determined by protein levels of IL1R1, IRAK1, phospho-RELA and RELA in DKFZ-BT66 upon OIS induction measured by western blot. Actin serves as loading control. C) Fold change of *IL6Ra* transcript levels as measured by RT-qPCR in DKFZ-BT66 upon OIS induction relative to levels during proliferation (=day 0). Depicted are mean +/- SD of three independent experiments. D) IL6 pathway activity was determined by protein levels of IL6Ra and pSTAT3/STAT3 upon OIS induction measured by western blot. Actin serves as loading control.

3.4 Examination of the regulation of OIS by SASP factors

3.4.1 The role of the SASP candidate genes in OIS induction

Up to now, presence of the two cytokines IL1B and IL6 was detected in primary PA, the cytokines were shown to be secreted by senescent PA cells and their respective pathways were regulated during induction of OIS in DKFZ-BT66 cells. As observed in the CM experiments, the secreted SASP factors were able to induce growth arrest of proliferating PA cells. The role of both cytokines for induction of growth arrest, and subsequent OIS, was now determined by recombinant cytokine treatments. The IL1 pathway was actively stimulated by addition of increasing concentrations of rIL1B to proliferating DKFZ-BT66 cells (Fig. 27A,B). A concentration dependent reduction in cell growth was observed after 20 days of rIL1B treatment (Fig. 27A). A significant reduction of growth was observed starting from concentrations of 100 pg/mL rIL1B. At the same concentration, the IL1 pathway was activated, as evident by a considerable decrease in IRAK1 levels and an increase in the precursor version of IL1B, pro-IL1B (Fig. 27B). The latter results from positive feedback activation, by which IL1B initiates its own transcription and expression (155). The direct correlation between cell growth and IL1 pathway activation can be deduced from the maximum effects being observed at the same concentration of rIL1B (100 pg/mL).

However, when proliferating DKFZ-BT66 cells were treated with rIL6 instead of rIL1B, no effect on cell growth was observed (Fig. 27C). Short-term treatment with rIL6 actively stimulated the IL6 pathway, evident by increased phosphorylation of STAT3 in a concentration dependent manner (Fig. 27D). In an attempt to recapitulate the effects of the SASP, which is a complex mixture of multiple inflammatory factors, a combination treatment of both cytokines was conducted. However, no additional effect on cell counts by the treatment with a combination of rIL1B plus increasing rIL6 concentrations could be observed (Fig. 27E). Therefore, only IL1B significantly reduced cell growth in contrast to rIL6.

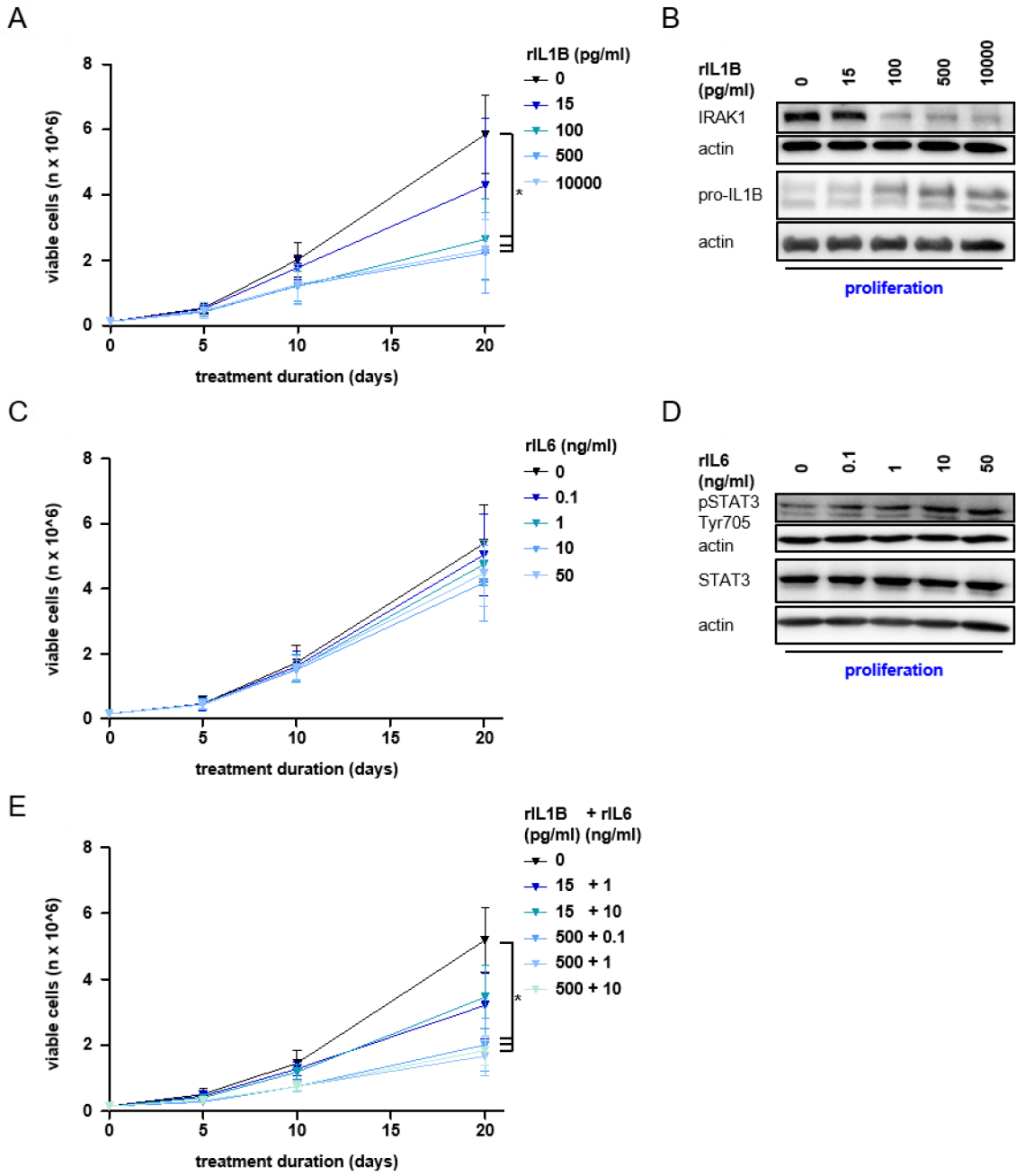

Figure 27: IL1B signaling contributes to reduced PA cell proliferation. From Buhl *et al.* (150). A) Cell count of proliferating DKFZ-BT66 cells under rIL1B treatment in the concentrations indicated for 20 days. Depicted are mean +/- SD of three independent experiments. Significant differences are indicated as * $p<0.05$ (Student´s t-Test). B) Protein levels of IRAK1 and pro-IL1B were determined by western blot under stimulation with rIL1B in the depicted concentrations for 4 hours in DKFZ-BT66 cells in proliferation. Actin serves as loading control. C) Cell count of proliferating DKFZ-BT66 cells under rIL6 treatment in the concentrations indicated for 20 days. Depicted are mean +/- SD of three independent experiments. D) Protein levels of pSTAT3 and STAT3 were determined by western blot under stimulation with rIL6 in the depicted concentrations for 15 minutes in DKFZ-BT66 cells in proliferation. Actin serves as loading control. E) Cell count under combination treatment with rIL1B and rIL6 in the depicted concentrations for 20 days. Depicted are mean +/- SD of three independent experiments. Significant differences are indicated as * $p<0.05$ (Student´s t-Test).

The effect of rIL1B on PA cells was further characterized and analyzed for markers of OIS, such as cell morphology and SASP factor expression.

In order to exclude confounding factors responsible for the reduction in cell numbers upon rIL1B treatment, such as cell death or SV40-TAg downregulation, viability and protein expression was determined. Measurement of cell viability indicated that the reduction of cell growth did not result from cell death under treatment (Fig. 28A). Neither did the reduction in cell proliferation originate from reduced levels of SV40-TAg protein expression, as shown by steady protein levels of SV40-TAg (Fig. 28B). SV40-TAg signaling remained active, as proven by continuous absence of CDKN1A protein (Fig. 28B). The IL1 pathway was activated by rIL1B treatment for the entire duration of the 20 day treatment, as evident by IRAK1 degradation (Fig. 28B). IL1, part of the described SASP factors (87), has been described as a major regulator of the SASP itself previously (50), in a positive feedback manner. In line with this, treatment of proliferating DKFZ-BT66 cells with rIL1B significantly induced gene expression of the SASP factors in comparison to untreated cells (Fig. 28C). Finally, rIL1B treatment altered the shape of proliferating DKFZ-BT66 cells to an enlarged, flat morphology characteristic for senescence (Fig. 28D).

In summary, this data indicates that IL1B reduces growth of proliferating PA cells, induces expression of the SASP as well as changes in morphology typical for OIS. Concluding from this, the SASP factor IL1 plays a major role in inducing OIS in PA.

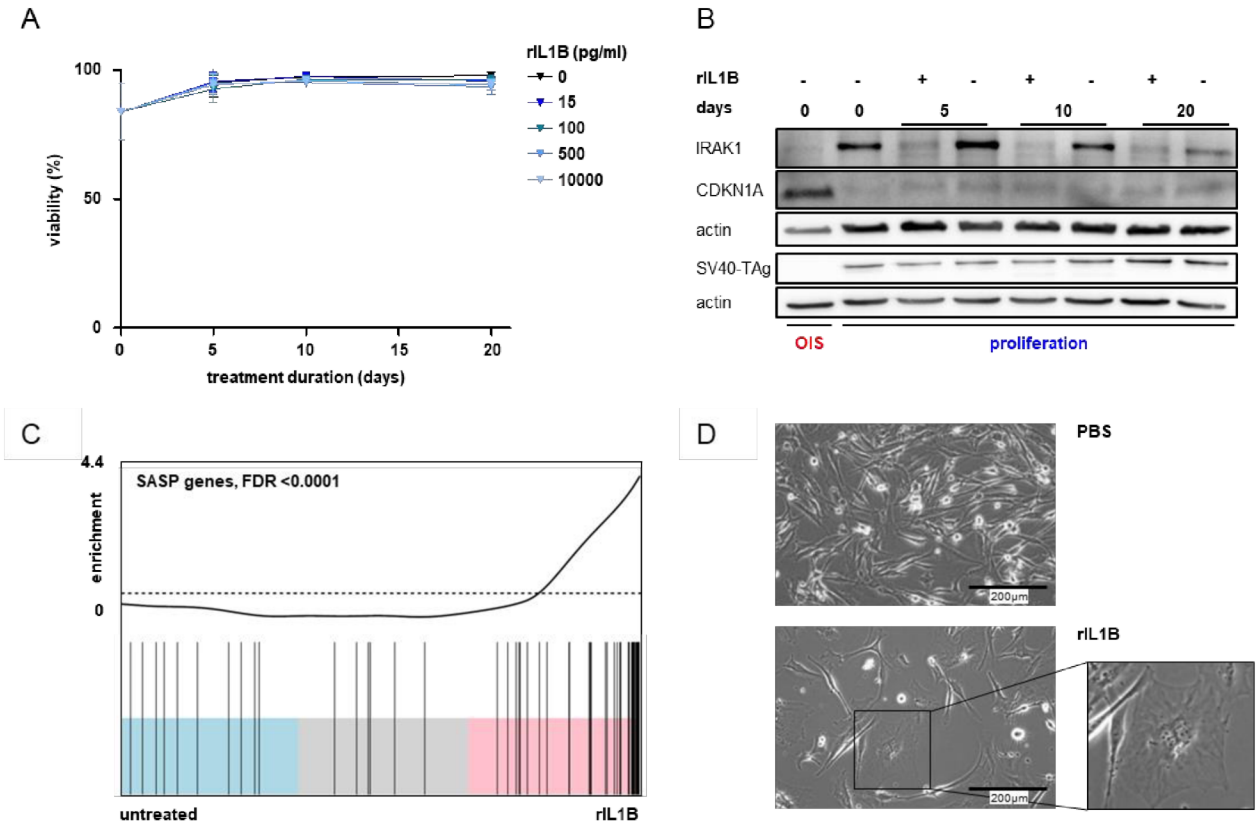

Figure 28: IL1B signaling induces expression of SASP factors and other markers of OIS. Adapted from Buhl *et al.* (150). A) Viability, determined by automated trypan blue exclusion staining, of proliferating DKFZ-BT66 cells (+ DOX) under rIL1B treatment in the concentrations indicated for 20 days. Depicted are mean +/- SD of three independent experiments. B) Protein levels of IRAK1, CDKN1A and SV40-TAg measured by western blot after long-term treatment with rIL1B (500 pg/mL) (+) for 0, 5, 10 and 20 days versus solvent control (-) treatment in DKFZ-BT66 in proliferation (+ DOX). Actin serves as loading control. C) Barcode plot of GSEA depicting significant upregulation of the SASP genes in DKFZ-BT66 cells under treatment with 500 pg/mL rIL1B and doxycycline for five days versus DKFZ-BT66 cells in proliferation. D) Light microscopic comparison of proliferating DKFZ-BT66 cells (+ DOX) grown under treatment with 500 pg/mL rIL1B versus solvent control at day 20.

3.4.2 The role of the SASP candidates for OIS maintenance

3.4.2.1 Pharmacological inhibition of SASP candidate pathways

After showing the relevance of cytokines for induction of OIS, next, the role of IL1 and IL6 in OIS maintenance was assessed via pharmacological inhibition of both pathways. Senescent DKFZ-BT66 cells were treated with neutralizing antibodies targeting the cytokines directly or their respective receptors.

The IL1 pathway was targeted with anakinra, a recombinant antagonist of the IL1 receptor. After doxycycline withdrawal for five days, treatment was initiated, but the resulting growth arrest could not be circumvented by treatment with anakinra, as determined by cell counts conducted over the course of 20 days (Fig. 29A). IL1 signaling was sufficiently inhibited even under co-treatment of rIL1B and anakinra,

as determined by rescued IRAK1, reduced pro-IL1B and reduced p-RELA protein levels (Fig. 29B). As anakinra did not exert any effect on cell growth, a neutralizing IL1B antibody was tested in addition. When comparing the effect of anakinra versus anti-IL1B treatment, the neutralizing antibody did not rescue IRAK1 levels to the same extent as anakinra (Fig. 29C). For this reason, the neutralizing antibody leading to only partial suppression of IL1 signaling was not tested in cell count experiments, since even the full abrogation of IL1 signaling by anakinra did not affect cell growth. The effect of anakinra was further tested in a rescue experiment treating proliferating DKFZ-BT66 cells with rIL1B +/- anakinra for 20 days. The reduction in growth observed under rIL1B treatment could be rescued by anakinra (Fig. 29D). However, this effect was not statistically significant, due to high standard deviations in this experiment, resulting from combination of cell counts in early and late passages of DKFZ-BT66 cells. Overall, anakinra inhibits the IL1 pathway, can rescue growth arrest induced by rIL1B treatment, but cannot reverse OIS-induced growth arrest, suggesting that OIS in PA cells is maintained not by IL1B alone.

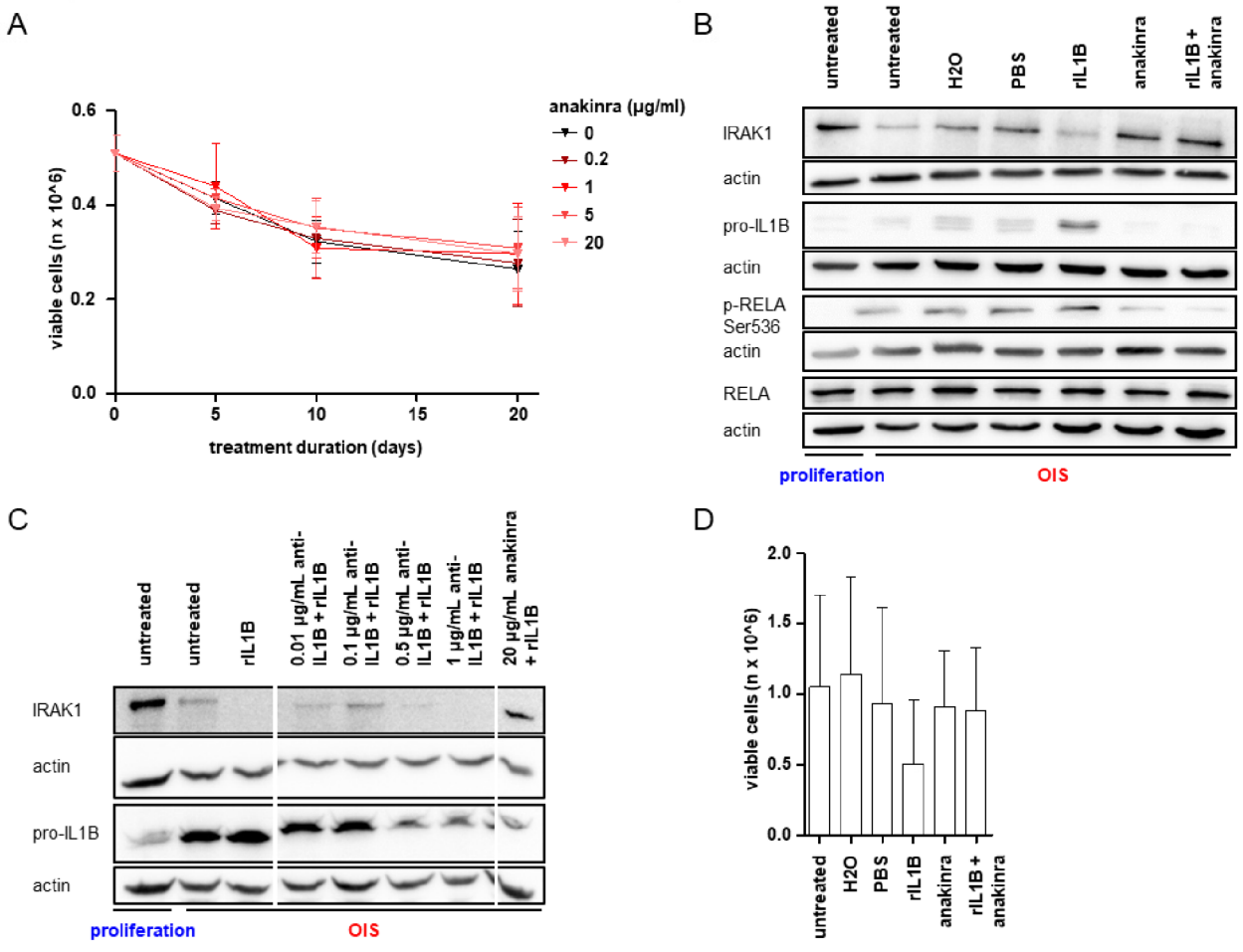

Figure 29: Inhibition of IL1 signaling during OIS does not bypass OIS. Adapted from Buhl *et al.* (150). A) Cell count of senescent DKFZ-BT66 cells under anakinra treatment in the depicted concentrations for 20 days. Cells were cultured without doxycycline 5 days prior to treatment as well as throughout the duration of the entire experiment. Shown are mean +/- SD of three independent experiments. B) Protein levels of IRAK1, pro-IL1B, p-RELA and RELA determined by western blot in DKFZ-BT66 cells in OIS treated with rIL1B (500 pg/mL) +/- anakinra (20 µg/mL) for 4 hours. Actin serves as loading control. C) Protein levels of IRAK1 and pro-IL1B determined by western blot in DKFZ-BT66 cells in OIS treated with rIL1B (500 pg/mL) + different concentrations of a neutralizing IL1B antibody (anti-IL1B) or + anakinra (20 µg/mL) for 4 hours. Actin serves as loading control. All samples were loaded on the same gel per antibody tested. The image was cut after development of the membrane to only show the relevant bands. D) Cell count at day 20 of senescent DKFZ-BT66 cells treated with rIL1B (500 pg/mL) +/- anakinra (20 µg/mL) for 20 days. Cells were cultured without doxycycline 5 days prior to treatment as well as throughout the duration of the entire experiment. Shown are mean +/- SD of three independent experiments.

A monoclonal antibody, tocilizumab, targeting the IL6Ra was used to inhibit IL6 signaling. Treatment of senescent DKFZ-BT66 cells with tocilizumab could not circumvent OIS-induced growth arrest (Fig. 30A), despite reliable suppression of IL6 signaling, as shown by rescued pSTAT3 levels during the OIS state even under co-treatment with rIL6 (Fig. 30B).

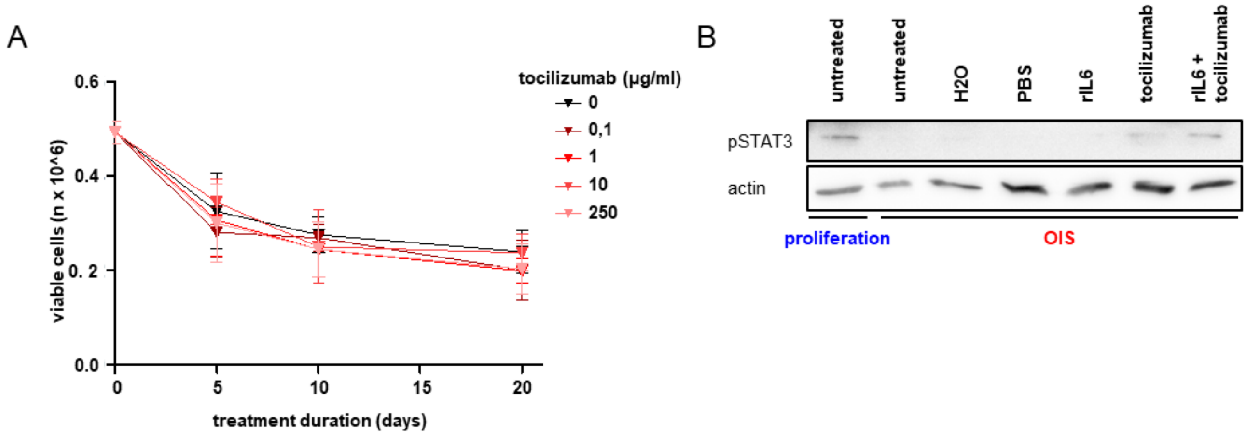

Figure 30: Inhibition of IL6 signaling during OIS does not bypass OIS. A) Cell count of senescent DKFZ-BT66 cells under tocilizumab treatment in the depicted concentrations for 20 days. Cells were cultured without doxycycline 5 days prior to treatment as well as throughout the duration of the entire experiment. Shown are mean +/- SD of three independent experiments. B) Protein levels pSTAT3 determined by western blot in DKFZ-BT66 cells in OIS treated with rIL6 (50 ng/mL) +/- tocilizumab (250 µg/mL) for 4 hours. Actin serves as loading control.

In conclusion, pharmacological inhibition of the IL1 or the IL6 pathway alone cannot bypass OIS in the PA model DKFZ-B66, as has been reported in other OIS models by others (46).

3.4.2.2 shRNA-mediated knock-down of SASP candidate pathways

To further investigate the role of the IL1 and IL6 pathway for OIS maintenance, enhanced inhibition of the cytokine pathways was attemtped with a stable knock-down.

For this purpose, the DKFZ-BT66 hTERT cell line was used to avoid replicative senescence occuring during the long-term process of stable transduction. Transduction with hTERT did not interfere with the onset of OIS once doxycycline was withdrawn and SV40-TAg was inactivated (Fig. 31).

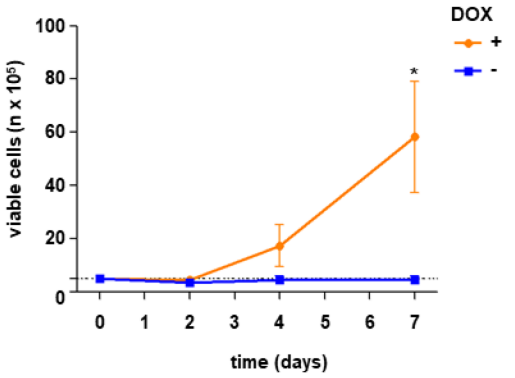

Figure 31: DKFZ-BT66 hTERT cell count upon doxycycline withdrawal. Adapted from Selt *et al.* (31). Cell count of DKFZ-BT66 hTERT cells under treatment with doxycycline (+ DOX) or without (- DOX) for one week. Depicted are mean +/- SD of three independent experiments. Significant differences are indicated as * p<0.05 (Student´s t-Test). The dashed line represents the number of cells seeded at day 0.

A lentiviral shRNA system was utilized to achieve knock-down using three shRNA constructs per cytokine. After lentiviral transduction cells were sorted for GFP by fluorescence activated cell sorting, which was encoded as a marker on the shRNA constructs. The mRNA level of both cytokines was not decreased to a significant level, indicating that the knock-down efficiency was low (Fig. 32A,B). In a cell count conducted with the transduced DKFZ-BT66 hTERT cells in OIS, none of the transduced cells showed increased growth after 20 days (Fig. 32C). Concluding from this, the attempt of knocking-down the soluble cytokines was not successful.

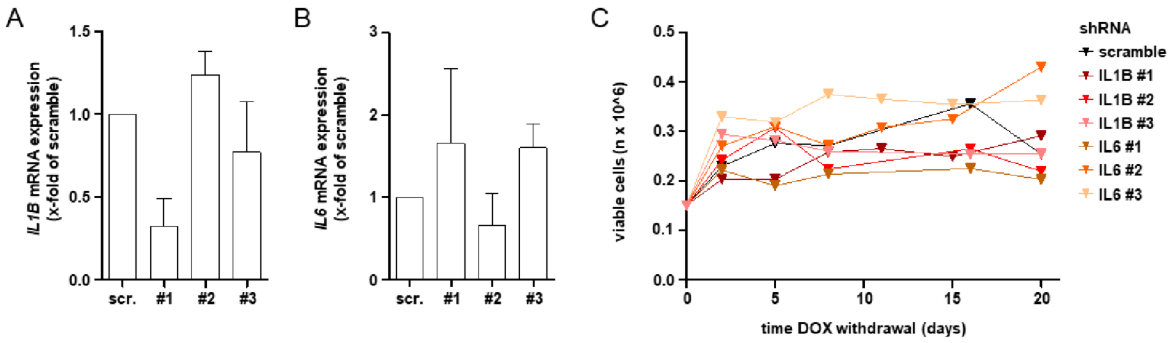

Figure 32: Attempt of a stable knock-down of IL1B and IL6. A,B) Fold change of *IL1B* (A) and *IL6* (B) transcript levels measured by RT-qPCR in DKFZ-BT66 hTERT cells in OIS transduced with 3 shRNAs targeting IL1B or IL6 in comparison to cells transduced

with scramble (scr.) shRNA. Depicted are mean +/- SD of three independent experiments. C) Cell count of senescent DKFZ-BT66 hTERT cells transduced with the depicted shRNAs for 20 days. Shown is one experiment.

As the know-down of the cytokines was not successful, a stable knock-down of the two cytokine receptors was attempted. For this purpose, the DKFZ-BT66 hTERT cell line was transduced with three shRNA constructs per receptor and sorted for GFP expression, encoded on the shRNA constructs. The mRNA level of the receptor was significantly decreased for one of the shRNAs (#2) targeting *IL1R1* (Fig. 33A). For shIL1R1 #2, protein levels of the receptor were still detectable by western blot, but IRAK1 levels were slightly increased, indicating reduced IL1 signaling (Fig. 33B). For the IL6Ra, two shRNAs (#2 and #3) induced a significant reduction of *IL6Ra* mRNA levels (Fig. 33C). IL6Ra protein levels were reduced for shRNA #1 and #3, but not for constructs #2 (Fig. 33D), indicating a discrepancy between mRNA and protein expression. In a cell count conducted with the transduced DKFZ-BT66 hTERT cells in OIS, the cell line with shIL1R1 #2 showed increased growth after 20 days, but none of the other constructs induced a similar effect (Fig. 33E). To rule out off-target effects, the knock-down of *IL1R1* was repeated with three additional shRNA constructs (Fig. 33F-H). A significant decrease in *IL1R1* levels was achieved with constructs #1,2,4,5,6 (Fig. 33F). All shRNA constructs reduced the protein levels of IL1R1, but only #3-5 fully rescued IRAK1 degradation (Fig. 33G), again indicating a discrepancy between mRNA and protein expression. In a cell count conducted with the transduced, senescent DKFZ-BT66 hTERT cells for 30 days, none of the senescent cells started to regrow (Fig. 33H). Concluding from this, the observed effect in cells transduced with shRNA #2 targeting *IL1R1* most likely was an off-target effect, however it would be interesting to analyze the transduced cell line for additional mutations (e.g. by integration effects) to identify the OIS escape mechanism.

Knock-down of the cytokine receptors was partially successful, as evident from reduced mRNA and protein levels (with a discrepancy between mRNA and protein expression), but did not lead to bypass of OIS-induced growth arrest in DKFZ-BT66 cells, and the results remain inconclusive.

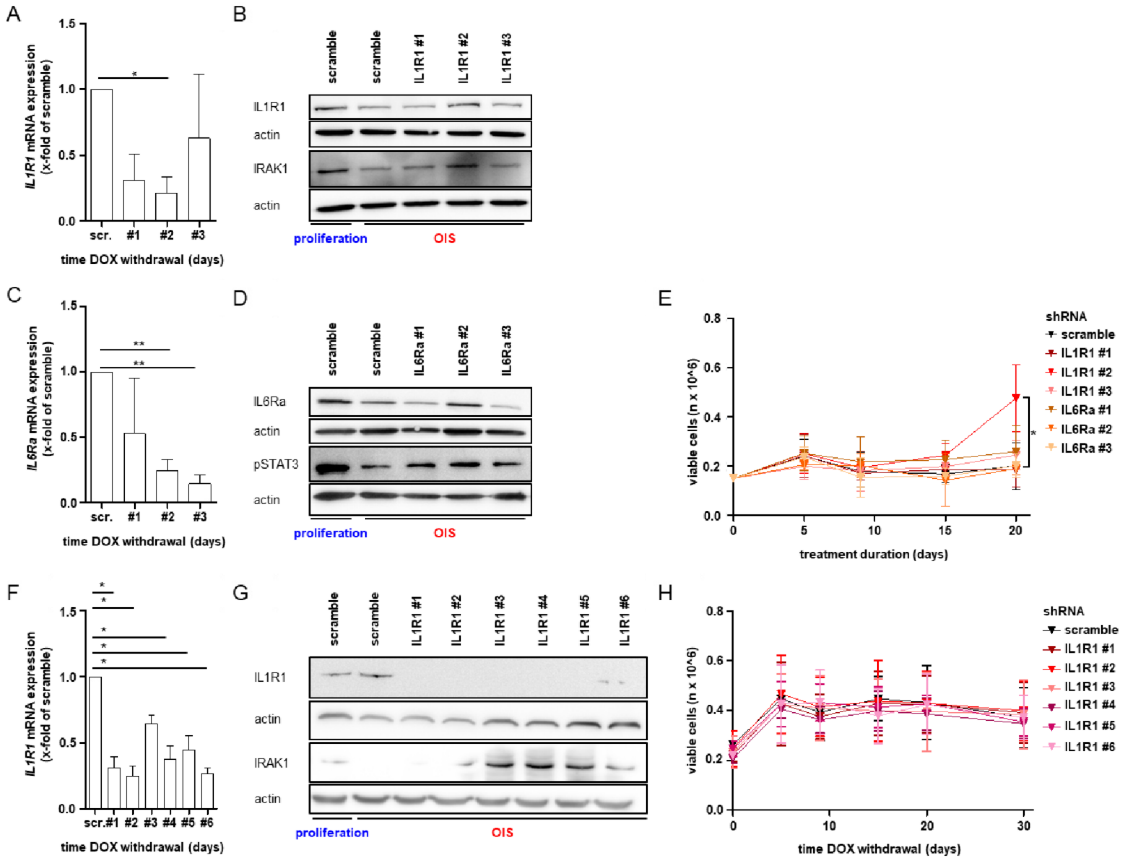

Figure 33: Attempt of a stable knock-down of IL1R1 and IL6Ra. A) Fold change of *IL1R1* transcript levels measured by RT-qPCR in DKFZ-BT66 hTERT cells in OIS transduced with three shRNAs targeting the *IL1R1* in comparison to cells transduced with scramble (scr.) shRNA. Depicted are mean +/- SD of three independent experiments. Significant differences are indicated as * p<0.05 (Student´s t-Test). B) IL1 pathway activity was determined by protein levels of IL1R1 and IRAK1 in DKFZ-BT66 hTERT in OIS measured by western blot. Actin serves as loading control. C) Fold change of *IL6Ra* transcript levels measured by RT-qPCR in DKFZ-BT66 hTERT cells in OIS transduced with three shRNAs targeting the *IL6Ra* in comparison to cells transduced with scramble (scr.) shRNA. Depicted are mean +/- SD of three independent experiments. Significant differences are indicated as ** p<0.01 (Student´s t-Test). D) IL6 pathway activity was determined by protein levels of IL6Ra and pSTAT3 in DKFZ-BT66 hTERT in OIS measured by western blot. Actin serves as loading control. E) Cell count of senescent DKFZ-BT66 hTERT cells transduced with the depicted shRNAs for 20 days. Shown are mean +/- SD of three independent experiments. Significant differences are indicated as * p<0.05 (Student´s t-Test). F) Fold change of *IL1R1* transcript levels measured by RT-qPCR in DKFZ-BT66 hTERT cells in OIS transduced with six shRNAs targeting the *IL1R1* in comparison to cells transduced with scramble (scr.) shRNA. Depicted are mean +/- SD of three independent experiments. Significant differences are indicated as * p<0.05 (Student´s t-Test). G) IL1 pathway activity was determined by protein levels of IL1R1 and IRAK1 in DKFZ-BT66 hTERT in OIS measured by western blot. Actin serves as loading control. H) Cell count of senescent DKFZ-BT66 hTERT cells transduced with the depicted shRNAs for 30 days. Shown are mean +/- SD of three independent experiments.

3.5 Translational relevance of the SASP in PA

3.5.1 Influence of anti-inflammatory treatment on DKFZ-BT66 cell growth

As the inhibition of single SASP factors did not allow bypass of growth arrest of senescent DKFZ-BT66 cells, treatment with the glucocorticoid dexamethasone, a broad anti-inflammatory drug, was tested. Glucocorticoids have previously been shown to inhibit multiple SASP factors (91,92,156). Senescent DKFZ-BT66 cells were treated with dexamethasone for 20 days. After five days, a significant increase in growth was detected in comparison to solvent-treated senescent cells (Fig. 34A). Exemplary for SASP signaling, the IL1 and IL6 pathway were both inhibited. IRAK1 levels were rescued under treatment with dexamethasone, indicative of IL1 pathway inhibition (Fig. 34B). In addition, increased levels of the IL6Ra and pSTAT3 were detectable under anti-inflammatory treatment (Fig. 34B). As the IL6Ra is degraded upon long-term IL6 secretion, presence of the receptor as well as pSTAT3 indicates inhibition of IL6 secretion and signaling. When comparing the gene expression of the SASP signature in senescent cells treated with dexamethasone for five days to untreated senescent cells, the SASP was significantly downregulated (Fig. 34C), confirming the previous description of glucocorticoids suppressing the SASP (91,92). Finally, on the basis of changes in gene expression under dexamethasone treatment versus untreated senescent DKFZ-BT66 cells, ingenuity pathway analysis predicted the inhibition of IL1B as the top upstream regulator of the shift in gene expression (Fig. 34D). Of note, IPA prediction of the top upstream regulators under dexamethasone treatment of senescent cells overlapped in 4/5 with the upstream regulators predicted under rIL1B treatment of proliferating DKFZ-BT66 cells, with regulation occurring in the opposite manner (Fig. 34D): four of the five top upstream regulators (*IL1B*, *TREM1*, *TNF*, NFκB complex) were identical, being inhibited by dexamethasone and activated under rIL1B treatment (appendix F). In conclusion, the growth reduction induced by rIL1B treatment seems to activate the same pathways that are inhibited under dexamethasone treatment during bypass of the OIS-related growth arrest.

In summary, treatment with dexamethasone induced regrowth of senescent cells, inhibited the SASP on gene expression level as well as the exemplary SASP signaling pathways, IL1 and IL6, on protein level. IL1B is indicated to be an important mediator of the gene expression changes observed under induction or bypass of growth arrest.

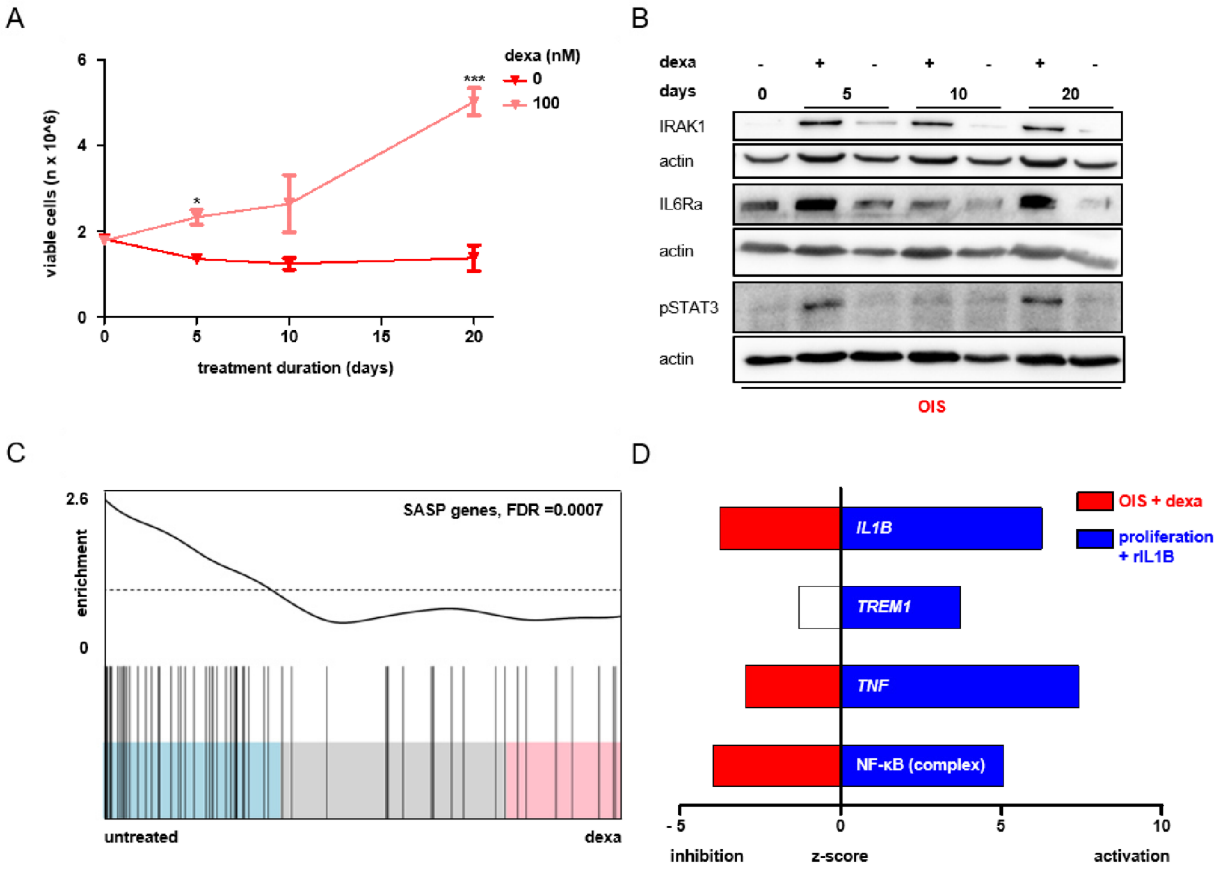

Figure 34: Inhibition of inflammatory signaling during OIS suppresses the SASP and leads to regrowth of senescent PA cells. Adapted from Buhl *et al.* (150). A) Cell count of senescent DKFZ-BT66 cells treated with 100 nM dexamethasone (dexa) or solvent control (0 nM dexa) for 20 days. Cells were cultured without doxycycline 5 days prior to treatment as well as throughout the duration of the entire experiment. Depicted are mean +/- SD of three independent experiments. Significant differences are indicated as * p<0.05, *** p<0.001 (Student´s t-Test). B) Protein levels of IRAK1, IL6Ra and pSTAT3 determined by western blot in DKFZ-BT66 cells in OIS treated with 100 nM dexamethasone (dexa) (+) or solvent control (-) for 0, 5, 10 and 20 days. Actin serves as loading control. C) Barcode plot of GSEA reveals significant downregulation of the SASP genes in DKFZ-BT66 cells in OIS under treatment with dexamethasone (dexa) for five days versus DKFZ-BT66 cells in OIS. D) IPA analysis of GEPs of DKFZ-BT66 cells in OIS treated with 100 nM dexamethasone (n=3 replicates) compared to proliferating DKFZ-BT66 cells (n=3 replicates) (red, OIS + dexa), or DKFZ-BT66 cells in proliferation treated with 500 pg/mL rIL1B (n=3 replicates) compared to DKFZ-BT66 cells in OIS (n=3 replicates) (blue, proliferation + rIL1B) for five days. The 4 common genes of the top 5 upstream regulators of each condition are displayed. The z-score predicts the activation status of the upstream regulator, positivity indicates activation, negativity indicates inhibition. Color indicates from which condition the z-score was calculated. White bar: z-score for *TREM1* in the OIS + dexa condition did not pass the threshold to indicate its inhibition/activation.

3.5.2 Correlation of SASP factor expression and clinical outcome

Considering that stimulation as well as inhibition of IL1B and the SASP were shown to effect growth of PA cells, the relevance of their expression for patient outcome was investigated. The unpredictable growth behavior, observed in PA patients, could be related to a SASP-dependent regulation of the OIS state. To test for a correlation between *IL1B* and SASP mRNA expression and clinical outcome, gene expression

data and annotations from the ICGC PedBrain PA cohort were utilized (n=112 patients, survival data available for 110/112 patients, annotations appendix E) (14).

First, the effect of *IL1B* was investigated by dividing the patient cohort in a “high *IL1B*” and “low *IL1B*” expression group according to median cut-off. A significant advantage in progression-free survival (PFS) could be observed for the “high *IL1B*” cohort (log-rank test) (Fig. 35A). 5-year PFS was significantly better in the “high *IL1B*” cohort with 85% compared to the “low *IL1B*” group with 46%. Patients with elevated *IL1B* expression had significantly better PFS, which was also true when examining *IL1B* expression as a continuous variable (HR=0.4, 95%CI 0.24-0.69, p=0.0008; n=110 patients, appendix G). *IL1B* remained a factor for favorable prognosis after multivariate analysis accounting for other relevant prognostic factors such as extend of tumor resection (HR=0.37, 95%CI 0.18-0.75, p=0.0056; n=90 patients, appendix H) or radiotherapy (HR=0.35, 95%CI 0.15-0.77, p=0.0079; n=75 patients, appendix I). As IL1B is not a specific factor for OIS and could be upregulated in pediatric patients for several reasons e.g. fever or infections, the expression of all SASP genes was analyzed in the same cohort.

To examine the relevance of the SASP on PFS, a score was calculated by summing up the expression values of all SASP genes per patient (SASP score). Patients with a higher SASP score (continuous variable, HR=0.56, 95%CI 0.34-0.93, p=0.026, n=110 patients, appendix G) had significantly better PFS. The SASP score remained a prognostic factor for favorable PFS when accounting for extend of tumor resection (HR=0.36, 95%CI 0.16-0.82, p=0.01; n=90, appendix J) as well as radiation therapy ((HR=0.19, 95%CI 0.06-0.52, p=0.0006; n=75 patients, appendix K) or the combination of both (HR=0.19, 95%CI 0.03-0.72, p=0.0100; n=58 patients, appendix L) in a multivariate analysis. When grouping PA patients according to SASP score tertiles, PFS was significantly different (log-rank test) with the 5-year PFS being 48% in the "SASP low" group, 61% for the "SASP intermediate" group and 90% for the "SASP high" group (Fig. 35B).

To account for the highly influential prognostic factor of extent of resection, the ICGC cohort was separated in patients with gross-total resection (GTR) or sub-total resection (STR). Analysis of SASP expression in the GTR subgroup revealed a cohort of PA patients with a 100% 5-year PFS in the “SASP high” as well as the “SASP intermediate” group. The “SASP low group” had a worse PFS, with a 5-year PFS of 63.3%. Survival was significantly different between the patient cohorts (log-rank test) (Fig. 35C). In comparison, PFS in the STR subgroup was very poor in general, as expected. However, by separating the patient cohort according to SASP tertiles, a group with particularly poor outcome was identified. The 2-year PFS in the “SASP low” cohort was 52% and at 0% at 3 years (Fig. 35D). In addition, all patients of the “SASP intermediate” cohort presented with a progression within six year years (5-year PFS 27.8%, 6-year

PFS 0%). In comparison, in the “SASP high” patient group had a 5-year PFS of 70%, which remained stable over the course of the observed follow-up time.

In summary, IL1B and the SASP are both prognostic factors for favorable PFS independent of extent of resection as well as radiation therapy. High expression of the SASP on mRNA level correlates with a high probability to remain progression-free, while low expression of the SASP was related to an elevated chance of progression, especially in patients with sub-total resection. The prognostic value of the SASP score will have to be validated in a prospective study.

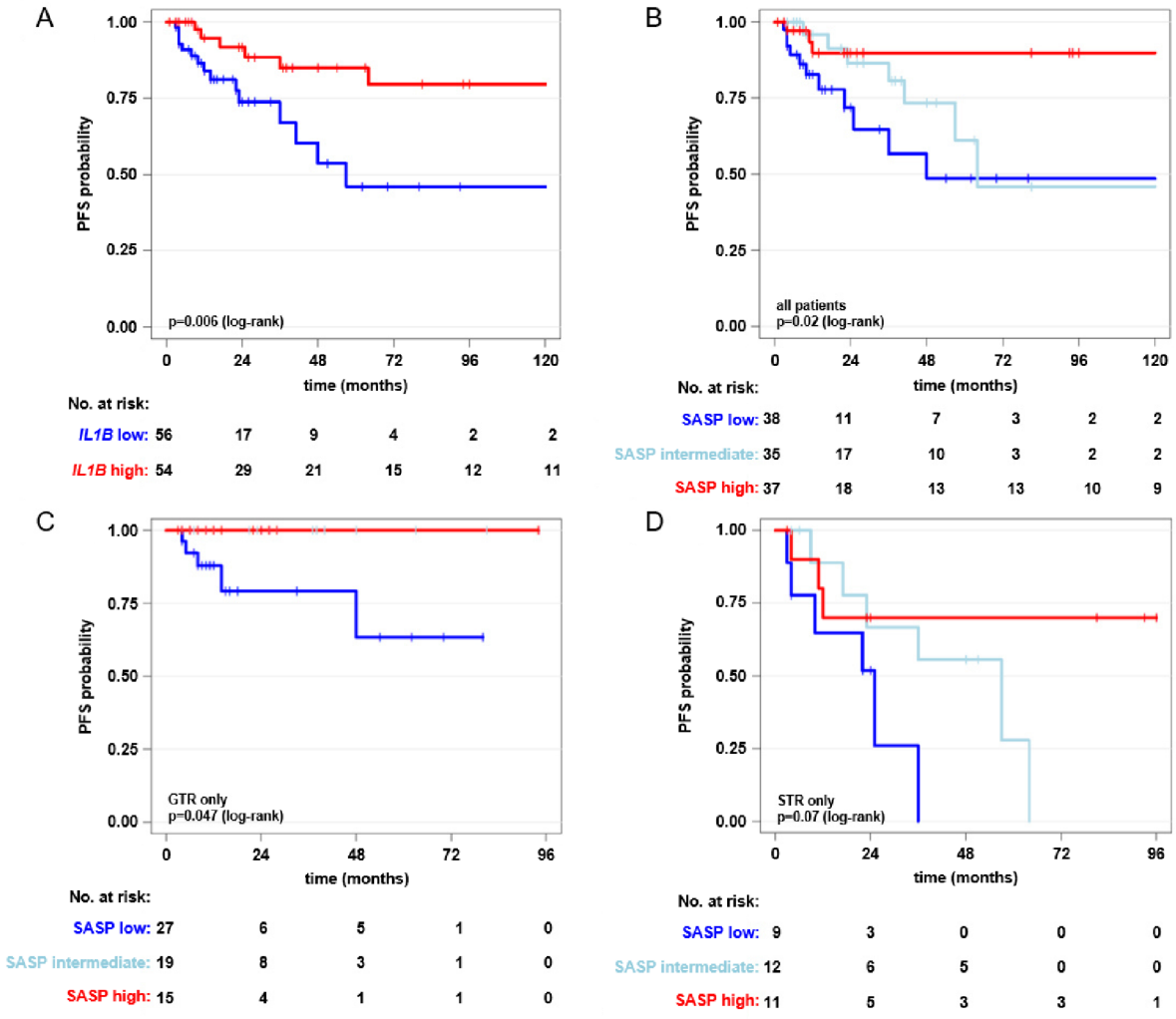

Figure 35: SASP factor expression predicts PFS independent of resection status implying a crucial role of inflammatory signaling for PA tumor growth behavior. From Buhl *et al.* (150). A) Kaplan-Meier analysis of PA patients (n=110) depicting superior progression-free survival (PFS) in the *IL1B* mRNA high expression group ("*IL1B* high") (p=0.006, log-rank). B) Kaplan-Meier analysis with PA patients (n=110) grouped into three groups according to SASP score tertiles, depicting significantly different PFS (p=0.02, log-rank). C) Kaplan-Meier analysis, only PA patients with gross-total resection (GTR) (n=61) are shown depicting significantly different PFS (p=0.047, log-rank). Both “SASP high” and “SASP intermediate” have no events and curves are fully overlapping. D) Kaplan-Meier analysis, only patients with sub-total resection (STR) (n=32) are shown. Panel A-D all depict patients from the same PA cohort from ICGC PedBrain (PFS available for n=110/112, 98.2%). Information on resection status was available for n=93/110 (84.5%) patients of the ICGC PA cohort.

3.5.3 Therapeutical exploitation of OIS in PA

Considering that the SASP can influence the growth of PA cells makes senescent cells a relevant therapeutical target. Most of the PA tumor cells seem to be arrested in a dormant, OIS state and only a small proportion of cells are actively cycling (19,144). Standard of care chemotherapy is highly dependent on cell division and effects observed in LGG patients in comparison to HGG patients only occur after extended treatment durations (clinical observation). Targeting the dormant, senescent PA cells may help to avoid the phenomenon of sudden progression or recurrence at a later time point (18). By combining chemotherapeutics together with agents targeting the non-cycling cells an improved response may be achieve in LGG patients, representing a novel treatment approach.

Preliminary results were generated to implement the novel findings in a treatment approach, by targeting senescent PA cells in a small drug screen with a class of drugs called senolytics. Single as well as combination treatments were conducted by screening the senolytic agents together with standard of care chemotherapeutics as well as novel targeted treatment approaches, MEK inhibitors, for reduction in metabolic activity in DKFZ-BT66 cells.

Senolytic agents are known to overcome resistance to apoptosis in senescent cells. Two inhibitors of anti-apoptotic BCL2 family members were analyzed, navitoclax targeting BCL2/-W/-XL and ABT-737 inhibiting BCL-W/-XL (157-159). Survival of senescent cells was shown to depend on BCL-XL and BCL-W (159,160). Reduction of metabolic activity was observed for both of the BCL2 family member inhibitors selective for senescent DKFZ-BT66 cells compared to proliferating DKFZ-BT66 cells (Fig. 36A,B). For navitoclax the IC50 values were 0,04 µM in senescent versus 0,28 µM in proliferating DKFZ-BT66 cells. The IC50 values of ABT-737 were 0,14 µM in senescent and 0,6 µM in proliferating PA cells. In addition, the well-known senolytic combination of dasatinib and quercetin (161) was used for treatments. Dasatinib is a tyrosine kinase inhibitor targeting multiple kinases involved in regulation of proliferation and apoptosis (162). Quercetin is a flavonoid targeting BCL2, BCL-X and the PI3K/AKT, p53 and p21 signaling pathway (163). The combination of dasatinib and quercetin was shown to target different senescent cell types (160). When tested in the senescent and proliferating DKFZ-BT66 cell state, no specific effect for senescent DKFZ-BT66 cells could be detected (Fig. 36C), as others have also described before (164).

As the standard of care for pediatric pilocytic astrocytoma is treatment with carboplatin or vincristine (25,165), these compounds were tested, to later explore possible combination treatments. Single treatments with standard of care chemotherapeutic did not show an effect on the non-cycling senescent

DKFZ-BT66 cells, as expected (Fig. 36D,E). For carboplatin, no effect was observed on the proliferating condition either, as expression of SV40-TAg in proliferating cells inhibits TP53-dependent apoptosis. To represent a targeted treatment approach, the MEK inhibitor trametinib was included in the screen. Trametinib led to increased metabolic activity (Fig. 36F), as observed previously without increase of cell numbers (31).

Finally, combination treatment of navitoclax, the most effective drug in senescent DKFZ-BT66 cells, with chemotherapy or targeted therapy resulted in slight additive effects compared to single treatments in senescent cells and no antagonistic effects, which would prevent their application in the clinic (Fig. 36G-I). Similar effects were observed for combination treatments with ABT-737 (Fig. 36J-L).

Current clinical trials on navitoclax show dose-dependent thrombocytopenia as the major adverse event, but evaluate the drug as well tolerated besides that (166). In accordance, response of control cells to navitoclax, normal human astrocytes, was observed at high concentrations only (Fig. 36M). This was also true for the other senolytic agents (Fig. 36N,O).

In summary, senolytic agents may be a novel treatment approach for PA patients and could enable eradication of senescent tumor cells. A combination treatment of chemotherapy, targeting the proliferating tumor cells, with senolytics, targeting senescent tumor cells, could improve treatment response in PA patients.

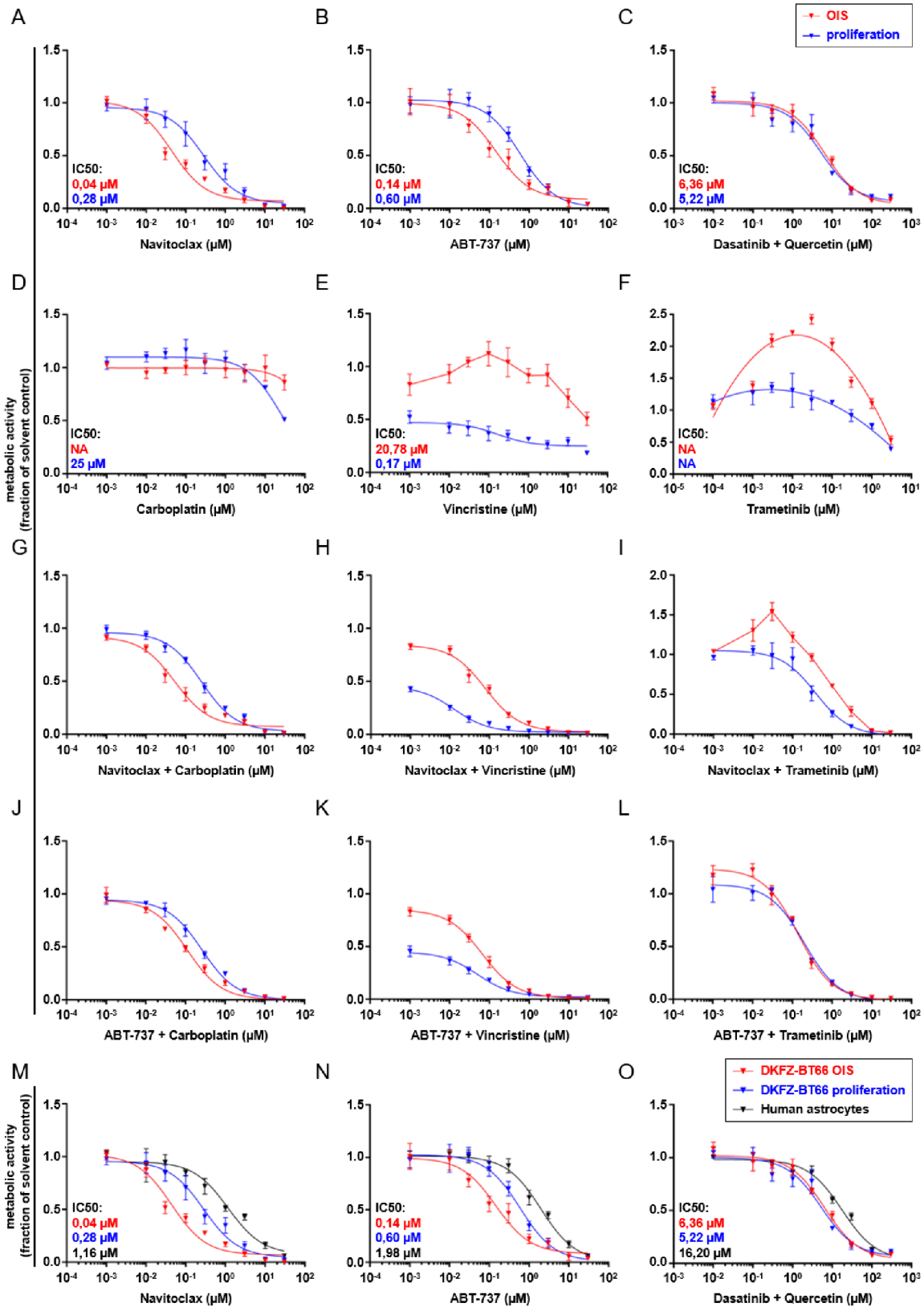

Figure 36: Senescent DKFZ-BT66 cells respond to senolytic agents. Adapted from Buhl *et al.* (150). A - F) Assessment of metabolic activity by CellTiter-Glo of senescent (red) or proliferating (blue) DKFZ-BT66 cells treated for 72 hours with navitoclax

(A), ABT-737 (B), dasatinib plus quercetin (C), carboplatin (D), vincristine (E) and trametinib (F) in the indicated concentrations. Shown are mean +/- SD of three technical replicates. IC50 concentrations are depicted for DKFZ-BT66 cells in OIS (red) and in proliferation (blue). NA = not available. G – I) Assessment of metabolic activity by CellTiter-Glo of senescent (red) or proliferating (blue) DKFZ-BT66 cells treated for 72 hours with navitoclax in combination with carboplatin (G), vincristine (H), or trametinib (I) in the indicated concentrations. Shown are mean +/- SD of three technical replicates. J - L) Assessment of metabolic activity by CellTiter-Glo of senescent (red) or proliferating (blue) DKFZ-BT66 cells treated for 72 hours with ABT-737 in combination with carboplatin (J), vincristine (K) and trametinib (L) in the indicated concentrations. Shown are mean +/- SD of three technical replicates. M – O) Assessment of metabolic activity by CellTiter-Glo of senescent (red) or proliferating (blue) DKFZ-BT66 cells and primary human astrocytes (black) treated for 72 hours with navitoclax (M), ABT-737 (N), dasatinib plus quercetin (O) in the indicated concentrations. Depicted are mean +/- SD of three technical replicates. IC50 concentrations are depicted for DKFZ-BT66 cells in OIS (red) and in proliferation (blue) and human astrocytes (black).

4. DISCUSSION

With the 2018 Nobel Prize in Physiology and Medicine being awarded to James Allison and Tasuku Honjo (167), two scientists pioneering cancer immunotherapy, the focus of cancer research has long shifted from analyzing the biology of the tumor cells alone, to the additional consideration of the effects and interactions of the tumor cells with the surrounding microenvironment. The tumor mass has to be considered as a whole, including infiltrating immune cells, stroma cells as well as secreted factors and their paracrine signaling. All of these factors play a role in tumor progression as well as response to therapy, and have to be studied in relation to each other.

The secretion of senescence-associated secretory phenotype (SASP) factors by senescent cells is part of this bigger picture (46,47,66). Depending on the biological context, the SASP can have deleterious or beneficial effects on tumor development in an autocrine as well as paracrine fashion (46). The pilocytic astrocytoma (PA) is characterized by a slow, benign growth behavior. However, recurrences and unpredictable tumor progression have been observed, even after years of stable disease (18). Markers of oncogene-induced senescence (OIS) have been detected in primary PA tissue, raising the question if the variable growth behavior is linked to alterations in the SASP signature and the OIS state (19). To further investigate the role of OIS and the SASP in PA, representative *in vitro* and *in vivo* models of this tumor entity are urgently needed.

In this study, the first patient-derived cell culture model of a PA, DKFZ-BT66, was generated and utilized to study OIS. The SASP signature was detected to be upregulated, not only in the senescent state of the *in vitro* PA model, but also in primary murine and human PA tumors. Stimulating proliferating PA cells with conditioned medium from senescent PA cells induced growth arrest, while inhibition of the SASP by anti-inflammatory treatment led to regrowth of previously senescent PA cells. A single SASP factor, IL1B, was found to be upregulated in the senescent state of the DKFZ-BT66 model as well as in primary PA. Stimulation of proliferating PA cells with the single SASP factor induced reduction of growth and led to increased SASP factor expression. Elevated mRNA expression of IL1B as well as the SASP was observed to be prognostic for favorable progression-free survival. Concluding from the presented results, the SASP does play a role in regulating tumor growth of PA cells, but the findings will have to be validated in further models, which are unfortunately limited to date.

4.1 LGG model development

The limited availability of representative LGG *in vitro* and *in vivo* models remains a challenge for LGG research until today. Novel treatment approaches could not be tested in suitable models until recently, but were rather tested in clinical trials directly, which led to unanticipated side effects in patients in the past (29). Primary cultures are difficult to handle over the long-term due to a fast onset of OIS-related growth arrest (19,32). *In vivo* models have been impossible to establish from patient tumors, as a consequence of the slow tumor growth in combination with replicative senescence, and most likely OIS as well (unpublished data from the CCU Pediatric Oncology).

Ever since Jones and colleagues discovered the main driver of PAs to be an activating fusion of *BRAF* in 2008, attempts to generate representative *in vitro* and *in vivo* models have been ongoing (22). Jones *et al.* provided proof of the transforming potential of the *BRAF* fusion by reporting independent growth of fusion-transduced murine fibroblasts in a soft agarose assay (22). A more representative model was later developed by Raabe and colleagues transducing the $BRAF^{V600E}$ mutation, the second most common MAPK alteration (14,168), into human neurospheres generated from fetal cortex (32). During their experiments, Raabe and colleagues, observed transformation of the transduced neurospheres, but in addition reported reduced proliferation over time, as well as positivity for markers of OIS (32). By transducing normal human cells with an oncogene, such as $BRAF^{V600E}$, Raabe *et al.* had generated a model of OIS. However, they were able to present evidence that the observed phenomenon plays a role in primary PA tumors by identifying markers of OIS, such as elevated levels of CDKN2A and positivity of SA-ß-Gal staining, in primary PA material. These findings were later confirmed by Jacob and colleagues (19). In addition, Jacob *et al.* detected elevated mRNA expression of OIS-associated genes in primary PAs (19). Jacob generated a similar PA *in vitro* model by overexpressing $BRAF^{V600E}$ in human immortalized astrocytes or fetal astrocytes and detected markers of OIS just like Raabe (19,32). Sievert and colleagues generated a model with the most common MAPK aberration, the *BRAF* fusion, however in a murine background using fibroblasts or cortical neurosphere cell lines (30). One further murine *in vitro* LGG model was generated by Sun *et al.* by transduction of the *BRAF* mutation as well as the *BRAF* fusion in *TP53* null murine progenitor cells (33). The authors had to knock-out *TP53* in their culture model to enable cell proliferation. However, LGG tumors do not harbor *TP53* aberrations, therefore the model is not representative of the benign genetic background of LGGs. All of the described PA *in vitro* models were generated by overexpression of the most common MAPK alterations and struggled with onset of growth arrest due to OIS. Sun *et al.* overcame this hurdle by ablation of *TP53*, which enabled cell proliferation, but is no longer representative of a PA. In addition, none of the models account for

endogenous expression of the MAPK alterations in PA tumor cells and several of them are generated in a murine (as opposed to human) background.

The first human patient-derived PA cell line, DKFZ-BT66, presented in this study, represents a human model of a WHO I LGG with endogenous expression of the *KIAA:BRAF* fusion (31). Controlled regulation of the OIS-restricted cell growth via reversible expression of SV40-TAg, enables cell expansion as well as analysis of the natural, senescent phenotype of LGG cells. The model is suitable for drug testing as well as detailed investigation of the tumor biology. Upon withdrawal of doxycycline and subsequent downregulation of SV40-TAg, markers of OIS such as growth arrest, enlarged cell morphology and expression of the SASP can be observed and studied. While the senescent state of the DKFZ-BT66 cell line is not affected by SV40-TAg expression and genetically representative of a LGG background, the proliferating condition is limited due to interference of SV40-TAg with the TP53 and RB1 pathway. As observed in Fig. 36, carboplatin treatment does not induce apoptosis in proliferating DKFZ-BT66 cells, as its apoptosis-mechanism depends on TP53 function (169). Inhibition of TP53-dependent apoptosis has proven to be a drawback of the established cell line, also for drug testing of targeted therapy, such as MAPK inhibitors (31).

Another aspect that is hampered by the doxycycline-inducible nature of the SV40-TAg is the establishment of a co-culture system of senescent and proliferating DKFZ-BT66 cells. Either all cells are in proliferation after addition of doxycycline or alternatively in OIS upon withdrawal of doxycycline. To mimic the growth pattern of PA tumors, characterized by a low proliferation index (144), a co-culture system of few proliferating cells together with senescent cells would be optimal. Especially to test combination treatment of senolytic agents, targeting cells in OIS, with standard of care chemotherapeutics, targeting cycling cells, a co-culture system would have been the best model. There is no possibility to combine both conditions in one cell culture flask. One possible option to combine the effects of both conditions is the treatment of both states, OIS and proliferation, in experiments side-by-side followed by a combined calculation of surviving cells. However, this is not truly representative of the interactions and cross-communication the two cell populations will impose on each other.

As described in chapter 3.1.2 further attempts of establishing additional LGG cell lines have failed. Optimization of culture techniques, media composition, coating strategies, filtering for surface markers and lentiviral production were conducted. These efforts did result in successful transduction of few primary samples with SV40-TAg. However, the success rate varies greatly in dependence on the quality of the virus. All successfully transduced and selected cells did not express markers of PA. Although the

analysis was restricted to the two PA markers, the *KIAA:BRAF* fusion, accounting for 70% of all PAs, and the $BRAF^{V600E}$ mutation, accounting for 5% of all PAs (14), and thus tumor cells with other alterations may have been missed. However, it is more likely that non-tumor cells overgrew the tumor cells. By transducing stroma cells with SV40-TAg, inhibition of the TP53 pathway may have given these cells an additional growth advantage. No surface marker or other measure of positive selection (such as e.g. magnetic bead-based sorting) for PA cells is available to date, which would allow separation of tumor from non-tumor cells in the primary cultures.

One further attempt to establish a PA model was the use of organotypic brain slice co-cultures, tested with the established DKFZ-BT66 cell line and the published protocol from Chadwick *et al.* (35). Sun and colleagues had reported successful culture of LGG cells using this co-culture system (33), however DKFZ-BT66 cells as well as the positive control medulloblastoma cells did not proliferate on the brain slices. A possible explanation is the addiction of the established cell lines to serum. Brain slices were preserved best in cell culture medium without serum. Finding a culture medium that enables proliferation of tumor cells on the one hand, and maintains the brain slices on the other hand, will be important to establish this system. In addition, fresh primary material could be used to establish the co-culture, as it is not dependent on serum. However, a possible caveat is that the secretion of inflammatory factors similar to the SASP from the freshly resected and cut brain slices could induce senescence in primary LGG cells and thus may inhibit proliferation. One further option to optimize the protocol is the use of neonatal E14 mice, used by Sun *et al.* (33) for their cultures of LGG cells in comparison to the original protocol by Chadwick *et al.* using P6 mice for the brain slices (35). The microenvironment of neonatal mice could be beneficial for the growth of primary pediatric LGG tumor samples.

One option to extend proliferation of senescent primary LGG cultures, deduced from results of this study, would be treatment of the cultures with dexamethasone. As glucocorticoids were shown to suppress the SASP (91,92) by others as well as in this study, treatment with dexamethasone could enable bypass of OIS-related growth arrest. This approach was tested in a preliminary experiment for four fresh, non-characterized, tumor samples (appendix A, Fig. 37) and showed increased cell proliferation for all samples. However, the approach will have to be tested in more tumor samples and the cultures have to be characterized to ensure the proliferating cells are indeed tumor cells. Finally, it will be crucial to show that the effect is indeed mediated by suppression of OIS and not an off-target effect.

Establishment of *in vivo* PA models has been hampered by OIS and replicative senescence. One murine PA-like model was generated by Gronych and colleagues (24) by overexpression of a truncated version of

$BRAF^{V600E}$ via RCAS-mediated gene delivery in cells of the cerebral hemisphere of neonatal Ntv-a mice. The developing tumors did resemble human PAs according to histopathological analysis and were characterized by a benign, non-lethal growth behavior. The same phenomenon was observed by Kaul *et al.* after injecting *BRAF*-fusion expressing NSCs in the cerebellum of 3-week old mice (23,39), mice did develop glioma-like lesions, but did not succumb to disease.

In the presented study, the established DKFZ-BT66 cell line was intracranially injected into 6-week old NSG mice and did not result in tumor formation (observation for 9 month). Only after transducing the cell line with a construct coding for hTERT, 2 out of 12 injected mice developed tumors. However, despite retaining the *BRAF* fusion, the tumors were not representative of a PA anymore, as shown by elevated proliferation index, atypical chromosomal aberrations observed in the copy number plot derived from methylation data and aggressive growth behavior after retransplantation. As a conclusion from this data, establishment of an LGG *in vivo* model remains difficult due to limitations resulting from replicative senescence and overcoming this obstacle by suppression of replicative senescence results in formation of tumors with aggressive features.

Due to the lack of comparable LGG models, the findings of this study could not be reproduced in other cell lines. This does represent a limitation of the presented work and further highlights the need for additional models. However, the key findings of this study could be validated in primary human and murine PA samples.

4.2 The influence of the SASP on the tumor and its microenvironment

OIS is a tumor-suppressive regulatory mechanism arresting premalignant cells in growth. As others have shown, OIS is regulated by a complex inflammatory network termed the SASP (46,47,87). Markers of OIS, including secretion of the SASP, have been detected in several preneoplastic lesions such as prostate intraepithelial neoplasia, papillomas, melanocytic naevi and dermal neurofibromas (47,49,51). The SASP is known to induce and maintain growth arrest in the described benign neoplasms, thereby limiting tumorigenesis (46). Additionally, the secreted SASP factors, including cytokines and chemokines were shown to attract immune cells which clear the senescent, genetically altered cells (53). However, the resulting shift in tissue microenvironment can also have deleterious effects. Some of the secreted cytokines have proangiogenic functions and thereby enhance growth of neighboring tumor as well as

non-tumor cells (63,64). Thus, the SASP can have both cancer protective as well as cancer promoting effects depending on the biological context.

One example for the promotion of tumor growth of the SASP has been reported in a mouse model of pediatric craniopharyngioma (170). By overexpressing oncogenic ß-catenin in SOX2+ pituitary stem cells or Hesx1+ embryonic pituitary precursors in young mice, Gonzalez-Meljem *et al.* observed induction of senescence in the targeted cells. The resulting SASP secretion induced cell growth and finally tumor formation in a paracrine manner with a latency of several weeks in surrounding cells (170). A perfect example for the tissue specific context of the SASP is the tumor suppression or formation described by Eggert *et al.* in senescent hepatocytes (171). The authors reported that $NRAS^{G12V}$-induced OIS *in vivo* in murine hepatocytes activated immune cells to clear the premalignant, senescent cells and may thereby prevent initiation of liver cancer. However, in case of established hepatocellular carcinoma (HCC), the tumor cells prevent maturation of myeloid cells into macrophages through secretion of cytokines, therefore the senescent hepatocytes are not cleared and can fuel HCC tumor growth (171).

In pilocytic astrocytoma, markers of OIS such as upregulation of CDKN2A, positive staining for SA-ß-Gal and elevated expression of several OIS-associated genes, have been described previously (19,32). The proliferative index, determined by Ki67 staining, is 1-2% in PAs on average (144). The entity is defined as a benign, WHO grade I glioma, exhibits slow tumor growth and has a fairly good prognosis of 94% 10-year overall survival (18,20). All of these factors indicate a tumor-protective role of OIS in PA. The functional role of the SASP in PA has not been studied to date. Although PA patients may have stable disease over a long period of time, PA tumors can resume growth at any time (18,20). Possibly alterations in OIS regulation e.g. by changes in SASP secretion, are related to this phenomenon.

In this study, further proof for the presence of OIS in primary PA tumor cells was provided. Markers of OIS, such as expression of CDKN2A, positivity for SA-ß-Gal and SAHF were observed in the established PA model, DKFZ-BT66. In addition, growth arrest of the primary PA cells was circumvented by transduction with SV40-TAg, which inhibits the OIS-relevant TP53/CDKN1A and CDKN2A/RB1 pathways. The OIS state of the established PA cell line was further characterized by elevated mRNA expression of SASP factors and elevated protein secretion of the exemplary SASP factors IL1B and IL6 (Fig. 21 and 24). Conditioned medium of senescent PA cells induced growth arrest of proliferating PA cells (Fig. 22), proving the secretory nature of the phenotype. Elevated SASP factor mRNA expression was additionally observed in primary human and murine PA (Fig. 21). The presented results provide proof for the presence of the

SASP in PA cells both *in vitro* and in human and murine PA tumors *in vivo*, and confirm the autocrine feedback signaling of the SASP in PA cells.

One mechanism of autocrine feedback signaling of the SASP has been described to be executed by IL1, a major regulator of the SASP (50,80). As shown in this study, the SASP factor IL1B reduced growth of proliferating PA cells and induced SASP factor expression (Fig. 27 and 28). As others have reported previously, IL1 signaling activated NFκB signaling (Fig. 26)(105) and thereby induced its own transcription and translation (106), as determined by elevated pro-IL1B levels (Fig. 27). IL1 is known to be an important regulator of the SASP, as demonstrated by its regulatory effect on the SASP factors IL6 and IL8, both involved in OIS induction and maintenance (46,47,50,80). IL1 was further shown to induce markers of OIS, such as growth arrest, SA-ß-Gal activity and CDKN1A expression (50,80,89). These findings were confirmed by the results presented in this study, showing reduced PA cell growth, enlarged cell morphology and elevated SASP expression under rIL1B treatment (Fig. 28). IL1B was shown to play a role in induction of OIS in the PA cell culture model, but it did not replicate the effect of the full SASP, which induced complete growth arrest in PA cells (Fig. 22). Furthermore, inhibition of IL1 signaling did not lead to bypass of OIS. Both, pharmacological as well as shRNA-mediated knock-down of the cytokine pathway did not result in regrowth of senescent PA cells, even though the IL1 pathway was repressed, as shown by rescued levels of IRAK1 (Fig. 29 and 33). While Orjalo and colleagues reported reduced proliferation under rIL1A treatment, they did not comment on any effects on growth of senescent cells treated with IL1 neutralizing antibodies or shRNAs targeting the IL1 pathway (80). Acosta *et al.* reported onset of senescence upon ectopic expression of *IL1A* in a human IMR90 fibroblast model (50). In addition, shRNA mediated knock-down of the IL1 receptor was shown to partially prevent OIS in a *RAS*-induced OIS fibroblast model (50). Furthermore, treatment of a murine model of $NRAS^{G12V}$-mediated OIS in hepatocytes with an IL1R inhibitor led to reduced levels of OIS markers, such as CDKN2A and CDKN1A, increased levels of NRAS-positive cells in proliferation and reduced clearance of senescent cells by the immune system (50). The precautious formulation by Acosta and colleagues of a ‘partial prevention’ of OIS after IL1 inhibition and no mention of effects on growth by Orjalo and colleagues indicate that the effects of IL1 inhibition on growth of senescent cells were not pronounced, but may be observed *in vivo* especially due to reduced clearance of senescent tumor cells (50,80). The *in vitro* data from Orjalo and Acosta are in line with the observations of this study, showing no effect of interference with IL1 signaling on cell growth during OIS. Thus, it can be concluded that IL1B is sufficient to partially induce OIS, but not necessary to maintain it.

Another regulator of autocrine SASP signaling is IL6 (46). In the study presented here, an increase of IL6 secretion of senescent PA cells was observed (Fig. 23 and 24). However, treatment of proliferating PA cells with the recombinant cytokine did not result in reduction of cell growth. Furthermore, inhibition of the IL6 pathway by pharmacological or shRNA-mediated interference, did not affect growth of senescent PA cells (Fig. 30 and 33). This stands in contrast to published data showing an induction of senescence upon IL6 signaling activation. Induction of markers of senescence, SA-ß-Gal activity and upregulated CDKN1A, CDKN2A expression, have been reported by Paola Ortiz-Montero *et al.* under treatment of the breast cancer cell line MCF with rIL6 (0.5 or 50 ng/mL) over the course of 5 to 10 days (172). Concerning interference with IL6 signaling, Kuilman *et al.* report no effects on growth of senescent fibroblasts under treatment with IL6 neutralizing antibodies, but the group showed bypass of OIS-induced growth arrest after shRNA-mediated inhibition of the IL6 pathway in $BRAF^{V600E}$-transduced fibroblasts (46). A similar phenomenon of regrowth of senescent cells under shRNA-mediated knock-down of the SASP factor, IL8 as well as its receptor CXCR2, was demonstrated by Acosta *et al.* and confirmed by Kuilman (46,47). Both authors demonstrated the effects of inhibition of single SASP factor pathways in OIS models, generated by overexpression of oncogenes in fibroblasts (46,47). This is in contrast to the DKFZ-BT66 cell line, representing a patient-derived model of OIS with endogenous expression of the oncogene. Therefore, the differences in the observed effects under knock-down of single SASP factors may be influenced by the artificial genetic aberrations introduced into the described OIS fibroblast models (46,47) versus the endogenous expression of the oncogene in the PA model used in the presented study. An alternative explanation could be that specific SASP factors play a different role in various biological environments. As the SASP is different for every cell type, for every oncogene etc., the single SASP factors may play different roles in each of the analyzed OIS models (66). Alternatively, inhibition of single SASP factors does not suffice to overcome OIS in the PA model, or another SASP factor not analyzed in this study may lead to bypass of OIS in DKFZ-BT66 cells.

However, bypass of OIS-related growth arrest was achieved in senescent DKFZ-BT66 cells by treatment with the anti-inflammatory drug dexamethasone (Fig. 34). In addition, dexamethasone treatment significantly reduced SASP factor mRNA expression (Fig. 34). SASP factor inhibition under glucocorticoid treatment has been reported previously (91,92), corroborating the presented results. Inhibition of several SASP factors may suffice to overcome OIS-induced growth arrest in the PA model. However, dexamethasone is a “dirty drug” influencing several biological mechanisms including metabolism (reviewed in (173)) and other glucocorticoids such as e.g. hydrocortisone have been shown to improve clonal growth of human endothelial cells due to sensitization to EGF stimulation (174). However,

treatment with glucocorticoids has been shown to induce both proliferation as well as inhibition in different cell types. Treatment of human cervical, lung, hepatocellular and breast carcinoma cell lines with 100 nM dexamethasone reduced growth of several tested cell lines (175). The human fibrosarcoma cell line HT-1080 was inhibited in growth *in vitro* by treatment with 100 nM dexamethasone. Mice s.c. injected with the HT-1080 cell line showed inhibition of tumor growth at high dexamethasone doses (200 µg/mouse), but increasing tumor sizes when treated with lower doses (5 µg/mouse) (176). Bose *et al.* even reported an induction of a senescence-like phenotype in rat embryonic neural stem cells treated with 1 µM dexamethasone, showing reduced proliferation and upregulation of CDKN1A and CDKN2A (177). On the other hand, Li *et al.* demonstrated increased proliferation of human fibroblasts and reduced levels of CDKN1A under dexamethasone (140 nM) treatment (178). Early studies conducted by Cristofalo and colleagues report increased proliferation and delayed onset of senescence in human fibroblast-like cells treated with hydrocortisone (14 µM), but the authors also observed growth inhibition of certain vertebrate cell lines grown under the same treatment conditions (179,180). It can be concluded that the effect of glucocorticoids is cell type specific and depends on the biological context such as e.g. senescence. The presented data suggests that in senescent DKFZ-BT66 cells the increase in proliferation upon dexamethasone treatment is at least partially caused by the inhibition of the SASP, as observed on the mRNA level and for the exemplary SASP factor pathways IL1 and IL6 on the protein level.

One drawback of the study presented here is the fact that all of the data was generated from pure cultures of the PA cell line, only accounting for the autocrine signaling mechanism of the senescent cells. The PA tumor mass does of course include other cell types, such as immune or stroma cells. Only few studies have been conducted to investigate the extent and role of immune infiltration in PA tumors. Yang *et al.* compared the infiltrating immune cells of high-grade glioblastoma to low-grade PAs in a total of n=91 samples via IHC (181). Glioblastoma samples showed increased perivascular infiltration with CD(8) T-cells (62%) in comparison to PAs (29%), as expected. But the infiltration with CD(8) T-cells in PAs was similar in the intratumoral space in comparison to the perivascular space. 86% of PA samples exhibited infiltration with CD68-positive macrophages in the perivascular as well as the intratumoral space. PAs did not show any intratumoral infiltration with CD56-positive natural killer cells. Gutman and colleagues observed CD68-positive cell infiltration by IHC in 35-55% in n=3 *NF1*-mutated PA patient samples (182). Similar results were reported by Klein *et al.* (183): the authors identified 32% of all cycling cell to be microglia in PA via IHC staining for Ki67 and CD68. However, only a small fraction of the tumor cells proliferate in PA, therefore this result is difficult to interpret in comparison to other tumor entities.

Further studies on immune infiltration of pediatric brain tumors were conducted by Griesinger *et al.* using FACS (184). A total of n=7 PAs were included in their pediatric brain tumor cohort, showing an increased infiltration with myeloid cells (31.6%), a 72-fold increase in comparison to normal pediatric brain (NB) (obtained from epilepsy patients). Markers for activated myeloid cells such as HLA-DR and CD64 were upregulated in PA in comparison to NB (3.5- and 2.5-fold, respectively). In addition, infiltration with T-cells, determined by combined expression of CD45, CD3 and CD8, was 3.28% on average in PA samples. Concluding from all these studies, PAs are infiltrated by myeloid and lymphoid cells, which should be considered when examining cytokine signaling, such as the SASP, in this tumor entity. This becomes especially relevant, when comparing gene expression data from bulk tumor samples, including immune cells. In an analysis of gene expression microarray data from gliomas, Huang *et al.* observed an immune system-related gene expression pattern in PA patients in comparison to normal cerebellum and grade II astrocytomas or oligodendrogliomas (185). It can therefore not be excluded that the identified SASP signature, containing several inflammatory genes, is also dependent on the extent of immune infiltration. In the study presented here, it was shown that an increased expression of the SASP signature correlates with favorable PFS, and it is likely that this is influenced by the extent of immune infiltration. It has been described that senescent cells attract and activate immune cells and thereby induce clearance of the senescent cells (53-55). Therefore, elevated SASP secretion may be correlated to favorable clinical outcome due to clearance of tumor cells by immune cell activation.

State-of-the-art techniques such as single cell RNA sequencing or mass cytometry will enable a detailed analysis of the PA tumor mass and help to identify most, if not all, subsets of infiltrating immune and stroma cells. Single cell RNA sequencing enables identification of cell subsets by unsupervised clustering of gene expression patterns and correlation of detected marker genes or pathway signatures to specific cell populations (186). Mass cytometry enables the detection of up to 40 antigens, including intracellular markers, using antibodies coupled to stable, elemental isotopes. Individual cells are analyzed via mass spectrometry distinguishing antigens by the distinct mass of the different elemental isotope (187,188). Both techniques will enable the detection of tumor and non-tumor cell populations in PA, give insights on the regulation of inflammatory pathways via gene expression data or activation status of intracellular markers and show potential interactions of immune and tumor cells.

Identified populations of immune cells could then be used in co-culture systems together with PA cells, such as DKFZ-BT66, to mimic the tumor in its microenvironment and investigate the effects of paracrine SASP signaling. A similar experimental setup was also considered for the study presented here. As the

DKFZ-BT66 model is a patient-derived cell line, an appropriate co-culture model would be the use of human microglia, the orthotopic immune cells of the brain. Human microglia can be cultured only for a limited time period, as the complex composition of microglia, astrocytes and fibroblasts quickly changes towards an increase of fibroblast-like cells (189). Primary cultures of microglia from pediatric patients are of course extremely difficult to obtain, which is why finally this type of experiment was not conducted. Another option would have been a co-culture system with murine microglia. However, major differences have been described between murine and human microglia and their expressed proteins (reviewed in (190)). For example, the baseline levels of cytokines and chemokines were shown to differ significantly between the two species and cytokine regulation is very different in response to stress stimuli (191). As the interaction between the secreted SASP, comprised of chemokines and cytokines, from human PA cells would be analyzed in a co-culture with murine microglia, these cross-species differences would greatly hinder interpretation of the results.

In summary, the effects of autocrine SASP signaling of senescent PA cells were investigated in the study presented here, however the effects of paracrine signaling especially in co-culture systems with microglia should be considered for further investigation.

4.3 Glucocorticoid use in LGG patients

Dexamethasone is a drug commonly used in neuro-surgery and -oncology (192). As shown in this study, treatment of senescent DKFZ-BT66 cells with dexamethasone induced proliferation, suppressed the SASP, as observed on the mRNA level and for the exemplary SASP factor pathways, IL1 and IL6 on the protein level. These findings are in concordance with previously published results, showing that glucocorticoids suppress the SASP (91,92,156). Shah *et al.* demonstrated inhibition of rIL1B-induced transcription of several inflammatory genes under dexamethasone treatment in human pulmonary epithelial A549 cells (156). Laberge and colleagues specifically set out to identify SASP-suppressing agents in a drug screen on radiation-induced senescent human fibroblasts and identified glucocorticoids as the most effective compounds (91). Glucocorticoids were shown to suppress SASP production and secretion, including IL1A, in *RAS*-induced OIS fibroblast models. However, growth arrest of irradiated senescent cells could not be reverted by glucocorticoid treatment (91). Conditioned medium of senescent fibroblasts stimulated a non-aggressive human breast cancer cell line (T47D) to invade a basement membrane of a Boyden chamber, while treatment with glucocorticoids suppressed this SASP-induced pro-tumorigenic effect (91). This proves that paracrine signaling of the SASP is interrupted by

glucocorticoid treatment. In addition, Ge *et al.* tested dexamethasone *in vitro* on non-small cell lung cancer (NSCLC) cells and observed reduced onset of senescence in response to DNA-damaging agents (92). The authors demonstrated that dexamethasone reduced the secretion of several SASP factors, including IL1B, on protein level, in line with the results presented in this study. In NSCLC, A549 and H1650 cell line-induced xenografts, treatment with the chemotherapeutic agent pemetrexed inhibited tumor growth and increased survival of mice, while co-treatment with dexamethasone blunted the tumor-suppressing effect of the chemotherapeutic (92). In summary, several scientists have reported on the potential of glucocorticoids to suppress the SASP, including their potential to prevent the effects of paracrine SASP signaling. Both Shah and Laberge (91,156) reported that the inhibitory effect of glucocorticoids on the SASP is related to repression of IL1 signaling. This is in accordance with the observed effects of this study, showing rescued IRAK1 levels under dexamethasone treatment and the IPA prediction of IL1B as top upstream regulator of the observed gene expression changes.

From a clinical perspective, these findings suggest that anti-inflammatory therapy for PA patients using dexamethasone should be carefully re-evaluated, as dexamethasone treatment may inhibit the SASP and thereby interfere with induction and maintenance of OIS, ultimately leading to tumor cell growth. In addition, treatment with chemotherapy may enforce SASP secretion by inducing DNA damage, as shown by Ge and colleagues (92), and this effect may be reduced under glucocorticoid treatment.

On the other hand, the observed phenomenon of tumor cell regrowth under dexamethasone therapy could be therapeutically exploited. Sensitization of tumor cells to either conventional chemotherapy or targeted therapy by SASP inhibition through dexamethasone treatment could be a novel therapeutic approach. As only 1-2% of PA tumor cells are actively dividing (144), dexamethasone could augment the amount of proliferating cells and thereby sensitizes PA cells to chemotherapeutic agents, which depend on proliferation for their effect. The downside of this approach is the high potential of triggering or increasing the speed of tumor progression, hence maximum caution should be exercised when considering this approach. The effect of a combination treatment of dexamethasone and standard of care chemotherapy first will have to be analyzed in appropriate PA models, such as the DKFZ-BT66 cell line.

4.4 The potential of senolytic agents for LGG patients

One aspect, just briefly touched upon in this study, is the possible benefit of senolytic agents for the treatment of PA patients. As mentioned, primary PA tissue is characterized by elevated expression of CDKN2A and low expression of the proliferation marker Ki67, indicating that most PA tumor cells are arrested in growth (19,144). Targeting the remaining senescent PA cells in patients may enable actual shrinkage of the tumor mass. This approach would be especially beneficial in patients with sub-total or partial tumor resection known to be prone to recurrence (20). Senolytic agents, such as the BCL2 family inhibitors, were recently shown to induce apoptosis specifically in senescent cells (159).

Chang *et al*. demonstrated induction of apoptosis under treatment with navitoclax in senescent human fibroblasts (WI-38) in irradiation-(IR), replicative-(RS) and oncogene-induced senescence (OIS) *in vitro* models (158). In addition, the authors were able to show that senescent cells in irradiated or naturally aged transgenic mice carrying a CKDN2A-dependent luciferase reporter were cleared by navitoclax treatment (158). Zhu *et al.* reported senolytic activity of navitoclax, inducing apoptosis in radiation-induced senescence models of human fibroblast as well as HUVECs, but showing no effects on cycling cells (157). The second senolytic compound tested in this study, ABT-737, was investigated in different human OIS, replicative and DNA-damage-induced senescence fibroblast models *in vitro* as well as *in vivo* by Yosef *et al.* (159). The group observed induction of apoptosis in response to ABT-737 *in vitro* specifically in senescent cells as well as reduction of SA-ß-Gal positive cells in irradiated mice and in transgenic mice with inducible CDKN2A expression (159). However, the compound ABT-737 was also reported to induce senescence and SASP expression in apoptosis-resistant renal, lung and prostate cancer cell lines (193). The effect of the senolytic agents therefore seems to be dependent on the biological context. One further novel approach to target senescent cells in preclinical development, is the use of FOXO4 peptides disrupting the interaction of FOXO4 with p53 and thereby inducing apoptosis through nuclear exclusion of p53 (164). The peptide was shown to be effective *in vitro* in radiation-induced senescent human fibroblasts and *in vivo* in aged mice or in DNA-damage induced senescence, using the transgenic mouse model with a CDKN2A promoter linked to a luciferase expression (164).

In the study presented here, enhanced sensitivity of senescent PA cells to senolytic agents, especially to navitoclax, in comparison to proliferating DKZF-BT66 cells as well as to normal human astrocytes was observed. No antagonistic effects were detected in combination treatments with standard of care chemotherapeutics or targeted therapy with a MEK inhibitor. On the basis of these preliminary results, the CCU Pediatric Oncology is currently investigating the potential of senolytic agents in combination

with chemotherapeutics and MEK inhibitors in further preclinical analyses. This is especially fascinating due to the potential synergism of the BCL2 family inhibitor navitoclax with chemotherapy, as shown in multiple cancer cell lines in combination with standard chemotherapeutics, including vincristine and carboplatin (194). In addition, treatment with targeted agents, such as MEK inhibitors, has been shown to elevate levels of the pro-apoptotic BCL2 family member BIM (BCL2L11). The turnover of BIM is regulated by ERK-dependent phosphorylation followed by proteasomal degradation, which is inhibited under MEK inhibitor treatment (195). Therefore, the combination of MEK inhibitors (increasing levels of pro-apoptotic BCL2 family members) with navitoclax (suppressing anti-apoptotic members of the BCL2 family) may be synergistic. On-target activity, such as reduction of BCL2 family member protein levels and onset of apoptosis under treatment with senolytic agents, as well as *in vivo* efficacy will have to be proven, before the drugs can be considered for a clinical trial.

One obstacle concerning the use of navitoclax for LGG patient treatment, are the reported side effects (196). In the phase I dose-escalation study of navitoclax, thrombocytopenia and neutropenia were observed as the most common higher-grade toxicities in a dose-dependent manner (197). In the following phase II study, navitoclax induced thrombocytopenia grade III-IV in 41% of n=39 patients with recurrent small cell lung cancer, a tumor entity characterized by overexpression of BCL2 (196). However, the side effects occurred in a dose-dependent manner and were shown to be reversible (198), therefore navitoclax may still be considered for a combination treatment strategy in LGG patients. Currently, a combination treatment of navitoclax and trametinib is evaluated in adult patients with *N-RAS* or *K-RAS* positive solid tumors in a clinical phase Ib/II trial (NCT02079740). Another phase I/II study is investigating the combination of trametinib, dabrafenib and navitoclax in *BRAF*-mutant melanoma or solid tumors that cannot be resected (NCT01989585). The outcome of these studies may give further indications of the feasibility of potential combination treatments by providing information on potential additive or synergistic effects as well as observed adverse events. The combination treatment strategy of senolytics and chemotherapeutics or targeted agents may be a novel approach to additionally target dormant, senescent PA cells which are not amenable to conventional chemotherapy.

4.5 Clinical implementations of the SASP in LGG patients

An intriguing aspect is the prospect of exploiting the growth suppressive effect of the SASP therapeutically. Drugs entertaining the SASP could be used to maintain tumor cells in OIS, either as a consolidation or a therapy upon progression. The SASP is a complex mixture of inflammatory molecules (87), which would be difficult to replicate in a therapeutical application. However, IL1 signaling was shown to regulate SASP expression by others (50,80) as well as in the study presented here.

From 1980 to 1990 approximately 20 phase I and II studies were conducted to test the antitumor activity of the cytokines IL1A/B (199). Treatment with IL-1 was investigated in melanoma, renal cell carcinoma, ovarian carcinoma and other malignancies due to its previously reported anti-angiogenic, anti-proliferative and immune stimulatory potential (199). While little antitumor activity was observed in the studied entities, toxicities such as fever, flu-like symptoms and dose-limiting hypotension were reported. Due to the toxicities and the lack of evidence for robust anticancer efficacy, IL-1 studies were discontinued early on (199). One example for a non-SASP factor (87), but a successful example for cytokines treatment, is the agonist of the IL-2 pathway, aldesleukin. Aldesleukin has been approved by the FDA and was shown to induce complete and durable response in patients with metastatic melanoma and renal cell carcinoma. However, similar severe toxicities, as observed with IL1, are common under aldesleukin treatment, allowing only for inpatient treatment and administration of the drug with intensive supportive care (199,200). The obstacles for the use of inflammatory cytokines, such as IL1B, in the treatment of malignancies therefore remain high.

In the study presented here, elevated SASP factor expression was shown to correlate with favorable progression-free survival (PFS). The calculated SASP score remained a factor for favorable PFS when accounting for extent of resection and/or radiation therapy in a multivariate analysis. The analysis of the ICGC PA patient cohort (14) revealed two patient populations who may benefit from the presented findings. First, none of the patients with complete tumor resection and high or intermediated SASP score expression had a progression over the course of the follow-up (FU) time analyzed. Monitoring of this patient cohort could be reduced, e.g. by longer FU intervals or a shorter period of FU overall. In contrast, all of the patients with sub-total tumor resection and low SASP factor expression had a progression within three years. This patient cohort could benefit from adjuvant therapy, as well as re-resection of the remaining tumor to improve PFS, and shorter FU intervals to improve early detection of progression. After validation of the SASP score in a prospective study, the score may serve as the first available biomarker with the potential to predict the variable growth behavior observed in PA patients. One

example for a similar gene expression-based predictive score is the “Oncotype DX Breast Recurrence Score®”, predictive for distant recurrence in breast cancer patients (201). The expression of n=21 genes is the basis for the calculation of a recurrence score, which predicts the risk of distant recurrence of breast cancer at 10 years, when patients are treated with tamoxifen only (201). This score has been implemented into the clinic and has been shown to have an impact on clinical decision making regarding adjuvant treatment administration (202). Potentially, the SASP score could play a similar role in the clinical management of LGG patients in the future.

4.6 The interplay between MAPK inhibitors and the SASP

After discovering the influence of the SASP on PA tumor cell growth, one concern is the possibility of interfering with the SASP by therapeutic agents used in LGG therapy. As standard chemotherapy is known to induce the SASP due to DNA damage-induced senescence (92), this treatment approach is not of concern and rather enforcing senescence. A novel treatment strategy, currently evaluated in LGG patients, is the use of targeted therapy, which has shown first promising results (28). However, there are unpublished clinical observations of tumor progression (i.e. a “rebound”) after discontinuation of e.g. MEK inhibitor treatment in LGG patients. In the light of the results presented in this study, the interplay between the PA oncogene (MAPK activation) and OIS induction could be impacted by MEK inhibitors, and an analysis of the interactions between the MAPK pathway and inflammatory signaling is of high interest.

The major players of the MAPK pathway are p38, JNK as well as MEK-ERK signaling. Several authors have reported on repression of inflammatory signaling under treatment with MAPK inhibitors targeting p38 and JNK (reviewed in (203)). However, treatment with p38 and JNK inhibitor did not show any effects on metabolic activity of the PA cell line DKFZ-BT66 in comparison to MEK inhibitor treatment (unpublished data from the CCU Pediatric oncology, (31)). As MEK inhibitors are currently tested in clinical trials (28), the focus should lie on the interaction between the SASP and the MEK-ERK signaling pathway.

Shah *et al.* reported MAPK pathway activation, as determined by phosphorylation of ERK, under treatment with rIL1B in human pulmonary epithelial cells (156). Recombinant IL1B additionally was shown to induce the transcription of inflammatory genes, which could at least be partially reversed under treatment with a MEK inhibitor at the same time (156). Inhibition of MAPK signaling was shown to partially inhibit inflammatory gene transcription, regulated by IL1, and may thereby interfere with the

SASP (50). In addition, Sumimoto *et al.* demonstrated decreased expression of the inflammatory genes *IL6, IL10* and *VEGFA* in $BRAF^{V600E}$-positive melanoma cell lines under inhibition of MEK signaling by U0126 treatment (204). Both studies indicate that there may be a repressive effect of MEK inhibitors on inflammatory signaling. Furthermore, Wang *et al.* demonstrated that MEK-ERK activation was necessary for the induction of senescence in an OIS model generated by transducing the human fibroblast cell line BJ with $HRAS^{G12V}$. Inhibition of MEK signaling using U0126 rescued transduced BJ cells from premature senescence (205). MEK-ERK activation does also play a role in OIS of LGG patients, being induced by *BRAF* alterations (19). However, the relevance of the described mechanism of rescue from onset of senescence by MEK inhibition may not be relevant in PA patients with fully established OIS.

On the contrary, MEK inhibitors may even be effective in senescent cells, as demonstrated by Kochetkova *et al.* (206). Induction of apoptosis under MEK inhibitor treatment (PD0325901) was demonstrated in senescent *RAS*-mutated A549 human lung adenocarcinoma cells (206). The authors observed that autophagy, a common mechanism of resistance to MEK inhibition in proliferating A549 cells, could not be activated in the senescent cells. Spatial separation of lysosomes and autophagosomes prevented their fusion and led to accumulation of damaged mitochondria, ROS and finally cell death (206). Furthermore, Ruscetti and colleagues showed that combination treatment with the MEK inhibitor trametinib and the CDK4/6 inhibitor palbociclib induced RB1-mediated senescence, including SASP secretion, in a human *KRAS*-mutant lung cancer cell line as well as a PDX lung cancer model and thereby led to clearance of senescent cells by NK cells (207). These studies demonstrate that induction of senescence and secretion of the SASP is still possible in presence of the MEK inhibitor trametinib, which will be tested in the upcoming LOGGIC trial in LGG patients. The induction of apoptosis by MEK inhibition may even be facilitated in senescent cells, due to disruption of the resistance mechanism autophagy. The DKFZ-BT66 cell line is the perfect model to test effects of the clinically applied MEK inhibitors on SASP secretion.

5. CONCLUSION AND PERSPECTIVES

The aim of this study was to develop representative models of LGG and to utilize these models to investigate molecular mechanisms governing tumor cell growth as well as implement the findings into a translational context. Evidence for the presence of OIS and the SASP in the established patient-derived PA cell line DKFZ-BT66 could be provided, and was further validated in primary human and murine PAs. The results presented show the regulatory effect of the SASP on PA tumor cell growth and the prognostic value of the SASP for PA patient outcome. The identified mechanism regulating PA tumor cell growth could be therapeutically exploited using anti-inflammatory and senolytic agents.

Aim 1: Establishing in vitro and in vivo LGG models

The goal to establish representative *in vitro* and *in vivo* LGG models remains an ongoing challenge for the LGG research community. The presented patient-derived DKFZ-BT66 cell line was generated by overcoming OIS-relevant pathways via inducible expression of the SV40-TAg. This may present an approach to establish further LGG models in the future, however optimization of the method is urgently needed. Intracranial injection of the established PA cell line into immunodeficient mice did not result in tumor formation, while transduction of the cell line with hTERT resulted in formation of tumors without LGG features. Establishing *in vivo* models of PAs, either as PDX models or genetically engineered mouse models (GEMMs), may simply not be possible due to growth arrest resulting from OIS as well as replicative senescence.

Aim 2: Characterization of OIS as well as the concurrent inflammatory signaling in LGG

In this study, identification of the SASP as a regulator of PA tumor cell growth was described for the first time. OIS was shown to be a mechanism governing PA cell growth inducing growth arrest via secretion of SASP factors. This may explain the benign tumor growth behavior and fairly good overall survival observed in PA patients.

Aim 3 and 4: Identification of specific markers for OIS in LGG and examination of their regulation during OIS

The SASP factors IL1B and IL6 were identified as candidate OIS-controlling genes in PA and found to be upregulated in primary PA. The cytokines were both secreted in the senescent state of the DKFZ-BT66 cell line and both pathways were regulated during OIS. Treatment with the recombinant cytokine IL1B, but not IL6, reduced growth of proliferating PA cells and induced SASP expression. Interference with the single cytokine pathways in senescent cells did not lead to bypass of OIS. Concluding from these results,

IL1B significantly contributes to OIS induction, but acts in concert with other SASP factors to induce and maintain OIS. Treatment with the broad anti-inflammatory drug dexamethasone resulted in regrowth of senescent PA cells and suppression of SASP expression. Care should be taken when considering anti-inflammatory treatment in pediatric PA patients due to the potential interference with the OIS-maintaining SASP signaling.

Aim 5: Implementation of the findings into a clinical context by the identification of novel targets or prognostic markers

The clinical relevance of the SASP was demonstrated by defining PA patient cohorts with significantly differing clinical outcome dependent on SASP factor expression. PA patients with high SASP factor expression had a favorable PFS independent of tumor resection status. The SASP score will have to be validated in prospective studies, but may serve as a prognostic marker to identify PA patients with a high or low chance of recurrence in the future. Finally, the mechanism of OIS could be therapeutically exploited in a treatment with senolytic BCL2 family member inhibitors, specifically targeting senescent PA cells. This novel approach will have to be evaluated in further pre-clinical studies. The combination of senolytic agents, targeting senescent PA cells, together with chemotherapy, targeting cycling PA cells, may enable reduction of tumor mass in patients with incomplete resection, which are prone to recurrence.

APPENDIX

A) Figure 37: Dexamethasone induces growth of PA short-term cultures without SV40 large T antigen expression.

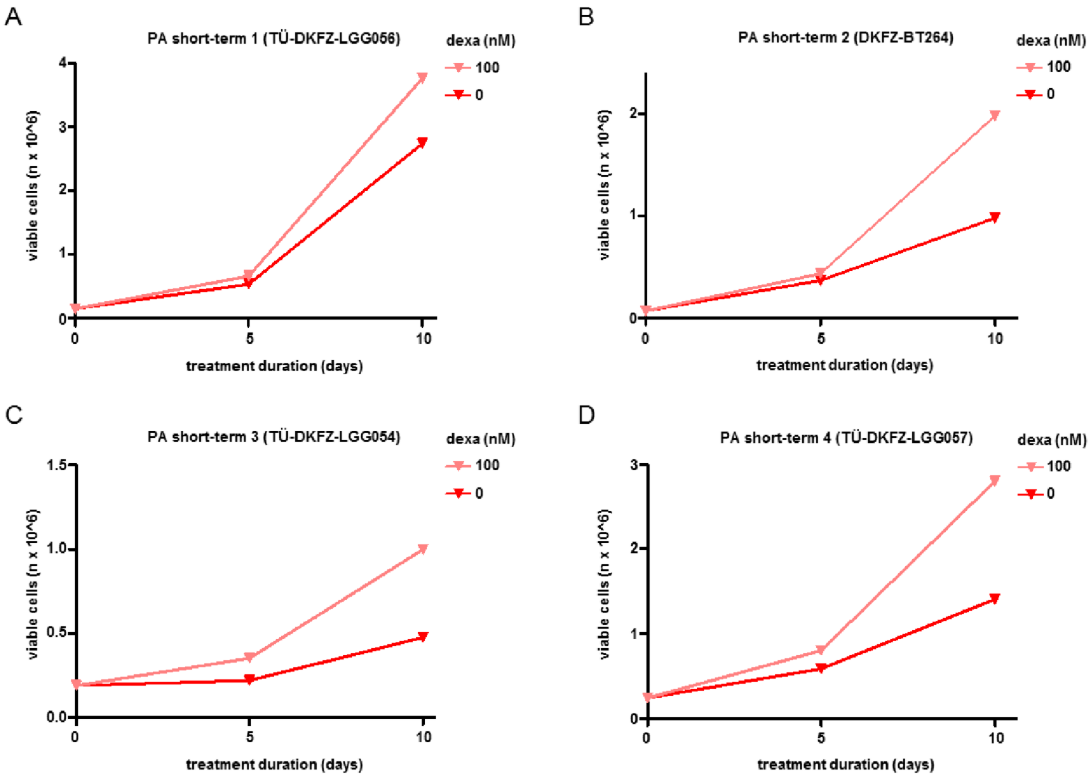

Figure 37: Dexamethasone induces growth of PA short-term cultures without SV40 large T antigen expression. A-D) Cell count of four PA short-term cultures treated with 100 nM dexamethasone (dexa) (light red) or solvent control (0 nM dexa) (red) for 10 days. Depicted is one independent experiment/culture.

B) Plasmid maps

1. Doxycycline-inducible pFRIPZ-IRES-EV plasmid (backbone of SV40-TAg plasmid):

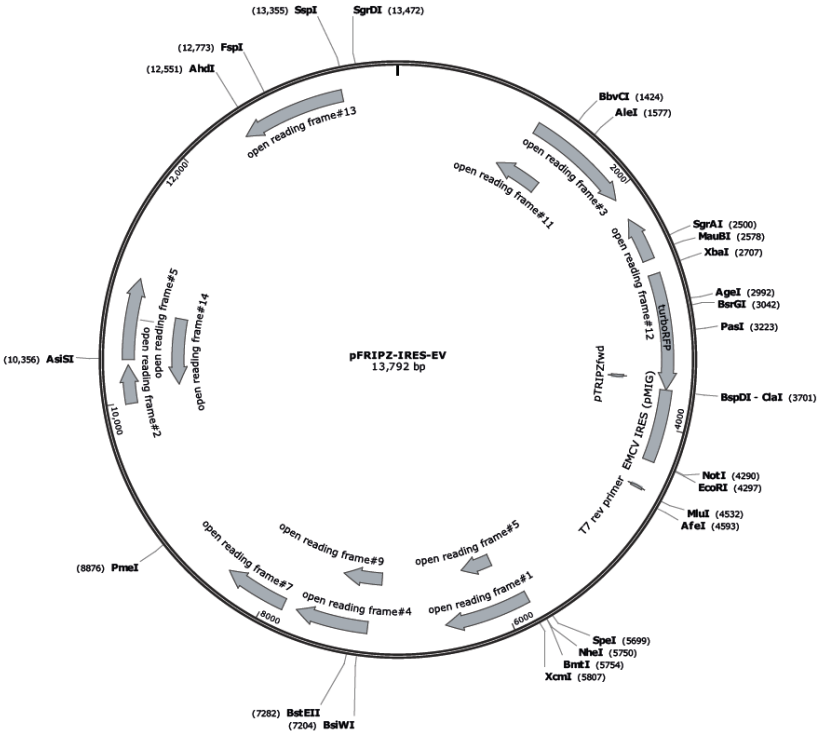

2. Full pFRIPZ-SV40-TAg:

3. Exemplary lentiviral packaging plasmid: pTLA1-Enz

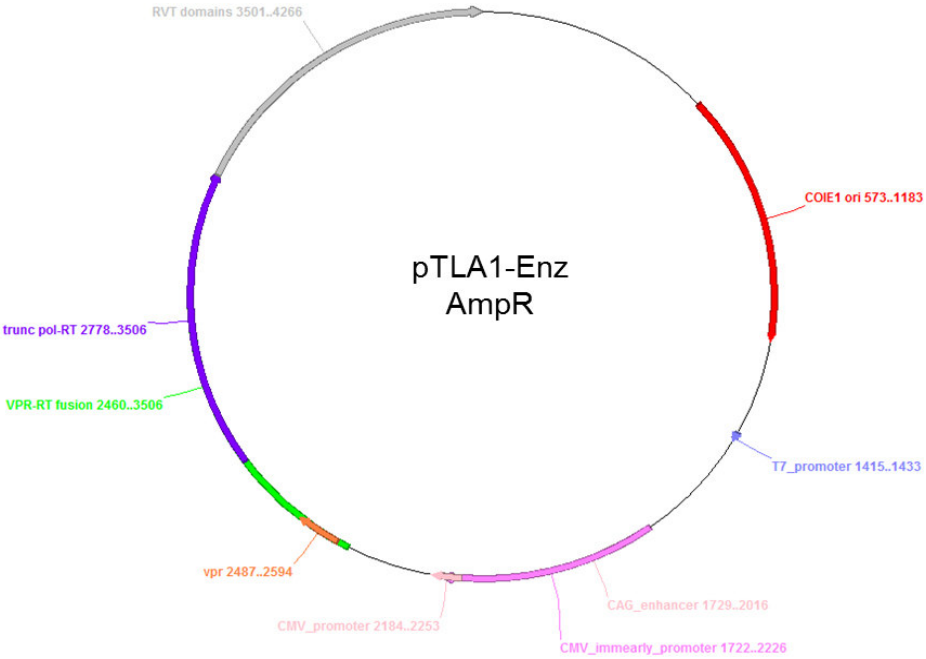

4. pCMV-VSV-G retroviral packaging plasmid:

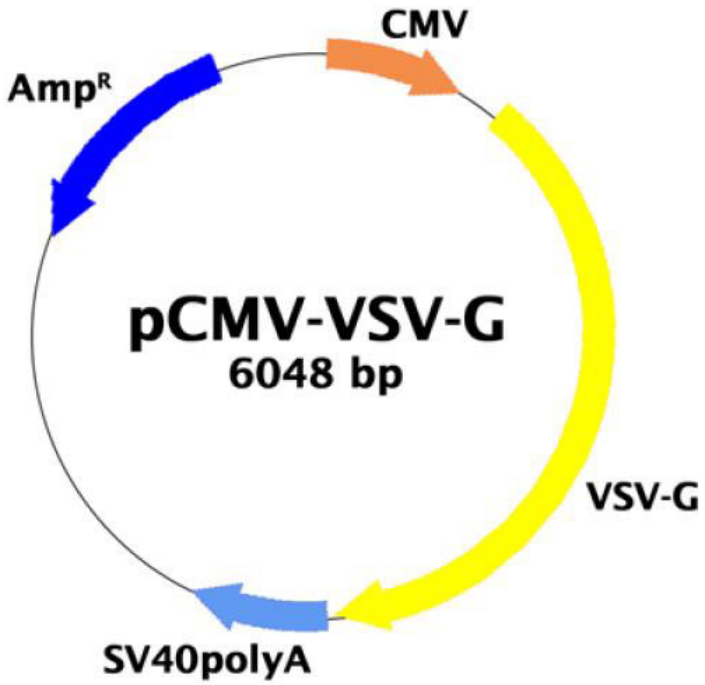

5. pGIPZ backbone of all shRNA constructs:

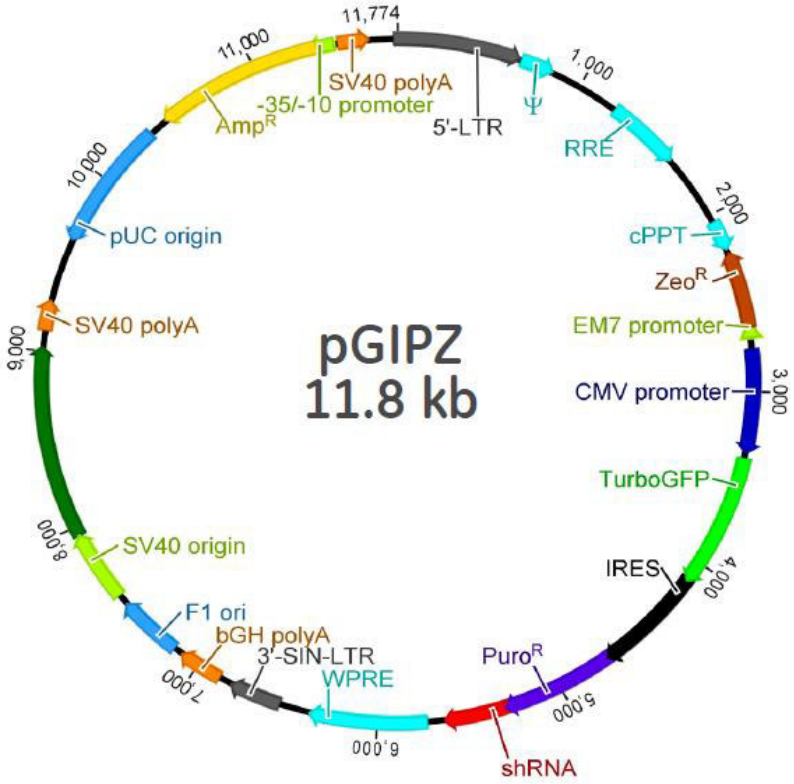

6. pBABE-hygro-hTERT:

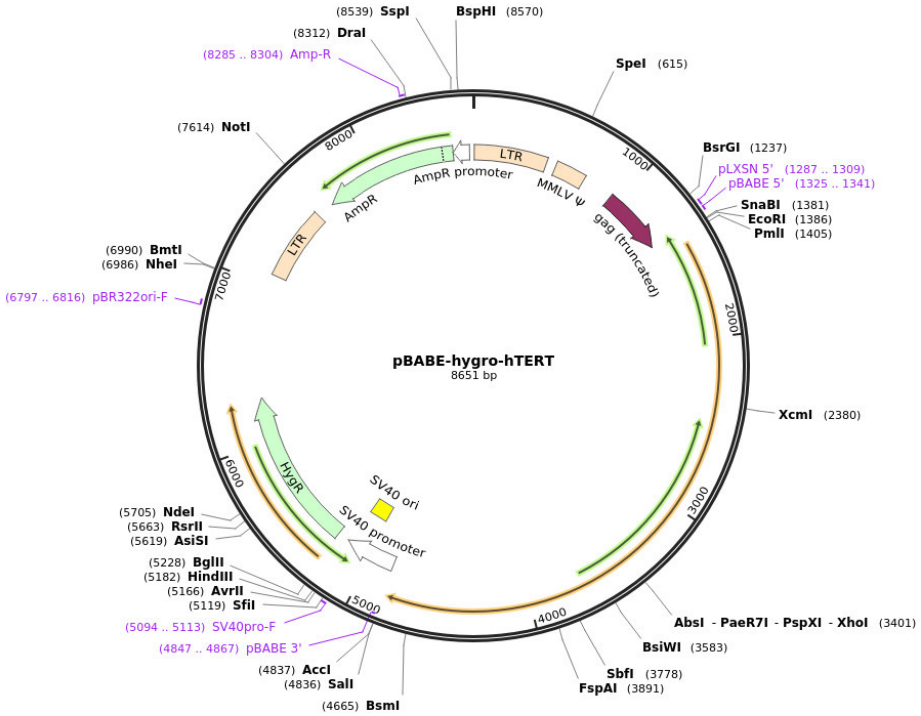

7. pGreenFire-CMV:

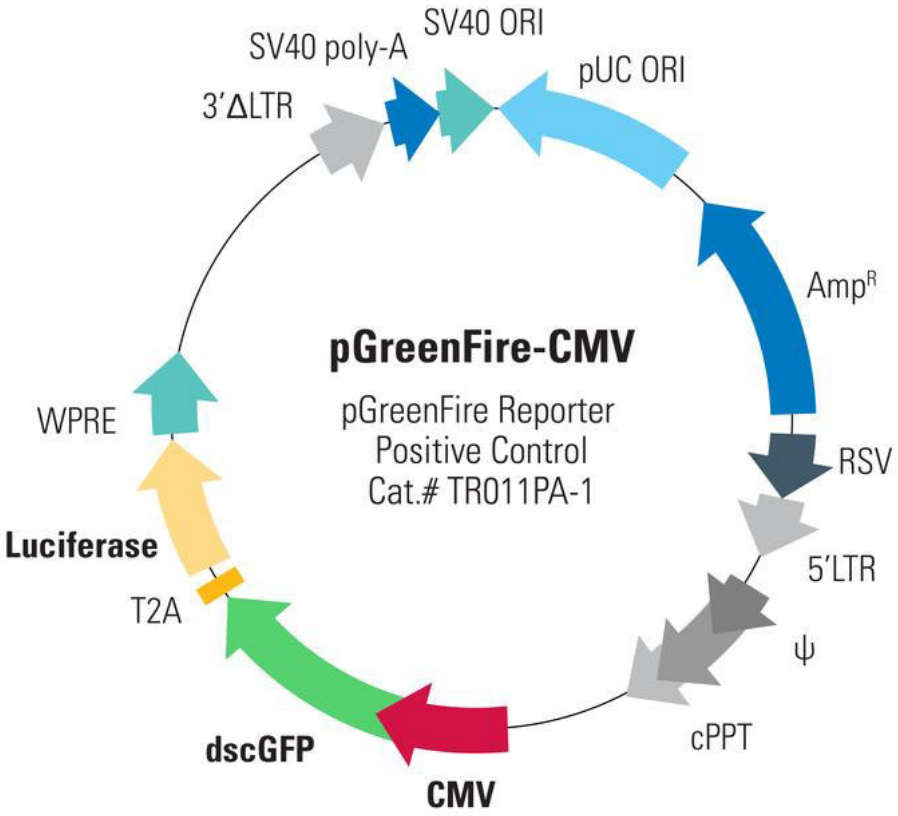

C) Clinical annotations of the multiplex PA cohort and normal brain

variable	n	% of total
samples	22	100
age (range: 1-16y, median: 4y)		
pediatric (<18y)	22	100
gender		
male	9	40.9
female	13	59.1
location		
infratentorial	9	40.9
- cerebellum	*5*	*22.7*
- 4th ventricle	*1*	*4.5*
- fossa posterior	*1*	*4.5*
- brain stem	*2*	*9.1*
supratentorial	10	45.5
- optic pathway	*2*	*9.1*
- diencephalon	*3*	*13.6*
- cerebral hemisphere	*2*	*9.1*
- 3rd ventricle	*1*	*4.5*
- parietooccipital	*1*	*4.5*
- suprasellar	*1*	*4.5*
NA	3	13.6
MAPK alteration		
KIAA-BRAF fusion	17	77.3
BRAF mutation	4	18.2
NF1	1	4.5
resection status		
sub-total	22	100
Normal brain samples	1	100
age	fetal	
gender		
female	1	100
location		
supratentorial	1	100
- cortex	1	100

D) Clinical annotations of IHC patient samples

variable	n	% of total
samples	14	100
age (range: 1-23y; median: 9y)		
pediatric (<18y)	10	71.4
adult (≥ 18y)	4	28.6
gender		
male	10	71.4
female	4	28.6
location		
infratentorial	7	50.0
- cerebellum	*6*	*42.9*
- brain stem	*1*	*7.1*
supratentorial	7	50.0
- fronal lobe	*2*	*14.3*
- temporal lobe	*2*	*14.3*
- occipital lobe	*1*	*7.1*
- 3rd ventricle	*1*	*7.1*
- 4th ventricle	*1*	*7.1*
MAPK alteration		
KIAA-BRAF fusion	3	21.4
unknown	11	78.6

E) Clinical annotations of the PA patient cohort (part 1)

SampleID_ICGC	Tumor Type_Diagnosis	Gender	Age	pedatric_vs_adult	Location	LocationGroup	Death	OS	Recurrence	PFS	BRAF_fusion	Fusion_Type	MAPK_alteration	MAPK_class	Trisomy_Yes_No	Radiation	Source
ICGC_PA3	PA	F	3	Ped	Cerebellum	Infra	0	28	0	28	1	16_9	1	BRAF_Fus	0	0	Heidelberg
ICGC_PA4	PA	M	1	Ped	Optic pathway	Supra	0	22	0	22	1	16_9	1	BRAF_Fus	0	0	Heidelberg
ICGC_PA5	PA	F	4	Ped	Optic pathway	Supra	0	16	1	11	0	0	1	NF1	0	0	Heidelberg
ICGC_PA8	PA	F	7	Ped	Cerebellum	Infra	0	18	0	18	1	15_9	1	BRAF_Fus	0	0	Heidelberg
ICGC_PA10	PA	F	3	Ped	Cerebellum	Infra	0	14	0	14	1	15_9	1	BRAF_Fus	0	0	Heidelberg
ICGC_PA11	PA	F	11	Ped	Cerebellum	Infra	0	21	0	21	1	16_9	1	BRAF_Fus	1	0	Heidelberg
ICGC_PA14	PA	F	5	Ped	3rd ventricle	Supra	0	23	0	23	1	15_9	1	BRAF_Fus	0	0	Heidelberg
ICGC_PA21	PA	F	15	Ped	Optic pathway	Supra	0	24	0	24	1	15_9	1	BRAF_Fus	0	1	Heidelberg
ICGC_PA22	PA	M	4	Ped	Cerebellum	Infra	0	22	0	22	1	15_9	1	BRAF_Fus	1	0	Heidelberg
ICGC_PA23	PA	F	1	Ped	Cerebellum	Infra	0	26	0	26	NA	NA	NA	NA	0	0	Heidelberg
ICGC_PA24	PA	M	2	Ped	Optic chiasm	Supra	0	21	0	21	1	16_9	1	BRAF_Fus	0	0	Heidelberg
ICGC_PA26	PA	F	3	Ped	Cerebellum	Infra	0	206	1	64	1	16_9	1	BRAF_Fus	0	0	Heidelberg
ICGC_PA27	PA	F	3	Ped	Optic nerve	Supra	0	219	0	219	0	0	1	BRAF_mut	0	1	Heidelberg
ICGC_PA28	PA	F	8	Ped	Cerebellum	Infra	0	1	0	1	1	16_9	1	BRAF_Fus	0	0	Heidelberg
ICGC_PA29	PA	M	12	Ped	Diencephalon	Supra	0	223	0	223	1	16_9	1	BRAF_Fus	0	0	Heidelberg
ICGC_PA30	PA	F	14	Ped	Cerebellum	Infra	0	207	0	207	1	GNAI1	1	BRAF_Fus	1	0	Heidelberg
ICGC_PA31	PA	M	9	Ped	4th ventricle	Infra	0	188	0	188	1	16_9	1	BRAF_Fus	0	0	Heidelberg
ICGC_PA33	PA	M	4	Ped	Cerebellum	Infra	0	176	0	176	1	16_9	1	BRAF_Fus	0	0	Heidelberg
ICGC_PA35	PA	M	16	Ped	Cerebellum	Infra	0	165	0	165	1	16_9	1	BRAF_Fus	1	0	Heidelberg
ICGC_PA39	PA	F	9	Ped	Cerebellum	Infra	0	254	0	254	1	16_9	1	BRAF_Fus	0	0	Heidelberg
ICGC_PA40	PA	M	3	Ped	Cerebellum	Infra	0	210	0	210	1	16_9	1	BRAF_Fus	0	0	Heidelberg
ICGC_PA41	PA	F	15	Ped	Brainstem	Infra	NA	NA	NA	NA	0	0	1	FGFR1	0	0	Heidelberg
ICGC_PA42	PA	M	3	Ped	Cerebellum	Infra	0	24	0	24	1	16_9	1	BRAF_Fus	0	0	Heidelberg
ICGC_PA48	PA	F	3	Ped	3rd ventricle	Supra	0	20	1	3	1	15_9	1	BRAF_Fus	0	0	Heidelberg

ICGC_PA9	PA	F	15	Ped	4th ventricle	Infra	0	23	0	23	1	15_9	1	BRAF_Fus	0	0	Heidelberg
ICGC_PA17	PA	M	4	Ped	Brainstem	Infra	0	24	0	24	1	16_9	1	BRAF_Fus	0	1	Heidelberg
ICGC_PA20	PA	F	23	Ad	Optic pathway	Supra	0	23	0	23	1	16_9	1	BRAF_Fus	0	0	Heidelberg
ICGC_PA36	PA	F	11	Ped	Cerebellum	Infra	0	183	0	183	1	16_9	1	BRAF_Fus	1	0	Heidelberg
ICGC_PA43	PA	F	6	Ped	Brainstem	Infra	0	24	1	10	1	15_9	1	BRAF_Fus	0	1	Heidelberg
ICGC_PA44	PA	F	0.8	Ped	Cerebral Hemisphere	Supra	0	16	0	16	NA	NA	NA	NA	NA	0	Heidelberg
ICGC_PA50	PA	M	6	Ped	Brainstem	Infra	0	22	1	4	1	16_9	1	BRAF_Fus	0	1	Heidelberg
ICGC_PA52	PA	F	6	Ped	Cerebellum	Infra	0	12	1	5	1	NA	1	BRAF_Fus	0	1	Heidelberg
ICGC_PA53	PA	M	10	Ped	Cerebellum	Infra	0	15	0	15	1	16_11	1	BRAF_Fus	0	0	Heidelberg
ICGC_PA55	PA	F	5	Ped	Cerebellum	Infra	0	24	1	4	1	16_9	1	BRAF_Fus	0	1	Heidelberg
ICGC_PA56	PA	M	9	Ped	Cerebellum	Infra	0	12	0	12	1	16_9	1	BRAF_Fus	0	0	Heidelberg
ICGC_PA57	PA	F	6	Ped	Cerebellum	Infra	0	14	1	8	1	19_9	1	BRAF_Fus	0	0	Heidelberg
ICGC_PA58	PA	M	13	Ped	Brainstem	Infra	0	12	0	12	1	MKRN1	1	BRAF_Fus	1	0	Heidelberg
ICGC_PA59	PA	F	5	Ped	Cerebellum	Infra	0	24	0	24	1	15_9	1	BRAF_Fus	0	1	Heidelberg
ICGC_PA63	PA	F	17	Ped	Brainstem	Infra	0	12	0	12	1	16_11	1	BRAF_Fus	1	1	Heidelberg
ICGC_PA65	PA	M	16	Ped	Optic pathway	Supra	0	10	0	10	0	0	1	BRAF_mut	1	0	Heidelberg
ICGC_PA70	PA	M	6	Ped	Cerebellum	Infra	0	12	0	12	1	16_9	1	BRAF_Fus	0	0	Heidelberg
ICGC_PA69	PA	F	6	Ped	Diencephalon	Supra	0	17	1	17	0	0	1	FGFR1	0	0	Heidelberg
ICGC_PA74	PA	M	7	Ped	Cerebellum	Infra	0	12	0	12	1	16_9	1	BRAF_Fus	NA	0	Heidelberg
ICGC_PA79	PA	M	6	Ped	Cerebellum	Infra	0	8	0	8	1	16_11	1	BRAF_Fus	0	0	Heidelberg
ICGC_PA81	PA	M	14	Ped	Cerebellum	Infra	0	10	0	10	1	18_10	1	BRAF_Fus	0	0	Heidelberg
2A1	PA	M	21	Ad	Cerebellum	Infra	0	70	0	70	0	0	0	NA	NA		Heidelberg
2A2	PA	F	5	Ped	Cerebellum	Infra	0	38	0	38	1	16_9	1	BRAF_Fus	0		Heidelberg
2A3	PA	M	4	Ped	Cerebellum	Infra	0	48	0	48	1	16_9	1	BRAF_Fus	0		Heidelberg
2A4	PA	M	10	Ped	Cerebellum	Infra	0	54	0	54	1	15_9	1	BRAF_Fus	0		Heidelberg
2A8	PA	M	4	Ped	Cerebellum	Infra	0	80	0	80	1	16_9	1	BRAF_Fus	0		Heidelberg
2A9	PA	F	6	Ped	Cerebellum	Infra	0	28	0	28	1	16_9	1	BRAF_Fus	0		Heidelberg
2A11	PA	M	9	Ped	Cerebellum	Infra	0	62	0	62	1	16_9	1	BRAF_Fus	0		Heidelberg
2A14	PA	M	17	Ped	Cerebral Hemisphere	Supra	0	6	0	6	0	0	0	NA	NA		Heidelberg
2A18	PA	F	4	Ped	Cerebellum	Infra	0	48	0	48	1	16_9	1	BRAF_Fus	1		Heidelberg
2A23	PA	M	16	Ped	Cerebral Hemisphere	Supra	0	94	0	94	1	FAM	1	BRAF_Fus	0		Heidelberg
2A24	PA	M	2	Ped	Cerebellum	Infra	0	93	0	93	1	15_9	1	BRAF_Fus	0		Heidelberg

2A27	PA	F	11	Ped	Cerebellum	Infra	0	26	0	26	1	15_9	1	BRAF_Fus	0		Heidelberg
2A34	PA	M	16	Ped	Cerebellum	Infra	0	42	1	9	1	16_9	1	BRAF_Fus	0		Heidelberg
2A35	PA	M	14	Ped	Cerebral Hemisphere	Supra	0	96	0	96	0	0	1	BRAF_mut	0		Heidelberg
2A38	PA	F	2	Ped	Diencephalon	Supra	1	24	1	22	1	NA	1	BRAF_Fus	0		Heidelberg
2A40	PA	M	13	Ped	Cerebellum	Infra	0	37	0	37	1	16_9	1	BRAF_Fus	1		Heidelberg
2A42	PA	M	3	Ped	Diencephalon	Supra	0	37	1	12	1	NA	1	BRAF_Fus	0		Heidelberg
2A43	PA	M	19	Ad	Cerebellum	Infra	0	12	0	12	1	15_9	1	BRAF_Fus	0		Heidelberg
2A44	PA	M	11	Ped	Cerebellum	Infra	0	8	0	8	1	16_11	1	BRAF_Fus	1		Heidelberg
2A46	PA	F	3	Ped	Diencephalon	Supra	0	58	1	36	1	15_9	1	BRAF_Fus	0		Heidelberg
2A47	PA	F	17	Ped	Cerebellum	Infra	0	63	1	23	0	0	1	BRAF_mut	1		Heidelberg
2A48	PA	F	12	Ped	Diencephalon	Supra	0	48	0	48	1	16_9	1	BRAF_Fus	0		Heidelberg
2A50	PA	F	22	Ad	Cerebellum	Infra	0	40	0	40	1	16_9	1	BRAF_Fus	0		Heidelberg
2A52	PA	F	11	Ped	Cerebellum	Infra	0	63	0	63	0	0	1	KRAS_mut	1		Heidelberg
2A59	PA	M	10	Ped	Cerebellum	Infra	0	41	1	25	1	16_9	1	BRAF_Fus	0		Heidelberg
2A60	PA	F	3	Ped	Diencephalon	Supra	0	51	0	51	0	0	1	BRAF_mut	0		Heidelberg
2A61	PA	M	2	Ped	Cerebellum	Infra	0	81	1	48	1	16_9	1	BRAF_Fus	0		Heidelberg
2A62	PA	M	4	Ped	Cerebellum	Infra	0	33	0	33	1	16_9	1	BRAF_Fus	0		Heidelberg
2A63	PA	M	6	Ped	Cerebellum	Infra	0	81	0	81	1	16_9	1	BRAF_Fus	0		Heidelberg
2A64	PA	M	5	Ped	Cerebellum	Infra	0	68	1	36	1	16_9	1	BRAF_Fus	0		Heidelberg
2A68	PA	M	7	Ped	Brainstem	Infra	0	84	1	57	1	15_9	1	BRAF_Fus	1		Heidelberg
2A69	PA	F	8	Ped	Cerebral Hemisphere	Supra	0	81	0	81	1	15_9	1	BRAF_Fus	0		Heidelberg
ICGC_PA128	PA	F	20	Ad	Cerebellum	Infra	0	224	0	224	1	16_9	1	BRAF_Fus	0	0	Heidelberg
ICGC_PA129	PA	M	25	Ad	Cerebellum	Infra	0	181	0	181	1	16_11	1	BRAF_Fus	1	0	Heidelberg
ICGC_PA130	PA	F	26	Ad	Cerebellum	Infra	0	177	0	177	1	16_9	1	BRAF_Fus	1	0	Heidelberg
ICGC_PA131	PA	F	20	Ad	Cerebellum	Infra	0	12	0	12	1	16_9	1	BRAF_Fus	1	0	Heidelberg
ICGC_PA132	PA	F	12	Ped	Cerebral Hemisphere	Supra	0	161	0	161	0	0	1	NF1	1	1	Heidelberg
ICGC_PA133	PA	F	26	Ad	Cerebellum	Infra	0	254	1	41	1	15_9	1	BRAF_Fus	1	1	Heidelberg
ICGC_PA82	PA	M	12	Ped	Optic pathway	Supra	0	7	0	7	0	0	1	NTRK2	0	0	Heidelberg
ICGC_PA83	PA	F	8	Ped	Brainstem	Infra	0	12	0	12	1	16_9	1	BRAF_Fus	0	0	Heidelberg
ICGC_PA85	PA	F	4	Ped	Cerebellum	Infra	0	7	0	7	1	15_9	1	BRAF_Fus	0	0	Heidelberg
ICGC_PA86	PA	M	11	Ped	Cerebellum	Infra	0	8	0	8	1	15_9	1	BRAF_Fus	0	0	Heidelberg
ICGC_PA87	PA	F	4	Ped	Cerebellum	Infra	0	10	0	10	1	16_9	1	BRAF_Fus	0	0	Heidelberg

ICGC_PA88	PA	F	6	Ped	Cerebellum	Infra	0	8	0	8	1	15_9	1	BRAF_Fus	0	0	Heidelberg
ICGC_PA89	PA	M	8	Ped	Brainstem	Infra	0	6	0	6	0	0	1	FGFR1	0	0	Heidelberg
ICGC_PA91	PA	F	3	Ped	Brainstem	Infra	0	6	0	6	1	16_9	1	BRAF_Fus	0	0	Heidelberg
ICGC_PA92	PA	M	12	Ped	4th ventricle	Infra	0	4	0	4	0	0	1	FGFR1	1	0	Heidelberg
ICGC_PA93	PA	F	21	Ad	Cerebellum	Infra	0	7	0	7	1	15_9	1	BRAF_Fus	0	0	Heidelberg
ICGC_PA94	PA	F	4	Ped	Cerebellum	Infra	0	14	1	14	1	15_9	1	BRAF_Fus	0	0	Heidelberg
ICGC_PA95	PA	F	7	Ped	Cerebellum	Infra	0	8	0	8	1	19_9	1	BRAF_Fus	0	0	Heidelberg
ICGC_PA96	PA	F	15	Ped	Brainstem	Infra	0	7	0	7	1	RNF130	1	BRAF_Fus	0	0	Heidelberg
ICGC_PA97	PA	F	8	Ped	Cerebellum	Infra	0	12	0	12	1	16_9	1	BRAF_Fus	0	0	Heidelberg
ICGC_PA99	PA	M	9	Ped	Cerebellum	Infra	0	7	0	7	1	16_9	1	BRAF_Fus	0	0	Heidelberg
ICGC_PA100	PA	F	1	Ped	Cerebellum	Infra	0	11	0	11	1	15_9	1	BRAF_Fus	0	0	Heidelberg
ICGC_PA102	PA	M	15	Ped	Cerebellum	Infra	0	4	0	4	1	FAM131B	1	BRAF_Fus	0	0	Heidelberg
ICGC_PA103	PA	M	7	Ped	3rd ventricle	Supra	0	8	0	8	1	16_9	1	BRAF_Fus	0	0	Heidelberg
ICGC_PA105	PA	F	13	Ped	Cerebellum	Infra	0	4	0	4	1	15_9	1	BRAF_Fus	0	0	Heidelberg
ICGC_PA106	PA	M	12	Ped	Cerebellum	Infra	0	4	0	4	1	NA	1	BRAF_Fus	NA	0	Heidelberg
ICGC_PA107	PA	F	4	Ped	3rd ventricle	Supra	0	8	0	8	1	13_9	1	BRAF_Fus	0	0	Heidelberg
ICGC_PA108	PA	F	5	Ped	Brainstem	Infra	0	4	0	4	1	16_9	1	BRAF_Fus	0	0	Heidelberg
ICGC_PA109	PA	F	5	Ped	Cerebellum	Infra	0	9	0	9	1	16_9	1	BRAF_Fus	0	0	Heidelberg
ICGC_PA110	PA	M	12	Ped	Cerebellum	Infra	0	3	0	3	1	16_9	1	BRAF_Fus	0	0	Heidelberg
ICGC_PA112	PA	M	14	Ped	Cerebral Hemisphere	Supra	0	8	0	8	1	RNF130	1	BRAF_Fus	0	0	Heidelberg
ICGC_PA113	PA	F	1	Ped	Spine	Spine	0	3	0	3	NA	NA	1	BRAF_mut	NA	0	Heidelberg
ICGC_PA116	PA	F	50	Ad	Cerebellum	Infra	0	6	0	6	1	16_11	1	BRAF_Fus	1	0	Heidelberg
ICGC_PA117	PA	F	40	Ad	4th ventricle	Infra	0	4	0	4	0	0	1	KRAS_mut	0	0	Heidelberg
ICGC_PA118	PA	F	7	Ped	Optic nerve	Supra	0	NA	NA	NA	1	NA	1	BRAF_Fus	1	0	Heidelberg
ICGC_PA166	PA	F	8	Ped	Diencephalon	Supra	0	31	1	4	0	0	1	FGFR1	0	1	Heidelberg
jm110324njo016	PA	M	21	Ad	Cerebellum	Infra					1	16_9	1	BRAF_Fus			Montreal
jm110324njo017	PA	F	33	Ad	Cerebellum	Infra					0						Montreal
jm110324njo018	PA	F	11	Ped	Cerebellum	Infra					1	15_9	1	BRAF_Fus			Montreal
jm110324njo020	PA	F	19	Ad	Thalamus	Supra					0						Montreal
jm110324njo021	PA	F	45	Ad	Cerebellum	Infra					0						Montreal
jm110324njo022	PA	M	19	Ad	Thalamus	Supra					0						Montreal
jm110324njo023	PA	M	45	Ad	Cerebellum	Infra					0						Montreal
jm110324njo024	PA	M	20	Ad	Cerebellum	Infra					1	15_9	1	BRAF_Fus			Montreal
jm110324njo025	PA	M	4	Ped	Brainstem	Infra					1	16_9	1	BRAF_Fus			Montreal

jm110324njo028	PA	M	1	Ped	Cerebellum	Infra					1	15_9	1	BRAF_Fus			Montreal
jm110324njo029	PA	F	12	Ped	Cerebellum	Infra					1	16_9	1	BRAF_Fus			Montreal
jm110324njo030	PA	M	2	Ped	Cerebellum	Infra					1	16_9	1	BRAF_Fus			Montreal
jm110324njo032	PA	NA	4	Ped	NA	Infra					1	NA	1	BRAF_Fus			Montreal
jm110324njo034	PA	M	8	Ped	Optic pathway	Supra					0						Montreal
jm110324njo037	PA	M	0.3	Ped	Cerebral Hemisphere	Supra					0		1	NF1			Montreal
jm110324njo043	PA	F	1	Ped	NA	Infra					1	NA	1	BRAF_Fus			Montreal
jm110324njo044	PA	M	0.9	Ped	suprasellar	Supra					1	15_9	1	BRAF_Fus			Montreal
jm110324njo047	PA	F	1	Ped	3rd ventricle	Supra					1	16_11	1	BRAF_Fus			Montreal
jm110324njo050	PA	M	25	Ad	Cerebellum	Infra					0						Montreal
jm110324njo051	PA	F	4	Ped	Cerebellum	Infra					1	16_9	1	BRAF_Fus			Montreal
jm110324njo052	PA	F	17	Ped	Cerebellum	Infra					1	16_9	1	BRAF_Fus			Montreal

Clinical annotations of the PA patient cohort (part 2)

Sample ID	Tumor Type_Diagnosis	Source	Published in:	GSE #
gsm405306	PA	Rotterdam	Gravendeel et al., PMID 19920198	GSE16011
gsm405346	PA	Rotterdam	Gravendeel et al., PMID 19920198	GSE16011
gsm405348	PA	Rotterdam	Gravendeel et al., PMID 19920198	GSE16011
gsm405480	PA	Rotterdam	Gravendeel et al., PMID 19920198	GSE16011
gsm405481	PA	Rotterdam	Gravendeel et al., PMID 19920198	GSE16011
gsm405482	PA	Rotterdam	Gravendeel et al., PMID 19920198	GSE16011
gsm405483	PA	Rotterdam	Gravendeel et al., PMID 19920198	GSE16011
gsm132714	PA	St. Louis	Sharma et al., PMID 17283119	GSE5675
gsm132715	PA	St. Louis	Sharma et al., PMID 17283119	GSE5675
gsm132716	PA	St. Louis	Sharma et al., PMID 17283119	GSE5675
gsm132717	PA	St. Louis	Sharma et al., PMID 17283119	GSE5675
gsm132718	PA	St. Louis	Sharma et al., PMID 17283119	GSE5675
gsm132719	PA	St. Louis	Sharma et al., PMID 17283119	GSE5675
gsm132720	PA	St. Louis	Sharma et al., PMID 17283119	GSE5675
gsm132722	PA	St. Louis	Sharma et al., PMID 17283119	GSE5675
gsm132723	PA	St. Louis	Sharma et al., PMID 17283119	GSE5675
gsm132728	PA	St. Louis	Sharma et al., PMID 17283119	GSE5675
gsm132729	PA	St. Louis	Sharma et al., PMID 17283119	GSE5675
gsm132730	PA	St. Louis	Sharma et al., PMID 17283119	GSE5675
gsm132733	PA	St. Louis	Sharma et al., PMID 17283119	GSE5675
gsm132736	PA	St. Louis	Sharma et al., PMID 17283119	GSE5675
gsm132738	PA	St. Louis	Sharma et al., PMID 17283119	GSE5675
gsm132741	PA	St. Louis	Sharma et al., PMID 17283119	GSE5675
gsm132744	PA	St. Louis	Sharma et al., PMID 17283119	GSE5675
gsm132747	PA	St. Louis	Sharma et al., PMID 17283119	GSE5675
gsm132748	PA	St. Louis	Sharma et al., PMID 17283119	GSE5675
gsm132750	PA	St. Louis	Sharma et al., PMID 17283119	GSE5675
gsm132751	PA	St. Louis	Sharma et al., PMID 17283119	GSE5675

gsm132752	PA	St. Louis	Sharma et al., PMID 17283119	GSE5675
gsm132753	PA	St. Louis	Sharma et al., PMID 17283119	GSE5675
gsm132754	PA	St. Louis	Sharma et al., PMID 17283119	GSE5675
gsm132759	PA	St. Louis	Sharma et al., PMID 17283119	GSE5675
gsm132761	PA	St. Louis	Sharma et al., PMID 17283119	GSE5675
gsm132763	PA	St. Louis	Sharma et al., PMID 17283119	GSE5675
gsm132765	PA	St. Louis	Sharma et al., PMID 17283119	GSE5675
gsm132768	PA	St. Louis	Sharma et al., PMID 17283119	GSE5675
gsm132769	PA	St. Louis	Sharma et al., PMID 17283119	GSE5675
gsm132770	PA	St. Louis	Sharma et al., PMID 17283119	GSE5675
gsm132771	PA	St. Louis	Sharma et al., PMID 17283119	GSE5675
gsm132772	PA	St. Louis	Sharma et al., PMID 17283119	GSE5675
gsm132773	PA	St. Louis	Sharma et al., PMID 17283119	GSE5675
gsm132774	PA	St. Louis	Sharma et al., PMID 17283119	GSE5675
gsm132775	PA	St. Louis	Sharma et al., PMID 17283119	GSE5675
gsm132776	PA	St. Louis	Sharma et al., PMID 17283119	GSE5675
gsm132777	PA	St. Louis	Sharma et al., PMID 17283119	GSE5675
gsm132778	PA	St. Louis	Sharma et al., PMID 17283119	GSE5675
gsm132779	PA	St. Louis	Sharma et al., PMID 17283119	GSE5675
gsm132780	PA	St. Louis	Sharma et al., PMID 17283119	GSE5675

F) IPA upstream regulator

rank	gene	p-value of overlap	predicted effect	z-score
Condition: DEXA + OIS				
1	*IL1B*	5,83E-24	inhibited	-3.77
2	*TREM1*	4.01E-22	NA	-1.311
3	*TNF*	1,39E-21	inhibited	-2.976
4	NFKB (complex)	3.37E-20	inhibited	-3.989
5	*RELA*	6.69E-17	inhibited	-2.032
Condition: rIL-1B + proliferation				
1	*TNF*	1,20E-42	activated	7.417
2	*IL1B*	1,66E-34	activated	6.263
3	*TREM1*	4,24E-30	activated	3.721
4	*IL1A*	8,21E-29	activated	5.298
5	NFKB (complex)	3,49E-29	activated	5.074

G) Univariate analysis of *IL1B* and SASP in the PA cohort

variable				n	events	HR	lower CI	upper CI	p-value
IL1B (continuous)				110	21	0.40	0.24	0.69	**0.0008**
IL1B (grouped)	high	vs.	low	110	21	0.28	0.11	0.73	**0.0097**
SASP (continuous)				110	21	0.56	0.34	0.93	**0.0256**
SASP (grouped)	intermediate	vs.	low	110	21	0.53	0.20	1.37	0.1867
	high	vs.	low			0.19	0.05	0.69	**0.0119**
	high	vs.	intermediate			0.36	0.09	1.42	0.1460
age (continuous)				110	21	0.93	0.86	1.01	0.0702
gender	male	vs.	female	110	21	0.53	0.21	1.32	0.1726
resection status	STR	vs.	GTR	93	20	4.52	1.63	12.50	**0.0037**
location grouped	supratentorial	vs.	infratentorial	109	21	1.51	0.61	3.73	0.3774
MAPK alteration	BRAF_fusion	vs.	other	108	21	0.77	0.26	2.29	0.6369
radiation	yes	vs.	no	78	12	5.19	1.67	16.14	**0.0045**
chemotherapy	yes	vs.	no	18	3	5.48	0.49	61.76	0.1687

H) Cox proportional hazards model for progression-free surival (PFS) - multivariate analysis of *IL1B* and resection status in the PA cohort (n=90 patients)

variable				HR	lower CI	upper CI	p-value
IL1B (continuous)				0.37	0.18	0.75	**0.0056**
resection status	STR	vs.	GTR	4.61	1.45	14.62	**0.0095**
gender	male	vs.	female	0.47	0.17	1.33	0.1500
age				0.94	0.86	1.04	0.2500
location	supratentorial	vs.	infratentorial	0.60	0.19	1.85	0.3700
MAPK alteration	BRAF_fusion	vs.	other	0.59	0.17	2.09	0.4100

I) Cox proportional hazards model for progression-free surival (PFS) - multivariate analysis of *IL1B* and radiation in the PA cohort (n= 75 patients)

variable				HR	lower CI	upper CI	p-value
IL1B (continuous)				0.35	0.15	0.77	**0.0079**
radiation	yes	vs.	no	2.99	0.75	10.99	0.1155
gender	male	vs.	female	0.29	0.03	1.32	0.1163
age (continuous)				0.92	0.80	1.02	0.1592
location	supratentorial	vs.	infratentorial	0.80	0.06	4.16	0.8154
MAPK alteration	BRAF_fusion	vs.	other	0.39	0.02	4.20	0.4394

J) Cox proportional hazards model for progression-free surival (PFS) - multivariate analysis of SASP and resection status in the PA cohort (n= 90 patients)

variable				HR	lower CI	upper CI	p-value
SASP (continuous)				0.36	0.16	0.82	**0.0100**
resection status	STR	vs.	GTR	5.17	1.56	17.11	**0.0072**
gender	male	vs.	female	0.64	0.23	1.80	0.4000
age (continuous)				0.96	0.86	1.06	0.3800
location	supratentorial	vs.	infratentorial	1.30	0.40	4.24	0.6600
MAPK alteration	BRAF_fusion	vs.	other	0.65	0.19	2.27	0.5000

K) Cox proportional hazards model for progression-free surival (PFS) - multivariate analysis of SASP and radiation in the PA cohort (n= 75 patients)

variable				HR	lower CI	upper CI	p-value
SASP (continuous)				0.19	0.06	0.52	**0.0006**
radiation	yes	vs.	no	4.84	1.50	16.37	**0.0092**
gender	male	vs.	female	0.30	0.03	1.55	0.1687
age (continuous)				0.92	0.79	1.03	0.1544
location	supratentorial	vs.	infratentorial	6.70	0.44	68.95	0.1436
MAPK alteration	BRAF_fusion	vs.	other	0.42	0.03	3.54	0.4320

L) Cox proportional hazards model for progression-free surival (PFS) - multivariate analysis of SASP, resection status and radiation in the PA cohort (n=58 patients)

variable				HR	lower CI	upper CI	p-value
SASP (continuous)				0.19	0.03	0.72	**0.0100**
resection status	STR	vs.	GTR	0.08	0.01	0.71	**0.024**
radiation	1	vs.	0	48.39	5.83	644.98	**0.0005**
gender	M	vs.	F	0.36	0.02	2.19	0.2943
age (continuous)				0.75	0.55	0.93	0.0230
location	supratentorial	vs.	infratentorial	53.73	1.81	3833.55	0.0230
MAPK alteration	BRAF_fusion	vs.	other	0.15	0.01	1.24	0.0793

Abbreviations:
HR= hazard ratio
CI = confidence interval
STR = sub-total resection
GTR = gross-total resection

REFERENCES

1. Kaatsch P, Grabow D., Spix C. German Childhood Cancer Registry - Annual Report 2017 (1980-2016). Institute of Medical Biostatistics, Epidemiology and Informatics (IMBEI) at the University Medical Center of the Johannes Gutenberg University Mainz **2018**.

2. Rossig C, Juergens H, Schrappe M, Moericke A, Henze G, von Stackelberg A*, et al.* Effective childhood cancer treatment: the impact of large scale clinical trials in Germany and Austria. Pediatr Blood Cancer **2013**;60(10):1574-81 doi 10.1002/pbc.24598.

3. Louis DN, Perry A, Reifenberger G, von Deimling A, Figarella-Branger D, Cavenee WK*, et al.* The 2016 World Health Organization Classification of Tumors of the Central Nervous System: a summary. Acta neuropathologica **2016**;131(6):803-20 doi 10.1007/s00401-016-1545-1.

4. Capper D, Jones DTW, Sill M, Hovestadt V, Schrimpf D, Sturm D*, et al.* DNA methylation-based classification of central nervous system tumours. Nature **2018**;555(7697):469-74 doi 10.1038/nature26000.

5. Hovestadt V, Remke M, Kool M, Pietsch T, Northcott PA, Fischer R*, et al.* Robust molecular subgrouping and copy-number profiling of medulloblastoma from small amounts of archival tumour material using high-density DNA methylation arrays. Acta Neuropathol **2013**;125(6):913-6 doi 10.1007/s00401-013-1126-5.

6. Sahm F, Schrimpf D, Jones DT, Meyer J, Kratz A, Reuss D*, et al.* Next-generation sequencing in routine brain tumor diagnostics enables an integrated diagnosis and identifies actionable targets. Acta Neuropathol **2016**;131(6):903-10 doi 10.1007/s00401-015-1519-8.

7. International Cancer Genome C, Hudson TJ, Anderson W, Artez A, Barker AD, Bell C*, et al.* International network of cancer genome projects. Nature **2010**;464(7291):993-8 doi 10.1038/nature08987.

8. Sturm D, Orr BA, Toprak UH, Hovestadt V, Jones DTW, Capper D*, et al.* New Brain Tumor Entities Emerge from Molecular Classification of CNS-PNETs. Cell **2016**;164(5):1060-72 doi 10.1016/j.cell.2016.01.015.

9. Stratton MR, Campbell PJ, Futreal PA. The cancer genome. Nature **2009**;458(7239):719-24 doi 10.1038/nature07943.

10. Baker SJ, Ellison DW, Gutmann DH. Pediatric gliomas as neurodevelopmental disorders. Glia **2016**;64(6):879-95 doi 10.1002/glia.22945.

11. Alexandrov LB, Nik-Zainal S, Wedge DC, Aparicio SA, Behjati S, Biankin AV*, et al.* Signatures of mutational processes in human cancer. Nature **2013**;500(7463):415-21 doi 10.1038/nature12477.

12. Ostrom QT, de Blank PM, Kruchko C, Petersen CM, Liao P, Finlay JL*, et al.* Alex's Lemonade Stand Foundation Infant and Childhood Primary Brain and Central Nervous System Tumors Diagnosed in the United States in 2007-2011. Neuro-oncology **2015**;16 Suppl 10:x1-x36 doi 10.1093/neuonc/nou327.

13. Jones DTW, Kieran MW, Bouffet E, Alexandrescu S, Bandopadhayay P, Bornhorst M*, et al.* Pediatric low-grade gliomas: next biologically driven steps. Neuro-oncology **2018**;20(2):160-73 doi 10.1093/neuonc/nox141.

14. Jones DT, Hutter B, Jager N, Korshunov A, Kool M, Warnatz HJ*, et al.* Recurrent somatic alterations of FGFR1 and NTRK2 in pilocytic astrocytoma. Nat Genet **2013**;45(8):927-32 doi 10.1038/ng.2682.

15. Zhang J, Wu G, Miller CP, Tatevossian RG, Dalton JD, Tang B*, et al.* Whole-genome sequencing identifies genetic alterations in pediatric low-grade gliomas. Nature genetics **2013**;45(6):602-12 doi 10.1038/ng.2611.

16. Qaddoumi I, Orisme W, Wen J, Santiago T, Gupta K, Dalton JD*, et al.* Genetic alterations in uncommon low-grade neuroepithelial tumors: BRAF, FGFR1, and MYB mutations occur at high frequency and align with morphology. Acta neuropathologica **2016**;131(6):833-45 doi 10.1007/s00401-016-1539-z.

17. Ostrom QT, Gittleman H, Liao P, Vecchione-Koval T, Wolinsky Y, Kruchko C*, et al.* CBTRUS Statistical Report: Primary brain and other central nervous system tumors diagnosed in the United States in 2010-2014. Neuro-oncology **2017**;19(suppl_5):v1-v88 doi 10.1093/neuonc/nox158.

18. Jones DT, Gronych J, Lichter P, Witt O, Pfister SM. MAPK pathway activation in pilocytic astrocytoma. Cell Mol Life Sci **2012**;69(11):1799-811 doi 10.1007/s00018-011-0898-9.

19. Jacob K, Quang-Khuong DA, Jones DT, Witt H, Lambert S, Albrecht S*, et al.* Genetic aberrations leading to MAPK pathway activation mediate oncogene-induced senescence in sporadic pilocytic astrocytomas. Clin Cancer Res **2011**;17(14):4650-60 doi 10.1158/1078-0432.CCR-11-0127.

20. Gnekow AK, Falkenstein F, von Hornstein S, Zwiener I, Berkefeld S, Bison B*, et al.* Long-term follow-up of the multicenter, multidisciplinary treatment study HIT-LGG-1996 for low-grade glioma in children and adolescents of the German Speaking Society of Pediatric Oncology and Hematology. Neuro Oncol **2012**;14(10):1265-84 doi 10.1093/neuonc/nos202.

21. Armstrong GT, Conklin HM, Huang S, Srivastava D, Sanford R, Ellison DW*, et al.* Survival and long-term health and cognitive outcomes after low-grade glioma. Neuro Oncol **2011**;13(2):223-34 doi 10.1093/neuonc/noq178.

22. Jones DT, Kocialkowski S, Liu L, Pearson DM, Backlund LM, Ichimura K*, et al.* Tandem duplication producing a novel oncogenic BRAF fusion gene defines the majority of pilocytic astrocytomas. Cancer Res **2008**;68(21):8673-7 doi 10.1158/0008-5472.CAN-08-2097.

23. Kaul A, Chen YH, Emnett RJ, Dahiya S, Gutmann DH. Pediatric glioma-associated KIAA1549:BRAF expression regulates neuroglial cell growth in a cell type-specific and mTOR-dependent manner. Genes Dev **2012**;26(23):2561-6 doi 10.1101/gad.200907.112.

24. Gronych J, Korshunov A, Bageritz J, Milde T, Jugold M, Hambardzumyan D*, et al.* An activated mutant BRAF kinase domain is sufficient to induce pilocytic astrocytoma in mice. J Clin Invest **2011**;121(4):1344-8 doi 10.1172/JCI44656.

25. Gnekow AK, Walker DA, Kandels D, Picton S, Giorgio P, Grill J*, et al.* A European randomised controlled trial of the addition of etoposide to standard vincristine and carboplatin induction as part of an 18-month treatment programme for childhood (</=16 years) low grade glioma - A final report. Eur J Cancer **2017**;81:206-25 doi 10.1016/j.ejca.2017.04.019.

26. Lassaletta A, Scheinemann K, Zelcer SM, Hukin J, Wilson BA, Jabado N*, et al.* Phase II Weekly Vinblastine for Chemotherapy-Naive Children With Progressive Low-Grade Glioma: A Canadian Pediatric Brain Tumor Consortium Study. J Clin Oncol **2016**;34(29):3537-43 doi 10.1200/JCO.2016.68.1585.

27. Banerjee A, Jakacki RI, Onar-Thomas A, Wu S, Nicolaides T, Young Poussaint T*, et al.* A phase I trial of the MEK inhibitor selumetinib (AZD6244) in pediatric patients with recurrent or refractory low-grade glioma: a Pediatric Brain Tumor Consortium (PBTC) study. Neuro Oncol **2017**;19(8):1135-44 doi 10.1093/neuonc/now282.

28. Fangusaro JR, Onar-Thomas A, Young-Poussaint T, Wu S, Ligon AH, Lindeman NI*, et al.* A phase II prospective study of selumetinib in children with recurrent or refractory low-grade glioma (LGG): A Pediatric Brain Tumor Consortium (PBTC) study. Journal of Clinical Oncology **2017**;35(15_suppl):10504- doi 10.1200/JCO.2017.35.15_suppl.10504.

29. Karajannis MA, Legault G, Fisher MJ, Milla SS, Cohen KJ, Wisoff JH*, et al.* Phase II study of sorafenib in children with recurrent or progressive low-grade astrocytomas. Neuro Oncol **2014**;16(10):1408-16 doi 10.1093/neuonc/nou059.

30. Sievert AJ, Lang SS, Boucher KL, Madsen PJ, Slaunwhite E, Choudhari N*, et al.* Paradoxical activation and RAF inhibitor resistance of BRAF protein kinase fusions characterizing pediatric astrocytomas. Proceedings of the National Academy of Sciences of the United States of America **2013**;110(15):5957-62 doi 10.1073/pnas.1219232110.

31. Selt F, Hohloch J, Hielscher T, Sahm F, Capper D, Korshunov A*, et al.* Establishment and application of a novel patient-derived KIAA1549:BRAF-driven pediatric pilocytic astrocytoma model for preclinical drug testing. Oncotarget **2017**;8(7):11460-79 doi 10.18632/oncotarget.14004.

32. Raabe EH, Lim KS, Kim JM, Meeker A, Mao XG, Nikkhah G*, et al.* BRAF activation induces transformation and then senescence in human neural stem cells: a pilocytic astrocytoma model. Clin Cancer Res **2011**;17(11):3590-9 doi 10.1158/1078-0432.CCR-10-3349.

33. Sun Y, Alberta JA, Pilarz C, Calligaris D, Chadwick EJ, Ramkissoon SH*, et al.* A brain-penetrant RAF dimer antagonist for the noncanonical BRAF oncoprotein of pediatric low-grade astrocytomas. Neuro Oncol **2017**;19(6):774-85 doi 10.1093/neuonc/now261.

34. Garnett S, Dutchak KL, McDonough RV, Dankort D. p53 loss does not permit escape from Braf(V600E)-induced senescence in a mouse model of lung cancer. Oncogene **2017**;36(45):6325-35 doi 10.1038/onc.2017.235.

35. Chadwick EJ, Yang DP, Filbin MG, Mazzola E, Sun Y, Behar O*, et al.* A Brain Tumor/Organotypic Slice Co-culture System for Studying Tumor Microenvironment and Targeted Drug Therapies. J Vis Exp **2015**(105):e53304 doi 10.3791/53304.

36. DeCaprio JA, Ludlow JW, Figge J, Shew JY, Huang CM, Lee WH*, et al.* SV40 large tumor antigen forms a specific complex with the product of the retinoblastoma susceptibility gene. Cell **1988**;54(2):275-83.

37. Bargonetti J, Reynisdottir I, Friedman PN, Prives C. Site-specific binding of wild-type p53 to cellular DNA is inhibited by SV40 T antigen and mutant p53. Genes Dev **1992**;6(10):1886-98.

38. Bajenaru ML, Hernandez MR, Perry A, Zhu Y, Parada LF, Garbow JR*, et al.* Optic nerve glioma in mice requires astrocyte Nf1 gene inactivation and Nf1 brain heterozygosity. Cancer Res **2003**;63(24):8573-7.

39. Kaul A, Chen YH, Emnett RJ, Gianino SM, Gutmann DH. Conditional KIAA1549:BRAF mice reveal brain region- and cell type-specific effects. Genesis **2013**;51(10):708-16 doi 10.1002/dvg.22415.

40. Hayflick L, Moorhead PS. The serial cultivation of human diploid cell strains. Exp Cell Res **1961**;25:585-621.

41. Bartkova J, Rezaei N, Liontos M, Karakaidos P, Kletsas D, Issaeva N*, et al.* Oncogene-induced senescence is part of the tumorigenesis barrier imposed by DNA damage checkpoints. Nature **2006**;444(7119):633-7 doi 10.1038/nature05268.

42. Frey N, Venturelli S, Zender L, Bitzer M. Cellular senescence in gastrointestinal diseases: from pathogenesis to therapeutics. Nat Rev Gastroenterol Hepatol **2018**;15(2):81-95 doi 10.1038/nrgastro.2017.146.

43. Foster SA, Wong DJ, Barrett MT, Galloway DA. Inactivation of p16 in human mammary epithelial cells by CpG island methylation. Mol Cell Biol **1998**;18(4):1793-801.

44. Jarrard DF, Sarkar S, Shi Y, Yeager TR, Magrane G, Kinoshita H*, et al.* p16/pRb pathway alterations are required for bypassing senescence in human prostate epithelial cells. Cancer Res **1999**;59(12):2957-64.

45. Kim NW, Piatyszek MA, Prowse KR, Harley CB, West MD, Ho PL*, et al.* Specific association of human telomerase activity with immortal cells and cancer. Science **1994**;266(5193):2011-5.

46. Kuilman T, Michaloglou C, Vredeveld LC, Douma S, van Doorn R, Desmet CJ*, et al.* Oncogene-induced senescence relayed by an interleukin-dependent inflammatory network. Cell **2008**;133(6):1019-31 doi 10.1016/j.cell.2008.03.039.

47. Acosta JC, O'Loghlen A, Banito A, Guijarro MV, Augert A, Raguz S*, et al.* Chemokine signaling via the CXCR2 receptor reinforces senescence. Cell **2008**;133(6):1006-18 doi 10.1016/j.cell.2008.03.038.

48. Serrano M, Lin AW, McCurrach ME, Beach D, Lowe SW. Oncogenic ras provokes premature cell senescence associated with accumulation of p53 and p16INK4a. Cell **1997**;88(5):593-602.

49. Michaloglou C, Vredeveld LC, Soengas MS, Denoyelle C, Kuilman T, van der Horst CM*, et al.* BRAFE600-associated senescence-like cell cycle arrest of human naevi. Nature **2005**;436(7051):720-4 doi 10.1038/nature03890.

50. Acosta JC, Banito A, Wuestefeld T, Georgilis A, Janich P, Morton JP*, et al.* A complex secretory program orchestrated by the inflammasome controls paracrine senescence. Nat Cell Biol **2013**;15(8):978-90 doi 10.1038/ncb2784.

51. Courtois-Cox S, Genther Williams SM, Reczek EE, Johnson BW, McGillicuddy LT, Johannessen CM*, et al.* A negative feedback signaling network underlies oncogene-induced senescence. Cancer Cell **2006**;10(6):459-72 doi 10.1016/j.ccr.2006.10.003.

52. Chen Z, Trotman LC, Shaffer D, Lin HK, Dotan ZA, Niki M*, et al.* Crucial role of p53-dependent cellular senescence in suppression of Pten-deficient tumorigenesis. Nature **2005**;436(7051):725-30 doi 10.1038/nature03918.

53. Xue W, Zender L, Miething C, Dickins RA, Hernando E, Krizhanovsky V*, et al.* Senescence and tumour clearance is triggered by p53 restoration in murine liver carcinomas. Nature **2007**;445(7128):656-60 doi 10.1038/nature05529.

54. Krizhanovsky V, Yon M, Dickins RA, Hearn S, Simon J, Miething C*, et al.* Senescence of activated stellate cells limits liver fibrosis. Cell **2008**;134(4):657-67 doi 10.1016/j.cell.2008.06.049.

55. Kang TW, Yevsa T, Woller N, Hoenicke L, Wuestefeld T, Dauch D*, et al.* Senescence surveillance of pre-malignant hepatocytes limits liver cancer development. Nature **2011**;479(7374):547-51 doi 10.1038/nature10599.

56. Lujambio A, Akkari L, Simon J, Grace D, Tschaharganeh DF, Bolden JE*, et al.* Non-cell-autonomous tumor suppression by p53. Cell **2013**;153(2):449-60 doi 10.1016/j.cell.2013.03.020.

57. Jun JI, Lau LF. The matricellular protein CCN1 induces fibroblast senescence and restricts fibrosis in cutaneous wound healing. Nat Cell Biol **2010**;12(7):676-85 doi 10.1038/ncb2070.

58. Munoz-Espin D, Canamero M, Maraver A, Gomez-Lopez G, Contreras J, Murillo-Cuesta S*, et al.* Programmed cell senescence during mammalian embryonic development. Cell **2013**;155(5):1104-18 doi 10.1016/j.cell.2013.10.019.

59. Rajagopalan S, Long EO. Cellular senescence induced by CD158d reprograms natural killer cells to promote vascular remodeling. Proc Natl Acad Sci U S A **2012**;109(50):20596-601 doi 10.1073/pnas.1208248109.

60. Storer M, Mas A, Robert-Moreno A, Pecoraro M, Ortells MC, Di Giacomo V*, et al.* Senescence is a developmental mechanism that contributes to embryonic growth and patterning. Cell **2013**;155(5):1119-30 doi 10.1016/j.cell.2013.10.041.

61. Munoz-Espin D, Serrano M. Cellular senescence: from physiology to pathology. Nat Rev Mol Cell Biol **2014**;15(7):482-96 doi 10.1038/nrm3823.

62. Baker DJ, Perez-Terzic C, Jin F, Pitel KS, Niederlander NJ, Jeganathan K*, et al.* Opposing roles for p16Ink4a and p19Arf in senescence and ageing caused by BubR1 insufficiency. Nat Cell Biol **2008**;10(7):825-36 doi 10.1038/ncb1744.

63. Coppe JP, Kauser K, Campisi J, Beausejour CM. Secretion of vascular endothelial growth factor by primary human fibroblasts at senescence. J Biol Chem **2006**;281(40):29568-74 doi 10.1074/jbc.M603307200.

64. Krtolica A, Parrinello S, Lockett S, Desprez PY, Campisi J. Senescent fibroblasts promote epithelial cell growth and tumorigenesis: a link between cancer and aging. Proc Natl Acad Sci U S A **2001**;98(21):12072-7 doi 10.1073/pnas.211053698.

65. Bavik C, Coleman I, Dean JP, Knudsen B, Plymate S, Nelson PS. The gene expression program of prostate fibroblast senescence modulates neoplastic epithelial cell proliferation through paracrine mechanisms. Cancer Res **2006**;66(2):794-802 doi 10.1158/0008-5472.CAN-05-1716.

66. Coppe JP, Patil CK, Rodier F, Sun Y, Munoz DP, Goldstein J*, et al.* Senescence-associated secretory phenotypes reveal cell-nonautonomous functions of oncogenic RAS and the p53 tumor suppressor. PLoS Biol **2008**;6(12):2853-68 doi 10.1371/journal.pbio.0060301.

67. Liu D, Hornsby PJ. Senescent human fibroblasts increase the early growth of xenograft tumors via matrix metalloproteinase secretion. Cancer Res **2007**;67(7):3117-26 doi 10.1158/0008-5472.CAN-06-3452.

68. Bhatia B, Multani AS, Patrawala L, Chen X, Calhoun-Davis T, Zhou J*, et al.* Evidence that senescent human prostate epithelial cells enhance tumorigenicity: cell fusion as a potential mechanism and inhibition by p16INK4a and hTERT. Int J Cancer **2008**;122(7):1483-95 doi 10.1002/ijc.23222.

69. Rodier F, Campisi J. Four faces of cellular senescence. J Cell Biol **2011**;192(4):547-56 doi 10.1083/jcb.201009094.

70. Narita M, Lowe SW. Senescence comes of age. Nat Med **2005**;11(9):920-2 doi 10.1038/nm0905-920.

71. Dimri GP, Lee X, Basile G, Acosta M, Scott G, Roskelley C*, et al.* A biomarker that identifies senescent human cells in culture and in aging skin in vivo. Proc Natl Acad Sci U S A **1995**;92(20):9363-7.

72. Sharpless NE, Sherr CJ. Forging a signature of in vivo senescence. Nat Rev Cancer **2015**;15(7):397-408 doi 10.1038/nrc3960.

73. Kiyono T, Foster SA, Koop JI, McDougall JK, Galloway DA, Klingelhutz AJ. Both Rb/p16INK4a inactivation and telomerase activity are required to immortalize human epithelial cells. Nature **1998**;396(6706):84-8 doi 10.1038/23962.

74. Sage J, Mulligan GJ, Attardi LD, Miller A, Chen S, Williams B*, et al.* Targeted disruption of the three Rb-related genes leads to loss of G(1) control and immortalization. Genes Dev **2000**;14(23):3037-50.

75. Hara E, Tsurui H, Shinozaki A, Nakada S, Oda K. Cooperative effect of antisense-Rb and antisense-p53 oligomers on the extension of life span in human diploid fibroblasts, TIG-1. Biochem Biophys Res Commun **1991**;179(1):528-34.

76. Hayflick L. The Limited in Vitro Lifetime of Human Diploid Cell Strains. Exp Cell Res **1965**;37:614-36.

77. Harper JW, Adami GR, Wei N, Keyomarsi K, Elledge SJ. The p21 Cdk-interacting protein Cip1 is a potent inhibitor of G1 cyclin-dependent kinases. Cell **1993**;75(4):805-16.

78. Hannon GJ, Beach D. p15INK4B is a potential effector of TGF-beta-induced cell cycle arrest. Nature **1994**;371(6494):257-61 doi 10.1038/371257a0.

79. Kamijo T, Zindy F, Roussel MF, Quelle DE, Downing JR, Ashmun RA*, et al.* Tumor suppression at the mouse INK4a locus mediated by the alternative reading frame product p19ARF. Cell **1997**;91(5):649-59.

80. Orjalo AV, Bhaumik D, Gengler BK, Scott GK, Campisi J. Cell surface-bound IL-1alpha is an upstream regulator of the senescence-associated IL-6/IL-8 cytokine network. Proc Natl Acad Sci U S A **2009**;106(40):17031-6 doi 10.1073/pnas.0905299106.

81. Narita M, Nunez S, Heard E, Narita M, Lin AW, Hearn SA*, et al.* Rb-mediated heterochromatin formation and silencing of E2F target genes during cellular senescence. Cell **2003**;113(6):703-16.

82. Kurz DJ, Decary S, Hong Y, Erusalimsky JD. Senescence-associated (beta)-galactosidase reflects an increase in lysosomal mass during replicative ageing of human endothelial cells. J Cell Sci **2000**;113 (Pt 20):3613-22.

83. Lasry A, Ben-Neriah Y. Senescence-associated inflammatory responses: aging and cancer perspectives. Trends Immunol **2015**;36(4):217-28 doi 10.1016/j.it.2015.02.009.

84. Bhaumik D, Scott GK, Schokrpur S, Patil CK, Orjalo AV, Rodier F*, et al.* MicroRNAs miR-146a/b negatively modulate the senescence-associated inflammatory mediators IL-6 and IL-8. Aging (Albany NY) **2009**;1(4):402-11 doi 10.18632/aging.100042.

85. Bignell GR, Greenman CD, Davies H, Butler AP, Edkins S, Andrews JM*, et al.* Signatures of mutation and selection in the cancer genome. Nature **2010**;463(7283):893-8 doi 10.1038/nature08768.

86. Mason DX, Jackson TJ, Lin AW. Molecular signature of oncogenic ras-induced senescence. Oncogene **2004**;23(57):9238-46 doi 10.1038/sj.onc.1208172.

87. Coppe JP, Desprez PY, Krtolica A, Campisi J. The senescence-associated secretory phenotype: the dark side of tumor suppression. Annu Rev Pathol **2010**;5:99-118 doi 10.1146/annurev-pathol-121808-102144.

88. Mason DX, Keppler D, Zhang J, Jackson TJ, Seger YR, Matsui S*, et al.* Defined genetic events associated with the spontaneous in vitro transformation of EIA/Ras-expressing human IMR90 fibroblasts. Carcinogenesis **2006**;27(2):350-9 doi 10.1093/carcin/bgi264.

89. Chien Y, Scuoppo C, Wang X, Fang X, Balgley B, Bolden JE*, et al.* Control of the senescence-associated secretory phenotype by NF-kappaB promotes senescence and enhances chemosensitivity. Genes Dev **2011**;25(20):2125-36 doi 10.1101/gad.17276711.

90. Hubackova S, Krejcikova K, Bartek J, Hodny Z. IL1- and TGFbeta-Nox4 signaling, oxidative stress and DNA damage response are shared features of replicative, oncogene-induced, and drug-induced paracrine 'bystander senescence'. Aging (Albany NY) **2012**;4(12):932-51 doi 10.18632/aging.100520.

91. Laberge RM, Zhou L, Sarantos MR, Rodier F, Freund A, de Keizer PL*, et al.* Glucocorticoids suppress selected components of the senescence-associated secretory phenotype. Aging Cell **2012**;11(4):569-78 doi 10.1111/j.1474-9726.2012.00818.x.

92. Ge H, Ke J, Xu N, Li H, Gong J, Li X*, et al.* Dexamethasone alleviates pemetrexed-induced senescence in Non-Small-Cell Lung Cancer. Food Chem Toxicol **2018**;119:86-97 doi 10.1016/j.fct.2018.05.025.

93. Santos AA, Scheltinga MR, Lynch E, Brown EF, Lawton P, Chambers E*, et al.* Elaboration of interleukin 1-receptor antagonist is not attenuated by glucocorticoids after endotoxemia. Arch Surg **1993**;128(2):138-43; discussion 43-4.

94. Auphan N, DiDonato JA, Rosette C, Helmberg A, Karin M. Immunosuppression by glucocorticoids: inhibition of NF-kappa B activity through induction of I kappa B synthesis. Science **1995**;270(5234):286-90.

95. Scheinman RI, Cogswell PC, Lofquist AK, Baldwin AS, Jr. Role of transcriptional activation of I kappa B alpha in mediation of immunosuppression by glucocorticoids. Science **1995**;270(5234):283-6.

96. March CJ, Mosley B, Larsen A, Cerretti DP, Braedt G, Price V*, et al.* Cloning, sequence and expression of two distinct human interleukin-1 complementary DNAs. Nature **1985**;315(6021):641-7.

97. Apte RN, Dotan S, Elkabets M, White MR, Reich E, Carmi Y*, et al.* The involvement of IL-1 in tumorigenesis, tumor invasiveness, metastasis and tumor-host interactions. Cancer Metastasis Rev **2006**;25(3):387-408 doi 10.1007/s10555-006-9004-4.

98. Sims JE, March CJ, Cosman D, Widmer MB, MacDonald HR, McMahan CJ*, et al.* cDNA expression cloning of the IL-1 receptor, a member of the immunoglobulin superfamily. Science **1988**;241(4865):585-9.

99. Thornberry NA, Bull HG, Calaycay JR, Chapman KT, Howard AD, Kostura MJ*, et al.* A novel heterodimeric cysteine protease is required for interleukin-1 beta processing in monocytes. Nature **1992**;356(6372):768-74 doi 10.1038/356768a0.

100. Cerretti DP, Kozlosky CJ, Mosley B, Nelson N, Van Ness K, Greenstreet TA*, et al.* Molecular cloning of the interleukin-1 beta converting enzyme. Science **1992**;256(5053):97-100.

101. Garfinkel S, Brown S, Wessendorf JH, Maciag T. Post-transcriptional regulation of interleukin 1 alpha in various strains of young and senescent human umbilical vein endothelial cells. Proc Natl Acad Sci U S A **1994**;91(4):1559-63.

102. Greenfeder SA, Nunes P, Kwee L, Labow M, Chizzonite RA, Ju G. Molecular cloning and characterization of a second subunit of the interleukin 1 receptor complex. J Biol Chem **1995**;270(23):13757-65.

103. Dinarello CA. Biologic basis for interleukin-1 in disease. Blood **1996**;87(6):2095-147.

104. Yamin TT, Miller DK. The interleukin-1 receptor-associated kinase is degraded by proteasomes following its phosphorylation. J Biol Chem **1997**;272(34):21540-7.

105. Kwon G, Corbett JA, Rodi CP, Sullivan P, McDaniel ML. Interleukin-1 beta-induced nitric oxide synthase expression by rat pancreatic beta-cells: evidence for the involvement of nuclear factor kappa B in the signaling mechanism. Endocrinology **1995**;136(11):4790-5 doi 10.1210/endo.136.11.7588208.

106. Dinarello CA, Ikejima T, Warner SJ, Orencole SF, Lonnemann G, Cannon JG*, et al.* Interleukin 1 induces interleukin 1. I. Induction of circulating interleukin 1 in rabbits in vivo and in human mononuclear cells in vitro. J Immunol **1987**;139(6):1902-10.

107. Kimura H, Inukai Y, Takii T, Furutani Y, Shibata Y, Hayashi H*, et al.* Molecular analysis of constitutive IL-1alpha gene expression in human melanoma cells: autocrine stimulation through NF-kappaB activation by endogenous IL-1alpha. Cytokine **1998**;10(11):872-9.

108. Colotta F, Dower SK, Sims JE, Mantovani A. The type II 'decoy' receptor: a novel regulatory pathway for interleukin 1. Immunol Today **1994**;15(12):562-6 doi 10.1016/0167-5699(94)90217-8.

109. Martin MU, Wesche H. Summary and comparison of the signaling mechanisms of the Toll/interleukin-1 receptor family. Biochim Biophys Acta **2002**;1592(3):265-80.

110. Hirano T, Kishimoto T. Interleukin-6: possible implications in human diseases. Ric Clin Lab **1989**;19(1):1-10.

111. Ancrile B, Lim KH, Counter CM. Oncogenic Ras-induced secretion of IL6 is required for tumorigenesis. Genes Dev **2007**;21(14):1714-9 doi 10.1101/gad.1549407.

112. Taga T, Hibi M, Hirata Y, Yamasaki K, Yasukawa K, Matsuda T*, et al.* Interleukin-6 triggers the association of its receptor with a possible signal transducer, gp130. Cell **1989**;58(3):573-81.

113. Lutticken C, Wegenka UM, Yuan J, Buschmann J, Schindler C, Ziemiecki A*, et al.* Association of transcription factor APRF and protein kinase Jak1 with the interleukin-6 signal transducer gp130. Science **1994**;263(5143):89-92.

114. Rodig SJ, Meraz MA, White JM, Lampe PA, Riley JK, Arthur CD*, et al.* Disruption of the Jak1 gene demonstrates obligatory and nonredundant roles of the Jaks in cytokine-induced biologic responses. Cell **1998**;93(3):373-83.

115. Zhong Z, Wen Z, Darnell JE, Jr. Stat3: a STAT family member activated by tyrosine phosphorylation in response to epidermal growth factor and interleukin-6. Science **1994**;264(5155):95-8.

116. Heinrich PC, Behrmann I, Muller-Newen G, Schaper F, Graeve L. Interleukin-6-type cytokine signalling through the gp130/Jak/STAT pathway. Biochem J **1998**;334 (Pt 2):297-314.

117. Fukada T, Hibi M, Yamanaka Y, Takahashi-Tezuka M, Fujitani Y, Yamaguchi T*, et al.* Two signals are necessary for cell proliferation induced by a cytokine receptor gp130: involvement of STAT3 in anti-apoptosis. Immunity **1996**;5(5):449-60.

118. Schiemann WP, Bartoe JL, Nathanson NM. Box 3-independent signaling mechanisms are involved in leukemia inhibitory factor receptor alpha- and gp130-mediated stimulation of mitogen-activated protein kinase. Evidence for participation of multiple signaling pathways which converge at Ras. J Biol Chem **1997**;272(26):16631-6.

119. Takahashi-Tezuka M, Yoshida Y, Fukada T, Ohtani T, Yamanaka Y, Nishida K*, et al.* Gab1 acts as an adapter molecule linking the cytokine receptor gp130 to ERK mitogen-activated protein kinase. Mol Cell Biol **1998**;18(7):4109-17.

120. Zohlnhofer D, Graeve L, Rose-John S, Schooltink H, Dittrich E, Heinrich PC. The hepatic interleukin-6 receptor. Down-regulation of the interleukin-6 binding subunit (gp80) by its ligand. FEBS Lett **1992**;306(2-3):219-22.

121. Starr R, Willson TA, Viney EM, Murray LJ, Rayner JR, Jenkins BJ*, et al.* A family of cytokine-inducible inhibitors of signalling. Nature **1997**;387(6636):917-21 doi 10.1038/43206.

122. Heinrich PC, Behrmann I, Haan S, Hermanns HM, Muller-Newen G, Schaper F. Principles of interleukin (IL)-6-type cytokine signalling and its regulation. Biochem J **2003**;374(Pt 1):1-20 doi 10.1042/BJ20030407.

123. Zacarias-Fluck MF, Morancho B, Vicario R, Luque Garcia A, Escorihuela M, Villanueva J*, et al.* Effect of cellular senescence on the growth of HER2-positive breast cancers. J Natl Cancer Inst **2015**;107(5) doi 10.1093/jnci/djv020.

124. Jones TA, Jeyapalan JN, Forshew T, Tatevossian RG, Lawson AR, Patel SN*, et al.* Molecular analysis of pediatric brain tumors identifies microRNAs in pilocytic astrocytomas that target the MAPK and NF-kappaB pathways. Acta Neuropathol Commun **2015**;3:86 doi 10.1186/s40478-015-0266-3.

125. Bid HK, Kibler A, Phelps DA, Manap S, Xiao L, Lin J*, et al.* Development, characterization, and reversal of acquired resistance to the MEK1 inhibitor selumetinib (AZD6244) in an in vivo model of childhood astrocytoma. Clin Cancer Res **2013**;19(24):6716-29 doi 10.1158/1078-0432.CCR-13-0842.

126. Lindsey JC, Lusher ME, Anderton JA, Bailey S, Gilbertson RJ, Pearson AD*, et al.* Identification of tumour-specific epigenetic events in medulloblastoma development by hypermethylation profiling. Carcinogenesis **2004**;25(5):661-8 doi 10.1093/carcin/bgh055.

127. Schmitt M, Pawlita M. High-throughput detection and multiplex identification of cell contaminations. Nucleic Acids Res **2009**;37(18):e119 doi 10.1093/nar/gkp581.

128. Mazia D, Schatten G, Sale W. Adhesion of cells to surfaces coated with polylysine. Applications to electron microscopy. J Cell Biol **1975**;66(1):198-200.

129. Winer J, Jung CK, Shackel I, Williams PM. Development and validation of real-time quantitative reverse transcriptase-polymerase chain reaction for monitoring gene expression in cardiac myocytes in vitro. Anal Biochem **1999**;270(1):41-9 doi 10.1006/abio.1999.4085.

130. Nelson DM, McBryan T, Jeyapalan JC, Sedivy JM, Adams PD. A comparison of oncogene-induced senescence and replicative senescence: implications for tumor suppression and aging. Age (Dordr) **2014**;36(3):9637 doi 10.1007/s11357-014-9637-0.

131. Pawlikowski JS, McBryan T, van Tuyn J, Drotar ME, Hewitt RN, Maier AB*, et al.* Wnt signaling potentiates nevogenesis. Proc Natl Acad Sci U S A **2013**;110(40):16009-14 doi 10.1073/pnas.1303491110.

132. Takebayashi S, Tanaka H, Hino S, Nakatsu Y, Igata T, Sakamoto A*, et al.* Retinoblastoma protein promotes oxidative phosphorylation through upregulation of glycolytic genes in oncogene-induced senescent cells. Aging Cell **2015**;14(4):689-97 doi 10.1111/acel.12351.

133. Smyth GK. Linear models and empirical bayes methods for assessing differential expression in microarray experiments. Stat Appl Genet Mol Biol **2004**;3:Article3 doi 10.2202/1544-6115.1027.

134. Smyth GK. Limma: linear models for microarray data. In: R. Gentleman VC, S. Dudoit, R. Irizarry, W. Humber, editor. Bioinformatics and Computational Biology Solutions using R and Bioconductor. New York: Springer; 2005. p 397-420.

135. Breitling R, Armengaud P, Amtmann A, Herzyk P. Rank products: a simple, yet powerful, new method to detect differentially regulated genes in replicated microarray experiments. FEBS Lett **2004**;573(1-3):83-92 doi 10.1016/j.febslet.2004.07.055.

136. Eisinga R, Breitling R, Heskes T. The exact probability distribution of the rank product statistics for replicated experiments. FEBS Lett **2013**;587(6):677-82 doi 10.1016/j.febslet.2013.01.037.

137. Gravendeel LA, Kouwenhoven MC, Gevaert O, de Rooi JJ, Stubbs AP, Duijm JE*, et al.* Intrinsic gene expression profiles of gliomas are a better predictor of survival than histology. Cancer Res **2009**;69(23):9065-72 doi 10.1158/0008-5472.CAN-09-2307.

138. Sharma MK, Mansur DB, Reifenberger G, Perry A, Leonard JR, Aldape KD*, et al.* Distinct genetic signatures among pilocytic astrocytomas relate to their brain region origin. Cancer Res **2007**;67(3):890-900 doi 10.1158/0008-5472.CAN-06-0973.

139. Lambert SR, Witt H, Hovestadt V, Zucknick M, Kool M, Pearson DM*, et al.* Differential expression and methylation of brain developmental genes define location-specific subsets of pilocytic astrocytoma. Acta Neuropathol **2013**;126(2):291-301 doi 10.1007/s00401-013-1124-7.

140. Subramanian A, Tamayo P, Mootha VK, Mukherjee S, Ebert BL, Gillette MA*, et al.* Gene set enrichment analysis: a knowledge-based approach for interpreting genome-wide expression profiles. Proc Natl Acad Sci U S A **2005**;102(43):15545-50 doi 10.1073/pnas.0506580102.

141. Wu D, Smyth GK. Camera: a competitive gene set test accounting for inter-gene correlation. Nucleic Acids Res **2012**;40(17):e133 doi 10.1093/nar/gks461.

142. Li Q, Birkbak NJ, Gyorffy B, Szallasi Z, Eklund AC. Jetset: selecting the optimal microarray probe set to represent a gene. BMC Bioinformatics **2011**;12:474 doi 10.1186/1471-2105-12-474.

143. Baracskay KL, Kidd GJ, Miller RH, Trapp BD. NG2-positive cells generate A2B5-positive oligodendrocyte precursor cells. Glia **2007**;55(10):1001-10 doi 10.1002/glia.20519.

144. Sengupta S, Chatterjee U, Banerjee U, Ghosh S, Chatterjee S, Ghosh AK. A study of histopathological spectrum and expression of Ki-67, TP53 in primary brain tumors of pediatric age group. Indian J Med Paediatr Oncol **2012**;33(1):25-31 doi 10.4103/0971-5851.96965.

145. Porras A, Gaillard S, Rundell K. The simian virus 40 small-t and large-T antigens jointly regulate cell cycle reentry in human fibroblasts. J Virol **1999**;73(4):3102-7.

146. Haupt Y, Maya R, Kazaz A, Oren M. Mdm2 promotes the rapid degradation of p53. Nature **1997**;387(6630):296-9 doi 10.1038/387296a0.

147. Oren M, Maltzman W, Levine AJ. Post-translational regulation of the 54K cellular tumor antigen in normal and transformed cells. Mol Cell Biol **1981**;1(2):101-10.

148. Yang NC, Hu ML. The limitations and validities of senescence associated-beta-galactosidase activity as an aging marker for human foreskin fibroblast Hs68 cells. Exp Gerontol **2005**;40(10):813-9 doi 10.1016/j.exger.2005.07.011.

149. Di Micco R, Sulli G, Dobreva M, Liontos M, Botrugno OA, Gargiulo G*, et al.* Interplay between oncogene-induced DNA damage response and heterochromatin in senescence and cancer. Nat Cell Biol **2011**;13(3):292-302 doi 10.1038/ncb2170.

150. Buhl JL, Selt F, Hielscher T, Guiho R, Ecker J, Sahm F*, et al.* The Senescence-associated Secretory Phenotype Mediates Oncogene-induced Senescence in Pediatric Pilocytic Astrocytoma. Clin Cancer Res **2018** doi 10.1158/1078-0432.CCR-18-1965.

151. Kumar S, Millis AJ, Baglioni C. Expression of interleukin 1-inducible genes and production of interleukin 1 by aging human fibroblasts. Proc Natl Acad Sci U S A **1992**;89(10):4683-7.

152. Uekawa N, Nishikimi A, Isobe K, Iwakura Y, Maruyama M. Involvement of IL-1 family proteins in p38 linked cellular senescence of mouse embryonic fibroblasts. FEBS Lett **2004**;575(1-3):30-4 doi 10.1016/j.febslet.2004.08.033.

153. Dinarello CA. The many worlds of reducing interleukin-1. Arthritis Rheum **2005**;52(7):1960-7 doi 10.1002/art.21107.

154. Adler AS, Sinha S, Kawahara TL, Zhang JY, Segal E, Chang HY. Motif module map reveals enforcement of aging by continual NF-kappaB activity. Genes Dev **2007**;21(24):3244-57 doi 10.1101/gad.1588507.

155. Hiscott J, Marois J, Garoufalis J, D'Addario M, Roulston A, Kwan I*, et al.* Characterization of a functional NF-kappa B site in the human interleukin 1 beta promoter: evidence for a positive autoregulatory loop. Mol Cell Biol **1993**;13(10):6231-40.

156. Shah S, King EM, Chandrasekhar A, Newton R. Roles for the mitogen-activated protein kinase (MAPK) phosphatase, DUSP1, in feedback control of inflammatory gene expression and repression by dexamethasone. J Biol Chem **2014**;289(19):13667-79 doi 10.1074/jbc.M113.540799.

157. Zhu Y, Tchkonia T, Fuhrmann-Stroissnigg H, Dai HM, Ling YY, Stout MB*, et al.* Identification of a novel senolytic agent, navitoclax, targeting the Bcl-2 family of anti-apoptotic factors. Aging Cell **2016**;15(3):428-35 doi 10.1111/acel.12445.

158. Chang J, Wang Y, Shao L, Laberge RM, Demaria M, Campisi J*, et al.* Clearance of senescent cells by ABT263 rejuvenates aged hematopoietic stem cells in mice. Nat Med **2016**;22(1):78-83 doi 10.1038/nm.4010.

159. Yosef R, Pilpel N, Tokarsky-Amiel R, Biran A, Ovadya Y, Cohen S*, et al.* Directed elimination of senescent cells by inhibition of BCL-W and BCL-XL. Nat Commun **2016**;7:11190 doi 10.1038/ncomms11190.

160. Zhu Y, Tchkonia T, Pirtskhalava T, Gower AC, Ding H, Giorgadze N*, et al.* The Achilles' heel of senescent cells: from transcriptome to senolytic drugs. Aging Cell **2015**;14(4):644-58 doi 10.1111/acel.12344.

161. Xu M, Pirtskhalava T, Farr JN, Weigand BM, Palmer AK, Weivoda MM*, et al.* Senolytics improve physical function and increase lifespan in old age. Nat Med **2018**;24(8):1246-56 doi 10.1038/s41591-018-0092-9.

162. Xi HQ, Wu XS, Wei B, Chen L. Eph receptors and ephrins as targets for cancer therapy. J Cell Mol Med **2012**;16(12):2894-909 doi 10.1111/j.1582-4934.2012.01612.x.

163. Kirkland JL, Tchkonia T. Cellular Senescence: A Translational Perspective. EBioMedicine **2017**;21:21-8 doi 10.1016/j.ebiom.2017.04.013.

164. Baar MP, Brandt RMC, Putavet DA, Klein JDD, Derks KWJ, Bourgeois BRM*, et al.* Targeted Apoptosis of Senescent Cells Restores Tissue Homeostasis in Response to Chemotoxicity and Aging. Cell **2017**;169(1):132-47 e16 doi 10.1016/j.cell.2017.02.031.

165. Ater JL, Zhou T, Holmes E, Mazewski CM, Booth TN, Freyer DR*, et al.* Randomized study of two chemotherapy regimens for treatment of low-grade glioma in young children: a report from the Children's Oncology Group. J Clin Oncol **2012**;30(21):2641-7 doi 10.1200/JCO.2011.36.6054.

166. Montero J, Letai A. Why do BCL-2 inhibitors work and where should we use them in the clinic? Cell Death Differ **2018**;25(1):56-64 doi 10.1038/cdd.2017.183.

167. Ledford H, Else H, Warren M. Cancer immunologists scoop medicine Nobel prize. Nature **2018**;562(7725):20-1 doi 10.1038/d41586-018-06751-0.

168. Jones DT, Kocialkowski S, Liu L, Pearson DM, Ichimura K, Collins VP. Oncogenic RAF1 rearrangement and a novel BRAF mutation as alternatives to KIAA1549:BRAF fusion in activating the MAPK pathway in pilocytic astrocytoma. Oncogene **2009**;28(20):2119-23 doi 10.1038/onc.2009.73.

169. Singh S, Upadhyay AK, Ajay AK, Bhat MK. p53 regulates ERK activation in carboplatin induced apoptosis in cervical carcinoma: a novel target of p53 in apoptosis. FEBS Lett **2007**;581(2):289-95 doi 10.1016/j.febslet.2006.12.035.

170. Gonzalez-Meljem JM, Haston S, Carreno G, Apps JR, Pozzi S, Stache C*, et al.* Stem cell senescence drives age-attenuated induction of pituitary tumours in mouse models of paediatric craniopharyngioma. Nat Commun **2017**;8(1):1819 doi 10.1038/s41467-017-01992-5.

171. Eggert T, Wolter K, Ji J, Ma C, Yevsa T, Klotz S*, et al.* Distinct Functions of Senescence-Associated Immune Responses in Liver Tumor Surveillance and Tumor Progression. Cancer Cell **2016**;30(4):533-47 doi 10.1016/j.ccell.2016.09.003.

172. Ortiz-Montero P, Londono-Vallejo A, Vernot JP. Senescence-associated IL-6 and IL-8 cytokines induce a self- and cross-reinforced senescence/inflammatory milieu strengthening tumorigenic capabilities in the MCF-7 breast cancer cell line. Cell Commun Signal **2017**;15(1):17 doi 10.1186/s12964-017-0172-3.

173. Rose AJ, Herzig S. Metabolic control through glucocorticoid hormones: an update. Mol Cell Endocrinol **2013**;380(1-2):65-78 doi 10.1016/j.mce.2013.03.007.

174. Knedler A, Ham RG. Optimized medium for clonal growth of human microvascular endothelial cells with minimal serum. In Vitro Cell Dev Biol **1987**;23(7):481-91.

175. Lu YS, Lien HC, Yeh PY, Yeh KH, Kuo ML, Kuo SH*, et al.* Effects of glucocorticoids on the growth and chemosensitivity of carcinoma cells are heterogeneous and require high concentration of functional glucocorticoid receptors. World J Gastroenterol **2005**;11(40):6373-80.

176. Walker MJ, Lim C, Das Gupta TK, Beattie CW. Effects of glucocorticoids on the growth of human fibrosarcoma cell line HT-1080. Cancer Res **1986**;46(10):4927-32.

177. Bose R, Moors M, Tofighi R, Cascante A, Hermanson O, Ceccatelli S. Glucocorticoids induce long-lasting effects in neural stem cells resulting in senescence-related alterations. Cell Death Dis **2010**;1:e92 doi 10.1038/cddis.2010.60.

178. Li S, Mawal-Dewan M, Cristofalo VJ, Sell C. Enhanced proliferation of human fibroblasts, in the presence of dexamethasone, is accompanied by changes in p21Waf1/Cip1/Sdi1 and the insulin-like growth factor type 1 receptor. J Cell Physiol **1998**;177(3):396-401 doi 10.1002/(SICI)1097-4652(199812)177:3<396::AID-JCP3>3.0.CO;2-K.

179. Cristofalo VJ. The effect of hydrocortisone on DNA synthesis and cell division during aging in vitro. Adv Exp Med Biol **1975**;53:7-22.

180. Rosner BA, Cristofalo VJ. Hydrocortisone: a specific modulator of in vitro cell proliferation and aging. Mech Ageing Dev **1979**;9(5-6):485-96.

181. Yang I, Han SJ, Sughrue ME, Tihan T, Parsa AT. Immune cell infiltrate differences in pilocytic astrocytoma and glioblastoma: evidence of distinct immunological microenvironments that reflect tumor biology. J Neurosurg **2011**;115(3):505-11 doi 10.3171/2011.4.JNS101172.

182. Gutmann DH, McLellan MD, Hussain I, Wallis JW, Fulton LL, Fulton RS*, et al.* Somatic neurofibromatosis type 1 (NF1) inactivation characterizes NF1-associated pilocytic astrocytoma. Genome Res **2013**;23(3):431-9 doi 10.1101/gr.142604.112.

183. Klein R, Roggendorf W. Increased microglia proliferation separates pilocytic astrocytomas from diffuse astrocytomas: a double labeling study. Acta Neuropathol **2001**;101(3):245-8.

184. Griesinger AM, Birks DK, Donson AM, Amani V, Hoffman LM, Waziri A*, et al.* Characterization of distinct immunophenotypes across pediatric brain tumor types. J Immunol **2013**;191(9):4880-8 doi 10.4049/jimmunol.1301966.

185. Huang H, Hara A, Homma T, Yonekawa Y, Ohgaki H. Altered expression of immune defense genes in pilocytic astrocytomas. J Neuropathol Exp Neurol **2005**;64(10):891-901.

186. Tang F, Barbacioru C, Wang Y, Nordman E, Lee C, Xu N*, et al.* mRNA-Seq whole-transcriptome analysis of a single cell. Nat Methods **2009**;6(5):377-82 doi 10.1038/nmeth.1315.

187. Bandura DR, Baranov VI, Ornatsky OI, Antonov A, Kinach R, Lou X*, et al.* Mass cytometry: technique for real time single cell multitarget immunoassay based on inductively coupled plasma time-of-flight mass spectrometry. Anal Chem **2009**;81(16):6813-22 doi 10.1021/ac901049w.

188. Bendall SC, Simonds EF, Qiu P, Amir el AD, Krutzik PO, Finck R*, et al.* Single-cell mass cytometry of differential immune and drug responses across a human hematopoietic continuum. Science **2011**;332(6030):687-96 doi 10.1126/science.1198704.

189. Gibbons HM, Hughes SM, Van Roon-Mom W, Greenwood JM, Narayan PJ, Teoh HH*, et al.* Cellular composition of human glial cultures from adult biopsy brain tissue. J Neurosci Methods **2007**;166(1):89-98 doi 10.1016/j.jneumeth.2007.07.005.

190. Smith AM, Dragunow M. The human side of microglia. Trends Neurosci **2014**;37(3):125-35 doi 10.1016/j.tins.2013.12.001.

191. Du Y, Deng W, Wang Z, Ning M, Zhang W, Zhou Y*, et al.* Differential subnetwork of chemokines/cytokines in human, mouse, and rat brain cells after oxygen-glucose deprivation. J Cereb Blood Flow Metab **2017**;37(4):1425-34 doi 10.1177/0271678X16656199.

192. Schiff D, Lee EQ, Nayak L, Norden AD, Reardon DA, Wen PY. Medical management of brain tumors and the sequelae of treatment. Neuro Oncol **2015**;17(4):488-504 doi 10.1093/neuonc/nou304.

193. Song JH, Kandasamy K, Zemskova M, Lin YW, Kraft AS. The BH3 mimetic ABT-737 induces cancer cell senescence. Cancer Res **2011**;71(2):506-15 doi 10.1158/0008-5472.CAN-10-1977.

194. Chen J, Jin S, Abraham V, Huang X, Liu B, Mitten MJ*, et al.* The Bcl-2/Bcl-X(L)/Bcl-w inhibitor, navitoclax, enhances the activity of chemotherapeutic agents in vitro and in vivo. Mol Cancer Ther **2011**;10(12):2340-9 doi 10.1158/1535-7163.MCT-11-0415.

195. O'Reilly LA, Kruse EA, Puthalakath H, Kelly PN, Kaufmann T, Huang DC*, et al.* MEK/ERK-mediated phosphorylation of Bim is required to ensure survival of T and B lymphocytes during mitogenic stimulation. J Immunol **2009**;183(1):261-9 doi 10.4049/jimmunol.0803853.

196. Rudin CM, Hann CL, Garon EB, Ribeiro de Oliveira M, Bonomi PD, Camidge DR*, et al.* Phase II study of single-agent navitoclax (ABT-263) and biomarker correlates in patients with relapsed small cell lung cancer. Clin Cancer Res **2012**;18(11):3163-9 doi 10.1158/1078-0432.CCR-11-3090.

197. Wilson WH, O'Connor OA, Czuczman MS, LaCasce AS, Gerecitano JF, Leonard JP*, et al.* Navitoclax, a targeted high-affinity inhibitor of BCL-2, in lymphoid malignancies: a phase 1 dose-escalation study of safety, pharmacokinetics, pharmacodynamics, and antitumour activity. Lancet Oncol **2010**;11(12):1149-59 doi 10.1016/S1470-2045(10)70261-8.

198. Xiong H, Pradhan RS, Nada A, Krivoshik AP, Holen KD, Rhodes JW*, et al.* Studying navitoclax, a targeted anticancer drug, in healthy volunteers--ethical considerations and risk/benefit assessments and management. Anticancer Res **2014**;34(7):3739-46.

199. Veltri S, Smith JW, 2nd. Interleukin 1 trials in cancer patients: a review of the toxicity, antitumor and hematopoietic effects. Stem Cells **1996**;14(2):164-76 doi 10.1002/stem.140164.

200. Wrangle JM, Velcheti V, Patel MR, Garrett-Mayer E, Hill EG, Ravenel JG*, et al.* ALT-803, an IL-15 superagonist, in combination with nivolumab in patients with metastatic non-small cell lung cancer: a non-randomised, open-label, phase 1b trial. Lancet Oncol **2018**;19(5):694-704 doi 10.1016/S1470-2045(18)30148-7.

201. Paik S, Shak S, Tang G, Kim C, Baker J, Cronin M*, et al.* A multigene assay to predict recurrence of tamoxifen-treated, node-negative breast cancer. N Engl J Med **2004**;351(27):2817-26 doi 10.1056/NEJMoa041588.

202. Zhang YN, Zhou YD, Mao F, Sun Q. Impact of the 21-Gene Recurrence Score Assay in adjuvant chemotherapy selection for node-negative, hormone receptor-positive breast cancer in the Chinese population. Neoplasma **2015**;62(4):658-65 doi 10.4149/neo_2015_079.

203. Kaminska B. MAPK signalling pathways as molecular targets for anti-inflammatory therapy--from molecular mechanisms to therapeutic benefits. Biochim Biophys Acta **2005**;1754(1-2):253-62 doi 10.1016/j.bbapap.2005.08.017.

204. Sumimoto H, Imabayashi F, Iwata T, Kawakami Y. The BRAF-MAPK signaling pathway is essential for cancer-immune evasion in human melanoma cells. J Exp Med **2006**;203(7):1651-6 doi 10.1084/jem.20051848.

205. Wang W, Chen JX, Liao R, Deng Q, Zhou JJ, Huang S*, et al.* Sequential activation of the MEK-extracellular signal-regulated kinase and MKK3/6-p38 mitogen-activated protein kinase pathways mediates oncogenic ras-induced premature senescence. Mol Cell Biol **2002**;22(10):3389-403.

206. Kochetkova EY, Blinova GI, Bystrova OA, Martynova MG, Pospelov VA, Pospelova TV. Targeted elimination of senescent Ras-transformed cells by suppression of MEK/ERK pathway. Aging (Albany NY) **2017**;9(11):2352-75 doi 10.18632/aging.101325.

207. Ruscetti M, Leibold J, Bott MJ, Fennell M, Kulick A, Salgado NR*, et al.* NK cell-mediated cytotoxicity contributes to tumor control by a cytostatic drug combination. Science **2018**;362(6421):1416-22 doi 10.1126/science.aas9090.

ACKNOWLEDGMENTS

There are so many people who have supported, guided and inspired me during my PhD and I would like to thank all of them:

First, I would like to thank Prof. Dr. Olaf Witt for giving me the opportunity to work in the CCU Pediatric Oncology. Thanks to your translational focus and critical input I always questioned my hypotheses from different angles. You have created such a supportive and motivating work environment in your department. It was very inspiring to see how collaborative science can be.

I would like to thank my supervisor PD Dr. Till Milde: Dear Till, I cannot believe how lucky I have been to have you as my PhD supervisor and mentor. Your trust and belief in me allowed me to develop into an independent scientist and I am so thankful for all your support. I want to thank you for all the advice you have given me scientifically and personally, your calm, humorous and patient way of dealing with a project on senescence in LGG tumors, your fairness, reliability and crazy fast corrections.

I would like to thank my TAC members: Prof. Dr. Peter Angel for always keeping the focus on my project and all the invaluable input on cell signaling interactions; Prof. Dr. Tilman Brummer for his expertise in BRAF signaling and generous collaborative spirit; Prof. Dr. Thomas Hofmann for his invaluable input on senescence and a huge thank you to Dr. David Jones, my personal LGG guru, for always supporting me and my project with new ideas, precious PA samples, invaluable input and time.

I would like to thank Prof. Dr. Peter Angel, Prof. Dr. Frauke Melchior and Dr. Sevin Turcan for their willingness to participate in my thesis examination committee.

A big thank you to all of our collaborators and the amazing support each and every one of you provided to this exciting project: I would like to thank Thomas Hielscher for his support with the bioinformatic analyses, for helping out with last minute changes and providing us with high quality data in a speed of light timely fashion. I would like to thank all of the clinicians and scientists supporting our LGG project by providing tumor material: Prof. Dr. Martin Schuhmann, Prof. Dr. Christel Herold- Mende, Prof. Dr. David Capper, Dr. Mark Remke, Daniel Picard, Dr. Annika Wefers, Dr. Cornelis van Tilburg, Prof. Dr. Andreas von Deimling and Prof. Dr. Andrey Korshunov. Without your support our research would not be possible. I would like to thank Dr. Felix Sahm and his amazing team for their support and time invested in establishing IHC for the tricky cytokine receptors. I would like to thank Dr. Dennis Riehl and his amazing team for their support with the multiplex assay. I would like to thank Britta Ismer and Alexander Sommerkamp for providing us with the PA mouse model and all their invaluable help during the revision

process. Thanks both of you also for the great time we had in Denver and Cagliari. I would like to thank J.P. Maritnez-Barbera and Romain Guiho for their advice and fantastic help with the senolytic drug screen. I would like to thank Dr. Stefan Pusch for his support and advice on our cloning efforts. I would like to thank Dr. Jan Gronych for providing advice and support with the PA mouse model. I would like to thank Dr. Marcel Kool for has amazing support with gene-expression datasets and Prof. Dr. Stefan Pfister for his invaluable input, support and highly inspiring scientific and collaborative mindset.

Then, I would like to thank our amazing lab family! You all made this such a fun and enjoyable experience. I would like to thank Dr. Ina Oehme for her invaluable, critical input to the project and her amazing help during the manuscript preparation and revision phase. I would like to thank Dr. Heike Peterziel for teaching me the fascinating technique of brain slice co-cultures and for always being there for scientific advice. A special thank you goes to Florian, for taking me on board on the LGG project, for teaching me everything I needed to know to get started, for being a personal and scientific inspiration and so much fun to work with. I would like to thank Daniela, Carina and Isabel for enabling all of us to work in a beautifully organized and well running lab. A specially thank you goes to Daniela, for her amazing technical support, great patience with me, for all the funny lab chair races and I just wish I could take you with me. I would like to thank our technicians in training Anne Kittler and Lio Böse, who supported my project with their excellent work. Then I would like to thank our amazing “Postdoc office”, I don’t know where I would be without our morning coffees, so a huge thanks to: Ginny for her amazing humor, design expertise and for being such an inspiring power woman, Jonas for his invaluable input, inspiring scientific conversations and awesome parties in Kirchheim, Romain for his beautiful pathway pictures and knowing that the project will continue in excellent hands, Lisa for our fun trips to Mannheim and being an amazing Christmas decoration & singing companion, Diren for his infectious enthusiasm, Johanna for making us go climbing and giving us synergy math lessons, Jagoda for her calm, supportive spirit and for joining in on the Career Day organization, Sina for being the most inspiring Pharmacist I ever met, Johannes for just being himself and of course for his invaluable technical support in the lab with FACS and microscopy, Sara for her super cool fish experiments and inspiring courage, Emily for her kind support in the beginning of my PhD, our extremely talented and fun MD students Michael, Fiona, Katharina and Simon, and to Aileen, Alex, Ramona and Annika for always being there with advice and support. Also a big thank you to Nicola Hermann-Wichmann, for her amazing organizational skills and for always helping out with all the little questions outside of science.

Finally, I would like to thank my friends, family and husband for all their support, encouragement and fun distractions outside of the lab. I could not have done this without you!